Josephson Junctions and SQUIDs Based on CVD Graphene

Tianyi Li

A thesis submitted in partial fulfilment

of the requirements for the degree of

Doctor of Philosophy

Supervised by:

Dr Edward J Romans

Department of Electronic and Electrical Engineering

University College London

February 2019

I, Tianyi Li confirm that the work presented in this thesis is my own. Where information has been derived from other sources, I confirm that this has been indicated in the thesis.

Signature: Date:

Abstract

Josephson junctions and superconducting quantum interference devices (SQUIDs) with graphene as the weak link between the superconductors have been intensely studied in recent years, with respect to both fundamental physics and potential applications. Since the carrier density and resistivity of graphene are heavily dependent on the Fermi level, Josephson junctions and SQUIDs with graphene as the weak link can have their *I-V* properties easily tuned by the gate voltage. However, most of the previous work on superconductor-graphene-superconductor (SGS) Josephson junctions and SQUIDs was based on mechanically exfoliated graphene, which is not compatible with wafer-scale production.

In this project, we have greatly improved the availability and applicability of graphene-based Josephson junctions and SQUIDs. We developed a method to fabricate Josephson junctions and SQUIDs with graphene grown by chemical vapour deposition (CVD) as the weak link. We demonstrate that very short, wide CVD-graphene-based Josephson junctions with Nb electrodes can work without any undesirable hysteresis in the electrical characteristics from 1.5 K down to a base temperature of 320 mK, and the critical current can be effectively tuned by the gate voltage by up to an order of magnitude. As a result, dc SQUIDs made up of these junctions can have their critical current tuned by both the magnetic field and the gate voltage. We also obtained evidence for ballistic transport in SGS junctions as short as 50 nm.

We found that even for junction as wide as 80 μm, the critical current shows an ideal Fraunhofer-like interference pattern in a perpendicular magnetic field, indicating the distribution of supercurrent is uniform. We studied the definition of Josephson penetration depth, and proposed a new formula for 2D coplanar junctions.

Impact Statement

To enable academic impact, the research work performed in this project has been published in a series of journal publications:

[1] Li T, Gallop J, Hao L and Romans E 2019 Scalable, tunable Josephson junctions and dc SQUIDs based on CVD graphene *IEEE Trans. Appl. Supercond.* **29** 1101004

[2] Li T, Gallop J, Hao L and Romans E 2018 Ballistic Josephson junctions based on CVD graphene *Supercond. Sci. Technol.* **31** 045004

[3] Hao L, Gallop J, Li B, Cox D, Galer S, Li T, Godfrey T, Romans E and Nisbet A 2018 Investigation of properties of nanobridge Josephson junctions and superconducting tracks fabricated by FIB *J. Phys. Conf. Ser.* **964** 012004

[4] Ma L, Lu Z, Tan J, Liu J, Ding X, Black N, Li T, Gallop J and Hao L 2017 Transparent Conducting graphene hybrid films to improve electromagnetic interference (EMI) shielding performance of graphene *ACS Appl. Mater. Interfaces* **9** 34221–9

[5] Patel T, Li B, Li T, Wang R, Gallop J C, Cox D C, Chen J, Romans E J and Hao L 2017 Toward the Use of NanoSQUIDs to Measure the Displacement of an NEMS Resonator *IEEE Trans. Appl. Supercond.* **27** 1602005

[6] Lolli L, Li T, Portesi C, Taralli E, Acharya N, Chen K, Rajteri M, Cox D, Monticone E, Gallop J and Hao L 2016 Micro-SQUIDs based on MgB_2 nano-bridges for NEMS readout *Supercond. Sci. Technol.* **29** 104008

[7] Li T, Patel T, Banerjee I, Pearce-Hill R, Gallop J, Hao L and Ray A K 2015

Plasma treated graphene oxide films: structural and electrical studies *J. Mater. Sci. Mater. Electron.* **26** 4810–5

The work has also been disseminated in presentations at UK and international conferences including:

[1] ASC 2018, Oral, Seattle, USA, 2018.

[2] QTech 2018, Oral, Paris, France, 2018.

[3] SQD18, Oral, Teddington, UK, 2018.

[4] SQD17, Poster, Lancaster, UK, 2017.

[5] Advances in Quantum Transport in Low Dimensional Systems, Poster, London, UK, 2017.

[6] SQD16, Poster, Cambridge, UK, 2016.

[7] IOP Superconducting Group Winter Science Meeting, Poster, London, UK, 2015.

[8] SQD15, Poster, Egham, UK, 2015.

[9] IOP Superconducting Group Winter Science Meeting, Poster, Bath, UK, 2014.

These publications and conference presentations will benefit many researchers in academia and national laboratories in the fields of superconducting electronics, 2D materials, and quantum information processing, and help boost the prosperity in these fields. Through this project, I have made an industrial link with the Quantum Detection group in the National Physical Laboratory (NPL). The work performed in this collaboration has benefited NPL's research projects as part of the UK National

Measurement System and the European Metrology Programme for Innovation and Research in the fields of quantum detection and quantum metrology.

For impact outside the academia, the project will benefit the continuing development of quantum technology, which has many potential applications such as improving security by quantum cryptography and designing new medicines by quantum computing and quantum simulation. The project also facilitates the long-term development of related industrial sectors such as those supplying superconductor and 2D materials, cryogenics or electronic instrumentation.

Contents

List of Figures

List of Tables

Chapter 1 Overview

1.1 Objectives of the Project

Due to their unique non-linear inductance, Josephson junctions and dc superconducting quantum interference devices (SQUIDs) have become the building blocks and key elements of superconducting qubits, which are a promising solid-state approach to realising quantum computing. The non-linear inductance makes it possible to develop anharmonic LC oscillator circuits with unequally spaced quantised energy levels, so that the lowest two states can be treated as the $|0\rangle$ and $|1\rangle$ state of a qubit and be uniquely addressable. When scaling up designs for more than one superconducting qubit, some of the qubits and their coupling resonators are required to have exactly the same energy-level spacing between $|0\rangle$ and $|1\rangle$ in order to achieve high-fidelity multi-qubit gates. However, due to limitations in fabrication techniques, it is almost impossible to make perfectly identical Josephson junctions based on conventional sandwich structures. Such a problem is normally solved by replacing a single Josephson junction with a dc SQUID and accompanying it with a nearby current-carrying control line. As a result, the critical current of the SQUID can be tuned by the local magnetic field, so that the energy-level spacing of the qubit or the resonator can also be tuneable. However, as the number of qubits and the number of coupling resonators increases on a chip, the configuration of magnetic current leads can become challenging, and crosstalk between magnetic fields will become a significant source of error. Therefore, Josephson junctions and dc SQUIDs with other degrees of freedom in their electronic properties are highly desirable.

The distinct band structure of graphene means that superconductor-graphene-superconductor (SGS) Josephson junctions have a critical current that can be

gradually tuned by a local electric gate. Since the first SGS junction was experimentally implemented by Heersche *et al*. in 2007, graphene-based Josephson junctions and SQUIDs have become a hot topic of research in the last decade, and many novel phenomena including multiple Andreev reflection and ballistic transport have been discovered and discussed. Previous research on SGS junctions and SQUIDs was mostly based on mechanically exfoliated graphene, which is not compatible with large-scale synthesis and device fabrication. The fabrication and measurement of SGS junctions compatible with real applications in superconducting circuits remains largely unexplored, and integrating SGS junctions and SQUIDs into superconducting qubits is still some way off.

Hence, the overall objective of my PhD project was to increase the availability and applicability of graphene-based Josephson junctions and SQUIDs. This was achieved firstly by developing techniques to fabricate Josephson junctions and SQUIDs based on graphene synthesised by chemical vapour deposition (CVD). As we will show such graphene samples have good enough electronic properties, and are compatible with large-scale synthesis and conventional micro-fabrication technology. We will study the electronic properties of those SGS junctions and SQUIDs at low temperature, particularly focusing on understanding the tuneability by the gate voltage and examine evidence for ballistic transport. We will also study new geometries allowed by using 2D material like graphene, such as 4-probe junctions, and the unique properties of the those SGS junctions, such as the ultra-long Josephson penetration depth.

1.2 Structure of the Thesis

The structure of the thesis is as follows:

In the next three chapters we will introduce the background to this project. In

Chapter 2, we will give a brief introduction to Josephson junctions and dc SQUIDs. Based on the resistively- and capacitively-shunted junction (RCSJ) model, we will obtain a quantitative understanding of the electronic characteristics of Josephson junctions and dc SQUIDs, and the effect of shunt resistance, shunt capacitance, thermal fluctuations, and microwave radiation etc. We will also introduce the two common methods to implementing Josephson elements: tunnel junctions and weak links, and discuss the difference in their electronic properties.

In Chapter 3, we will introduce the required background knowledge of graphene. We will give a brief introduction to the molecular and electronic structure of graphene, and enumerate the synthesis and characterisation techniques used to obtain and study it. The advantages and disadvantages of different synthesis and post-treatment techniques will be compared and act as our guide for choosing graphene samples for device fabrication.

In Chapter 4, we will make a detailed review of the previous work in the literature on graphene-based Josephson junctions and SQUIDs. We will make a list of all the related publications and compare their experimental results. We will show how the supercurrent is modulated by the gate voltage, which is a result of the bipolar density of states of graphene. Other commonly discussed topics in the literature including the depression of the product I_0R_n around the Dirac point, the observation of specular Andreev reflection and ballistic transport will also be introduced.

In Chapters 5-9 we will describe the main experimental work and results of my PhD project. In Chapter 5, the fabrication process of graphene-based Josephson junctions and SQUIDs will be discussed. We will start with the selection of graphene samples, which was based on their characterisation by atomic force microscope (AFM) and Kelvin probe force microscope (KPFM), and the measurements of their electronic properties. Then we will describe the fabrication process developed based on electron

beam lithography (EBL) patterning and lift-off, and discuss the optimisation of the fabrication parameters in detail.

In Chapter 6, we will present the detailed measurement results and analysis for the developed SGS Josephson junctions, including the electronic characteristics as a function of temperature, magnetic field, gate voltage and microwave radiation. We will also describe the evidence for ballistic transport in the shortest SGS junctions. We will then describe 4-probe SGS Josephson junctions, which consist of four superconducting electrodes directly connected to graphene. The critical current of those junctions can be tuned by the distribution of the current between the electrodes, which we will demonstrate is a thermal effect.

In Chapter 7, we will present the measurement results for the developed SGS dc SQUIDs. Similarly to the junction measurements, we will study how the electronic characteristics of the SQUIDs depend on the magnetic field and gate voltage. The asymmetry and the sensitivity of the SQUIDs will be estimated based on the measurement results.

In Chapter 8, we will focus on the Josephson penetration depth of SGS junctions. We will show both analytically and numerically that the definition of Josephson penetration depth for normal tunnel junctions is not valid for 2D coplanar junctions such as SGS junctions. The numerical calculation also predicts how the interference pattern under a perpendicular magnetic field will be affected when the junction width is larger than the Josephson penetration depth. We will also describe our experimental study of the manually introduced edge effect, where we try and control the junction width with a gate.

Finally in Chapter 9, we will make a summary of the whole project, and make suggestions for future work.

Chapter 2 Introduction to Josephson Junctions and dc SQUIDs

In this chapter, we briefly introduce the background knowledge of Josephson junctions and dc SQUIDs. In Section 2.1, we will start with the two Josephson relations, then introduce the resistively- and capacitively-shunted junction (RCSJ) model which describes the electronic properties of a Josephson junction with shunted resistance and capacitance, under the effect of thermal fluctuations and microwave radiation. We will then describe the quantum interference in a wide Josephson junction and conditions for realising a Fraunhofer-like interference pattern. In Section 2.2, we will introduce two common types of Josephson junctions: tunnel junctions and weak links; and compare the difference in the current-phase relations. In Section 2.3, we will introduce dc SQUIDs, and use the RCSJ model to predict their electronic properties.

2.1 Josephson junctions

2.1.1 Josephson effect

First observed by Kamerlingh-Onnes in 1911, superconductivity is a novel phenomenon that a material experiences a complete loss of electrical resistance to a flow of direct current, below a characteristic transition temperature T_c. When a material enters the superconducting state from the normal state, charge carriers (electrons or holes) tend to form Cooper pairs with charge of magnitude $2e$ [1]. The Cooper pairs are described by a macroscopic wave function or complex order parameter

$$\Psi(\boldsymbol{r},t) = \Psi_0(\boldsymbol{r},t)\exp[i\phi(\boldsymbol{r},t)] \tag{2.1}$$

which is a function of both position and time. The order parameter $|\Psi_0|^2$, is proportional to the density of Cooper pairs. The Cooper pairs can be excited to quasi-particles (electron- or hole-like excitations that are not paired), and the energy to excite a Cooper pair is 2Δ, where $\Delta(T)$ is referred to as the superconducting energy gap. At $T = 0$, all of the free electrons are bound as Cooper pairs, and the order parameter is at its maximum. As temperature increases, more Cooper pairs are broken into quasi-particles, and the order parameter decreases. When approaching T_c, the order parameter goes to zero.

Similar to the quantum mechanical relationship for the current due to a single electron, we can derive the supercurrent density carried by Cooper pairs in the presence of a magnetic vector potential $\boldsymbol{A}$

$$\boldsymbol{j}_s = -\frac{ie\hbar}{m}(\Psi^*\nabla\Psi - \Psi\nabla\Psi^*) - \frac{4e^2\boldsymbol{A}}{m}\Psi^*\Psi \tag{2.2}$$

Using Eq. (2.1) for Ψ, we can deduce that

$$\boldsymbol{j}_s = \frac{2e\hbar}{m}|\Psi_0|^2\nabla\phi - \frac{4e^2\boldsymbol{A}}{m}|\Psi_0|^2 = \frac{2e\hbar}{m}|\Psi_0|^2\left(\nabla\phi - \frac{2\pi}{\Phi_0}\boldsymbol{A}\right) \tag{2.3}$$

where $\Phi_0 \equiv h/2e \approx 2.067 \times 10^{-15}$ Wb is the flux quantum.

A Josephson junction is formed when two superconductors are separated from each other by a thin barrier (usually insulator) through which Cooper pairs can tunnel [2,3]. Similar Josephson effect also displays if the two superconductors are connected through normal metal or weakened superconductor. The geometry and properties of

various types of Josephson junctions will be discussed in Section 2.2. Here, for simplicity, let's start with the one-dimensional sandwich structure shown schematically in Figure 2.1. In this geometry, the supercurrent only flows in the z direction, so Eq. (2.3) becomes

$$j_{s,z} = \frac{2e\hbar}{m}|\Psi_0|^2\left(\frac{d\phi}{dz} - \frac{2\pi}{\Phi_0}A_z\right) = \frac{2e\hbar}{m}|\Psi_0|^2\frac{d\varphi}{dz} \tag{2.4}$$

where we have defined $\varphi(z) = \phi(z) - \frac{2\pi}{\Phi_0}\int_0^z A_z dz$. Current conservation requires that $j_{s,z}$ to be constant in the z direction, which means the product $|\Psi_0|^2 d\varphi/dz$ must have the same value everywhere. At the barrier, the Cooper pair density $|\Psi_0|^2$ is strongly reduced. Therefore, $d\varphi/dz$ must be much larger than in the bulk superconductors, which means $\varphi(z)$ experiences a step-like jump at the barrier:

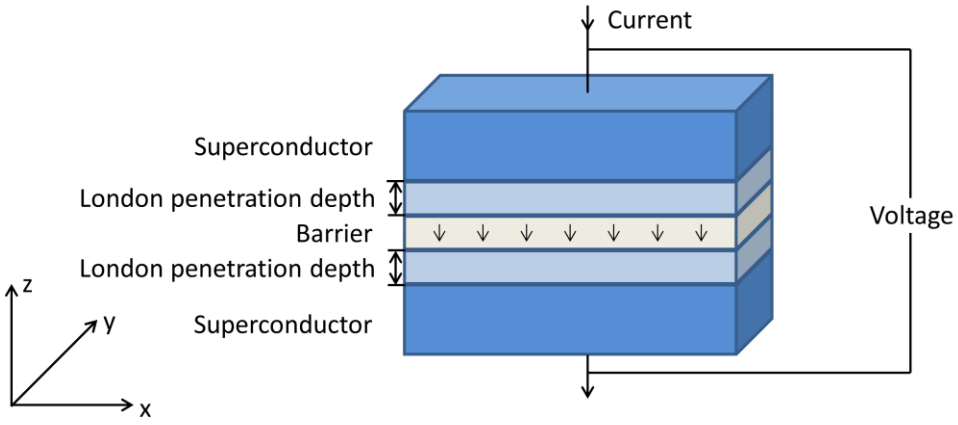

Figure 2.1 Schematic diagram of a Josephson junction with a sandwich structure. Compared with the barrier thickness and the London penetration depth, the dimensions of the junction in the *x* and *y* directions are much larger, so that the sandwich structure can be studied in a one-dimensional model.

$$\varphi = \phi_2 - \phi_1 - \frac{2\pi}{\Phi_0}\int_1^2 A_z dz \tag{2.5}$$

where "1" and "2" are positions near either side of the barrier. φ is defined as the "gauge invariant phase difference".

For a given junction, if the spatial dependence on z of Cooper pair density $|\Psi_0|^2$ is specified, the spatial dependence on z of $d\varphi/dz$ is also specified. It can only differ by a common factor, which will result in φ differing by the same factor. Therefore, the supercurrent across the barrier essentially becomes a function of the gauge invariant phase difference, i.e. $I_s = I_s(\varphi)$. A 2π change of the phase difference φ should yield the same wave function, and hence, the same supercurrent across the barrier. The supercurrent can be expanded as a Fourier series consisting of sine and cosine terms. The requirement of time reversal symmetry eliminates all the cosine terms, and thus the supercurrent can be written as

$$I_s = \sum_{k=1}^{\infty} I_{0,k} \sin k\varphi \tag{2.6}$$

It is found that, for many types of junction, this series converges very rapidly, i.e. only the first term needs to be considered, and we obtain the first Josephson relation

$$I_s = I_0 \sin \varphi \tag{2.7}$$

where I_0 is known as the critical current. The first Josephson relation is also regarded as dc Josephson effect.

To obtain the second Josephson relation, we can take the time derivative of Eq.

(2.5),

$$\dot{\varphi} = \dot{\phi}_2 - \dot{\phi}_1 - \frac{2\pi}{\Phi_0}\int_1^2 \dot{A}_z dz \tag{2.8}$$

Since the macroscopic wave function evolves as $\Psi \exp(-iEt/\hbar)$, the difference $\dot{\phi}_2 - \dot{\phi}_1$ is related to the energy difference of the two superconductors, $\dot{\phi}_2 - \dot{\phi}_1 = -(E_2 - E_1)/\hbar$, and the time derivative of the vector potential is related to the induced electrostatic potential. Therefore, the time derivation of the gauge invariant phase difference is determined by the total voltage difference U across the barrier, and we obtain the second Josephson relation (regarded as ac Josephson effect)

$$\frac{d\varphi}{dt} = \frac{2eU}{\hbar} \tag{2.9}$$

The two Josephson relations (Eq. (2.7) and (2.9)) are the basic rules to describe the Josephson effect. However, it is worth noticing that there is a significant difference between the two relations. Eq. (2.9) is derived solely from the main principles of quantum mechanics and contains only fundamental constants, while Eq. (2.7) is an approximate one, and we will discuss deviations from it in Section 2.2.

According to the two Josephson relations, if no voltage is applied across the junction, the phase difference is constant in time. A dc supercurrent with maximum value I_0 can flow across the junction. If a finite voltage is applied across the junction, the phase difference keeps increasing or decreasing with time, and the supercurrent will oscillate with the Josephson frequency $f_\mathrm{J} = V/\Phi_0$, where V is the time averaged voltage across the junction $\langle U(t)\rangle$. In this dynamic regime, besides the supercurrent I_s, we also need to consider the quasiparticle current I_qp and the

displacement current I_{d}. That leads to the "resistively- and capacitively-shunted junction model" (RCSJ model) which is discussed below.

2.1.2 RCSJ Model

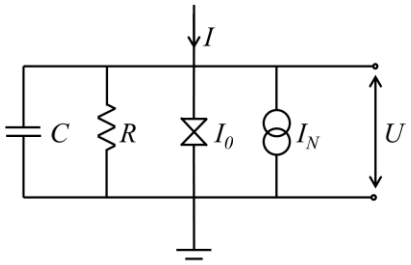

Figure 2.2 The equivalent circuit of a Josephson junction with the RCSJ model. A Josephson junction with critical current I_0 is shunted by a resistor R, a capacitor C and noise current source I_N.

The current-voltage (I-V) characteristics of most Josephson junctions are well described by the resistively- and capacitively-shunted junction (RCSJ) model [4,5]. In the following sections, we will show the electronic properties of Josephson junctions and dc SQUIDs based on the RCSJ model. We will only show the theoretical results that are crucial for the analysis of our experiments. For a complete theory, we recommend the textbook Ref. [6].

As the equivalent circuit shown in Figure 2.2, the Josephson junction which has a critical current I_0 is in parallel with a resistance R and a capacitance C. The characteristic voltage is defined as $V_{\mathrm{c}} \equiv I_0 R$, and the Josephson frequency at the characteristic voltage is defined as characteristic frequency $\omega_{\mathrm{c}} \equiv 2\pi I_0 R/\Phi_0$. In such a model, the current flowing through the device is a sum of the supercurrent I_{s}, the displacement current I_{d} and the quasiparticle current I_{qp}:

$$I = I_0 \sin\varphi + C\dot{U} + \frac{U}{R} \tag{2.10}$$

Using the second Josephson relation, the equation above can be written as a function of φ:

$$\frac{\Phi_0}{2\pi} C\ddot{\varphi} + \frac{\Phi_0}{2\pi}\frac{1}{R}\ \dot{\varphi} + I_0 \sin\varphi = I \tag{2.11}$$

Here we can introduce the Stewart-McCumber parameter (also called the hysteresis parameter) which determines whether hysteresis appears in the *I-V* characteristics

$$\beta_c = \frac{2\pi}{\Phi_0} I_0 R^2 C \tag{2.12}$$

In the strongly overdamped limit ($\beta_c \ll 1$), which corresponds to a negligible capacitance, the first term in Eq. (2.11) can be neglected. The *I-V* characteristics can be obtained by solving Eq. (2.11), which gives

$$V = 0 \qquad \text{for} \quad I < I_0$$

$$V = I_0 R\sqrt{(I/I_0)^2 - 1} \qquad \text{for} \quad I \geq I_0 \tag{2.13}$$

Note that here V is the dc component of junction voltage. As shown in Figure 2.3(a), no hysteresis appears in the *I-V* characteristics of Josephson junction in the overdamped limit.

In the strongly underdamped limit ($\beta_c \gg 1$), strong hysteresis appears in the *I-V* characteristics. When the current is increased from zero, the junction stays in the

zero-voltage state until the current reaches I_0. In contrast, when the current is reduced from above I_0, the dc voltage remains finite even for $I < I_0$ until the current decreases to zero.

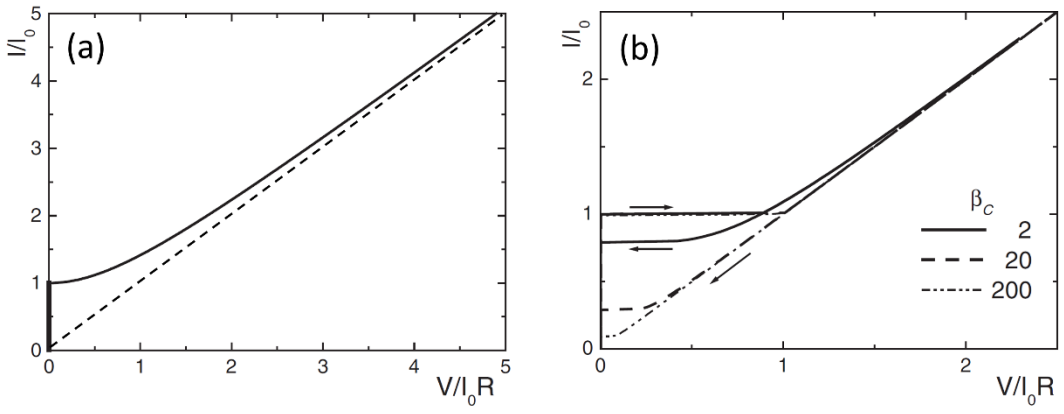

Figure 2.3 *I-V* characteristics calculated within the RCSJ model. (a) A strongly overdamped junction. (b) Several intermediately damped junctions. The dashed line in (a) shows the slope of 1/*R* as a guidance for eyes. Reproduced from Ref. [6] with permission from John Wiley and Sons.

In the general case of finite β_c, the *I-V* characteristics of the junction can be obtained by solving Eq. (2.11) numerically. Figure 2.3(b) shows some calculated *I-V* characteristics for different values of β_c. We can see that as β_c increases, stronger hysteresis is seen in the *I-V* characteristics. In order to obtain non-hysteretic Josephson junctions for practical application, the Stewart-McCumber parameter β_c should be below 1. In order to reach such a limit, a shunt resistance is often fabricated in parallel to the Josephson junction. However, the calculation above doesn't take thermal noise into consideration. At finite temperature, the hysteresis can be suppressed if β_c is not too large, as we will see in the next section. Therefore, the restriction on β_c for a non-hysteretic junction can be loosened a bit.

2.1.3 Effect of Thermal Fluctuation

At nonzero temperature, according to RCSJ model, the thermal fluctuations result in the classical Nyquist-Johnson noise. The power spectral density of current noise is

$$S_{\mathrm{I}}(f) = \frac{4k_{\mathrm{B}}T}{R} \tag{2.14}$$

where k_{B} is the Boltzmann constant. The spectral density is independent of frequency, thus is called white noise. The thermal noise level is usually characterised by the noise parameter Γ, which is defined as the ratio of the thermal energy to the Josephson energy $E_{\mathrm{J}} = I_0\Phi_0/2\pi$

$$\Gamma \equiv \frac{2\pi k_{\mathrm{B}}T}{I_0\Phi_0} \tag{2.15}$$

To work out the effect of the fluctuating current on the dc *I-V* characteristics, we can simply add a noise term to Eq. (2.11)

$$\frac{\Phi_0}{2\pi}C\ddot{\varphi} + \frac{\Phi_0}{2\pi}\frac{1}{R}\ \dot{\varphi} + I_0\sin\varphi = I + I_{\mathrm{N}}(t) \tag{2.16}$$

which is called the Langevin equation. The current noise is described by the following statistical properties

$$\langle I_{\mathrm{N}}(t)\rangle = 0 \quad \text{and} \quad \langle I_{\mathrm{N}}(t)I_{\mathrm{N}}(t+t_i)\rangle = \frac{2k_{\mathrm{B}}T}{R}\delta(t_i) = \frac{\Gamma I_0\Phi_0}{2\pi R}\delta(t_i) \tag{2.17}$$

with the definition of the delta function $\delta(t) = \frac{1}{\pi}\int_0^\infty \cos\omega t\, d\omega$.

The brackets here mean a statistical average over probable values for I_N at different times. The Langevin equation can be solved numerically and the dc *I-V* curves obtained are shown in Figure 2.4.

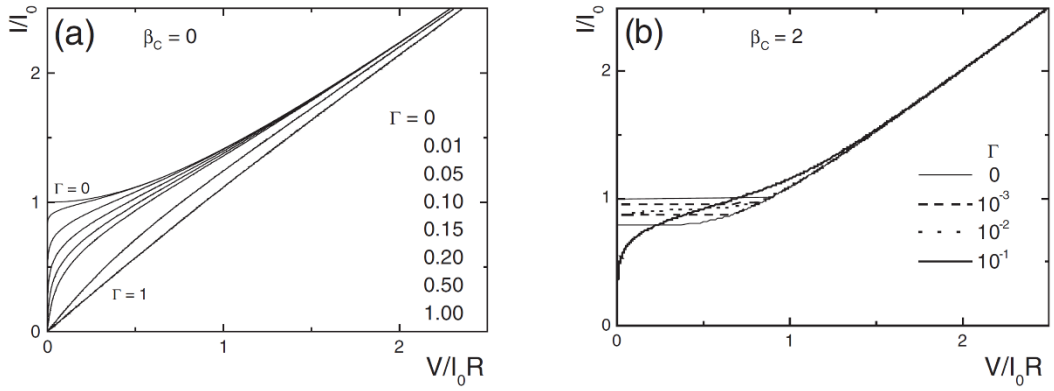

Figure 2.4 *I-V* characteristics calculated with RCSJ model with various values of noise parameter Γ. (a) A strongly overdamped junction. (b) An intermediately damped junction. Reproduced from Ref. [6] with permission from John Wiley and Sons.

For a strongly overdamped junction ($\beta_c = 0$), the *I-V* curve is rounded due to the thermal noise, as shown in Figure 2.4(a). That results in a decrease of the observed value of critical current as Γ increases. When Γ exceeds 0.2, it becomes difficult to determine a critical current.

In the case of finite β_c, the existence of a noise term can suppress the hysteresis in the *I-V* characteristics. As shown in Figure 2.4(b), which is obtained by numerical solution of Langevin equation with $\beta_c = 2$, the hysteresis becomes less obvious as Γ increases, and finally disappears when $\Gamma = 0.1$.

2.1.4 Shapiro Steps

Up to now, we have only considered the behaviour of a Josephson junction under a dc

current. If we apply add an ac component to the dc current, Eq. (2.11) would become

$$\frac{\Phi_0}{2\pi}C\ddot{\varphi} + \frac{\Phi_0}{2\pi}\frac{1}{R}\ \dot{\varphi} + I_0 \sin\varphi = I + I_{\mathrm{ac}} \sin\omega_{\mathrm{ac}} t \tag{2.18}$$

The most noticeable consequence of the ac term is the occurrence of constant voltage steps in the *I-V* curves (Shapiro steps), as shown in Figure 2.5. The voltage steps are of equal intervals, which only depend on the frequency of the ac component,

$$V_n = nV_1 = \frac{n\Phi_0\omega_{\mathrm{ac}}}{2\pi} \qquad (n = 0, 1, 2 \ldots) \tag{2.19}$$

while the lengths of the steps are functions of the ac current amplitude

$$\Delta I_n = \ |J_n(x)| \quad \text{with } x \equiv \frac{2\pi I_{\mathrm{ac}} R}{\omega_{\mathrm{ac}}\Phi_0\sqrt{1 + \frac{\omega_{\mathrm{ac}}^2\Phi_0 C}{2\pi I_0}}} = \frac{I_{\mathrm{ac}}\omega_{\mathrm{c}}}{I_0\omega_{\mathrm{ac}}\sqrt{1 + \frac{\omega_{\mathrm{ac}}\beta_{\mathrm{c}}}{\omega_{\mathrm{c}}}}} \tag{2.20}$$

where J_n is the first-kind Bessel function of order n.

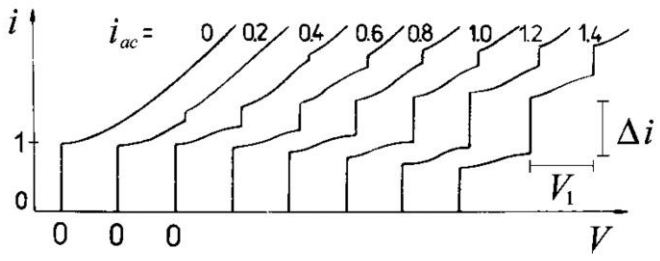

Figure 2.5 *I-V* characteristics of a Josephson junction driven by a dc current and an additional ac current. The different curves refer to ac currents of different normalised amplitudes $i_{\mathrm{ac}} = I_{\mathrm{ac}}/I_0$ at frequency $\omega_{\mathrm{ac}} = \omega_{\mathrm{c}} \equiv 2\pi I_0 R/\Phi_0$, calculated with RCSJ model. Reproduced from Ref. [6] with permission from John Wiley and Sons.

The fact that the interval of Shapiro steps is only related to the frequency of the ac current allows Josephson junctions to be widely used as the voltage standard in metrology [7,8]. Experimentally, the ac current can be applied by either directly connecting the junction to an ac current source, or by exposing the junction to microwave radiation.

2.1.5 Quantum Interference in Finite Size Junctions

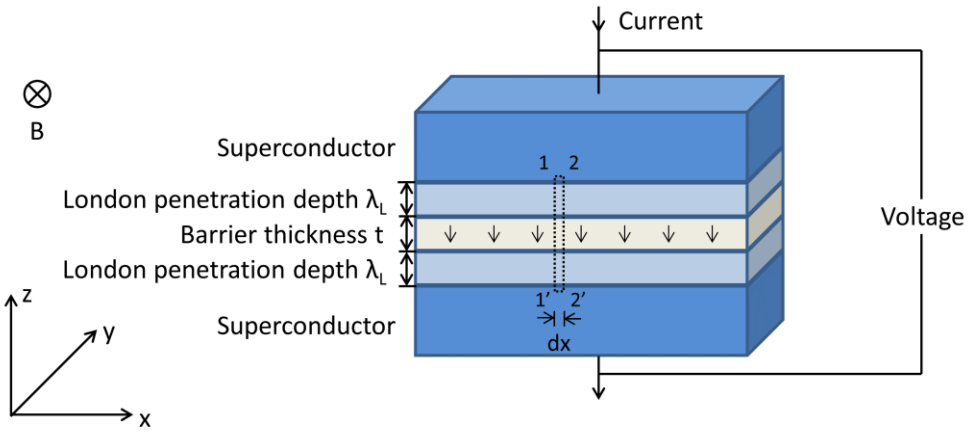

Figure 2.6 Schematic diagram of a Josephson junction in a magnetic field. The integration path is shown by the dotted line.

So far, we have assumed that the gauge invariant phase difference is uniform in the junction plane, and so is the critical current density. However, if we consider a finite size junction in the presence of a magnetic field, this assumption is no longer valid. Figure 2.6 shows the geometry where an external field is applied in the y direction and a current flow through the junction in the z direction. The gauge invariant phase difference φ will vary along the x direction. According to Eq. (2.5)

$$\varphi(x+dx)-\varphi(x)=\phi(2')-\phi(2)-\frac{2\pi}{\Phi_0}\int_2^{2'}A_z dz-\left[\phi(1')-\phi(1)-\frac{2\pi}{\Phi_0}\int_1^{1'}A_z dz\right]$$

$$=[\phi(2')-\phi(1')]+[\phi(1)-\phi(2)]+\left[\frac{2\pi}{\Phi_0}\int_1^{1'}A_z dz-\frac{2\pi}{\Phi_0}\int_2^{2'}A_z dz\right] \tag{2.21}$$

The differences $\phi(2')-\phi(1')$ and $\phi(1)-\phi(2)$ can be obtained by integration of Eq. (2.3):

$$\phi(2')-\phi(1')=\frac{m}{2e\hbar|\Psi_0|^2}\int_{1'}^{2'}\boldsymbol{j}_s\cdot d\boldsymbol{l}-\frac{2\pi}{\Phi_0}\int_{2'}^{1'}\boldsymbol{A}\cdot d\boldsymbol{l}$$

$$\phi(1)-\phi(2)=\frac{m}{2e\hbar|\Psi_0|^2}\int_{2}^{1}\boldsymbol{j}_s\cdot d\boldsymbol{l}-\frac{2\pi}{\Phi_0}\int_{1}^{2}\boldsymbol{A}\cdot d\boldsymbol{l} \tag{2.22}$$

Therefore,

$$\varphi(x+dx)-\varphi(x)=\frac{m}{2e\hbar|\Psi_0|^2}\left[\int_2^1\boldsymbol{j}_s\cdot d\boldsymbol{l}+\int_{1'}^{2'}\boldsymbol{j}_s\cdot d\boldsymbol{l}\right]+\frac{2\pi}{\Phi_0}\oint\boldsymbol{A}\cdot d\boldsymbol{l} \tag{2.23}$$

Since the integration of supercurrent density can be done along paths in the bulk of superconductors where the current density is exponentially small, the first term is thus exponentially small and can be neglected. The integration of the vector potential is equal to the flux through the integration path, yielding

$$\frac{d\varphi}{dx} = \frac{2\pi\Phi}{\Phi_0} \tag{2.24}$$

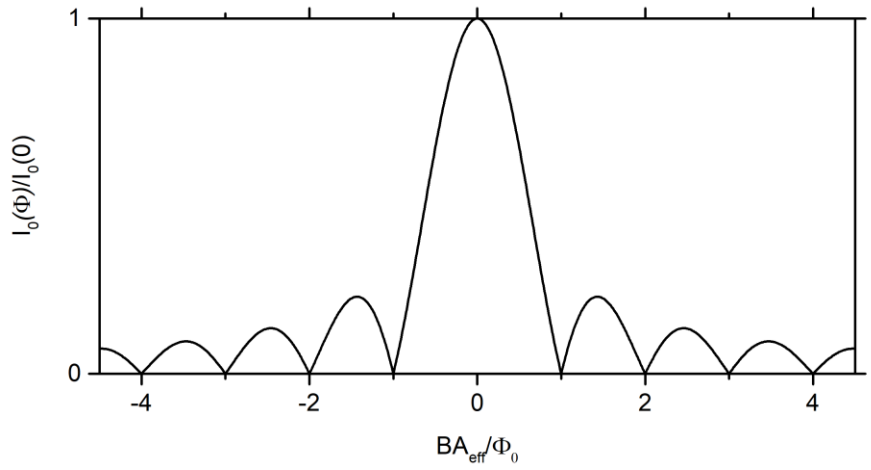

Figure 2.7 The critical current of a finite size junction as a function of applied magnetic field. The curve is similar to the optical Fraunhofer pattern of single slit.

The supercurrent across the junction is obtained by integration of the current density over the junction plane, and a pattern similar to the optical Fraunhofer pattern of single slit is formed due to the interference among current density with different phase. As shown in Figure 2.7, with the presence of external magnetic field B, the critical current of the junction is given by

$$I_0(\Phi) = I_0(0)\left|\frac{\sin(\pi B A_{\text{eff}}/\Phi_0)}{\pi B A_{\text{eff}}/\Phi_0}\right| \tag{2.25}$$

where $I_0(0)$ is the critical current without magnetic field, and A_{eff} is the effective area of the junction, which equals the effective length of the junction $t + 2\lambda_{\text{L}}$ times the junction width. λ_{L} is the London penetration depth, which is defined as the

characteristic length of the decay of the supercurrent and the magnetic field from the edge of the bulk superconductor.

2.1.6 Josephson Penetration Depth

In the last section, we have only discussed the effect of external magnetic field while ignoring the magnetic field generated by the supercurrent itself. In fact, the effect of the magnetic field generated by the supercurrent tends to redistribute the supercurrent so that the supercurrent would tend to accumulate at the edges of the junction. The supercurrent density would exponentially decay from its maximum on the edges of the junction as moving towards the centre of the junction, and the corresponding characteristic length is the so-called "Josephson penetration depth" λ_{J} [9]. Note that it should be distinguished from the London penetration depth λ_{L}.

Let's still consider the geometry shown in Figure 2.6, but assume the external magnetic field is zero. The local gauge invariant phase difference across the junction φ satisfies

$$\varphi(x+dx)-\varphi(x)=\frac{2\pi}{\Phi_0}\oint \boldsymbol{B}\cdot d\boldsymbol{s} \tag{2.26}$$

where $\boldsymbol{B}$ is the magnetic field generated by the supercurrent. Assuming a uniform magnetic field, $\oint \boldsymbol{B}\cdot d\boldsymbol{s}=B_y(t+2\lambda_{\mathrm{L}})dx$, where t is the thickness of the barrier and λ_{L} is the London penetration depth. Differentiating twice with respect to x, we obtain

$$\frac{\partial^2\varphi}{\partial x^2}=-\frac{2\pi(t+2\lambda_{\mathrm{L}})}{\Phi_0}\frac{\partial B_y}{\partial x} \tag{2.27}$$

The magnetic field generated by the supercurrent follows the Maxwell equations. In the static case, the magnetic field is governed by the 3rd and 4th Maxwell equations. The magnetic field will have no component in the *z* direction, and if we assume the junction is infinitely long in the *y* direction, all *y* derivatives of the magnetic field will be zero. As a result, the 4th Maxwell equation simply becomes

$$\frac{\partial B_y}{\partial x} = -\mu_0 j = -\mu_0 j_0 \sin\varphi \tag{2.28}$$

where j is the local supercurrent density, which according to the first Josephson relation, equals the critical current density j_0 times $\sin\varphi$. Substituting this into the equation above yields

$$\frac{\partial^2 \varphi}{\partial x^2} = \frac{2\pi(t + 2\lambda_{\mathrm{L}})}{\Phi_0} \mu_0 j_0 \sin\varphi \tag{2.29}$$

In the $\varphi \to 0$ limit, given a boundary condition at the edge of the junction, the local gauge invariant phase difference φ will decay nearly exponentially as approaching the centre of the junction, as does the supercurrent density j. Therefore, the Josephson penetration depth can be defined as

$$\lambda_{\mathrm{J}} = \sqrt{\frac{\Phi_0}{2\pi\mu_0 j_0 (t + 2\lambda_{\mathrm{L}})}} \tag{2.30}$$

For conventional low-T_c sandwich-structure tunnel junctions, the Josephson penetration depth is typically in the range of tens of micrometres, which is larger than the dimension (in the *x* direction) of most of the junctions. Thus, the effect of the magnetic field generated by the supercurrent can be neglected, and the critical current gives an ideal Fraunhofer-like pattern under external magnetic field.

2.2 Different Types of Josephson Junctions

2.2.1 Tunnel Junctions

Since the 1960s, Josephson junctions have been implemented in a wide range of materials using a vast variety of techniques. Essentially, these implementations can be divided into two categories: tunnel junctions where the barrier is insulator (S-I-S junctions), and weak-link junctions where the barrier is normal metal, doped semiconductor or weak superconductor (S-N-S, S-Se-S or S-S'-S junctions). We will introduce the tunnel junction in this section and leave weak-link junctions to the next section.

Tunnel junctions were extensively studied both theoretically and experimentally, especially at the early stage of Josephson effect research. In a tunnel junction, the Cooper pairs can tunnel through a region where they are classically forbidden, which is purely a quantum mechanical effect. Modern methods to fabricate tunnel junctions oxidised usually use Al or Nb as the superconducting electrodes, and AlO_x as the tunnel barrier. These materials are normally in-situ deposited to form a "sandwich" structure. To allow for a finite critical current density of 1~100 A/cm^2, the tunnelling barrier thickness is usually in the order of several nanometres, which is negligibly small compared to all other characteristic lengths in the superconductor, such as the coherence length ξ and the mean free path of the electrons l. This means that the tunnel barrier can be treated integrally, without introducing coordinate dependences of the superconducting energy gap Δ and local order parameter Ψ.

Such assumptions greatly simplify theoretical analysis. As shown by the Ambegaokar-Baratoff theory [10], the supercurrent in a tunnel junction always follows the sinusoidal relation shown in Eq. (2.7), and the critical current satisfies

$$I_0 = \frac{\pi}{2}\frac{\Delta(T)}{eR_\mathrm{n}}\tanh\frac{\Delta(T)}{2k_\mathrm{B}T} \tag{2.31}$$

where $\Delta(T)$ is the equilibrium value of the energy gap of the superconducting electrodes at temperature T, and R_n is the normal state resistance of the junction (equals the shunt resistance R in the RCSJ model). The normalised energy gap $\Delta(T)/\Delta(0)$ has been tabulated as a function of the normalised temperature T/T_c in the literature [11]. As an approximation, the energy gap can be written as

$$\Delta(T) \approx \Delta(0)\left[1 - \frac{2\pi k_\mathrm{B}T}{\Delta(0)}\exp\left(-\frac{\Delta(0)}{k_\mathrm{B}T}\right)\right] \tag{2.32}$$

for $T \leq 0.6T_\mathrm{c}$, with $\Delta(0) \approx 1.765k_\mathrm{B}T_\mathrm{c}$. As $T \to T_\mathrm{c}$, the energy gap falls off rapidly

$$\Delta(T) \approx 1.736\ \Delta(0)\sqrt{1 - T/T_\mathrm{c}} \tag{2.33}$$

Eq. (2.31) also indicates an interesting relation that the characteristic voltage satisfies

$$V_\mathrm{c} \equiv I_0R_\mathrm{n} = \frac{\pi}{2}\frac{\Delta(T)}{e}\tanh\frac{\Delta(T)}{2k_\mathrm{B}T} \tag{2.34}$$

which does not depend on any parameters of the barrier, and is solely determined by the operating temperature and the property of the superconductors.

Thanks to their mature fabrication techniques, tunnel junctions play a major role in many practical applications of Josephson junctions and SQUIDs nowadays, including superconducting qubits which are a promising candidate for implementing quantum computing. Tunnel junctions are almost perfect in every parameter except for the

large capacitance caused by the sandwich structure. The large capacitance will result in a large Stewart-McCumber parameter β_c, which tends to cause hysteresis in the *I-V* characteristics. That limits the application of tunnel junctions in certain areas, where weak-link junctions can be appreciated.

2.2.2 Weak-Link Junctions

Unlike in tunnel junctions where the barrier is insulator, in weak-link junctions, the barrier material is normal metal, doped semiconductor or weak superconductor. Actually, doped semiconductor can be treated in a similar way as normal metal, so we don't distinguish doped semiconductor from normal metal in this section. For an S-N-S junction, at the S-N interface, some Cooper pairs will penetrate into the normal region from the superconductor, resulting in a nonzero order parameter Δ in the normal metal and a reduction of order parameter in the superconductor. Such a phenomenon is called the superconducting proximity effect. The decay of order parameter in the superconductor happens in the range of the Ginzburg-Landau coherence length ξ_{GL} from the boundary, whereas in the normal metal the order parameter decreases over a distance of the order of normal state coherence length ξ_n. Thus, if the thickness of the normal metal is less than or comparable with ξ_n, there will be nonzero order parameter all the way from one superconductor to the other, so that a finite supercurrent can flow through the interlayer. For an S-S'-S junction, similar proximity effect will also happen, so that the order parameter changes gradually at the interface between two kinds of superconductors. For either an S-N-S or S-S'-S weak-link junction, we define the effective length L_{eff} to be the range where the order parameter varies from its bulk value in the electrodes. That means the effective length is usually larger than the geometric length of a junction. A weak-link junction is called "short" if $L_{eff} \ll \xi$ or "long" if $L_{eff} \geq \xi$. Here ξ refers to the coherence length of the weak-link material. In this thesis, we mainly concentrate on

the short junctions.

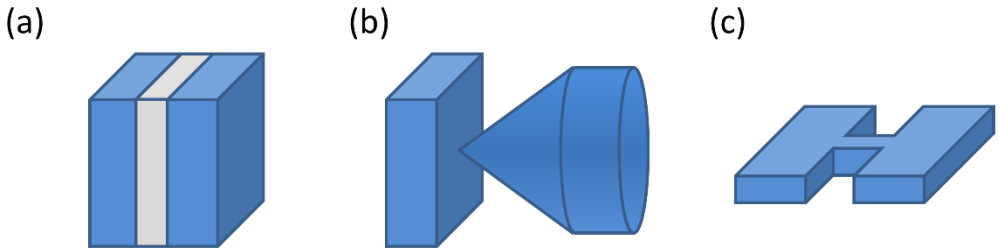

Figure 2.8 Schematic diagrams of three types of weak-link Josephson junctions. (a) Sandwich structure weak link. (b) Point-contact weak link. (c) Micro-bridges.

Weak-link junctions can be experimentally realised in a variety of techniques and structures. Figure 2.8 shows three of the most common types of weak-link junctions. The sandwich weak-link junction looks similar to the sandwich tunnel junctions. However, as the weak link has much lower resistivity, the thickness of the weak link material usually needs to be 0.1 to 10 μm to achieve a similar critical current density. The point-contact weak link is achieved by pressing a sharp superconducting tip into another flat superconductor. It was widely studied at the early stage of research thanks to the simplicity of its fabrication without the need for a cleanroom. However, its lack of irreproducibility meant its application was mainly limited to rf SQUIDs. Another way to implement weak-link junctions is by making a very small constriction in a superconducting thin film, also called a nano/micro-bridge or a Dayem bridge. The nano/micro-bridge has been made by a variety of techniques including electron beam lithography (EBL) [12] or focused ion beam (FIB) [13,14], and proved to be a relative reproducible method to fabricate weak-link junctions.

As the superconducting energy gap Δ and local order parameter Ψ in a weak-link junction is coordinate dependent, the theoretical analysis of weak-link junctions is

more complicated than that of tunnel junctions. The complex geometry shown in Figure 2.8(b) and (c) may even make the simple one-dimensional model inappropriate. Kulik and Omelyanchuk have developed the theory for different weak-link junctions, and demonstrated that the current-phase relationship and characteristic voltage are different from those of tunnel junctions (originally in Ref. [15,16], summarised in Ref [17]). Their theories show that for short weak links, their properties can be different depending on the mean free path l.

In the "dirty" limit where $l \ll L_{\mathrm{eff}} \ll \xi$, the behaviour of the weak link is described by the KO-1 theory. The supercurrent I_{s} satisfies

$$I_{\mathrm{s}}(\varphi) = \frac{2\pi k_{\mathrm{B}} T}{eR_{\mathrm{n}}} \sum_{\omega>0} \frac{2\Delta \cos(\varphi/2)}{\delta} \arctan \frac{\Delta \sin(\varphi/2)}{\delta} \tag{2.35}$$

where $\omega = (2n+1)\pi k_{\mathrm{B}} T/\hbar$ is called the Matsubara frequency, and $\delta = \sqrt{\Delta^2 \cos^2(\varphi/2) + (\hbar\omega)^2}$. Eq. (2.35) indicates the current-phase relation is not simply sinusoidal. As shown in Figure 2.9(a), for $T \to T_{\mathrm{c}}$, $I_{\mathrm{s}}(\varphi)$ is a sinusoidal function, but at lower temperatures, the current-phase relation is slightly tilted. Specifically, the derivative $(dI_{\mathrm{s}}/d\varphi)|_{\pi}$ tends logarithmically to infinity as $T \to 0$.

In the "clean" limit where $L_{\mathrm{eff}} \ll l, \xi$, the behaviour of the weak link is described by the KO-2 theory. The supercurrent I_{s} satisfies

$$I_{\mathrm{s}}(\varphi) = \frac{\pi\Delta}{eR_{\mathrm{n}}} \sin(\varphi/2) \tanh \frac{\Delta \cos(\varphi/2)}{2k_{\mathrm{B}} T} \tag{2.36}$$

Such a current-phase relation is plotted in Figure 2.9(b). Again, for $T \to T_{\mathrm{c}}$, $I_{\mathrm{s}}(\varphi)$ is a sinusoidal function, but at lower temperatures, the current-phase relation is strongly

tilted. For $T = 0$, the current-phase relation is highly non-sinusoidal, and suffers jumps at $\varphi = (2n + 1)\pi$.

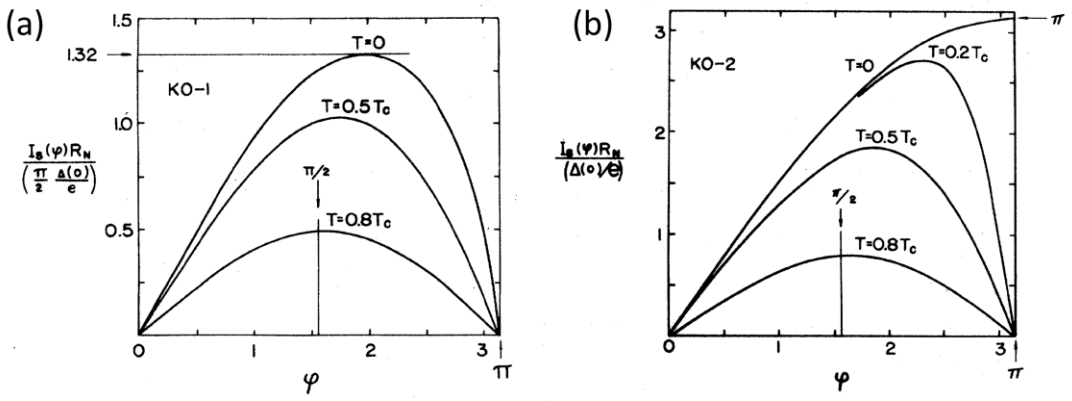

Figure 2.9 Current-phase relations for weak-link junctions at different temperatures. (a) Dirty weak links according to the KO-1 theory. (b) Clean weak links according to the KO-2 theory. In either case, the curve becomes sinusoidal close to T_c. Because of the periodicity and symmetry of the current-phase relation, it is shown only on the [0, π] segment. Reproduced from Ref. [17] with permission from American Physical Society.

The critical current I_0 can be determined by maximising I_s over all possible φ. In Figure 2.10, we compare the critical current (or equivalently characteristic voltage V_c when multiplied by the same normal state resistance R_n) as a function of temperature, for tunnel junctions (Ambegaokar-Baratoff), dirty weak links (KO-1) and clean weak links (KO-2). The three curves coincide with each other and are almost linear for $T \to T_c$. As the temperature decreases, the critical current of tunnel junctions and dirty weak links gradually saturates, while the critical current of clean weak links keeps increasing. As a result, the critical currents of weak links in the dirty and clean limit at $T = 0$, are 1.32 and 2 times as large as the critical current of the tunnel junction, assuming that $\Delta(0)$ and R_n are the same.

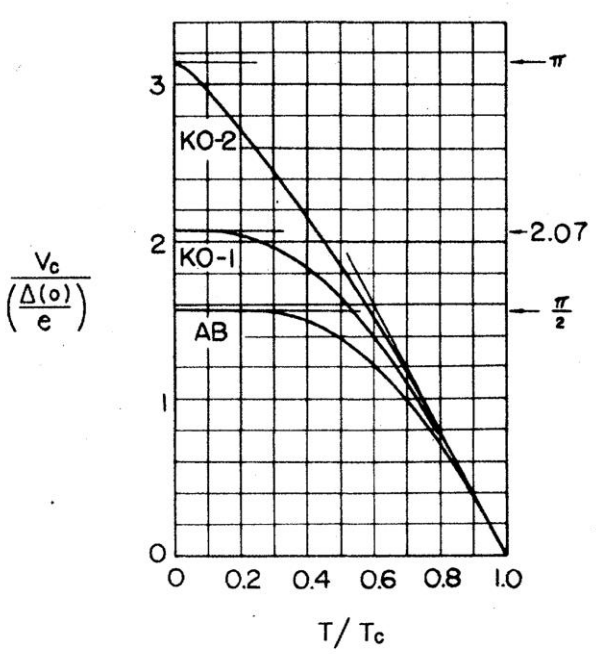

Figure 2.10 Temperature dependences of critical current for different types of Josephson junctions. (AB) tunnel junction; (KO-1) dirty weak links; (KO-2) clean weak links. Reproduced from Ref. [17] with permission from American Physical Society.

2.3 dc SQUID

2.3.1 Basic Properties

The dc SQUID (superconducting quantum interference device) consists of two Josephson junctions connected in parallel on a superconducting loop, as schematically shown in Figure 2.11. Similar to a single Josephson junction, a dc SQUID also has its critical current I_c, which is limited by the sum of the critical current of two Josephson junctions $2I_0$. I_c is a periodic function of the external magnetic flux applied inside the SQUID loop, with a period of $\Phi_0 \equiv h/2e$. Such properties of dc SQUID can be well explained by the RCSJ model.

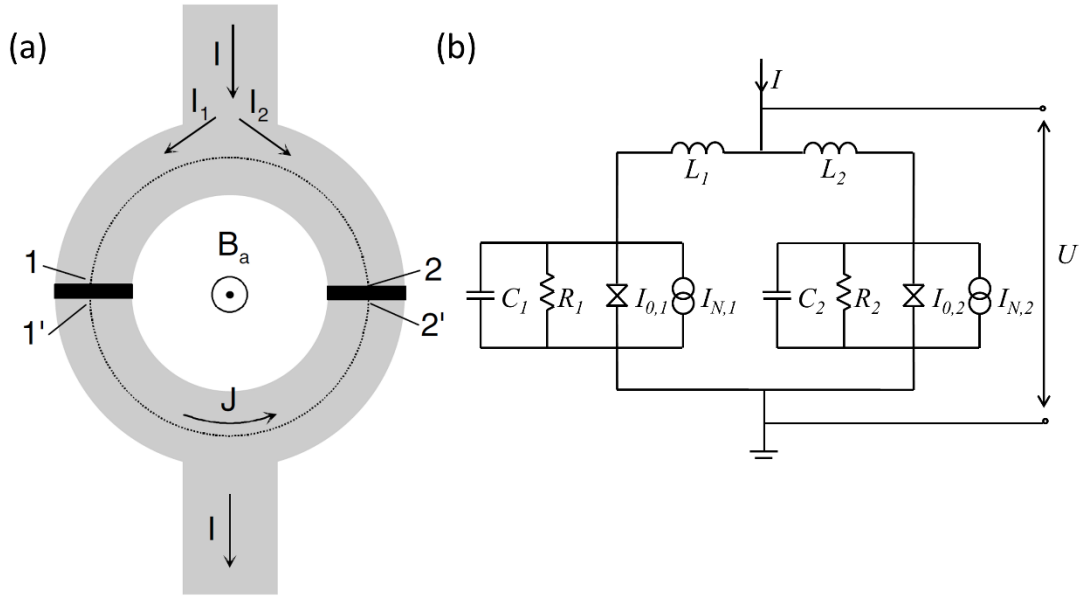

Figure 2.11 Schematic diagram and the equivalent circuit of a dc SQUID. (a) Schematic diagram of a dc SQUID. Reproduced from Ref. [18] with permission from John Wiley and Sons. (b) The equivalent circuit of a dc SQUID within the RCSJ model.

As shown in Figure 2.11(a), the current through junction 1 can be written as half of the bias current I plus the circulating current J, $I_1 = I/2 + J$. Similarly, the current through junction 2 can be written as $I_2 = I/2 - J$. According to the RCSJ model, the current through each junction should be equal to the sum of supercurrent, quasiparticle current and displacement current:

$$\frac{I}{2} + J = I_{0,1} \sin \varphi_1 + \frac{\Phi_0}{2\pi R_1} \dot{\varphi}_1 + \frac{\Phi_0}{2\pi} C_1 \ddot{\varphi}_1$$

$$\frac{I}{2} - J = I_{0,2} \sin \varphi_2 + \frac{\Phi_0}{2\pi R_2} \dot{\varphi}_2 + \frac{\Phi_0}{2\pi} C_2 \ddot{\varphi}_2 \tag{2.37}$$

The phase difference φ_1 and φ_2 are related by

$$\varphi_2 - \varphi_1 = \frac{2\pi}{\Phi_0}\Phi_\mathrm{T} = \frac{2\pi}{\Phi_0}(\Phi_\mathrm{a} + LJ) \tag{2.38}$$

where $L = L_1 + L_2$ is the self-inductance of the SQUID loop. This equation can be derived in a similar way to Eq. (2.23). Φ_T is the total flux through the SQUID loop which consists of both the external magnetic flux Φ_a and the contribution of the circulating current J. Eq. (2.37) and (2.38) form the basis of our understanding of the properties of dc SQUIDs. For simplicity, in this section, we first discuss the symmetric SQUID, i.e. the critical current $I_0 = I_{0,1} = I_{0,2}$, shunt resistance $R = R_1 = R_2$, and capacitance $C = C_1 = C_2$ are identical for the two Josephson junctions.

Here we introduce another dimensionless parameter, the screening parameter, $\beta_\mathrm{L} = 2LI_0/\Phi_0$, which determines the ability that the critical current of the SQUID I_c can be modulated by the external magnetic flux Φ_a. Eq. (2.37) and (2.38) are numerically solved in the four circumstances discussed below, and the corresponding *I-V* characteristics are shown in Figure 2.12(a)-(d).

Let's start with the case that both β_c and β_L are negligible, as shown in Figure 2.12(a). In this case the dc *I-V* characteristics have analytical solution:

$$V = 0 \qquad \text{for} \quad I < I_\mathrm{c}$$

$$V = \frac{I_\mathrm{c}R}{2}\sqrt{(I/I_\mathrm{c})^2 - 1} \qquad \text{for} \quad I \geq I_\mathrm{c} \tag{2.39}$$

where

$$I_\mathrm{c} = 2I_0\left|\cos\left(\frac{\pi\Phi_\mathrm{a}}{\Phi_0}\right)\right| \tag{2.40}$$

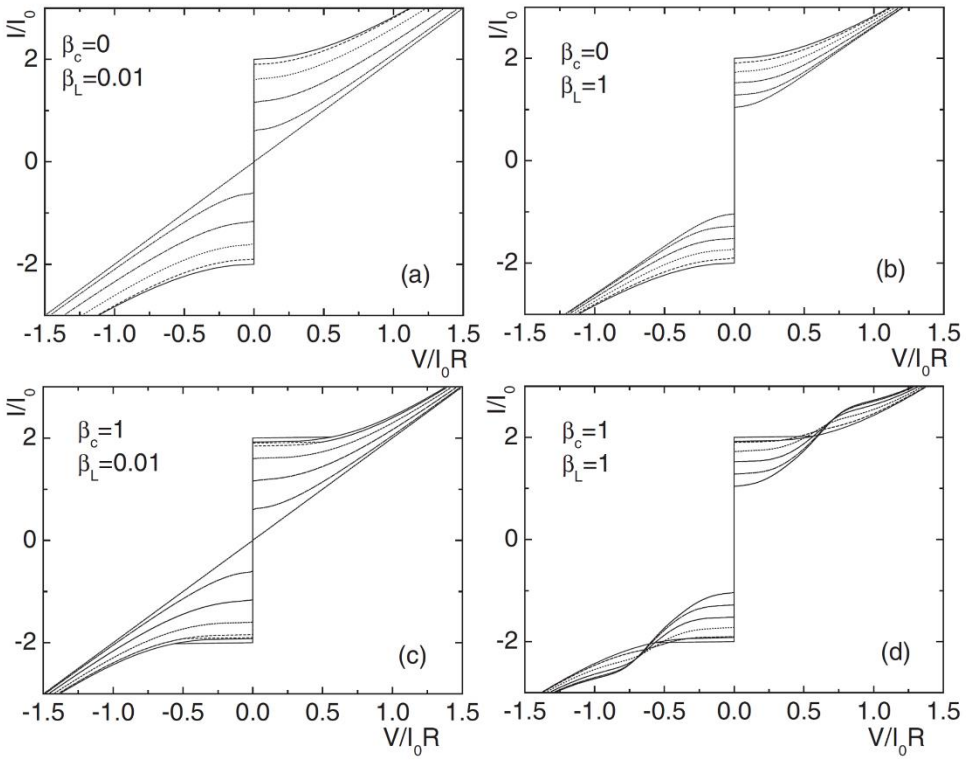

Figure 2.12 *I-V* characteristics calculated with RCSJ model for a dc SQUID. (a)-(d) refer to different values of parameters, with β_L=0.01 or 1 and β_c=0 or 1. Applied flux is increased from 0 (solid line) to $\Phi_0/2$ (short dashed line) in steps of $0.1\Phi_0$. Reproduced from Ref. [6] with permission from John Wiley and Sons.

Note that R still refers to the normal state resistance of a single junction. Eq. (2.40) means when the external flux is changed from 0 to $\Phi_0/2$, the critical current can be modulated from $2I_0$ to 0. As β_L increases, the modulation of critical current I_c decreases, as shown in Figure 2.12(b). This is more clearly shown in Figure 2.13(a), where the modulation of critical current I_c by the external flux Φ_a is plotted under different values of β_L. As shown in Figure 2.13(b), the modulation depth keeps decreasing as β_L increases. However, that doesn't mean the best SQUID is with β_L close to zero. If we take thermal fluctuations into consideration, the effect of which

will be shown in the next section, computer simulations have shown the optimal modulation is reached when $\beta_L \approx 1$ [6].

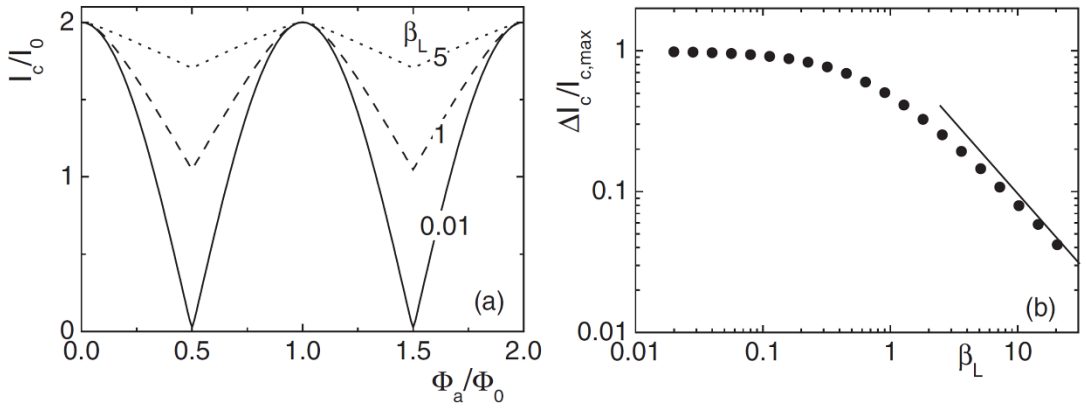

Figure 2.13 Modulation of the critical current of a dc SQUID by the magnetic field. (a) Critical current of the dc SQUID vs. applied flux for three values of the screening parameter β_L. Junction parameters are assumed to be identical and β_c=0. (b) Modulation depth $\Delta I_c/I_{c,max}$ vs β_L. The solid line is the function $1/\beta_L$. Reproduced from Ref. [6] with permission from John Wiley and Sons.

In the case of $\beta_c = 1$ and $\beta_L = 0.01$ (Figure 2.12(c)), the *I-V* characteristic exhibits a small hysteresis when $\Phi_a = 0$; however, this hysteresis disappears as the external flux increases. In the case of $\beta_c = 1$ and $\beta_L = 1$ (Figure 2.12(d)), a new feature appears that the $\Phi_a = \Phi_0/2$ curve intersects with the $\Phi_a = 0$ curve.

2.3.2 Effect of Thermal Fluctuation

Similar to the method we treat the thermal noise of Josephson junction, the thermal fluctuation of current in dc SQUIDs is represented by a stochastic current term in the coupled Langevin equations:

$$\frac{I}{2}+J=I_{0,1}\sin\varphi_1+\frac{\Phi_0}{2\pi R_1}\ \dot{\varphi}_1+\frac{\Phi_0}{2\pi}C_1\ddot{\varphi}_1+I_{\mathrm{N},1}$$

$$\frac{I}{2}-J=I_{0,2}\sin\varphi_2+\frac{\Phi_0}{2\pi R_2}\ \dot{\varphi}_2+\frac{\Phi_0}{2\pi}C_2\ddot{\varphi}_2+I_{N,2} \tag{2.41}$$

By numerically solving the Langevin equations above together with Eq. (2.38), *I-V* characteristics of dc SQUID with strongly overdamped junctions and intermediately damped junctions can be obtained, as shown in Figure 2.14. In comparison with the noise-free case (Figure 2.12(b) and (d)), we can find that due to thermal noise, the *I-V* curve is rounded near the critical current.

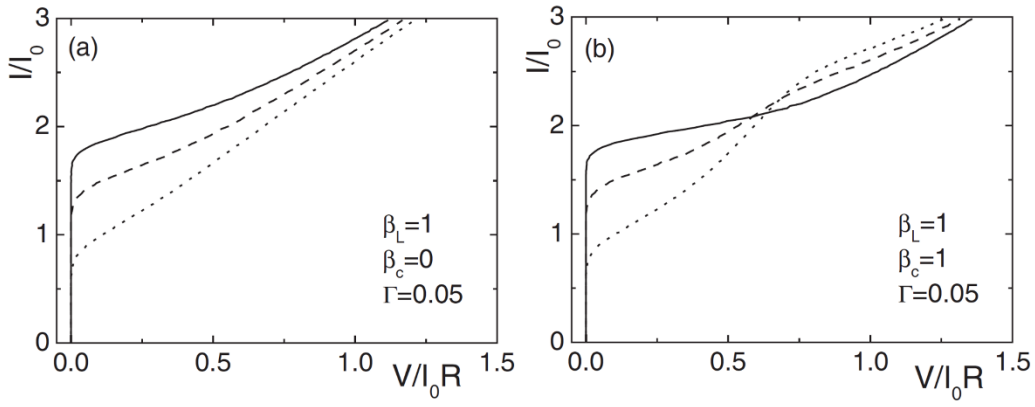

Figure 2.14 *I-V* characteristics calculated within the RCSJ model in the presence of thermal noise for a dc SQUID. (a) A strongly overdamped junction. (b) An intermediately damped junction. The solid line, long dashed line and short dashed line represent the cases when $\Phi_a=0$, $\Phi_a=\Phi_0/4$ and $\Phi_a=\Phi_0/2$, respectively. Reproduced from Ref. [6] with permission from John Wiley and Sons.

In practice, the modulation of critical current I_c by external magnetic flux Φ_a can be detected by repeatedly measuring the *I-V* characteristics. However, an easier way to reveal the dependence on external magnetic field is to bias the dc SQUID at a

current slightly larger than the critical current, and to measure the voltage across the dc SQUID as a function of external magnetic flux. Hence, the modulation of critical current is transferred to the modulation of voltage, and the dc SQUID thus acts as a flux-to-voltage transducer.

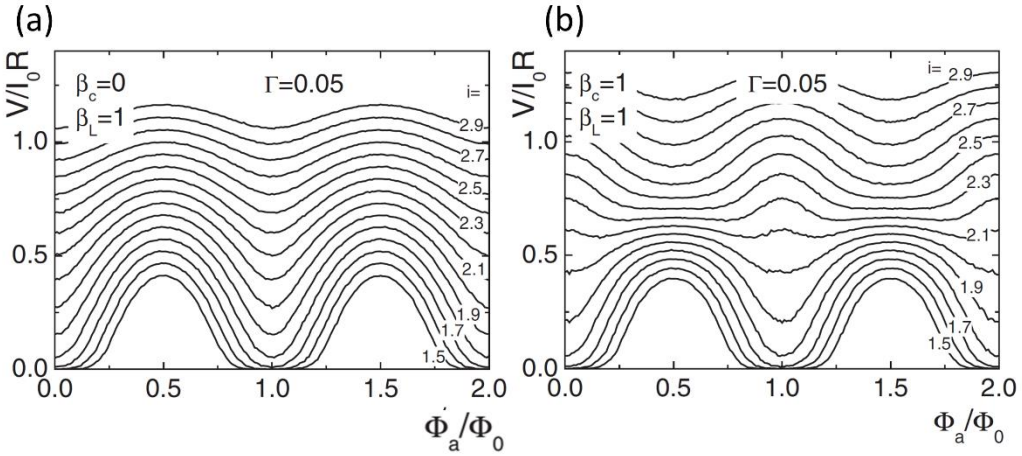

Figure 2.15 Voltage modulation $V(\Phi_a)$ of a dc SQUID by the magnetic field. (a) A strongly damped junction. (b) An intermediately damped junction. The modulation curves are simulated in the presence of thermal noise for several normalised bias current values from 1.5 to 2.9. Reproduced from Ref. [6] with permission from John Wiley and Sons.

Figure 2.15 shows the modulation of V by external magnetic flux Φ_a for various values of bias current under two sets of β_c and β_L at nonzero temperature. We can see that the oscillations of $V(\Phi_a)$ are almost sinusoidal, and that the modulation depth of V changes as the bias current changes. The maximum modulation depth of bias voltage is

$$\Delta V \approx \frac{I_0 R}{1+\beta_L} \tag{2.42}$$

In practical applications, dc SQUIDs are usually deployed to measure a small magnetic flux change $\delta\Phi_a \ll \Phi_0$. To realise the maximum sensitivity, the bias current is optimised to maximise the modulation depth ΔV, and an additional magnetic field is generally applied to sit at $(2n+1)\Phi_0/4$ to maximise the flux-to-voltage transfer coefficient, $|\partial V/\partial\Phi_a|$. Thus, the dc SQUID can produce a maximum response δV to a small magnetic flux change $\delta\Phi_a$ of interest.

Note that the optimum bias current and the optimum flux-to-voltage transfer coefficient depend on the parameters of the dc SQUID: β_c, β_L, and Γ. Up to now, there is no analytic solution of $\max(|\partial V/\partial\Phi_a|)$ that is valid over a wide range of parameters. However, an enormous number of numerical calculations have been reported for different cases [19–21]. For example, for $\beta_c \leq 1$, $\beta_L \approx 1$, and $\Gamma = 0.05$, $\max(|\partial V/\partial\Phi_a|) \approx R/L$.

Besides the dc *I-V* properties above, numerical simulation can also calculate the noise spectrum density of dc SQUIDs. Assuming the noise is dominated by the Nyquist-Johnson noise across the shunt resistance, it is shown [22] that the voltage noise power spectral density of the dc SQUID has a minimum value of

$$S_V(f) \approx 16k_B TR \tag{2.43}$$

The sensitivity of the dc SQUID is limited by the voltage noise. Therefore, the sensitivity of the dc SQUID is

$$S_\Phi(f) = \frac{S_V(f)}{\max\left(\left|\frac{\partial V}{\partial\Phi_a}\right|\right)^2} \approx \frac{16k_B TL^2}{R} \tag{2.44}$$

For typical SQUIDs, that refers to a white flux noise level $S_\Phi^{1/2}(f)$ of a few

$\mu\Phi_0 \mathrm{Hz}^{-1/2}$ at 4.2 K.

2.3.3 Effect of Asymmetry

Up to now, we have neglected any asymmetry in the dc SQUID parameters. However, due to the uncontrollability in some fabrication processes, it is difficult to have two identical Josephson junctions in a dc SQUID. The asymmetry of parameters is particularly large for certain types of SQUID, such as the high-T_c SQUID. In this section, we will briefly discuss the effect of asymmetry of parameters on the modulation of critical current.

The asymmetry can be characterised by the asymmetry parameters α defined as follows

$$I_{0,1} = I_0(1-\alpha_\mathrm{I}), \quad R_1 = \frac{R}{(1-\alpha_\mathrm{R})}, \quad C_1 = C(1-\alpha_\mathrm{C})$$

$$I_{0,2} = I_0(1+\alpha_\mathrm{I}), \quad R_2 = \frac{R}{(1+\alpha_\mathrm{R})}, \quad C_2 = C(1+\alpha_\mathrm{C}) \tag{2.45}$$

An asymmetry may also exist in the SQUID inductance. The asymmetry parameter α_L can be defined as

$$L_1 = \frac{L(1-\alpha_\mathrm{L})}{2}, \quad L_2 = \frac{L(1+\alpha_\mathrm{L})}{2} \tag{2.46}$$

Thus, the total magnetic flux through the SQUID loop

$$\Phi_\mathrm{T} = \Phi_\mathrm{a} + L_1 I_1 - L_2 I_2 = \Phi_\mathrm{a} + LJ - \alpha_\mathrm{L} LI/2 \tag{2.47}$$

Therefore, for a given asymmetric dc SQUID, the *I-V* characteristics can be obtained by numerically solving Eq. (2.37) and (2.47) with asymmetric parameters α_{I}, α_{R}, α_{C}, and α_{L}. Here, we only introduce an effect of asymmetry on the modulation of critical current $I_{\mathrm{c}}(\Phi_{\mathrm{a}})$.

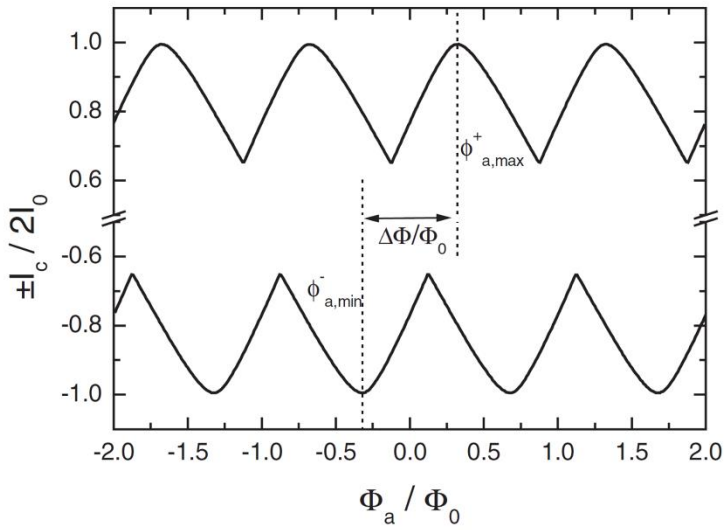

Figure 2.16 Critical current modulation $I_c(\Phi_a)$ of a dc SQUID with critical current asymmetry. The I_c maxima shift for opposite polarity of bias currents. Reproduced from Ref. [6] with permission from John Wiley and Sons.

For a symmetric dc SQUID, the maximum critical current I_{c} is reached when $\Phi_{\mathrm{a}} = n\Phi_0$. However, due to asymmetry of Josephson junctions, the maximum I_{c} is shifted by $\beta_{\mathrm{L}}(\alpha_{\mathrm{I}} + \alpha_{\mathrm{L}})/2$. When the polarity of the bias current is reversed, the maximum $|I_{\mathrm{c}}|$ is shifted by the same amplitude in the opposite direction, as shown in Figure 2.16. Note that for an arbitrary Φ_{a}, the *I-V* characteristics are no long symmetric on both polarities of bias current. By measuring the difference of the external magnetic flux at which $|I_{\mathrm{c}}|$ is maximum for both polarities of bias current, we can even calculate the values of $\alpha_{\mathrm{I}} + \alpha_{\mathrm{L}}$ experimentally.

A similar shift occurs for the minima in the $V(\Phi_a)$ characteristics if $|I_c| \approx 2I_0$. For variable bias current, the minima in the $V(\Phi_a)$ characteristics are shifted along the Φ_a axis proportional to $\alpha_L LI/2$, independent of α_I. This allows us to further determine α_L and α_I separately.

Chapter 3 Introduction to Graphene

In this chapter, we briefly introduce the background knowledge of graphene, which is the material we choose as the weak link between the two superconductors. In Section 3.1, we will start with introducing the unique molecular and electronic structures of graphene. Then we will outline the major synthesis and post-treatment techniques of graphene samples, comparing their quality and compatibility with large-scale production. In the last section, we will briefly introduce several common characterisation techniques of graphene, to study its properties such as number of layers, defect density, sheet resistance, mobility, etc.

3.1 Structure and Electronic Properties of Graphene

3.1.1 Structure of Graphene

Since its isolation in 2004, graphene has rapidly become a major topic of condensed matter physics and material science research [23]. With its unique two-dimensional structure, graphene is the thinnest and the strongest material ever known and exhibits a novel linear dispersion relation near the Fermi level. Thousands of papers have been published in the last decades, attempting to optimise its synthesis, explain its properties, and explore its applications.

The structure of graphene is quite simple. It is made out of carbon atoms arranged in a honeycomb structure of hexagons, as shown in Figure 3.1. Each carbon atom is tied to its three nearest neighbours via a strong σ bond, which is a result of the sp^2 hybridization of the $2s$, $2p_x$, and $2p_y$ orbitals. The σ bonds are the reason for the strong mechanical properties of graphene sheet. The unaffected $2p_z$ orbital, which is orthogonal to the graphene plane, can bind covalently with adjacent carbon atoms,

forming a half-filled π bond. The transport properties of graphene are determined by those delocalised π electrons.

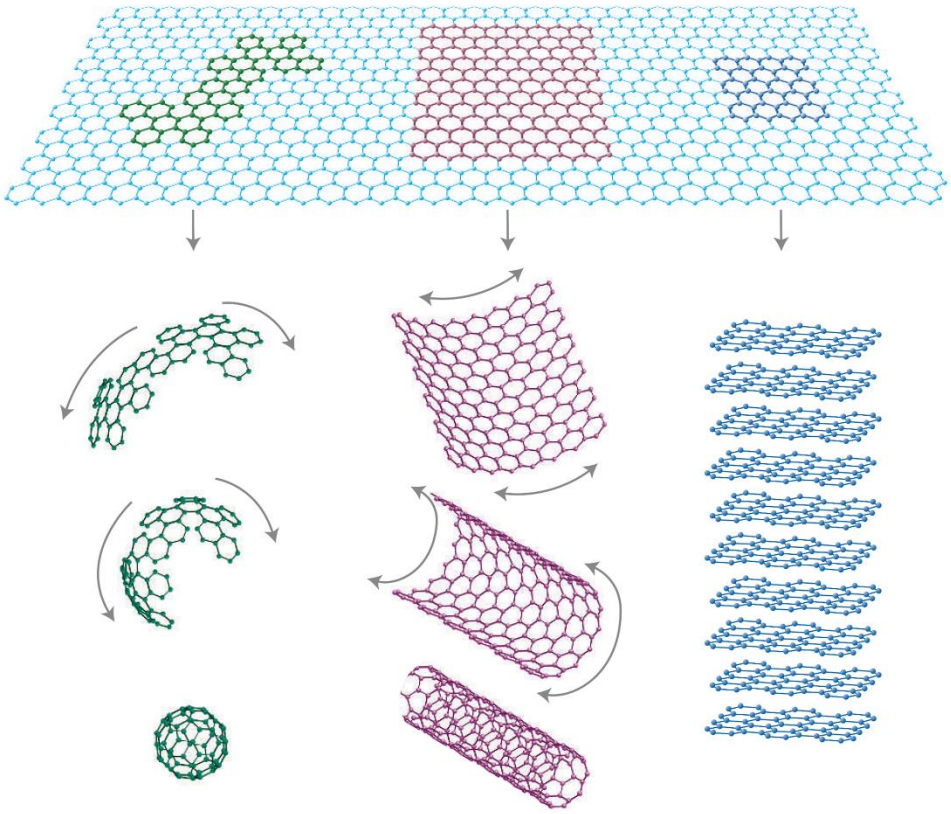

Figure 3.1 Schematic diagram of graphene structure. Graphene is the building material of other carbon allotropes, such as zero-dimensional fullerenes, one-dimensional carbon nanotubes and three-dimensional graphite. Reproduced from Ref. [24] with permission from Springer Nature.

Graphene can be viewed as the building blocks of other carbon allotropes, such as three-dimensional graphite, one-dimensional carbon nanotubes, and zero-dimensional fullerenes. In fact, it has acted as the basis of understanding the electronic properties of those allotropes [25,26], even before the experimental isolation.

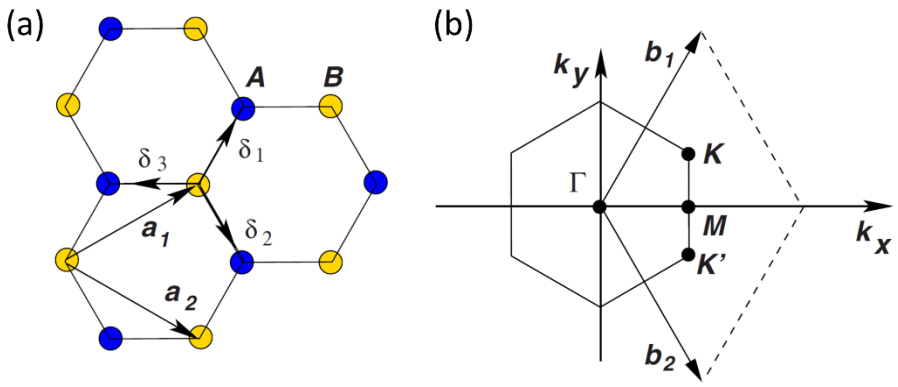

Figure 3.2 Lattice and reciprocal lattice structures of graphene. (a) The lattice structure of graphene. $\boldsymbol{a}_1$ and $\boldsymbol{a}_2$ are the base vectors in the real space, and δ_i, $i = 1, 2, 3$ are the nearest-neighbour vectors. (b) First Brillouin zone of graphene. $\boldsymbol{b}_1$ and $\boldsymbol{b}_2$ are the base vectors of the reciprocal space. Reproduced from Ref. [27] with permission from American Physical Society.

As shown in Figure 3.2, the honeycomb structure of graphene can be seen as a triangular lattice, with two atoms in a unit cell. The two base vectors of the lattice are

$$\boldsymbol{a}_1 = \frac{a}{2}(3, \sqrt{3}), \qquad \boldsymbol{a}_2 = \frac{a}{2}(3, -\sqrt{3}) \tag{3.1}$$

where $a \approx 1.42$ Å is the distance between nearest carbon atoms. The base vectors of the corresponding reciprocal lattice are

$$\boldsymbol{b}_1 = \frac{2\pi}{3a}(1, \sqrt{3}), \qquad \boldsymbol{b}_2 = \frac{2\pi}{3a}(1, -\sqrt{3}) \tag{3.2}$$

The first Brillouin zone of graphene is also hexagonal, with its six vertices equivalent to two points K and K' respectively. The two points are named Dirac points for reasons we will see below.

3.1.2 Band Structure of Graphene

The band structure of graphene was first derived in 1947 by Wallace, as a starting point to study graphite [25]. In the tight-binding approximation, the wave function of graphene is a linear combination of Bloch functions for sublattice A and B:

$$\Phi_\alpha = \frac{1}{\sqrt{N}} \sum_{\boldsymbol{R}_a} e^{i\boldsymbol{k}\cdot\boldsymbol{R}_\alpha} \varphi(\boldsymbol{r} - \boldsymbol{R}_a) \qquad \alpha = A, B \tag{3.3}$$

where N is the number of unit cells, $\boldsymbol{R}_a$ are the positions of a sublattice and $\varphi(\boldsymbol{r} - \boldsymbol{R}_a)$ is the $2p_z$ orbital of the atom at $\boldsymbol{R}_a$. The sum runs over all unit cells, i.e. all possible lattice vectors.

Following a normal tight binding calculation, and considering only the transfer of electrons between nearest atoms (nearest neighbour approximation), the energy eigenvalues can be obtained as

$$E(k_x, k_y) = \pm t \left[1 + 4\cos\frac{\sqrt{3}k_x a}{2} \cos\frac{k_y a}{2} + 4\cos^2\frac{k_y a}{2} \right]^{\frac{1}{2}} \tag{3.4}$$

where t is the transfer integral between the nearest neighbours [26]. This energy dispersion relationship is plotted in Figure 3.3(a). The upper half of the curved surface is called the π^* band while the lower half is called the π band. The dispersion spectrum is symmetric around zero, with the π band and the π^* band degenerate at the Dirac points *K* and *K'*. At zero temperature, the π band is filled while the π^* band is empty. Therefore, the Fermi level of graphene lies at the energy level where the two bands are degenerate.

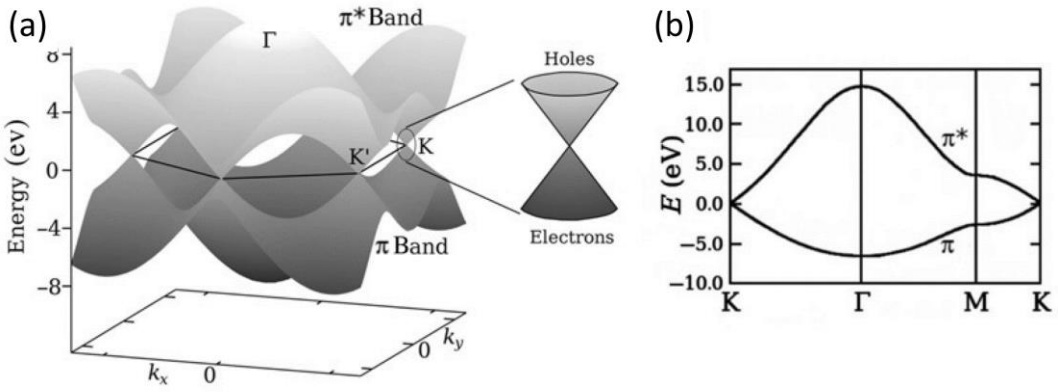

Figure 3.3 Energy dispersion relation for graphene. (a) Energy dispersion relation for graphene. The inset shows the linear dispersion near the Dirac points. (b) The dispersion along the high-symmetry points ΓMK. Reproduced from Ref. [28] with permission from Taylor & Francis.

Note that the derivation of Eq. (3.4) neglects the overlap integral between orbitals on the next nearest atoms. For a finite overlap integral, as shown in Figure 3.3(b), the π band and the π^* band symmetry is broken, resulting in electron-hole asymmetry in the transport properties.

3.1.3 Massless Dirac Fermions

As Figure 3.3(a) shows, if we zoom in to the band structure of graphene close to one of the Dirac points, the energy dispersion is like two cones with their tips meeting at the Dirac points. By writing $\boldsymbol{k} = \boldsymbol{K} + \boldsymbol{q}$, the dispersion relation close to the Dirac point can be expanded in a Taylor series

$$E_{\pm}(\boldsymbol{q}) \approx \pm\hbar v_{\mathrm{F}}|\boldsymbol{q}| + O[(q/K)^2] \tag{3.5}$$

where $\boldsymbol{q}$ is the wave vector relative to the Dirac point and $v_{\mathrm{F}} = \sqrt{3}ta/2\hbar \approx$

10^6 m/s is the Fermi velocity. The dispersion relation in Eq. (3.5) is essentially different from most metals or semiconductors, where $E(\boldsymbol{q}) = \hbar^2 q^2/2m$. In the usual case, $v_{\mathrm{F}} = q/m = \sqrt{2E/m}$, which is a function of energy or momentum, while in Eq. (3.5) the Fermi velocity is independent of energy or momentum. Corresponding to Eq. (3.5), the density of states near Dirac points is given by

$$D(E) \propto |E| \tag{3.6}$$

which is linear and vanishes at the Fermi level. If we consider the electron-hole asymmetry caused by the overlapping integral, the density of states will show slight asymmetry above and below the Fermi level.

The linear energy dispersion relation mimics that of massless relativistic particles. Therefore, the dynamics of those relativistic-like (Dirac) Fermions can be similarly described by a Dirac equation, with Hamiltonian in the vicinity of Dirac points

$$\widehat{H}_K(\boldsymbol{q}) = \hbar v_{\mathrm{F}} \boldsymbol{\sigma} \cdot \boldsymbol{q} = \hbar v_F \begin{pmatrix} 0 & q_x - iq_y \\ q_x + iq_y & 0 \end{pmatrix} = -\widehat{H}_{K'}^T(\boldsymbol{q}) \tag{3.7}$$

where $\boldsymbol{\sigma} = (\sigma_x,\ \sigma_y)$ is a vector of Pauli matrices. The wave functions of these Dirac Fermions have a spinor structure

$$\Psi_{\pm,\boldsymbol{K}}(\boldsymbol{q}) = \frac{e^{i\boldsymbol{k}\cdot\boldsymbol{r}}}{\sqrt{2}} \begin{pmatrix} e^{-i\theta_q/2} \\ \pm e^{i\theta_q/2} \end{pmatrix}, \qquad \Psi_{\pm,\boldsymbol{K}'}(\boldsymbol{q}) = \frac{e^{i\boldsymbol{k}\cdot\boldsymbol{r}}}{\sqrt{2}} \begin{pmatrix} e^{i\theta_q/2} \\ \pm e^{-i\theta_q/2} \end{pmatrix} \tag{3.8}$$

where $\theta_q = \arctan(q_y/q_x)$, and $\pm$ signs correspond to π^* and π bands respectively. The upper and lower terms in the spinor correspond to the quantum

mechanical amplitudes (or pseudospin) of finding the particle on one of the two sublattices, A and B, as shown in Figure 3.2. The massless Dirac Fermion nature of charge carriers in graphene has led to many novel effects, such as the anomalous integer quantum Hall effect [29,30], Klein's paradox [31], etc.

3.2 Synthesis and Post-Treatment Technology of Graphene

3.2.1 Mechanical Exfoliation

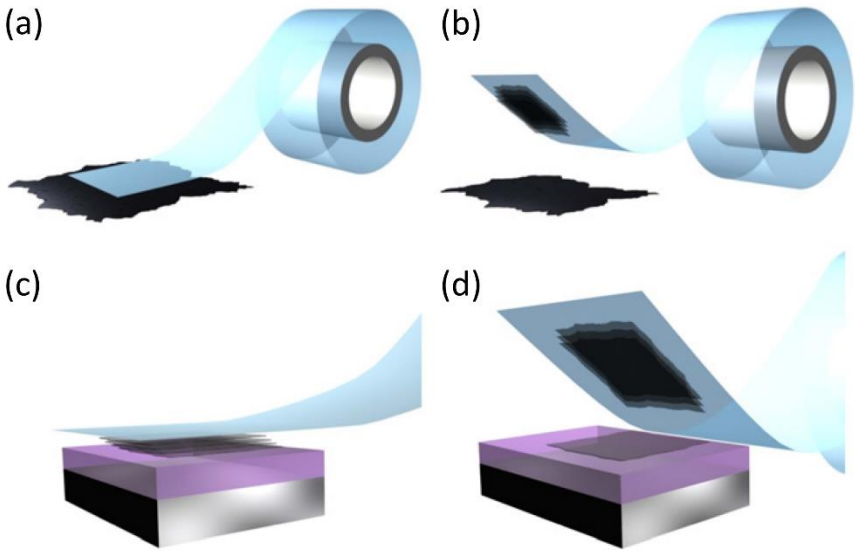

Figure 3.4 Schematic diagram of the mechanical exfoliation of graphene. (a) Adhesive tape is pressed against graphite. (b) The top few layers are attached to the tape. (c) The tape with few layer graphene is pressed against a surface of choice. (d) Upon peeling off, the bottom layer is left on the substrate. Reproduced from Ref. [32] with permission from IOP Publishing.

The unique properties of graphene predicted by theorists could not be tested experimentally until single-layer graphene was isolated in 2004. The method invented by Geim's group [23,33] is simple yet efficient: cleaving a graphite crystal with an

adhesive tape multiple times and transferring the thinned down graphite onto an oxidised silicon wafer by a gentle press of the tape, as shown in Figure 3.4. This method is feasible since the van der Waals interactions between adjacent layers of graphite is much weaker than the intra-layer covalent bonds. A crucial aspect in this method is the choice of substrates. It is found that on silicon substrates with an oxidised layer of either 90 nm or 300 nm, the contrast of single-layer graphene under an optical microscope is at its maximum [34]. As shown in Figure 3.5, on a 300-nm-thick SiO_2 substrate, graphite flakes thicker than 10 nm appear yellow, while sub-10 nm flakes will look purple. The lighter the purple shade is, the fewer layers of graphene it contains. Therefore, with the help of an optical microscope, few-layer graphene can be easily identified, located, and further, patterned with electrodes. Once this method was established, it marked the onset of the experimental study of graphene.

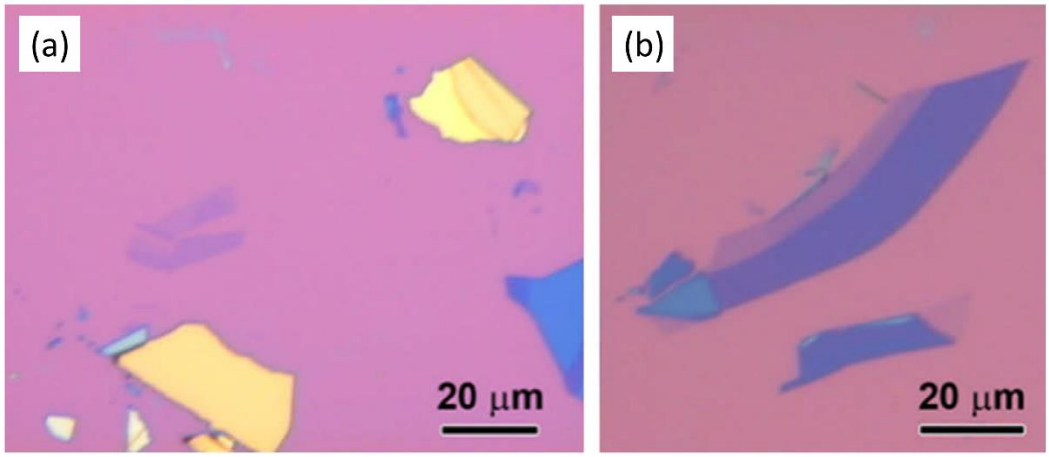

Figure 3.5 Optical images of mechanical exfoliated graphene on a ~300 nm thick SiO_2 layer. (a) Thin graphite about 100 nm thick (yellow area). (b) Few layer graphene (dark purple area) and single-layer graphene (light purple area). Reproduced from Ref. [35] with permission from Elsevier.

Up to now, mechanical exfoliated graphene remains the first choice for most

fundamental researchers, due to its high structural quality and near ideal electronic properties. With advances in the exfoliation technique, single-layer graphene flakes with size up to hundreds of microns can be made, which is enough for most experiments. However, it is challenging to bring this approach to large-scale production, and that is why other synthesis methods of graphene are valued.

3.2.2 Chemical Vapour Deposition

Chemical vapour deposition (CVD) is the most promising approach to synthesise large-area graphene on an industrial scale (refer to Ref. [36] for a review). As illustrated in Figure 3.6, in this method, a metal foil surface is placed in a hydrocarbon gas atmosphere at high temperature. The hydrocarbon molecules can be decomposed and carbon atoms are dissolved into the metal. Then the foil is allowed to cool at a predetermined rate and carbon atoms are segregated from the metal and form a continuous graphene film on the metal surface. The growth of graphene has been demonstrated on a variety of transition metals such as Ni [37], Pd [38], Ru [39], Ir [40] and Cu [41]. Among them, Cu substrates are the most popular because they are inexpensive, and feasible for the synthesis of large-area and high-quality graphene sheet. Nowadays, graphene sheet in square meter size can be fabricated, with 95% of the area covered by single-layer graphene [41]. Excellent electronic properties of CVD synthesised graphene have been demonstrated with its carrier mobility reaching 7350 $cm^2V^{-1}s^{-1}$ at low temperature [42], almost comparable to that of mechanical exfoliated graphene on SiO_2 substrates.

A problem emerging with this method is that, for most applications, graphene sheet must be transferred from the metal support to a dielectric surface or other substrate of interest. As shown in Figure 3.7, the transfer of graphene is usually achieved by depositing a polymer layer (such as PMMA) over the graphene and etching away the

metal support. Then the polymer film with graphene is transferred onto the target substrate and the polymer film is dissolved. Recent advances in the transfer technique can minimise the damage to graphene and leave little polymer residue after the transfer [42,43].

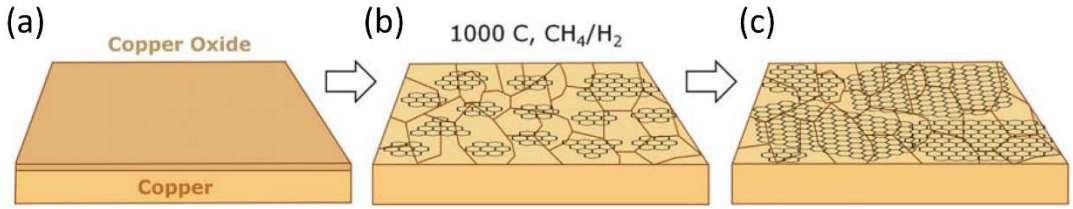

Figure 3.6 Schematic diagram of graphene growth on copper by CVD. (a) A copper foil with native oxide. (b) the exposure of the copper foil to CH_4/H_2 atmosphere at 1000 °C leading to the nucleation of graphene islands. (c) Enlargement of the graphene flakes with different lattice orientation. Reproduced from Ref. [43] with permission from Royal Society of Chemistry.

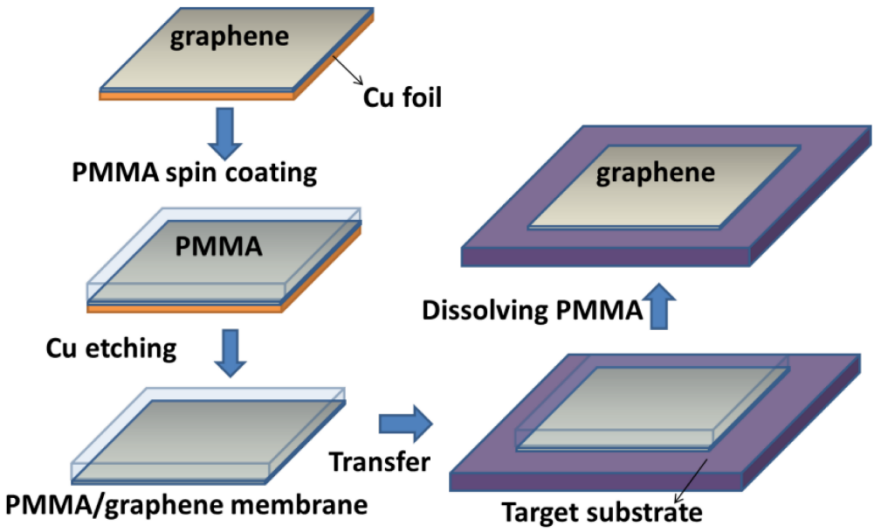

Figure 3.7 Schematic diagram of the transfer of graphene grown in copper foil to the target substrate by PMMA. Reproduced from Ref. [44].

Finally, it is worth noticing that high-quality CVD graphene samples require carefully controlled synthesis conditions and optimised transfer techniques. Therefore, it is a common practice to compare and to select CVD graphene samples based on characterisation and measurement, before utilising them to fabricate devices.

3.2.3 Epitaxial Growth

The other route to fabricate large-scale graphene sheet is epitaxial growth, developed by de Heer et al [45–49]. In the method, hexagonal silicon carbide crystals are heated to 1300 °C or even higher temperature in ultra-high vacuum or low-pressure argon atmosphere, allowing silicon atoms to sublimate from the surface. The carbon-enriched surface undergoes reorganization and graphitization. The properties of epitaxial graphene highly depend on which face of SiC crystal is used.

On the SiC (0001) (silicon-terminated) face, the sublimation of Si atoms can be well controlled, and high-quality single- or double-layer graphene tends to form. The interaction between graphene layer and the substrate is weak enough so that the linear dispersion relation is retained in the vicinity of Dirac point. However, the interaction with the substrate induces strong n-doping, which means the Fermi level is much higher than the Dirac point [50]. That is the reason why relatively low mobility is measured for epitaxial graphene on silicon surfaces (a typical value of mobility is 1000 $cm^2V^{-1}s^{-1}$ at room temperature and 2000 $cm^2V^{-1}s^{-1}$ at low temperature [47,49,51,52]). In fact, if we manage to dope the epitaxial graphene near the Dirac point, the measured mobility can be up to 2.9×10^4 $cm^2V^{-1}s^{-1}$ at 25 K [51], which is comparable to most mechanically exfoliated graphene.

On the SiC $(000\bar{1})$ (carbon-terminated) face, the sublimation of Si atoms is more rapid and multilayer graphene is formed. However, the distance between adjacent layers is slightly larger than that in graphite and these graphene layers exhibit a

rotational disorder. The decoupling between adjacent layers makes epitaxial graphene on the carbon-terminated face different to exfoliated multilayer graphene. In fact, epitaxial graphene on the carbon-terminated face exhibits the linear dispersion near Dirac point, like single-layer graphene [53]. Except for the innermost layers which are strongly doped by the substrate, the other layers are screened from built-in electric field and are rarely doped. Therefore, epitaxial graphene on the carbon-terminated face can exhibit a high mobility (typically 27000 $cm^2V^{-1}s^{-1}$ at low temperature [46,52,54]) which does not significantly depend on temperature.

3.2.4 Liquid Phase Exfoliation

Similar to mechanical exfoliation, another top-down approach to synthesising single-layer graphene is liquid phase exfoliation through a water dispersible intermediary, graphite oxide (GO) [55,56], as shown in Figure 3.8. By Hummers' method [57], graphite is first oxidised into GO, which is a layered stack of puckered sheets with AB stacking. The interlayer van der Waals cohesive force is weakened by the introduction of oxygen atoms and other oxygen-containing functional groups so that GO can be exfoliated into individual sheets by ultrasonic or other mechanical energy. After exfoliation of GO, the suspension may be further processed with centrifugation, and can then be deposited as a thin film on almost any surface. The reduction of GO back to graphene can be done either before deposition by chemical reducing agents, or after deposition by thermal annealing.

Due to a relatively high defect density and only partial removal of oxygen-containing functional groups, it is difficult to observe interesting physics phenomena in chemically derived graphene. However, the low cost and high throughputs of this method offset its drawbacks and pave the way for applications in areas such as electrochemistry, printed electronics, electromagnetic shielding, and

heat dissipation.

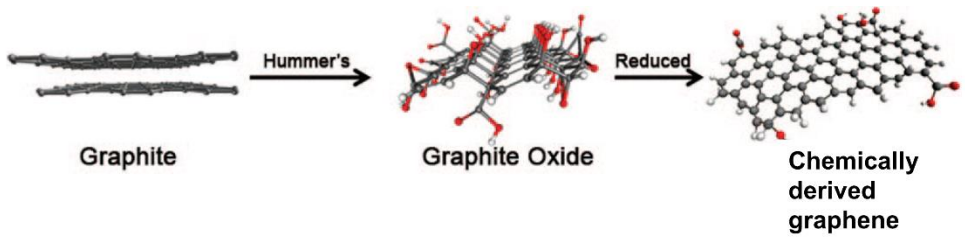

Figure 3.8 Schematic diagram of the conversion process from graphite to chemically derived graphene. Reproduced from Ref. [58] with permission from American Chemical Society.

3.2.5 Suspension of Graphene

Following the early studies, people soon realised that the substrate strongly reduces the quality of graphene so that the excellent properties promised by the perfect two-dimensional structure are not fully revealed. The effect of the substrate is mainly due to two mechanisms: the roughness of the substrate can deteriorate the mobility by introducing short-range scattering centres or by inducing quench-condensation of ripples within the graphene layer [59]; and charges trapped in the oxide or at the graphene-oxide interface can induce carrier inhomogeneity, leading to reduced mobility [60,61].

The first method developed to get rid of the impact of the substrate is to etch away the silicon oxide beneath the graphene. Thus, mechanically exfoliated single-layer graphene can be suspended from the substrate and held solely by metallic electrodes [59,62,63], as shown in Figure 3.9. Without the effect of the substrates, the measured electron mobility of suspended graphene is as high as 1.85×10^5 $cm^2V^{-1}s^{-1}$ at 100 K [63] and 2.3×10^5 $cm^2V^{-1}s^{-1}$ at 5 K [62], which is approximately an order of magnitude larger than exfoliated graphene on a substrate.

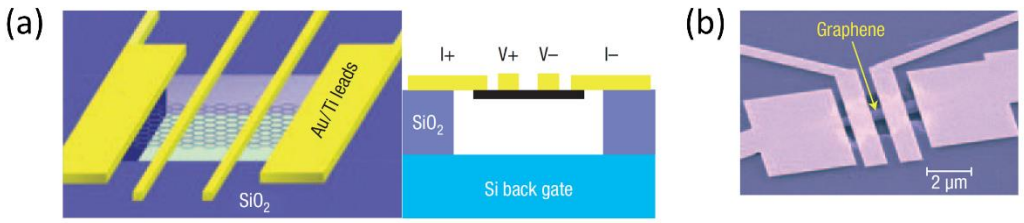

Figure 3.9 Suspended graphene devices. (a) Schematic diagram of the structure of suspended graphene devices. (b) Scanning electron microscope image of a suspended graphene device. Reproduced from Ref. [63] with permission from Springer Nature.

3.2.6 Encapsulation of Graphene

Another method to get rid of the rough SiO_2 surface is to encapsulate the graphene in hexagonal boron nitride (hBN) flakes. hBN is an insulating two-dimensional material, with a lattice constant similar with graphene. It can be mechanically exfoliated in a similar way to expose an atomically flat surface, and act as a perfect substrate for graphene while imposing little effect on the properties of graphene. What's more, the top surface of graphene can also be covered by a mechanically exfoliated hBN flake so that the effect of gas molecule absorption on graphene properties can also be eliminated.

Fabricating such an encapsulated graphene sample was enabled by the development of a deterministic transfer technique [64], which is illustrated in Figure 3.10. The deterministic transfer technique is based on the three-dimensional relative motions of a stamping stage and a sample stage under an optical microscope. The exfoliated flakes of two-dimensional materials are firstly transferred from a tape to a viscoelastic stamp, then aligned with the target on the substrate with the help of an optical microscope, and finally transferred from the stamp to the substrate. By repeating this

process several times with different materials, delicate structures such as graphene encapsulated in hBN can be fabricated. As different layers of two-dimensional materials are held together only by inter-layer van der Waals interactions, these structures are referred to as “van der Waals heterostructures” [65,66].

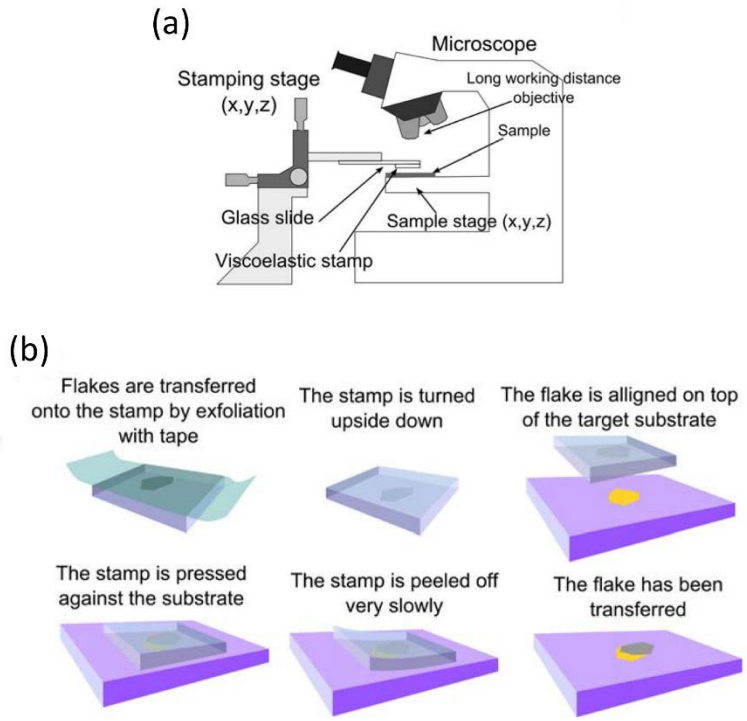

Figure 3.10 Schematic diagram of all-dry deterministic transfer of graphene and other 2D materials. (a) The experimental setup employed for the all-dry deterministic transfer process. (b) Diagram of the steps involved in the preparation of the viscoelastic stamp and the deterministic transfer of an atomically thin flake onto another atomically thin flake. Reproduced from Ref. [64] with permission from IOP Publishing.

Experiments have shown that encapsulating graphene in hBN can enormously increase the electron mobility in graphene. Room-temperature mobility as high as 1.4×10^5 $cm^2V^{-1}s^{-1}$ and low-temperature mobility as high as 1.0×10^6 $cm^2V^{-1}s^{-1}$ have

been measured [67]. It is worth noting that although such a method was initially designed for mechanically exfoliated graphene, it has also been effectively used for CVD graphene and a mobility as high as 3×10^6 $cm^2V^{-1}s^{-1}$ at 1.5 K has been reached [68,69].

3.2.7 Comparison of the Synthesis and Post-Treatment Techniques

We have introduced the major methods to synthesise graphene: either top-down such as mechanical exfoliation and liquid phase exfoliation, or bottom-up such as chemical vapour deposition and epitaxial growth. We have also described two approaches to

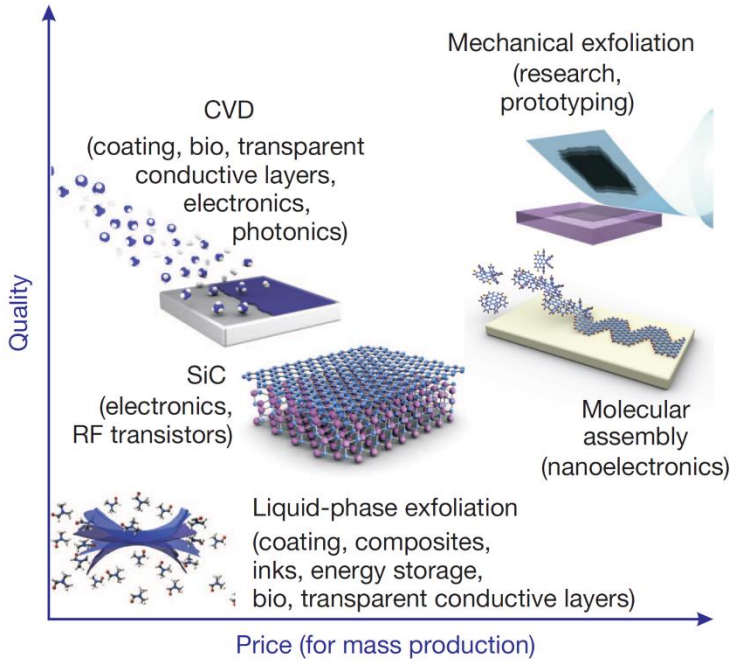

Figure 3.11 A comparison of the synthesis methods of graphene, in terms of the price (for mass production) and the quality. The position in the plot determines the applications of each method. Reproduced from Ref. [70] with permission from Springer Nature.

reduce the effect of the substrate. Here we summarise this section by Figure 3.11, which compares the price per unit and the quality of graphene synthesised by each method. Although great progress has been made in almost each method since 2012, when Ref. [70] was published, the relative positions of these methods in the two-dimensional plot remains the same.

Mechanically exfoliated graphene remains of the best quality, especially when treated by suspension or encapsulation. However, it has the highest price for mass production, if actually possible. Meanwhile, CVD graphene is a good compromise between quality and price. The quality of CVD graphene, although not as high as mechanically exfoliated graphene, is good enough for most applications, especially in electronic devices. The low price of CVD graphene also paves the ways for practical applications.

3.3 Characterisation of Graphene

3.3.1 AFM and Kelvin Probe Force Microscopy

As mentioned in Section 3.2.1, optical microscopy played a crucial role in the discovery of the mechanical exfoliation method and remains an easy method to identify and locate graphene. However, if we want to know more about the morphology and quality of graphene, more explicit characterisation techniques are needed.

Atomic force microscopy (AFM) is a natural choice to characterise the morphology of two-dimensional material. Although the thickness of single graphene layer (~0.34 nm) is well within the detection limits of an AFM, it is challenging to measure the real thickness of a single layer of graphene on a silicon substrate. In fact, single-layer graphene height measured by AFM typically ranges from 0.6 to 1.0 nm,

which is higher than expected due to the difference in tip attraction/repulsion between the insulating substrate and graphene [23,29].

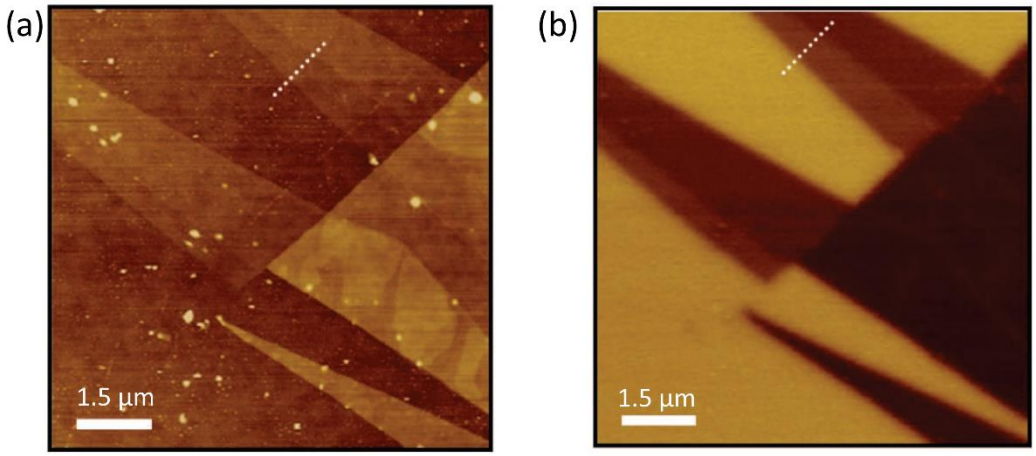

Figure 3.12 (a) AFM and (b) KPFM images of graphene in the same area. The region indicated by the dotted line shows the contrast of single-, double-, and tri-layer graphene (from left to right). Reproduced from Ref. [71] with permission from American Chemical Society.

Kelvin probe force microscopy (KPFM), which is based on AFM, can map the local surface potential of a two-dimensional material, which in turn shows the variations in work function of graphene [71–73]. Due to the different work function of single- and multi-layer graphene, KPFM turns out to be an explicit method to distinguish single-layer graphene from double- or multi-layer graphene and to calculate the percentage of single-layer graphene in a region of the substrate.

3.3.2 Raman Spectroscopy

In a Raman process, an electron in the material is excited by a photon with a certain wavelength. The excited electron can release or absorb the energy of a phonon, and release a photon with different wavelength when it jumps back to ground state.

Therefore, Raman spectroscopy is essentially a probe for the density of phonon states in material. Although it is not a direct topographical technique, it has proved to be the most useful approach to detect the number of layers and defect density in graphene. Raman spectroscopy can be scanned in a relatively large area of graphene samples, providing information such as the percentage of single-layer area and the density and distribution of defects.

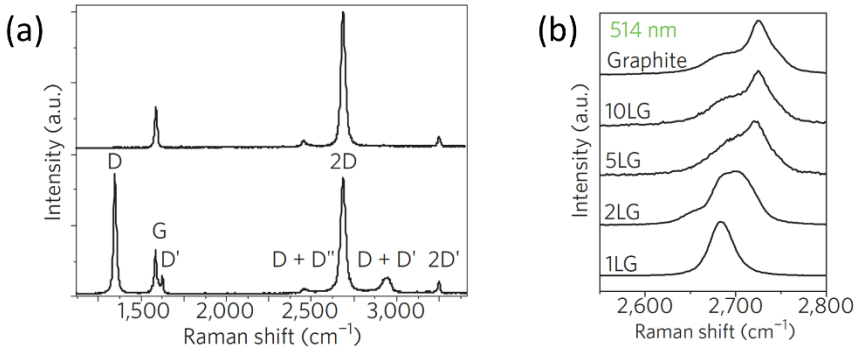

Figure 3.13 Raman spectra of different graphene samples. (a) Raman spectra of pristine (top) and defected (bottom) graphene. (b) Dependence of the 2D peak on number of layers for 514 nm excitation. Reproduced from Ref. [74,75] with permission from American Physical Society and Springer Nature.

As shown in Figure 3.13, the major features of the Raman spectra of graphene include G band at ~1584 cm^{-1}, D band at ~1350 cm^{-1} and 2D band at ~2700 cm^{-1}, as shown in Figure 3.10. The G peak corresponds to the E_{2g} phonon at the centre of the Brillouin zone. The D band is due to the out-of-plane breathing mode of the sp^2 atoms and is active when the symmetry is broken by an edge or in samples with a high density of defects [76,77]. Therefore, it acts as a probe to the level of defects and impurities in graphene. The 2D band shows a significant change in its shape, position and relative intensity to the G band, as the number of layers is increased [75,78,79]. In single-layer graphene, the 2D band is a single sharp peak centred on 2685 cm^{-1}, with

density roughly 4 times that of the G peaks. For loosely stacked graphene layers as epitaxial graphene on carbon-terminated face of SiC, the 2D can shift to 2655~2665 cm^{-1}. For two or more layers, another peak at 2730 cm^{-1} emerges and eventually dominates the 2D band for more than three layers.

3.3.3 Van der Pauw and Hall Measurements

No matter what sort of graphene sample is used, it is important to have a characterisation of the electronic properties before fabricating devices, especially when the synthesis technique is not mature. Conventionally, a combined van der Pauw and Hall measurements are the standard method to measure the resistivity, carrier density, and mobility of thin-film semiconductors [80–82]. It is also feasible to measure the sheet resistance, areal carrier density and mobility of two-dimensional materials including graphene.

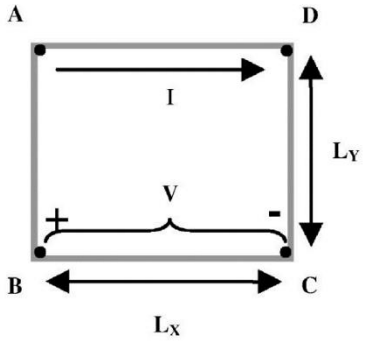

Figure 3.14 Schematic diagram of van der Pauw measurement setup. Reproduced from Ref. [82] with permission from American Physical Society.

The experimental setup for combined van der Pauw and Hall measurements is relatively easy. Four electrodes (named A, B, C, and D) are attached to four corners of a sample of arbitrary shape (usually rectangular), as shown in Figure 3.14. To measure

the sheet resistance, a dc current is applied between two adjacent electrodes, and the voltage across the other two electrodes is measured. The four-terminal resistance in both transport directions are derived by

$$R_{xx} \equiv R_{AD,BC} = \frac{V_{BC}}{I_{AD}}$$

$$R_{yy} \equiv R_{AB,DC} = \frac{V_{DC}}{I_{AB}} \tag{3.9}$$

The sheet resistance R_{s} can be obtained by solving

$$\exp\left(-\frac{\pi R_{xx}}{R_{\mathrm{s}}}\right) + \exp\left(-\frac{\pi R_{yy}}{R_{\mathrm{s}}}\right) = 1 \tag{3.10}$$

To measure the carrier density and mobility, a dc current is applied between two diagonal electrodes, and the voltage across the other two diagonal electrodes is measured with and without a constant magnetic field perpendicular to the sample plane. Since zero magnetic field is difficult to achieve, the two measurements are usually done under magnetic field B and $-B$, resulting in Hall resistance

$$R_{\mathrm{H}} = \frac{R_{AC,BD}(B) - R_{AC,BD}(-B)}{2} \tag{3.11}$$

The areal density of charge carriers is given by

$$n_{\mathrm{s}} = \frac{B}{eR_{\mathrm{H}}} \tag{3.12}$$

and the mobility

$$\mu = \frac{R_{\mathrm{H}}}{BR_{\mathrm{s}}} \tag{3.13}$$

Van der Pauw and Hall measurements can act as a primary identification of the quality of the graphene film. However, that doesn't mean one sample has better quality than another if it is measured with a low sheet resistance or high mobility. Since both sheet resistance and mobility are functions of doping level, it is difficult to compare two graphene samples unless the sheet resistance or mobility at various gate voltages is measured.

Note that the van der Pauw and Hall measurements are macroscopic methods that only measures the average properties of the sample. For measurement of local properties, smaller devices need to be patterned to get rid of spatial inhomogeneity.

3.3.4 Non-Contact Microwave Measurement

The van der Pauw and Hall measurements discussed above requires either deposition of metal contacts which is time-consuming or direct pin contact to the graphene, which may cause damage. A non-contact method to measure the sheet resistance of two-dimensional material based on a high-Q dielectric microwave cavity has recently been developed [83,84].

As shown in Figure 3.15, the dielectric microwave cavity is made up of a single-crystal sapphire puck contained in a cylindrical copper housing. In this dielectric cavity, a series of standing wave modes can be stimulated. The centre frequency and bandwidth of those modes can be measured by connecting the dielectric cavity to a vector network analyser (VNA) and measuring the S_{12} parameter. For a given mode TE_{011}, the centre frequency and bandwidth can be shifted if the local permittivity is changed inside the cavity. For example, a low loss dielectric

substrate in a certain position inside the cavity can cause a shift in both the centre frequency Δf_s and the bandwidth Δw_s. If the dielectric substrate is fully covered by graphene and placed in the same position, the shift in centre frequency and bandwidth is Δf_g and Δw_g respectively. According to perturbation theory, the sheet resistance of graphene can be expressed as

$$R_{\mathrm{s}} = \frac{\Delta f_{\mathrm{s}}}{\pi f_0 \varepsilon_0 (\Delta w_{\mathrm{g}} - \Delta w_{\mathrm{s}})(\varepsilon_{\mathrm{s}}' - 1) t_{\mathrm{s}}} \tag{3.14}$$

where f_0 is the centre frequency of bare housing, ε_0 is the vacuum permittivity, $\varepsilon_{\mathrm{s}}'$ is the real part of the permittivity of substrate, and t_{s} is the thickness of the substrate.

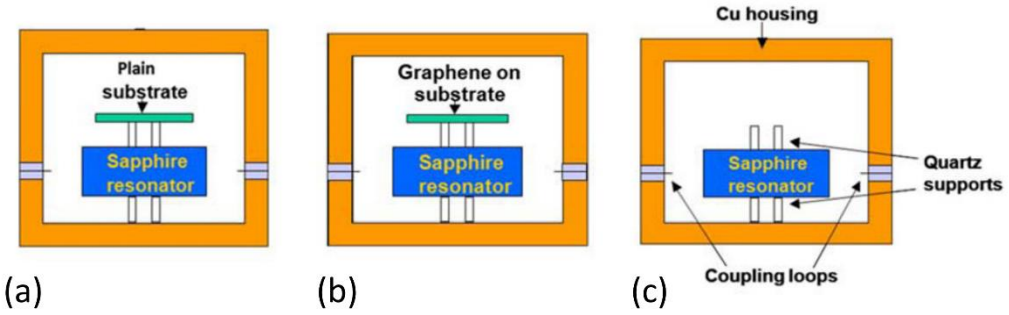

Figure 3.15 Schematic diagrams of non-contact microwave measurement of sheet resistance of graphene. (a) A plain substrate and (b) a substrate with graphene are placed in the same position in the dielectric resonator. The measured centre frequency and bandwidth of TE_{011} mode are compared with (c) the empty housing case. Reproduced from Ref. [83] with permission from AIP Publishing.

This method offers a quick and easy measurement of the sheet resistance of various graphene samples and other two-dimensional materials and shows promising applications in the quality control of roll-to-roll fabrication processes. However, the requirement that the substrate must have a relatively high resistivity (low loss) makes

it infeasible to measure graphene on a highly doped silicon substrate even if the substrate is covered by oxide layer.

Chapter 4 Introduction to Josephson Junctions and SQUIDs Based on Graphene

Josephson junctions and SQUIDs based on graphene and superconductor-graphene hybrid structures have become a hot topic of research in the last decades. In this chapter, we will give a detailed literature review of this research field, mainly focussing on experimental work. In the first section, we will list almost all the research papers we are aware of to date in this area and compare some key parameters reported. After that, we will select several physical properties of graphene-based Josephson junctions and SQUIDs that are particularly interesting or significant, and discuss previous work on these by other groups.

4.1 Overview

Due to the unique band structure of graphene, Josephson junctions with graphene as the barrier were predicted to have a bipolar critical current that can be tuned from electron band to hole band by the gate voltage [85]. Triggered by the successful isolation of single-layer graphene, the first superconductor-graphene-superconductor (SGS) junction was experimentally realised by Heersche et al. in 2007 [86]. Up to now, dozens of papers on graphene- or thin graphite-based Josephson junctions and SQUIDs have been published, and many novel phenomena have been discovered and discussed, which are the topics of the following sections. In Table 4.1, we list almost all the experimental work we can find in this area, with a comparison of the most important parameters. Note that Refs. [107-122] were all published after my PhD

project had started.

Table 4.1 Summary of literature on Josephson and SQUIDs based on graphene or thin graphite.

Refere-nce	Graphene type	No. of graphene layers	Electrode material	Length (μm)	Width (μm)	Critical current I_0 (μA)†	Normal state resistance R_n (Ω)	I_0R_n (μV)	V_g sweeping range (V)	Measure-ment temperat-ure (K)
[86]	EXF	1	Al	0.3	1.5	0.18	500	90	-50~50	0.03
[87]	EXF	~30	Al	0.4	3	0.27	93	25	-70~70	0.06
[88]	EXF	~30	Al	0.2~0.4	5	0.4	240	96	-75~75	0.175
[89]	EXF	1	Al	0.35	9	1.5	62	93	-45~35	0.2
[90]*	EXF	1	Al	0.05	4	6.5			-60~60	0.02
[91]	EXF	1	Al	0.2~0.55	7	0.03	400	12	-50~25	0.3
[92]	EXF	1	Al	0.34	27	0.085			-40~40	0.85
[93]	EXF	1	Ta	0.33	2.7	0.5	87.5	43.8		0.06
[94]	EXF	Multi	Al	0.25~0.54	3	0.7			-70~70	0.2
[95]	EXF	1	Al	0.3	3.2	0.08	140	11.2	-50~30	0.01
[96]	EXF	1	PbIn	0.3	4	3	110	330	-40~40	0.006
[97]	EXF	1	PbIn	0.3	4	6	60	360	-60~60	0.05
[98]	EXF	1	Pb	0.1	1.5~20	1.25	100	125	-40~40	1.3
[99]	EXF	1	Pb	0.265	214	90	1.1	99	-30~50	0.27
[100]	EXF	1	NbTiN	0.15	1.5	4			0~30	0.05
[101]	EXF	1	Nb	1.2	12	0.2	50	10	-30~20	0.2
			ReW	0.7	2.6	0.1	60	6	-25~25	0.055
[102]	EXF	1	Pb	0.4	20	0.5				1.3
[103]*	EXF	1	Al	0.07	2	0.18	200	36	-70~70	0.035
[104]	EXF	1	Al	0.3~0.45	3.2	0.5	100	50	-30~50	0.01

EXF: Mechanically exfoliated graphene. SUS: Suspended.

ENC: Encapsulated. EPI: Epitaxial graphene.

† In cases that V_g is swept, the maximum I_0 and the corresponding R_n is shown here.

* Only in these papers, graphene-based dc SQUIDs were fabricated and measured. I_0 and R_n in those rows refer to those of dc SQUIDs. All other research papers were on single SGS junctions.

Table 4.1 (continued) Summary of literature on Josephson and SQUIDs based on graphene or thin graphite.

Refere-nce	Graphene type	No. of graphene Layers	Electrode material	Length (μm)	Width (μm)	Critical current I_0 (μA)†	Normal state resistance R_n (Ω)	I_0R_n (μV)	V_g sweeping range (V)	Measure-ment temperat-ure (K)
[105]	EXF, SUS	1	NbN	0.5	1.8	0.1	140	14	1~6	2.2
[106]	EXF	1	Pb	0.3~2	5	0.028				0.035
[107]	EXF	1	Al	4.4 ×10^{-3}	5	13.3	21.4	285		0.05
[108]	EXF, ENC	1	MoRe	1.5	2	0.11			-30~30	0.06
[109]	EPI	1	Al	0.2	4	0.02	350	7		0.28
[110]	EXF, SUS	1	Al	0.35~ 0.5	1.5~ 3.2	0.18	90	16.2	-15~15	0.01
	EXF, ENC	1	Al	0.1	2.7					
[111]	CVD	1	Pb	0.4~1	9	6	15	90	-40~40	0.05
[112]	EXF	1	Al	0.07~ 0.35	0.3~ 10	0.2	200	40	-55~5	0.01
[113]	EXF	1	Al	0.3	4	0.3	100	30	-60~60	0.04
[114]	EXF, ENC	1	ReMo	0.2~2		6			-15~15	1.5
[115]	EXF, SUS	1	Nb	0.6	5.5	0.12			-10~10	1.5
[116]	EXF	1	Al	0.35~ 0.5	3.4~4	0.4			-35~35	0.1
			Nb	1.2	12				-30~20	
			ReW	0.7	5	0.2			-25~25	0.1
[117]	EXF, ENC	1	Nb	0.15~ 0.95	5	6			-12~5	0.01
[118]	EXF, ENC	1~2	Al	0.25~ 0.35	0.8~ 1.2	0.24				0.01
[119]	EXF, ENC	1	MoRe	0.3	2.4	5×10^{-3}	8500	4.25	-3~10	0.04
[120]*	EXF, ENC	1	Nb	0.4	3	1.8			-2~2	0.02
[121]*	EXF, ENC	1	MoRe	0.4	2~8	0.4			-10~10	4.2
[122]	EXF, ENC	1	MoRe	0.2~1	1.5~ 4.5	2.7	400	1080	-7~7	0.03

EXF: Mechanically exfoliated graphene. SUS: Suspended.

ENC: Encapsulated. EPI: Epitaxial graphene.

† In cases that V_g is swept, the maximum I_0 and the corresponding R_n is shown here.

* Only in these papers, graphene-based dc SQUIDs were fabricated and measured. I_0 and R_n in those

rows refer to those of dc SQUIDs. All other research papers were on single SGS junctions.

4.2 Fabrication of Graphene-Based Josephson Junctions and SQUIDs

In all the experimental research listed in Table 4.1, most of the SGS junctions and SQUIDs are based on mechanically exfoliated graphene. This is due to the high quality and easy availability of mechanically exfoliated graphene, as we introduced in Section 3.2.1. To further improve the properties of SGS junctions, a number of different treatments can be made on mechanically exfoliated graphene, such as suspending it, or encapsulating it in hexagonal boron nitride (hBN), which were discussed in detail in Sections 3.2.5 and 3.2.6. Especially in the last two years, graphene samples encapsulated in hBN flakes become a more mainstream technology thanks to the growing interest in van der Waals heterostructures. Although the quality of CVD graphene today is already comparable to mechanically exfoliated graphene, and the quality of epitaxial graphene can be even higher, only two research papers on SGS junctions based on CVD graphene or epitaxial graphene have been reported, both of which were published after my PhD project had started.

As to the superconducting electrode material, a couple of metals and alloys have been tried. In most of the initial work, Al was chosen as the electrode material, since Al has a reasonably obtainable T_c (≈1 K), is compatible with fabrication process based on EBL and is easy to evaporate. However, since the working temperature of a Josephson junction is typically lower than the T_c of superconducting material, measurements of Al-graphene-Al junctions generally require a ^{3}He-based refrigerator or dilution refrigerator, and the potential applications of such SGS junctions is severely restricted. Therefore, superconductors with higher T_c, such as Pb, Nb, and alloy superconductors, such as PbIn, and MoRe, have used for SGS junctions. As a

result, higher critical currents at a given temperature were achieved compared with Al electrodes.

Except for the only attempt to fabricate vertical SGS junctions [107], normally SGS junctions are fabricated by depositing two superconducting electrodes close to each other, on top of a graphene flake on an insulating substrate. The electrodes are usually defined by EBL, except in a few papers that the electrodes are directly patterned by FIB. After definition by EBL, a thin adhesive layer (usually Ti or Pd, 3~10 nm) is evaporated before depositing the superconducting material, to ensure good electrical contact with graphene. Sometimes another thin layer (Ti or Au) is evaporated over the superconducting material in-situ to prevent the superconducting material from oxidization.

The geometry of SGS junctions is also of importance since the normal state resistance R_{n} is the sum of the resistance of graphene in the junction and the contact resistance between graphene and the superconducting electrode, and the former depends on the length and width of the junction. The junction length, which is the separation between the two superconducting electrodes, is limited by the EBL and lift-off process in the fabrication, thus is usually in the range of hundreds of nanometres or a few micrometres. In Ref. [90], the authors succeeded in fabricating junctions as short as 50 nm by EBL (Figure 4.1(a)), however, no details of EBL parameters were mentioned in the short paper. To minimise the normal state resistance, wider junctions are desirable. In Ref. [99], two finger-shaped electrodes are defined (Figure 4.1(b)), yielding an extremely high effective junction width within a finite-size graphene flake. Therefore, R_{n} is reduced seriously and the corresponding critical current is several orders of magnitude higher than in other work.

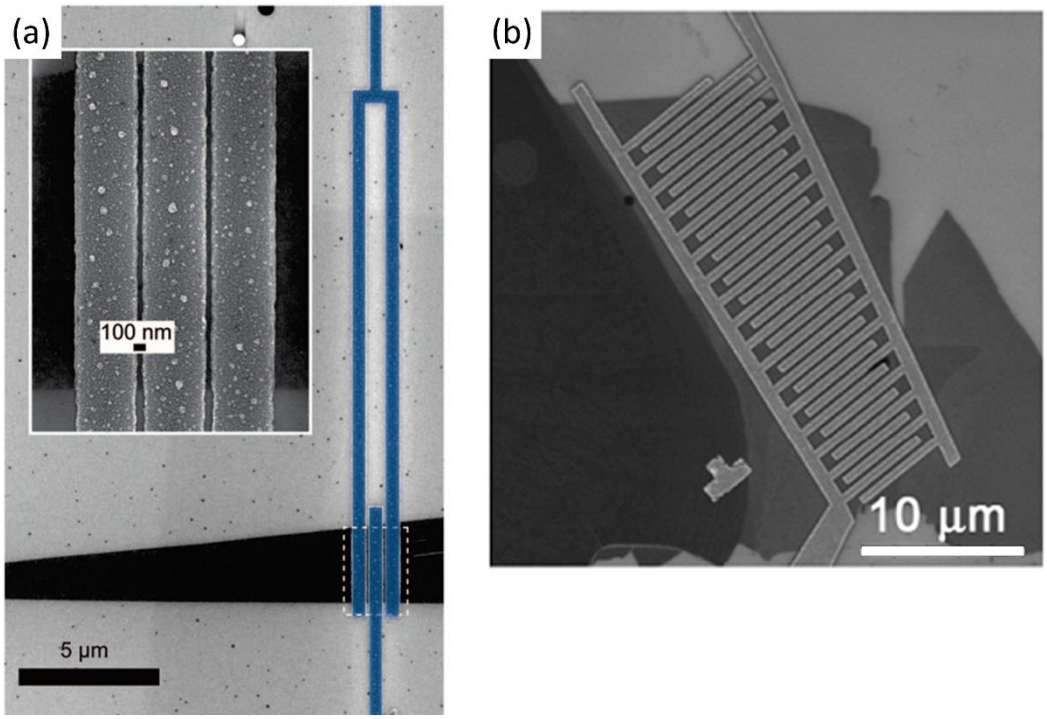

Figure 4.1 SEM images of an SGS junction and an SGS SQUID. (a) False-colour SEM image of a SQUID made with graphene. The superconductor is coloured blue and the graphene is black. Inset: close-up of the 50 nm long SGS junction. Reproduced from Ref. [90] with permission from American Chemical Society. (b) SEM image of an SGS junction with finger-shaped electrodes. Reproduced from Ref. [99] with permission from American Physical Society.

4.3 Bipolar Supercurrent

One of the most interesting and most iconic features of SGS junctions is the bipolar supercurrent, which means that the critical current can be modulated by the gate voltage (Figure 4.2(a)) and increases as the Fermi level is tuned far away from the Dirac point in either direction. The charge carriers can be either electrons or holes depending on the relative position of the Fermi level and the Dirac point. If we plot the differential resistance dV/dI as a function of both the gate voltage V_g and bias

current I, as shown in Figure 4.2(b), the modulation of critical current can be more obviously seen. In Figure 4.2(b), the blue region in the centre indicates the zero-resistance superconducting state, while the red lines surrounding the blue region represent the voltage jump at the critical current. Therefore, the red lines in the plot actually plot the critical current modulated by V_{g}. Here we can clearly see the bipolar characteristic of the critical current, and the critical current reaches its minimum when the Fermi level coincides with the Dirac point. Note that normally the Dirac point is not located at $V_{\mathrm{g}} = 0$, which means the graphene is either n-doped or p-doped, and a finite gate voltage V_{g} is required to tune the Fermi level down to the Dirac point. The dopant can be the substrate, chemical residues left during the transfer and fabrication, or absorbed gas molecules and/or free radicals.

Figure 4.2 Electronic properties of an SGS junction versus gate voltage. (a) *I-V* characteristics of an SGS junction at various gate voltages V_{g}, showing a modulation of the critical current. Inset: *I-V* characteristics with bias current swept up and down showing hysteretic behaviour. (b) Colour-scale plot of differential resistance *dV/dI* as a function of V_{g} and bias current *I*. Reproduced from Ref. [95]. The figure is not shown in the online version of this thesis since no permission could be obtained from the publisher.

Normally, the $I_c - V_g$ curve is not symmetric for the electron band and the hole band. Such an asymmetry originates from the asymmetry of conductance for the electron branch and hole branch. The reason for the asymmetry of conductance can be complicated. It may be an intrinsic asymmetry due to the electron-hole asymmetry that has been discussed in Section 3.1.2, or it may arise from the doping of electrons or holes from superconducting electrodes. Take the most commonly used Al electrodes for example. Since the work function of Al (4.08 eV) is lower than that of graphene (~5.0 eV) [123], the graphene close to the superconducting electrodes will therefore be n-doped. When the bulk graphene inside the junction is p-doped by the gate electrodes, a p-n junction appears near each electrode, forming an n-p-n structure along the junction, resulting in a higher resistance (lower critical current) for $V_g < V_D$.

The *I-V* characteristics of SGS junctions are likely to exhibit hysteresis [86,87,89,90,93,96–99,103,104,106–108,111,113,114,116,122], as shown in the inset of Figure 4.2(a). As we discussed in Section 2.1.2, the hysteresis in the *I-V* curve tends to appear in an underdamped junction with the Stewart-McCumber parameter $\beta_c = 2\pi I_0 R_n^2 C/\Phi_0 > 1$. However, a normal coplanar SGS junction has too small a geometric capacitance to cause hysteresis, if only the capacitance of the two superconducting electrodes is considered. Some researchers claim that the underdamping comes from an additional capacitance due to the presence of the degenerately doped Si substrate [98,108,113], while some others claim that the hysteresis in SGS junctions is caused by an effective capacitance due to diffusive motion of quasiparticles in graphene [96,97,104] or a heating effect [106,108,111,114]. Since the doping level of the Si substrate (which determines the additional capacitance), the thermal conductivity between the device and the thermal bath used (which determines the local temperature of the junction) and the geometry of the junction (which determines both) can vary significantly from one experiment to

another, it is reasonable that the hysteresis in different experiments can have different possible origins. That also explains why there is hardly any hysteresis in some other experiments [88,91,94,95,100,101,105,106,109,110,115,117,119–121].

4.4 Quantum Interference

Another phenomenon frequently reported in SGS junctions is the quantum interference of supercurrent due to the finite size of the junction [86,89,93,95,96,98,100–102,108,109,113,117,118,122], as shown in Figure 4.3(a). As we discussed in Section 2.1.5, in a magnetic field, the critical current of a finite-size junction is the integration of current density with different phase. As a result, the critical current is a Fraunhofer-like function of the applied magnetic field.

The period of the minima of the Fraunhofer-like pattern should be a flux quantum Φ_0. Comparing it with the period in magnetic field allows us to calculate the effective area of the junction, $A_{\mathrm{eff}} = \Phi_0/\Delta B$. However, a carefully measured interference pattern can provide much more information than simply the effective junctions area. Ref [110,118] have shown that the spatial distribution of supercurrent can be reconstructed from the interference pattern by Fourier methods.

For a dc SQUID with symmetric Josephson junctions and negligible β_{L}, the critical current of the SQUID I_{c} is related to the critical current of the junctions I_0 by $I_{\mathrm{c}} = 2I_0|\cos(\pi\Phi_{\mathrm{a}}/\Phi_0)|$, as given by Eq. (2.40). Since for SGS junctions, I_0 is a function of the gate voltage V_{g}, the critical current of a dc SQUID made up of SGS junctions will be modulated by both V_{g} and the applied flux Φ_{a} [90,120], as shown in Figure 4.3(b). This allows us to vary the SQUID sensitivity $|\partial I_{\mathrm{c}}/\partial\Phi_{\mathrm{a}}|$ or $|\partial V/\partial\Phi_{\mathrm{a}}|$ at fixed flux bias, which is potentially useful in increasing dynamic range and varying the coupling strength in quantum measurement.

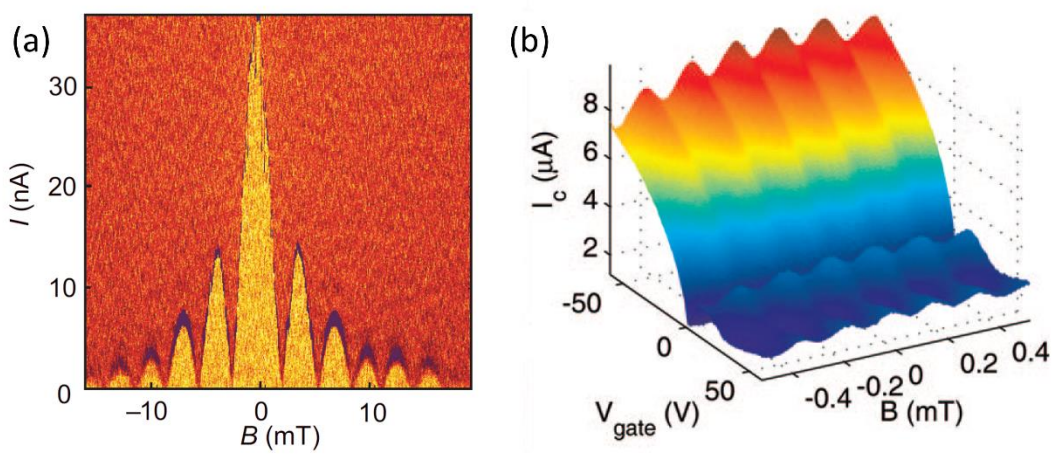

Figure 4.3 Modulation of the critical current of an SGS Josephson junction and an SGS SQUID by the magnetic field and the gate voltage. (a) Colour-scale plot of differential resistance *dV/dI* as a function of bias current *I* and magnetic field *B*. The critical current exhibits a series of oscillations analogous to the Fraunhofer diffraction pattern of a single slit. Reproduced from Ref. [86] with permission from Springer Nature. (b) Critical current I_c of a graphene-based dc SQUID as a function of gate voltage V_g and *B*. The sinusoidal oscillations indicate quantum interference between two SGS junctions. For a fixed magnetic field, the critical current can be controlled by the gate voltage. Reproduced from Ref. [90] with permission from American Chemical Society.

4.5 The Product I_0R_n

The product of critical current I_0 and normal state resistance R_n indicates the scale of the voltage jump from the superconducting state to normal state around the critical current. As we discussed in Section 2.2, for short SIS tunnel junctions ($L_{eff} \ll \xi$), the product I_0R_n is a figure of particular interest since it does not depend on any parameters of the barrier nor the shape of the junction. It is determined solely by the operating temperature and by the gap of the superconductor (or equivalently the T_c

of the superconductor):

$$I_0 R_\mathrm{n} = \frac{\pi}{2}\frac{\Delta(T)}{e}\tanh\frac{\Delta(T)}{2k_\mathrm{B}T} \tag{4.1}$$

If the temperature is much lower than T_c, the hyperbolic tangent term is close to 1. Therefore

$$I_0 R_\mathrm{n} \sim \frac{\pi}{2}\frac{\Delta(T)}{e} \tag{4.2}$$

For short weak-link junctions, either in the dirty or clean limit, there is no analytical expression for the product $I_0 R_\mathrm{n}$, but Eq. (4.2) still holds for the order of magnitude.

In the previous work on SGS junctions shown for example in Figure 4.2(b), the authors found that critical current roughly correlates to the normal state conductance $G_\mathrm{n} = 1/R_\mathrm{n}$ as expected. The black line refers to the normal state conductance, which roughly coincides with the shape of the red line (indicating the critical current). However, a closer look at the experimental results shows that they do not meet the expectation of Eq. (4.2) in two aspects. First, the product $I_0 R_\mathrm{n}$ is usually half or one order of magnitude smaller than $\Delta(T)/e$ [87,89,91,101,104,117]. Second, if we plot the product $I_0 R_\mathrm{n}$ as a function of the gate voltage, it is usually found that the $I_0 R_\mathrm{n}$ is suppressed by a factor of 1/3 to 1/2 around the Dirac point [86,87,89,91,96,98,101,104,105,111,117], as shown for example in Figure 4.4.

There still exist some controversies on the reason for the two phenomena. Some authors [111,117] claim that the SGS junctions in their experiments are long junctions ($L_\mathrm{eff} \geq \xi$). For long junctions, instead of Eq. (4.2), the product of critical current and normal state resistance should follow

$$I_0 R_\mathrm{n} \sim \frac{E_\mathrm{th}}{e} \tag{4.3}$$

where the Thouless energy $E_\mathrm{th} = h v_\mathrm{F}/L$. However, even replacing the superconducting energy gap by the Thouless energy can only explain how the product $I_0 R_\mathrm{n}$ changes with junction length L, but cannot qualitatively explain the suppression of critical current.

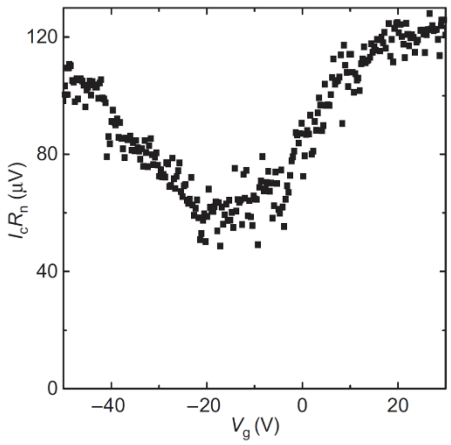

Figure 4.4 Product of critical current times the normal state resistance versus V_g. The normal state resistance is measured at zero source-drain bias, at 30 mK and with a small magnetic field to drive the electrodes into the normal state. The product exhibits a dip around the Dirac point. Reproduced from Ref. [86] with permission from Springer Nature.

For short SGS junctions, some authors [86,87,89,91,96] believe that such a suppression of critical current is caused by the discrepancy between the measured critical current (or switching current) and the intrinsic critical current. As we have discussed in 2.1.3, the thermal fluctuations at finite temperature can round the *I*-*V* curve near the critical current, resulting in a measured critical current lower than the intrinsic critical current. It is found out that the measured critical current I_0 can be

linked to the intrinsic critical current $I_{0\mathrm{i}}$ by [91]

$$I_0 = I_{0\mathrm{i}}\left\{1 - \left[\frac{ek_{\mathrm{B}}T}{\hbar I_{0\mathrm{i}}}\ln\frac{\omega_{\mathrm{p}}\Delta t}{2\pi}\right]^{2/3}\right\} \tag{4.4}$$

where $\omega_{\mathrm{p}} = (2\pi I_{0\mathrm{i}}/\Phi_0 C)^{1/2}$ is the plasma frequency of the junction and Δt is the sweeping time of the bias current through the dense part of the distribution of observed critical current values. According to Eq. (4.4), the critical current is more suppressed around the Dirac point, which explains the suppression of $I_0 R_{\mathrm{n}}$. However, there are other researchers who attribute it to the specular Andreev reflection around the Dirac point [101], which will be discussed in the next section.

4.6 Multiple Andreev Reflection

In Section 2.2.2, we have discussed the proximity effect that happens at a superconductor/normal metal interface. The microscopic process that enables the proximity effect is called Andreev reflection. As shown in Figure 4.5, at a superconductor/normal metal interface, the Fermi level of the normal metal lies in the centre of the gap of the superconductor 2Δ. Assume an excited incident electron in the metal with energy $E_{\mathrm{F}} + \varepsilon$. If $\varepsilon < \Delta$, the electron cannot penetrate into the superconductor. However, it can form a Cooper pair in the superconductor with the retro-reflection of a hole of opposite spin and velocity with energy $E_{\mathrm{F}} - \epsilon$, as shown in Figure 4.6(a). In such an Andreev reflection, both energy and momentum conservation are satisfied, and charge $2e$ is transmitted from normal metal to superconductor. Note that the time-reversal process, where an incident hole absorbs a Cooper pair and is reflected as an electron, can also happen.

In a superconductor-normal metal-superconductor (SNS) junction, Andreev

reflection can happen at both interfaces, so that a finite supercurrent can flow through the junction. The effect of Andreev reflection becomes visible when the junction is biased by a finite voltage V. As shown in Figure 4.7(a), once an electron (or hole) enters the normal metal, its energy will be lifted by eV by the bias voltage. The electron (or hole) can be reflected many times before it finally leaves the normal metal, and several Cooper pairs are transmitted from one superconductor to the other during this process. Particularly, whenever the bias voltage of the junction increases to a fraction of the superconductor gap, $V = \pm 2\Delta/ne$ $(\mathrm{n} = 1, 2, 3 \ldots)$, the minimum number of reflections needed is reduced by 1, so that a new "channel" of transmitting Cooper pairs is opened. The macroscopic effect is a peak in the differential conductance dI/dV or a dip in the differential resistance dV/dI. Therefore, if we plot dV/dI as a function of the bias voltage V, a series of dips will appear at $V = \pm 2\Delta/ne$, due to multiple Andreev reflection (MAR). These peaks provide a precise way to experimentally measure the superconductor gap of the electrodes.

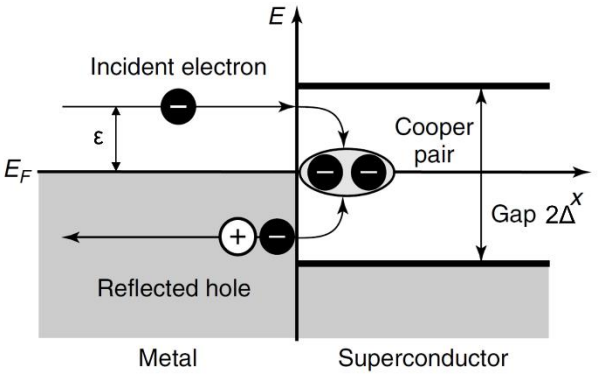

Figure 4.5 Schematic diagram of Andreev reflection at a superconductor/normal metal interface. Reproduced from Ref. [124] with permission from John Wiley and Sons.

For an SGS junction, if the Fermi level is far away from the Dirac point (graphene is highly doped), $|E_{\mathrm{F}} - E_{\mathrm{D}}| \gg \varepsilon$, the incident electron (or hole) and the reflected hole

(or electron) are in the same band, which is the same as in SNS junctions. Therefore, MAR is also observed in SGS junctions. Since the superconductor gap is in the range from hundreds of μV to several mV, if we measure the *I-V* characteristics in a larger range of mV and plot the differential conductance dV/dI as a function of bias voltages. MAR dips will appear as shown in Figure 4.7(b). Multiple Andreev reflection is a robust phenomenon observed in many SGS junctions [86,88–91,93,95,96,100,101,103,104,107,109,110,114–116], even in SGS structures in which the Josephson effect does not emerge [125].

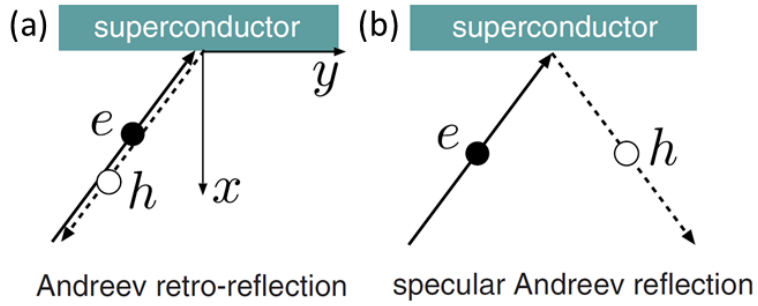

Figure 4.6 Schematic diagrams of Andreev retro-reflection and specular Andreev reflection. (a) Andreev retro-reflection at a superconductor/normal metal interface. (b) Specular Andreev reflection at a superconductor-undoped graphene interface. Reproduced from Ref. [126] with permission from American Physical Society.

However, if the Fermi level is located close to the Dirac point, $|E_F - E_D| \ll \varepsilon$, the incident electron (or hole) and reflected hole (or electron) will be in different bands. In such an interband reflection, as shown in Figure 4.6(b), the reflection is specular rather than retro, which means than the reflected particle will no longer retrace the path of the incident particle [126,127]. In this case, the incident particle and the reflected particle (which can be called an Andreev pair) will follow different paths in the normal metal and accumulate different phase. Since all particles contribute to the macroscopic current with their phase, specular-reflected Andreev pairs with random

phase will suppress the current more than retro-reflected Andreev pairs. Such suppression resulting from specular Andreev reflection is theoretically predicted for intrinsic graphene, however, it is difficult to verify in experiment since the doping inhomogeneity in the graphene, of several meV, is much larger than the superconductor gap.

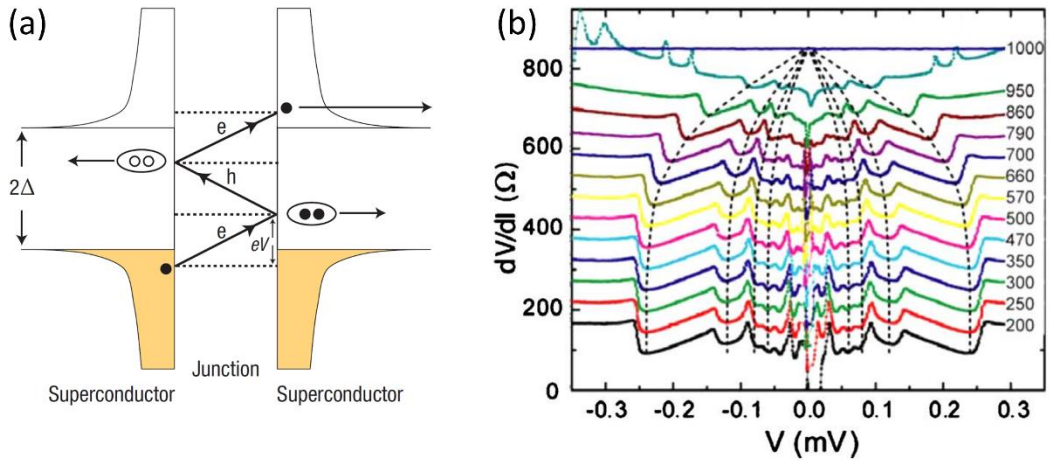

Figure 4.7 Multiple Andreev reflection (MAR) of an SGS junction. (a) Schematic diagram of MAR at the interfaces of an SGS junction. In the 3-step process shown here, an electron entering from the left superconductor undergoes an Andreev reflection at the right interface, and a subsequent reflection at the left interface to end up as an electron in the right superconductor. Each time the electron or hole traverses the junction, it increases in energy by eV. The reflection occurs until either electron or hole has enough energy to propagate into the superconductor. Reproduced from Ref. [128] with permission from Springer Nature. (b) Differential resistance *dV/dI* as a function of bias voltage measured at temperature from 200 mK to 1000 mK. The curves at different temperature are shifted vertically for clarity. The dotted lines show dips of differential resistance caused by MAR. Reproduced from Ref. [89] with permission from American Physical Society.

As shown in Figure 4.8(a), for doped graphene, even though inhomogeneity in the

doping level exists, it is easy to find a path that Andreev pairs transmitted solely in one band. Thus, only retro-reflection happens, and the Andreev pairs are in the same phase. However, in zero-doped graphene with doping inhomogeneity, electron-doped regions coexist with hole-doped ones, forming a network of so-called puddles, as shown in Figure 4.8(b). The electron-doped regions and hole-doped regions are separated from each other by zero-doped regions. As the junction length increases, it becomes more and more difficult to find a path that connects the two superconductors solely in one band. The authors of Ref. [101] claimed that it is the increase of probability of specular reflection at the superconductor/graphene interface and specular-like reflection at the doped-graphene/zero-doped-graphene interface that results in the suppression of critical current, especially in long SGS junctions. However, this explanation still needs further experimental verification.

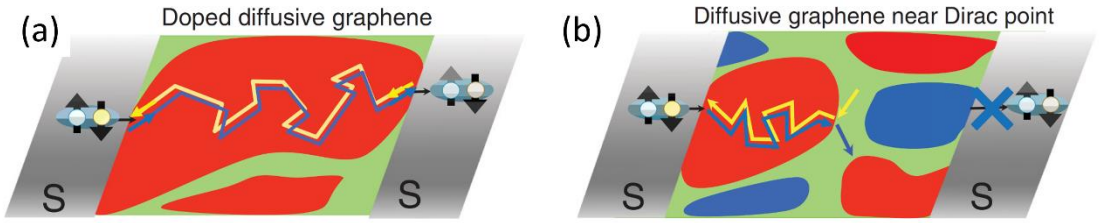

Figure 4.8 Schematic diagrams of the charge transport in a diffusive SGS junction. (a) The graphene is highly doped. (b) The graphene is zero-doped. The red region is electron doped, the blue region is hole doped, and the green region is zero-doped. Reproduced from Ref. [101] with permission from American Physical Society.

4.7 Diffusive or Ballistic

The first theoretical predictions of the characteristics of SGS junctions were based on ballistic SGS junctions [85]. However, the early experiments based on graphene on silicon oxide substrates were in the diffusive regime [89], and only match qualitatively with the theoretical prediction.

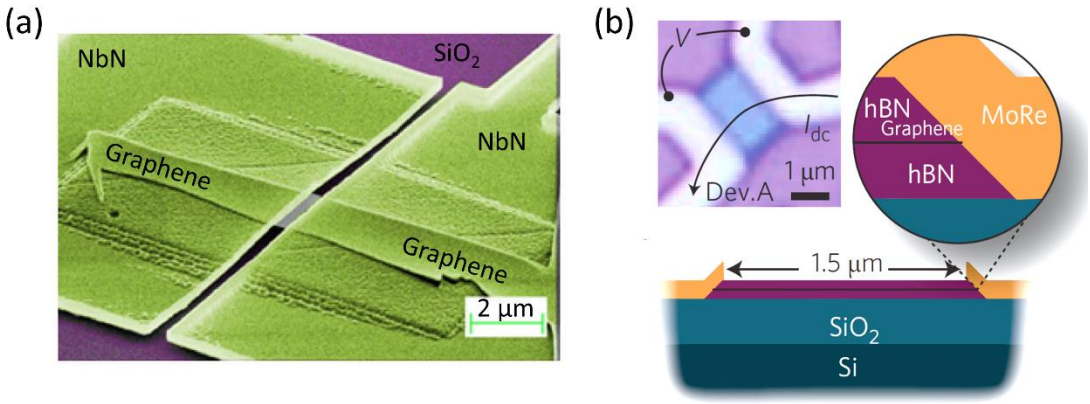

Figure 4.9 SGS junctions based on suspended graphene or encapsulated graphene. (a) False-colour SEM image of an SGS junction based on suspended graphene. Reproduced from Ref. [105] with permission from Springer Nature. (b) Schematic diagram of an SGS junction based on graphene encapsulated in hBN. Inset: optical image of the device. Reproduced from Ref. [108] with permission from Springer Nature.

The criterion for a ballistic or diffusive junction is whether the mean free path of charge carriers in graphene is larger or smaller than the junction length. The mean free path can be calculated by [105]

$$l = \frac{\sigma h}{2e^2\sqrt{n\pi}} \tag{4.5}$$

where σ is the normal state conductivity and n is the carrier density. The normal state conductivity σ can be directly measured at low temperature while the carrier density n can be measured either by the Hall effect or by measuring the normal state conductivity as a function of gate voltage, or simply roughly estimated by $n = \varepsilon_r\varepsilon_0 V_g/ed$. For a typical SGS junction fabricated on a SiO_2 substrate, the mean free path is normally within the range of 10~160 nm [88,89,92,93,95–97,99–

101,103,106,109,111–113,116], which is normally an order of magnitude smaller than the junction length (except for Ref. [90] in which the junctions are as short as 50 nm). Therefore, most SGS junctions on a SiO_2 substrate are typically working in the diffusive regime.

In recent research, methods such as suspending graphene [105,110,115] or encapsulating graphene in hBN [108,110,114,117–122] can increase the mean free path in graphene up to several μm, making it much easier to realise ballistic transport. In Ref. [105], a suspended graphene junction is fabricated with the help of double-layer polymer resist, to eliminate the surface roughness from substrate, as shown in Figure 4.9(a). In Ref. [108], single-layer graphene is carefully encapsulated in hexagonal boron nitride crystals using van der Waals pick-up method, as shown in Figure 4.9(b).

The most convincing evidence for ballistic transport in SGS junctions is the Fabry-Pérot resonance of critical current I_0 (and normal state resistance R_n) [108,109,114,117,120–122], as shown in Figure 4.10. The Fabry-Pérot resonance of critical current normally only happens when the gate voltage is smaller than the Dirac point ($V_\mathrm{g} < V_\mathrm{D}$) so that the graphene inside the junction is p-doped while the graphene under or close to the superconducting electrodes is n-doped. The p-n interface is highly reflective so that the n-p-n junction acts as a Fabry-Pérot cavity for the wavefunction of the charge carriers in graphene. Similar to the Fabry-Pérot cavity in optics, the transmission of charge carriers reaches a maximum when the length of the n-p-n junction (which should be slightly shorter than the geometric length of the Josephson junction due to strong doping from the electrode) is a multiple of the Fermi wavelength of the charge carrier. As a result, the critical current and the normal state resistance will oscillate with the gate voltage.

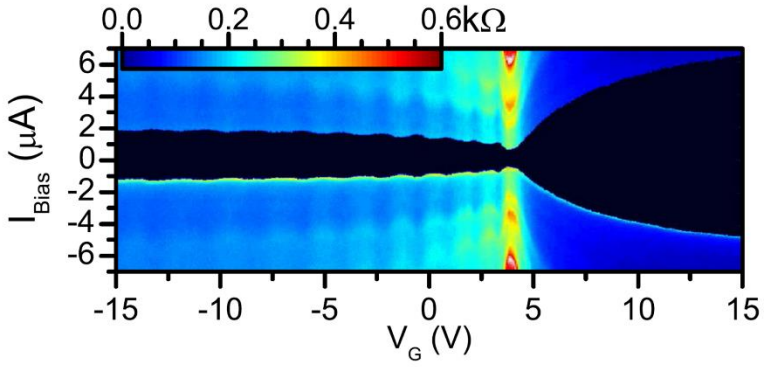

Figure 4.10 Differential resistance vs bias current *I* and gate voltage V_g. The superconducting region of zero resistance can be observed around *I*=0. The graph shows the critical current and the normal state resistance show Fabry-Pérot-like oscillation when the gate voltage is smaller than the Dirac point. Reproduced from Ref. [114] with permission from American Physical Society.

Chapter 5 Fabrication of Josephson Junctions and SQUIDs based on CVD graphene

In this chapter, we show the detailed fabrication methods of Josephson junctions and SQUIDs based on CVD graphene developed on the present project. In Section 5.1, we will start with the characterisation of various graphene samples, and show why CVD synthesised graphene samples from Graphenea™ became a natural choice for use in device development. In Section 5.2, we will outline the complete fabrication process. The following Sections 5.3-5.6 will discuss the challenges we met in the development and optimisation of the fabrication process and how we solved the problems.

5.1 Characterisation and Selection of Graphene Samples

5.1.1 Overview

As we have discussed in the Chapter 3, the synthesis of large-scale high-quality graphene (CVD synthesised graphene or epitaxial graphene) have been intensively studied, and it is easy to obtain various graphene samples from collaborators or companies. In this case, we decided to directly use graphene samples from collaborators or companies, rather than synthesise graphene by ourselves. However, it was essential to examine the quality of those graphene samples before we started fabricating devices with them.

The samples we have examined include:

a) CVD synthesised graphene from the company Graphenea™: Graphene was

grown on copper foils, and transferred to target substrates by the company.

b) CVD synthesised graphene from the company Graphene Supermarket™: Graphene was grown on copper foils, and transferred to target substrates by ourselves.

c) CVD synthesised graphene from a group at Imperial College London: Graphene was grown on copper foils, and transferred to target substrates by our collaborators.

d) Epitaxial graphene from a group at in Linkoping University, Sweden: Graphene was grown on silicon carbide substrate of various qualities, on both the silicon surface and the carbon surface.

Those samples were characterised by AFM/KPFM, macroscopic van der Pauw and Hall measurements and non-contact microwave measurement. The techniques and results are discussed in the following sections.

5.1.2 AFM/KPFM Characterisation

The atomic force microscope (AFM) used in our experiments (Veeco Dimension Icon® with probes PFQNE-AL) can work in an electrical and magnetic lift mode (PeakForce Kelvin probe force microscope (KPFM) mode), which is basically the combination of PeakForce Tapping™ mode [129] and non-contact mode. For each scan line, two passes are needed in total (each includes trace and re-trace). During the first pass, the AFM works in the PeakForce Tapping™ mode. By intermittently tapping the sample at frequencies well below the cantilever resonance frequency, the force-position curves at each point are measured so that the height profile is obtained. At the end of the first pass, the probe is lifted typically tens of nanometres above the surface. Then it is moved along the just-acquired height contour at a constant lift

height for the second pass. During this second pass, the changes of the probe resonance frequency or the phase, which are caused by the long-range magnetic or electric forces, are monitored. In this way, the AFM height image is recorded on the first pass and the KPFM surface potential image is recorded on the second pass. This allows us to characterise the height and surface potential of the same area, although it takes twice the time as conventional AFM. Note that, KPFM requires the samples to be conductive and connected to the sample stage. For graphene samples on insulating substrates such as quartz, to ensure that the graphene layer is properly grounded, a copper tape is generally adhered to the edge of the sample to connect graphene to the sample stage.

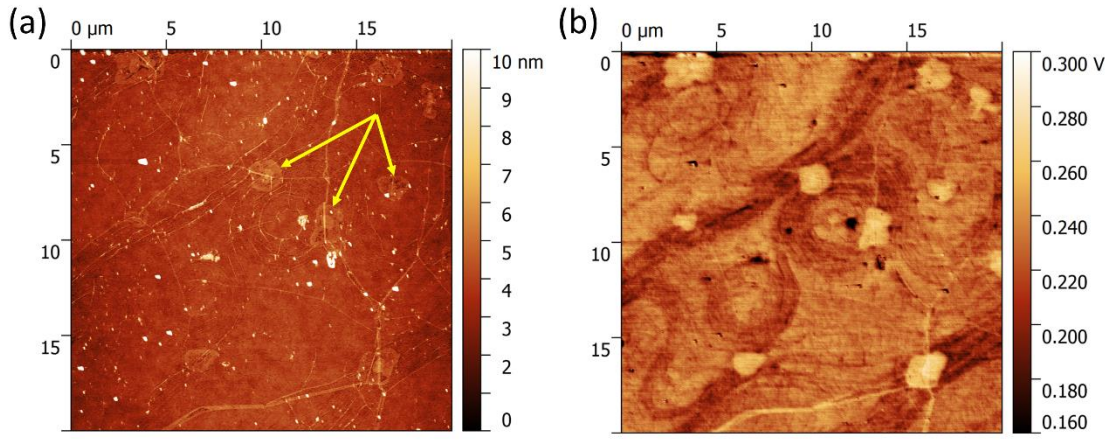

Figure 5.1 (a) AFM and (b) KPFM images of a Graphenea™ CVD synthesised single-layer graphene sample. The graphene was transferred to a silicon substrate with an oxide layer. The yellow arrows in (a) indicate some of the double-layer areas.

Figure 5.1 shows the AFM and KPFM images of a Graphenea™ sample, B1143-2, which is CVD synthesised single-layer graphene transferred to a silicon substrate with an oxide layer. From the AFM image, we can see that, the whole area (20 µm × 20 µm) is fully covered by graphene. The bright patches are double-layer graphene, while the bright lines are the wrinkles generated in the transfer process. The small white spots

in the image, are probably the polymer residues induced during the transfer. Compared with the AFM image, the KPFM image of the same area as the AFM image is a bit blurred, however, the double-layer regions show an even stronger contrast in the KPFM images.

Figure 5.2 shows the AFM and KPFM images of a Graphene Supermarket™ sample, GS-SG-3a, which is CVD synthesised single-layer graphene transferred to a quartz substrate. Similar to Figure 5.1, the AFM image here also shows a contrast between the single-layer graphene and double-layer graphene, as well as the wrinkles and polymer residue caused by transfer (shown as bright lines and large bright areas). However, it is easy to find dark areas in this image, which indicates that this area is not covered. This may be caused by partially covered synthesis or damage in the transfer process. The KPFM image is extremely noisy in the uncovered insulating substrate regions.

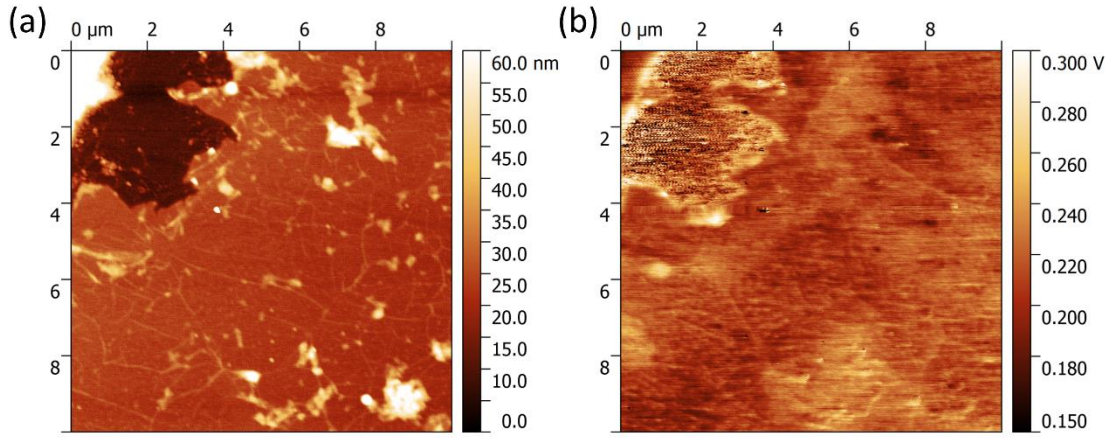

Figure 5.2 (a) AFM and (b) KPFM images of a Graphene Supermarket™ CVD synthesised single-layer graphene sample. The graphene was transferred to a quartz substrate.

Figure 5.3 shows the AFM and KPFM images of an Imperial College sample,

ICM1, which is CVD synthesised single-layer graphene transferred to a quartz substrate. As we can see in the AFM image, the whole graphene surface is covered by those white dots, which are probably the polymer residues induced by the transfer, or the graphene flakes from the other side of the copper foil that are adhered to the graphene layer during the transfer. Because of those contaminants, it is difficult to obtain information about the graphene layer from either the AFM or the KPFM image.

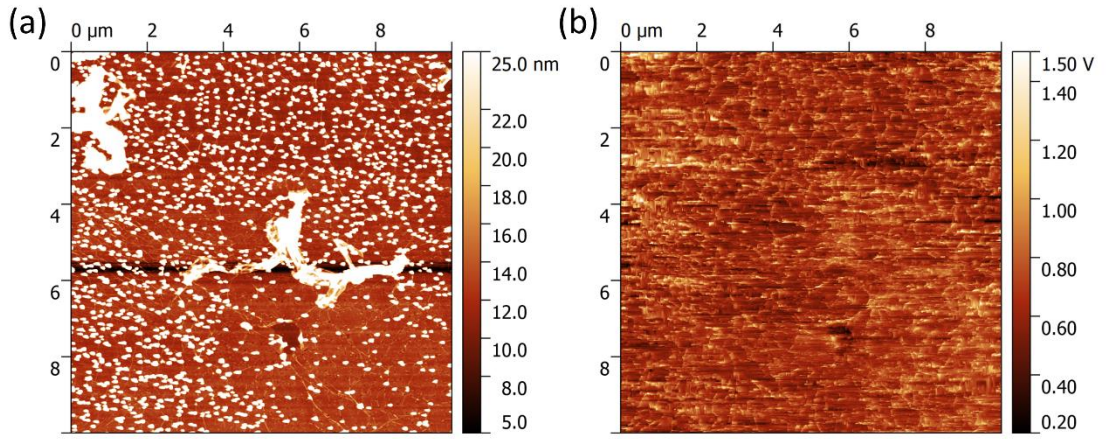

Figure 5.3 (a) AFM and (b) KPFM images of an Imperial College CVD synthesised single-layer graphene sample. The graphene was transferred to a quartz substrate.

Unlike those CVD synthesised graphene samples, epitaxial graphene shows unique morphology under AFM and KPFM. As we can see in Figure 5.4(a), the epitaxial graphene grown on the silicon-terminated face of the SiC substrate (Sample G600) is free from those wrinkles and contaminated observed in CVD synthesised graphene. However, it exhibits a unique step-like structure which originates from the atomic terraces of the SiC surface. Due to such terraces, it is difficult to tell the number of layers of graphene, since the substrate itself is not flat. Hence, the KPFM image plays an important role in determining the number of graphene layers. As shown in Figure 5.4(b), the double-layer region, which appears bright in the image, tends to locate along the step edge. This is reasonable since the epitaxial graphene is grown by the

sublimation of Si atoms and the graphitization of the C atoms, and the sublimation of silicon atoms is easier at the step edges.

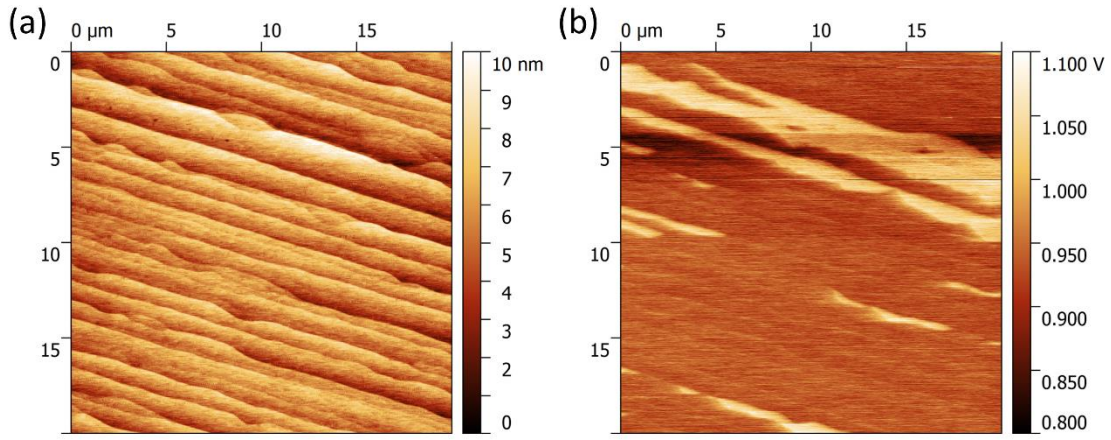

Figure 5.4 (a) AFM and (b) KPFM images of a Linkoping epitaxial graphene sample on the SiC (0001) (silicon-terminated) face of the substrate.

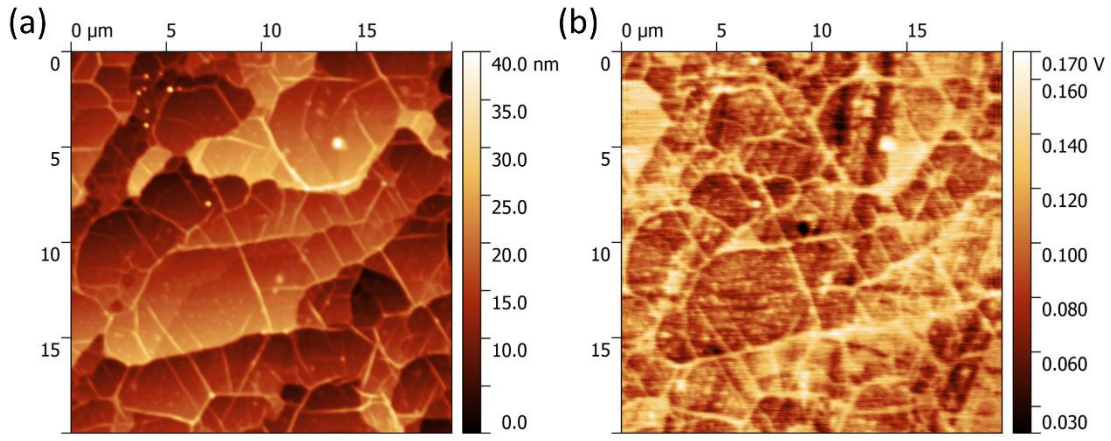

Figure 5.5 (a) AFM and (b) KPFM images of a Linkoping epitaxial graphene sample on the SiC ($000\bar{1}$) (carbon-terminated) face of the substrate.

The morphology of epitaxial graphene on the carbon-terminated face is totally different from the silicon-terminated face. As shown in Figure 5.5, the graphene on the carbon surface (Sample G267) tends to form patches with threefold symmetry

(with the grain boundaries tend to be parallel or at an angle of ±120° with each other). However, the graphene on the carbon surface is generally multi-layer. AFM and KPFM images only characterise the surface layers of graphene.

5.1.3 Macroscopic van der Pauw and Hall Measurements

To measure the sheet resistance and mobility of the samples, macroscopic van der Pauw and Hall measurements were performed on the graphene samples. This provides us a quick way to measure the spatial average values of important transport properties (including sheet resistance, mobility, etc.) of the samples without patterning the sample by micro-fabrication process. To increase throughput and to minimise the damage to graphene samples, a home-made apparatus with four pogo pins was designed and assembled, as shown in Figure 5.6. The graphene sample is placed into the sample holder, and the four screws are adjusted to allow the pogo pins slightly touching the sample surface. The other ends of the pogo pins are soldered to wires connecting a breakout box. The changing of the source and measurement leads thus can be easily achieved by switching connections on the breakout box. The dc current is applied by a Keithley 6221 current source, while the voltage is measured by a Vigol DM3068 digital multimeter. Both the current source and the voltmeter are controlled by a LabVIEW program, in which the current is swept from zero to positive maximum, from positive maximum to negative maximum, and from negative maximum back to zero. At the same time, the voltmeter readout is recorded, and the obtained *I-V* curve is linearly fitted to obtain the resistance. The maximum current is not a fixed value for different samples. Since heat generated by current crowding close to the pins may cause damage to graphene, the applied current is as small as possible, as long as a linear low-noise *I-V* curve can be obtained.

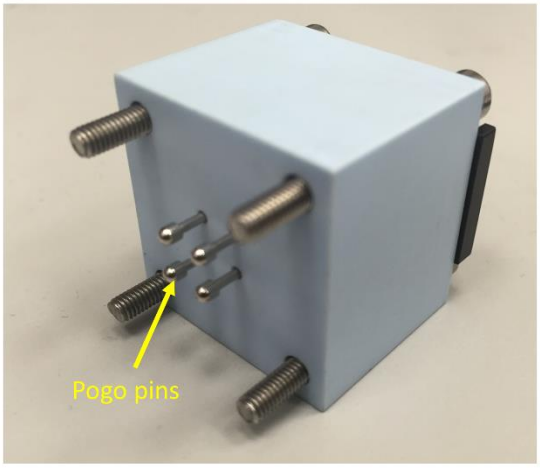

Figure 5.6 The home-made van der Pauw and Hall measurement apparatus for graphene and other two-dimensional samples.

Table 5.1 Different connections used in the van der Pauw measurements. A, B, C, and D refer to the four corners of the sample as shown in Figure 3.14.

Connection	**1**	**2**	**3**	**4**	**5**	**6**	**7**	**8**
I+	B	A	D	C	C	D	A	B
I-	A	B	B	A	D	C	C	D
V+	C	D	A	B	B	A	D	C
V-	D	C	C	D	A	B	B	A

As we have discussed in Section 3.3.3, van der Pauw measurement requires measuring the resistance in at least two directions. In our experiments, to minimise the errors, resistance for eight different connections is measured, as summarised in Table 5.1. The resistances measured in connections 1, 2, 5, and 6 are averaged to give R_{xx}, while the resistances measured in connections 3, 4, 7, and 8 are averaged to give R_{yy}. Then the sheet resistance of the sample is calculated by solving Eq. (3.10). In the Hall measurement, four different connections are used, and each measured in both

positive and negative magnetic field of 0.2 T, as shown in Table 5.2. The magnetic field is applied by a pair of Helmholtz coils, and the magnetic field in the centre is nearly uniform. The Hall resistance is calculated in each of the four connections according to Eq. (3.11), and then averaged. The carrier density and mobility can thus be obtained by Eq. (3.12) and (3.13).

Table 5.2 Different connections of the Hall measurement. A, B, C, and D refer to the four corners of the sample as shown in Figure 3.14.

Connection	**1**	**2**	**3**	**4**	**5**	**6**	**7**	**8**
I+	A	A	B	B	C	C	D	D
I-	C	C	D	D	A	A	B	B
V+	B	B	A	A	D	D	C	C
V-	D	D	C	C	B	B	A	A
B (T)	+0.2	-0.2	+0.2	-0.2	+0.2	-0.2	+0.2	-0.2

In Table 5.3, we list the results of van der Pauw and Hall measurements of dozens of samples. Note that CVD synthesised graphene transferred to a silicon substrate with an oxide layer can yield misleading results in the macroscopic van der Pauw and Hall measurements above, since it is very easy for the graphene on the edge to contact the doped silicon. For some epitaxial graphene samples we measured (not listed in Table 5.3), the results of van der Pauw and Hall measurements are not reliable either, because graphene can grow not only on the two surfaces, but also on the edges, forming very complex conducting routes in the sample. In these two cases, it is better to pattern the sample into a microscopic Hall bar structure to measure the sheet resistance and the mobility.

Table 5.3 Results of van der Pauw and Hall measurements of graphene samples, and the mean free path and normal state coherence length derived from the results.

Sample	Sheet resistance R_s (Ω)	Carrier type	Carrier density n (cm^{-2})	Mobility μ ($cm^2V^{-1}s^{-1}$)	Mean free path l† (300 K) (nm)	Normal state coherence length ξ_n† (300 mK) (nm)
Graphenea CVD graphene on quartz						
F2325	6.5×10^2	Hole	1.0×10^{13}	9.7×10^2	36	280
Graphene Supermarket CVD graphene on quartz						
GS5d	6.4×10^2	Hole	1.8×10^{13}	5.5×10^2	27	240
RSGS1	1.6×10^3	Hole	2.6×10^{13}	1.5×10^2	8.9	140
RSGS2	6.5×10^3	Hole	7.9×10^{13}	1.2×10^2	1.2	49
Imperial College CVD graphene on quartz						
ICM1	2.8×10^3	Hole	6.6×10^{12}	3.4×10^2	10	140
Linkoping University epitaxial graphene						
G267 Si surface	4.2×10^3	Electron	3.3×10^{12}	4.5×10^2	9.6	140
G267 C surface	5.7×10^2	Hole	2.8×10^{13}	3.8×10^2	2.4	70

† The mean free path l and normal state coherence length ξ_n are calculated by Eq. (4.5) and (5.3) respectively.

5.1.4 Non-Contact Microwave Measurement

Another method to measure the sheet resistance is the non-contact microwave

measurement discussed in Section 3.3.4. The experimental setup we use is the same as in Ref. [83], as shown in Figure 5.7. For each graphene sample, the centre frequency and linewidth of the TE_{011} mode are measured in three different configurations: the empty housing only with a sapphire puck and quartz support, a bare substrate without graphene on quartz support, and an identical substrate covered by graphene on quartz support. The quartz support here just acts as a spacer between the substrate and the sapphire. The S_{12} parameters obtained by a vector network analyser (VNA) are collected by a LabVIEW program and the centre frequency and linewidth are derived by fitting the peak in the S_{12} spectrum to a skewed Lorentzian line shape. The sheet resistance can then be calculated according to Eq. (3.14).

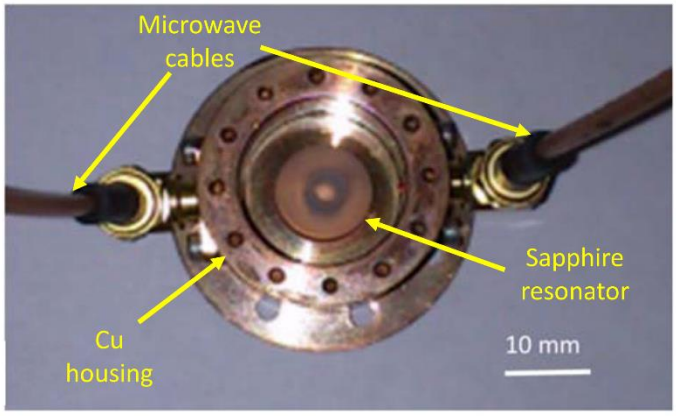

Figure 5.7 The home-made microwave measurement apparatus for graphene and other two-dimensional samples. Reproduced from [83] with permission from AIP Publishing.

Note that although this microwave method is much faster compared with the van der Pauw measurement, it can only be applied to graphene on an insulating substrate such as quartz. Graphene on a silicon substrate with an oxide layer is not feasible unless the silicon substrate is undoped. However, epitaxial graphene on a SiC substrate is feasible, as we have theoretically proved that the measured sheet

resistance equals the sheet resistance of graphene on each surface in parallel, as shown in Appendix A.

Table 5.4 Results of microwave measurement of sheet resistance of graphene samples.

Sample	Sheet resistance R_s (Ω)
Graphenea CVD graphene on quartz	
F2325	4.6×10^{2}
Graphene Supermarket CVD graphene on quartz	
RSGS1	1.1×10^{3}
RSGS2	3.2×10^{3}
Imperial College CVD graphene on quartz	
ICM1	4.4×10^{3}
Linkoping University epitaxial graphene (sheet resistance on each surface in parallel)	
G267	9.3×10^{1}
G489	1.6×10^{2}
G490	1.0×10^{2}

Here we list the results of microwave measurements of several graphene samples in Table 5.4. In comparison with Table 5.3, we can find that for all samples, the sheet resistance measured by the microwave method is a bit lower than that in van der Pauw measurement. We attribute such discrepancy to the systematic errors of the two techniques. For example, the microwave method is based on the 1st-order perturbation theory, which assumes that the microwave is still rotationally symmetric around the *z*-axis even with the existence of the graphene and the substrate, and that

the electric field density does not change significantly within the thickness of the substrate, whereas the van der Pauw measurement requires the pins are connected as close to the edge of the sample as possible. Those assumptions and requirements are usually not perfectly satisfied and can be the origins of the systematic errors.

5.1.5 Raman spectroscopy

Normally, the characterisation by AFM/KPFM together with the information provided by our collaborators or the companies is enough for determining the number of layers in the graphene sample. Therefore, we only characterised one particular kind of sample using Raman spectroscopy: CVD synthesised graphene from Graphenea™.

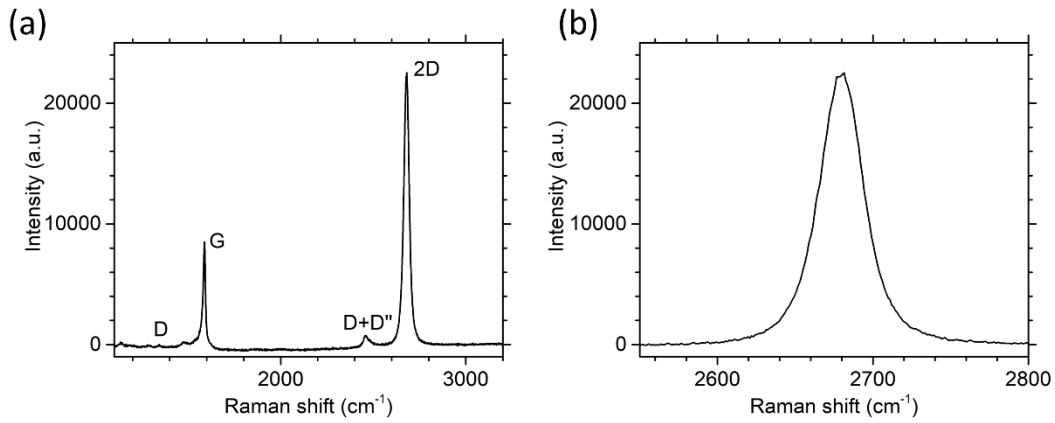

Figure 5.8 Raman spectrum of a Graphenea™ CVD synthesised single-layer graphene sample. The graphene was transferred to a silicon substrate with an oxide layer. (a) The full spectrum; (b) Zoomed-in view around the 2D band. Reproduced from [130] with permission from IEEE.

The Raman spectra are collected on the Graphenea™ CVD synthesised single-layer graphene sample transferred to a silicon substrate with an oxide layer. The measurements are performed at room temperature with a Renishaw inVia Raman spectroscope. The laser wavelength is 532 nm with an incident power of 10 mW. The

spot size of the laser is around 10 μm. In Figure 5.8(a) we display one of the Raman spectra. The intensity of the 2D peak is more than 2.5 times as that of the G peak, indicating that the graphene is mostly single-layer. The D peak is hardly seen in the spectrum, which means impurities and defects are rare in the sample. In Figure 5.8(b) we zoom in to the spectrum around the 2D band. We can see than the 2D band only consists of a single peak, which further indicates that the sample is single-layer. We have collected seven spectra from different positions on the sample, all of which share similar spectrum shape. A couple of the spectra show a bit more obvious D peak, which may be due to some local defects or grain boundaries.

5.1.6 Selection of Graphene Samples

Based on the characterisation and measurements above, we found that CVD synthesised graphene has comparable sheet resistance and mobility compared with epitaxial graphene on SiC substrates. However, the relatively high price of the SiC substrate of epitaxial graphene means that CVD synthesised graphene is more promising in scalable production. The high resistance of SiC also means that a top gate is required to control the *I-V* properties of the Josephson junction, making the fabrication a bit more complicated. Therefore, CVD synthesised graphene seems to be more appealing in building scalable and tuneable Josephson junctions and SQUIDs.

Among the CVD synthesised graphene samples, we mainly consider the two characteristic lengths of the graphene samples: the normal state coherence length ξ_n and the mean free path l. As we have discussed in Section 2.2.2 and Section 4.7, the normal state coherence length determines whether the junction is in the short or the long regime, while the mean free path determines whether the junction is in the “clean” or “dirty” limit. Longer normal state coherence length and mean free path are more desirable since they make it easier to fabricate SGS junctions with apparent Josephson

effect and ballistic transport behaviour. The mean free path l at room temperature can be calculated by Eq. (4.5) using the sheet resistance and carrier density obtained from the van der Pauw and Hall measurements. The normal state coherence length ξ_{n} can be obtained by [131]

$$\xi_{\mathrm{n}} = \sqrt{\frac{\hbar D}{2\pi k_{\mathrm{B}} T}} \tag{5.1}$$

where D is the diffusion constant in the Drude model. The diffusion constant in a 2D material is related to the mean free path by [132]

$$D = v_{\mathrm{F}} l/2 \tag{5.2}$$

where $v_{\mathrm{F}} \approx 10^6$ m/s is the Fermi velocity. So the normal state coherence length ξ_{n} can be calculated by

$$\xi_{\mathrm{n}} = \sqrt{\frac{\hbar l v_F}{4\pi k_{\mathrm{B}} T}} \tag{5.3}$$

Thus, we can estimate the normal state coherence length in graphene at 300 mK by assuming that the mean free path doesn't change too much with temperature. The calculated mean free path l at room temperature and normal state coherence length ξ_{n} at 300 mK obtained in this way are summarised in the last two columns of Table 5.3, from which we can see that the CVD graphene samples from Graphenea™ have the cleanest surface and longest characteristic lengths, and also have the narrowest spread in the parameters. Thus, we decided to use Graphenea™ CVD synthesised graphene samples to fabricate Josephson junctions and SQUIDs. To fabricate the gate

electrode easily, we use the CVD graphene samples transferred to silicon substrates with a 300-nm-thick oxide layer rather than to quartz.

5.2 Fabrication procedure of Josephson junctions and SQUIDs based on CVD graphene

5.2.1 Introduction to EBL

Electron beam lithography (EBL) is an essential technique in micro- and nano-fabrication. Essentially, it is the practice of scanning a focused beam of electrons to draw custom patterns on a surface covered with an electron-sensitive film called a resist. The solubility of the resist can be changed (either increased or reduced) by the electron beam, so that either the exposed or the non-exposed regions of the resist can be selectively removed by immersing in a solvent. The patterns are thus defined on the resist.

The purpose of EBL is to create very small structures in the resist that can be subsequently transferred to the substrate material, which is similar to the purpose of photolithography or nanoimprinting. Compared with the other two techniques, EBL has higher resolution but lower throughput. The most attractive feature of EBL is its flexibility. Since the electron beam is controlled by a beam blanker during scanning, no pre-patterned masks or stamps are needed. That allows researchers to change the pattern freely and optimise the process efficiently.

A typical EBL process includes the following steps:

a) Spin-coating: The surface of the sample is spin-coated with a layer of resist. A resist that increases its solubility after being exposed to the electron beam is called a positive resist. In contrast, a negative resist decreases its solubility after

exposure. The most widely used positive resist is poly(methyl methacrylate) (PMMA), and an available negative resist in our laboratory is hydrogen silsesquioxane (HSQ). The thickness of the resist layer depends on the concentration and the solvent of the resist, and can be controlled by the rotational speed. Normally, after spin-coating, the sample is baked on a hotplate for several minutes to increase adhesion to the surface.

b) Exposure: The scanning of an electron beam is performed in a system similar to an SEM with a beam blanker. The electron beam emitted from the source is optimised by a series of electromagnetic lens and focused on the resist. The acceleration voltage is a vital parameter since it determines the energy of the electron beam. Other parameters include the aperture size which can tune the beam current, the electron dose per unit area and the step size of scanning.

c) Developing: The exposed sample is immersed in a solution called the developer, which can dissolve the exposed or non-exposed resist. The developer varies for different resist, as does the developing time. For example, the corresponding developer for PMMA is methyl isobutyl ketone (MIBK) dissolved in isopropyl alcohol (IPA). After developing, the sample is usually immersed into another solution named the stopper to wash away the developer, for precise control of developing time. After exposure and developing, the custom pattern is defined on the resist.

d) Transfer of pattern: The transfer of patterns from the resist to another layer can be achieved by etching, either dry etching or wet etching, if the layer to pattern is already deposited on the substrate. Undissolved resist will protect the region underneath, while the dissolved region is etched. An alternative way to transfer pattern is called lift-off. The layer we want to pattern is deposited after developing. As a result, only in the dissolved region, is the layer deposited onto

the substrate; while in the undissolved region, the layer is deposited on the top of resist, which can be removed together with the resist.

e) Removal of resist: The resist is finally removed by dissolving the sample in solvents such as acetone.

The EBL system we use in the cleanroom of London Centre for Nanotechnology (LCN) is a Raith 150-TWO. The scanning area of the electron beam, which is called a writing field, is 100 μm × 100 μm or 200 μm × 200 μm. A large pattern is normally divided into several writing fields. After exposing one writing field, the sample stage moves so that the next writing field coincides with the scanning area of electron beam. To ensure that the writing fields are tiled exactly against each other, an accurate laser-aligned stage is critical, and the scanning area must be carefully aligned according to the writing field. Such "writing field alignment" is normally done in two different ways:

a) If a new pattern is to be defined on a substrate without any pattern, a marker on the substrate (usually a dust particle) is found and zoomed in to a relatively large magnitude, and the stage moves to three different positions one by one. The scanning area is aligned to the writing field defined by the same marker in three positions. Essentially, the scanning area is aligned to the movement of the stage.

b) If a pattern is to be aligned to a previously made one, the scanning area should be alignment to the writing fields defined by the markers in the existing pattern.

5.2.2 Deposition of Superconducting Electrodes

Figure 5.9 shows a schematic diagram of an SGS Josephson junction developed in the present project. The entire fabrication procedure of such graphene-based Josephson

junctions or dc SQUIDs involves at least three EBL processes in total.

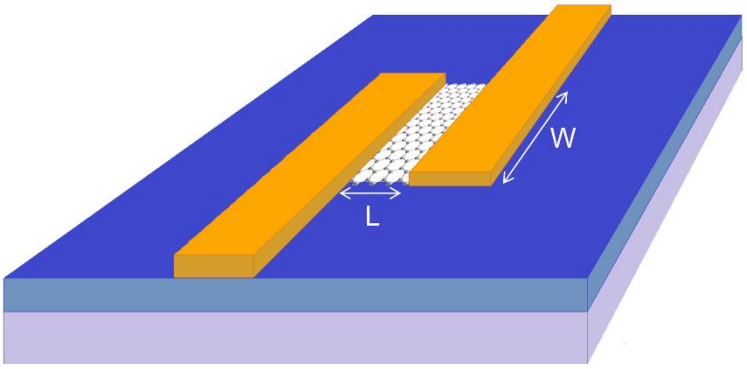

Figure 5.9 Schematic diagram of an SGS Josephson junction fabricated on a silicon substrate with oxide layer. The length of the junction is marked as *L* and the width is *W*. The diagram is not to scale. For real junctions, *W*>>*L*. Reproduced from [133].

The first EBL process is used to deposit the superconducting electrodes. For a Josephson junction (shown in Figure 5.10(a)), two superconducting electrodes are defined in close vicinity, together with the cross markers in the centre writing fields. The long and narrow gap between the two electrodes defines the junction area. The junctions fabricated are of a length L in the range of 50 ~ 850 nm, and a width W in the range of 10 ~ 80 μm. For a dc SQUID (shown in Figure 5.10(b)), two Josephson junctions are defined in parallel with each other. After developing the e-beam resist, a tri-layer of Ti(5 nm)/Nb(70 nm)/Au(8 nm) was sputtered onto the sample in a Scientific Vacuum System V6000. Ti was used here as an adhesive layer, while Au was sputtered in-situ after Nb to prevent its oxidation. A base pressure as low as 5.0×10^{-7} mbar is reached before sputtering. To increase the quality of Nb film, a 15 min pre-sputtering is conducted to remove the surface of Nb target that is contaminated by oxygen. The pattern is then transferred from PMMA to the metal film by lift-off. To prevent possible damage to graphene, all the lift-off processes used in the fabrication are without sonication. For dc SQUIDs, it is important that the entire SQUID loop is defined and deposited in the same process to prevent the formation of $Nb/NbO_x/Nb$

tunnel junctions at interfaces between multiple Nb films.

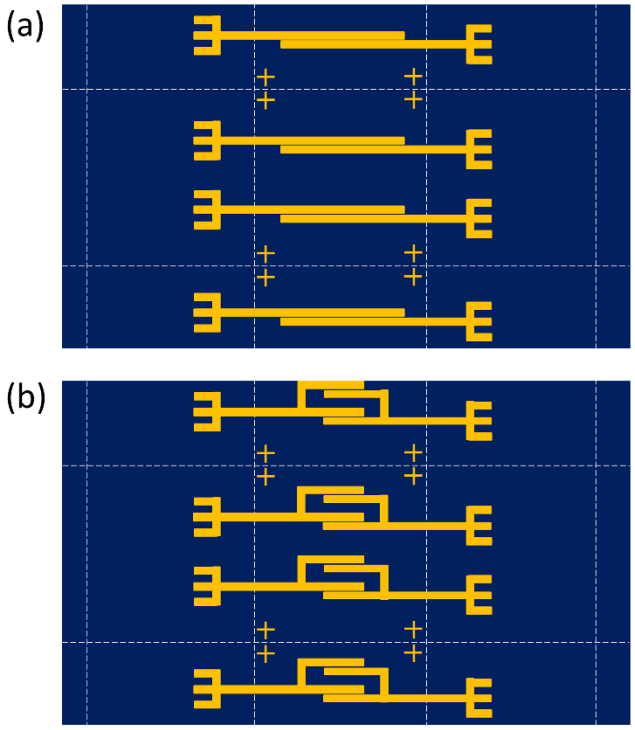

Figure 5.10 Schematic diagrams of devices (top view) after the first EBL process. (a) A series of Josephson junctions, (b) a series of dc SQUIDs. The dark blue areas indicate the substrate covered by graphene. The yellow areas indicate the deposited Nb. The white dashed lines indicate the boundaries of the writing fields (100 μm × 100 μm each).

Hundreds of devices are patterned in the first EBL process. The junctions are designed to have gradually changing lengths, widths and dose factors, whereas the two junctions in the same SQUID loop are designed to be the same.

5.2.3 Deposition of Leads and Bonding Pads

After the first EBL processes, the devices are characterised by SEM. SEM provides a screening of the junctions, and only junctions with appropriate lengths and widths,

and without possible leakage points are selected for further fabrication.

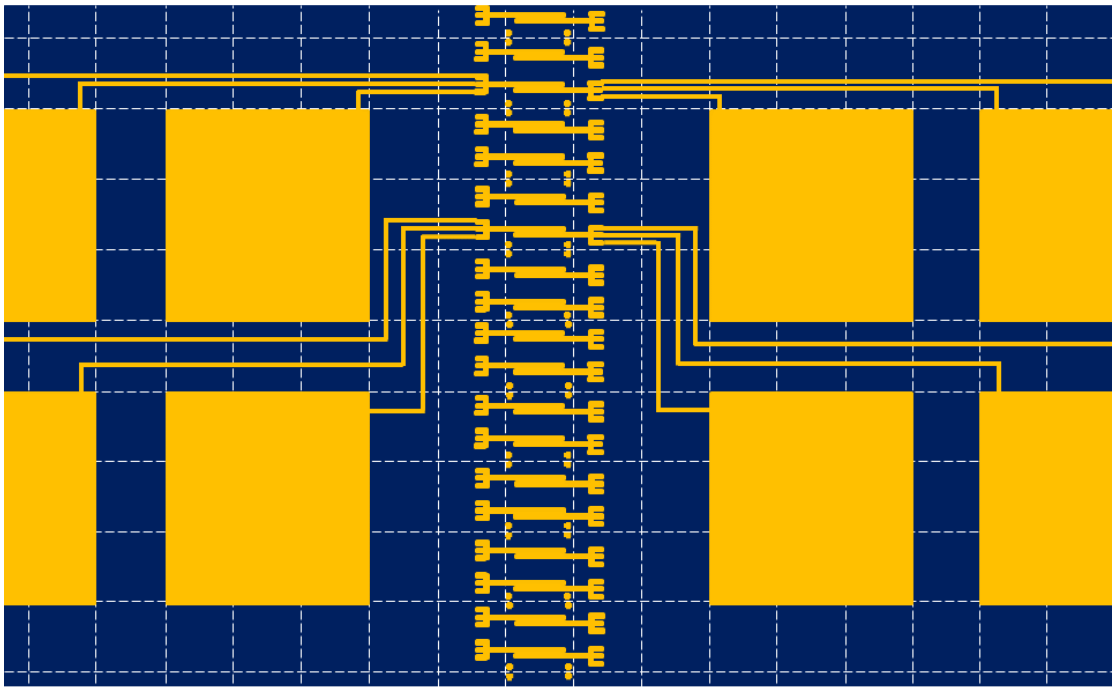

Figure 5.11 Schematic diagram of devices (top view) after the second EBL process. The bonding pads and leads were defined and deposited.

In the second EBL process, the pads for wire bonding are defined, together with the leads from the selected devices to the bonding pads, as shown in Figure 5.11. Note that, in this EBL process, the area exposed is much larger than the previous two, and the requirement of precision in location is lower. Therefore, the EBL is operated with the largest aperture (120 μm) to reduce the exposure time. After developing, the sample is sputtered with 5 nm Ti and 55 nm Au, followed by lift-off without sonication. We have also tried using Nb film as the leads and the bonding pads. However, this again raises the concern of Nb/NbO_x/Nb tunnel junctions formed at the interface between the two layers of Nb. Thus, we finally chose to use Au for the leads and the bonding pads.

5.2.4 Isolation of the Devices

The fabrication of the devices is almost finished in the first two EBL process. However, the graphene layer is still connecting all the devices and electrode pads. In order to measure the properties of a single device, the device has to be electrically isolated from others. The way we realise that is to expose the regions surrounding the device and inside the SQUID loop by the fourth EBL process, allowing graphene in these regions to be etched by Ar milling, as shown in Figure 5.12. After that, the fabrication of the devices is finished, and the devices are ready for measurement, as shown in Figure 5.13.

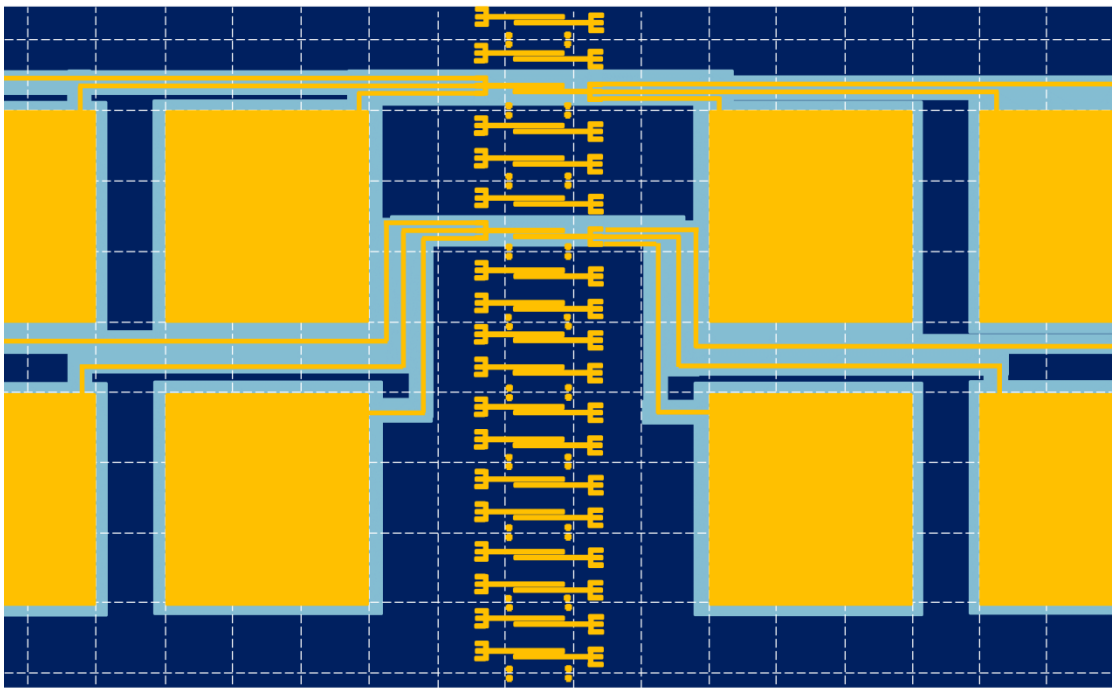

Figure 5.12 Schematic diagram of devices (top view) after the third EBL process. The light blue areas indicate where the graphene is removed.

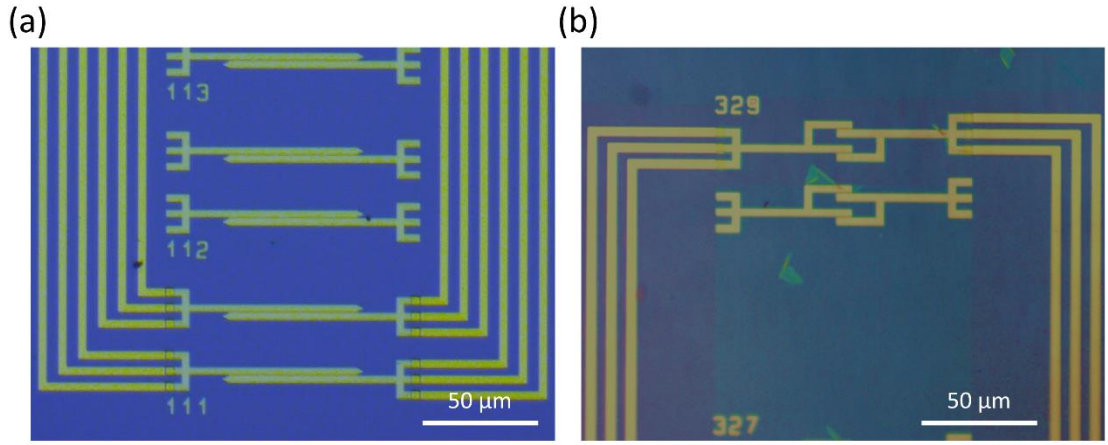

Figure 5.13 Optical microscope images of SGS junctions and SQUIDs. (a) Josephson junctions based on CVD graphene. (b) dc SQUIDs based on CVD graphene.

5.2.5 Connection of the gate electrode

The p-doped silicon substrate (with a resistivity < 0.005 Ω·cm at room temperature) is used as the back gate. The insulating oxide layer between the gate and the device is 300 nm thick. To make connection to the back gate, the highly doped layer on a corner of the sample needs to be exposed and deposited with a metal film. An easy way to do that is to remove the silicon oxide layer on a corner mechanically using a file, after the sample is spin-coated with PMMA for the second EBL process. Thus, the exposed doped layer is then covered by a Ti/Au layer after sputtering.

We also tried etching the oxide layer on the corner by immersing the corner in HF buffer solution for 5 min, while the rest of the surface is protected by 300-nm-thick PMMA. The method also works well in removing the oxide layer. However, we found out later that the devices fabricated in this way were easy to be short to the back gate. The oxide layer was likely to break down under a gate voltage. That indicates the PMMA layer is not dense enough as a protecting layer and the oxide layer under the PMMA is still partially corroded. Therefore, this method was abandoned later.

5.3 Reduction of Junction Length and Electrode Roughness

5.3.1 The Trade-off between Achieving Fine Structures and Easy Lift-off

As we have discussed in Section 4.5, theoretically, the product of critical current I_0 and normal state resistance R_n of a Josephson junction only depends on the energy gap of the superconductor and the temperature. To fabricate graphene-based Josephson junctions and SQUIDs that work at relatively high temperature, one of the key issues to be considered is to reduce the length of the junction while increasing the width of the junction, in order to obtain a low normal state resistance R_n and a high critical current I_c. That means the two superconducting electrodes are to be separated by a very long but narrow gap. Nowadays, it is easy to define a structure on PMMA as small as 20 nm with EBL, but to transfer the pattern from PMMA to a gap as narrow as 50 nm between electrodes can still be challenging, as we need to lift off a long and narrow PMMA "wall".

The quality of the EBL patterning and lift-off process is affected by many factors. Among them, the key parameters are the acceleration voltage of the electron beam, the size of aperture, the electron dose, the thickness of PMMA film and the developing time etc. To quickly find out the best recipe, we performed a lift-off test on a substrate without graphene. The test pattern (shown for one sample DoseTest1 in Figure 5.14) is made up of several rectangular apertures separated by different spacings. Each unit contains ten apertures (200 μm × 10 μm). The spacing (PMMA wall thickness) between two adjacent apertures is 20 μm, 10 μm, 5 μm, 2 μm, 1 μm, 500 nm, 200 nm, 100 nm, and 50 nm respectively.

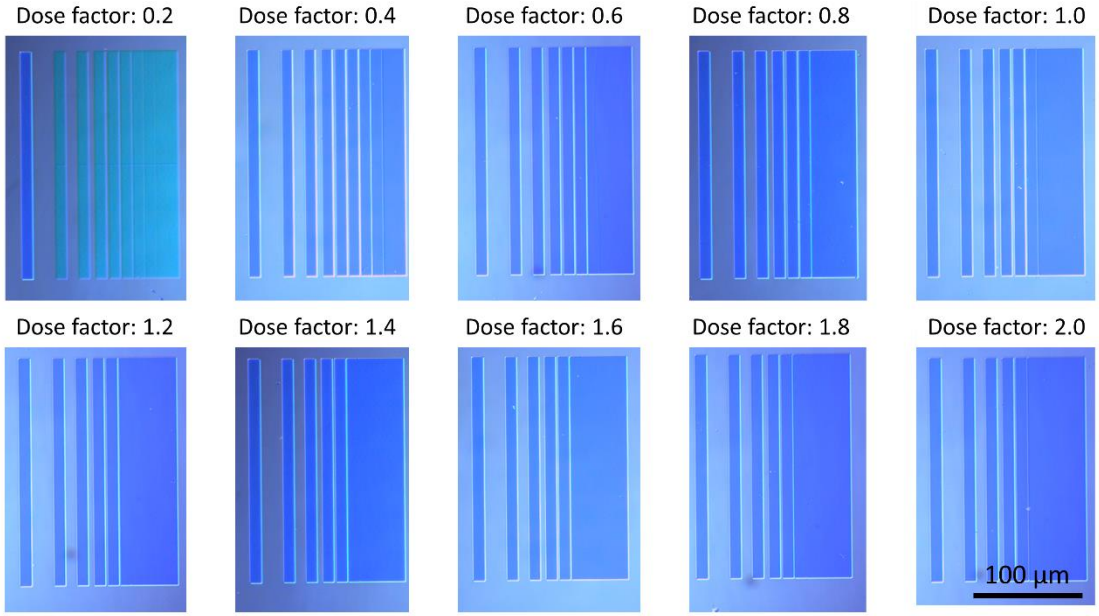

Figure 5.14 Optical microscope images of a test sample (DoseTest1) after EBL patterning and developing. In each unit, apertures with different spacing are defined. The dose factor of each unit is gradually changed in small steps from 0.2 to 1.0.

In every exposure, tens of units with different dose factors are patterned, while other parameters are kept the same. Note that the actual electron dose equals the dose factor times the pre-set dose (100 µAs/cm^2 for area structure). By this means, the best dose for a certain electron beam and developing condition can be quickly found.

We firstly started with a custom electron beam condition (10 keV acceleration voltage and 30 µm aperture). After patterning, the samples are developed by 1:3 MIBK to IPA solution. After developing, patterns defined on PMMA layer are observed under an optical microscope. We can see that below a certain dose factor, the depeloped region is a bit rough, which means the PMMA layer is not fully developed. (This may be not obvious in the CCD-captured images in Figure 5.14, but can be clearly seen from the eyepiece.) So we can define a concept called “the minimum dose factor needed to fully expose”. This is always the dose factor at which the narrowest PMMA wall can be developed. If the dose increases, more and more fine

structures tends to disappear due to overdosing. If the dose decreases, although narrower PMMA wall may be preserved, the PMMA in the exposed area cannot be fully removed, making it useless for electrode deposition.

For the sample DoseTest1, the PMMA 950 A4 solution was spin-coated at 2000 rpm to achieve a thickness of 300 nm, and baked at 180 °C for 5 min. The optical microscope images after developing are shown in Figure 5.14. When the dose factor is 0.2, it is underexposed. The minimum dose factor for full exposure is 0.4, and at this dose, a PMMA wall as narrow as 100 nm is developed. When the dose factor increases to 0.6, both 100-nm- and 200-nm-wide PMMA walls disappear, so the narrowest PMMA wall remaining is 500 nm. As the dose factor increases to 1.2, even the 500-nm-wide PMMA wall disappears and the narrowest PMMA walls for dose factors higher than 1.2 are all 1 μm wide.

After that, a 40-nm-thick Nb film is sputtered onto the sample. To lift-off the PMMA layer, the samples are immersed in acetone for 2 min and further sonicated for 30 s. After that, we observed the samples under optical microscope again.

As we can see in Figure 5.15, the lift-off for low dose factors is not perfect. For dose factor 0.4, although the narrowest PMMA wall of 100 nm wide is formed, only the widest gap (20 μm) is lifted off. This is reasonable since a low dose of the electron beam tends to leave some residue at the bottom corner of the PMMA wall, while a high dose tends to form straight and sharp walls, even walls with the bottom narrower than the top (so-called “undercut” effect).

If we simply plot the narrowest wall developed and narrowest gap lifted off against the dose factor, we can see the trend more clearly in Figure 5.16. As the dose factor increases, the narrowest wall developed increases while the narrowest gap lifted off decreases. The minimum width of a gap between electrodes locates where these two

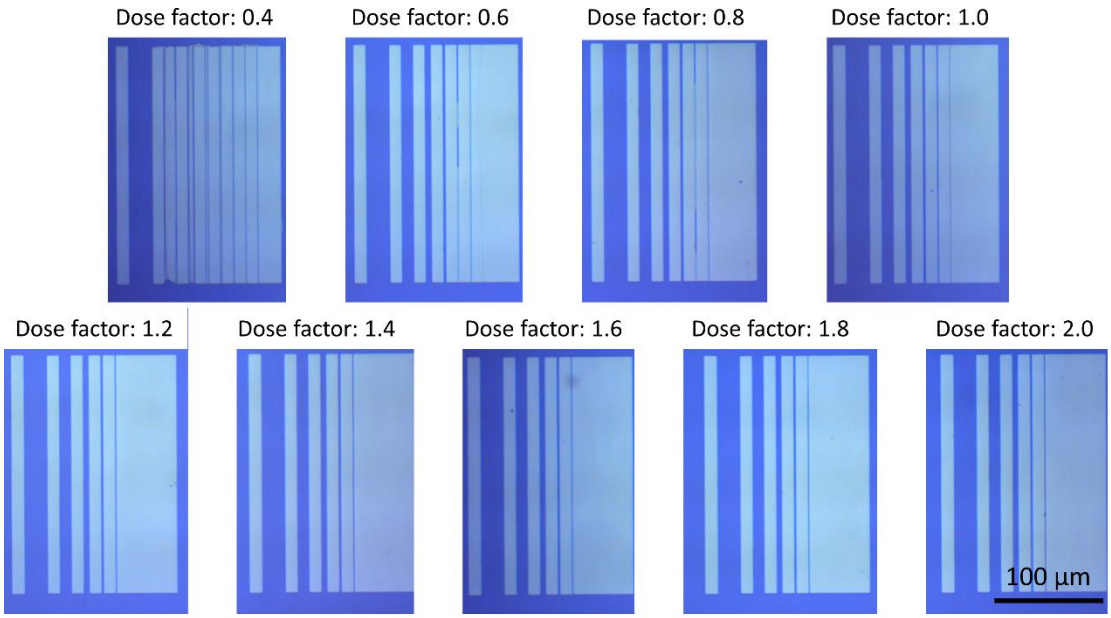

Figure 5.15 Optical microscope images of the same sample (DoseTest1) as in Figure 5.14 after sputtering Nb and lift-off. Note that not all gaps between electrodes are successfully lifted-off, depending on the gap width and dose factor.

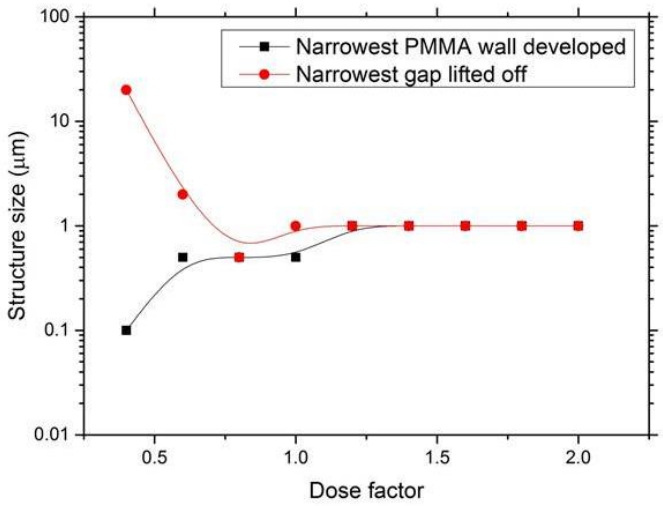

Figure 5.16 Summary of narrowest PMMA wall developed and narrowest gap lifted off as a function of dose factor. The data is collected from the same sample (DoseTest1) as in Figure 5.14 and 5.15.

lines meet. For this sample (DoesTest1), the minimum is 500 nm at dose factor 0.8.

We further tried to change the thickness of PMMA film and the acceleration voltage of the electron beam and summarised the results in Table 5.5. A comparison of samples DoseTest1, 2, and 3 shows that, as PMMA thickness is reduced, a PMMA wall as narrow as 50 nm can be developed. That is because, for thicker PMMA films, the undercut effect discussed above is more likely to cause the PMMA wall to collapse, as schematically shown in Figure 5.17(a). However, although narrower PMMA walls can be defined on thinner PMMA film, the lift-off process becomes more difficult (Figure 5.17(b)). As a result, the narrowest gap lifted off is even wider for thinner PMMA film.

Table 5.5 Results of deposition of Nb electrodes with a narrow gap.

Sample	DoseTest1	DoseTest2	DoseTest3	DoseTest4	DoseTest5	DoseTest6
PMMA thickness (nm)	300	200	100	300	200	100
Acceleration voltage (keV)	10	10	10	30	30	30
Aperture (μm)	30	30	30	20	20	20
Developing time (s)	75	75	30	30	30	30
Dose factor range	0.2~2.0	0.1~1.0	0.1~1.0	0.2~3.6	0.2~3.6	0.2~2.0
Minimum dose factor to fully expose	0.4	0.7	0.7	2.2	2.0	1.6
Narrowest PMMA wall developed	100 nm	100 nm	50 nm	50 nm	50 nm	50 nm
Narrowest gap lifted off	500 nm	1 μm	5 μm	200 nm	200 nm	>20 μm

Another way to get rid of the undercut effect is to use an electron beam with higher acceleration voltage. That is because an electron beam with higher energy tends to penetrate deeper inside the material, rather than being scattered near the surface, as shown Figure 5.18. Again, three samples (4, 5, and 6) with different PMMA thickness were tested. It is evident that undercut is significantly reduced since 50-nm-wide PMMA walls are easily defined under a 30 keV electron beam. However, the sputtered Nb film tends to deposit not only on the top of PMMA film, but also on the side walls (Figure 5.17(c)). The PMMA films are therefore wrapped by the Nb layer, again resulting in difficulty in lift-off.

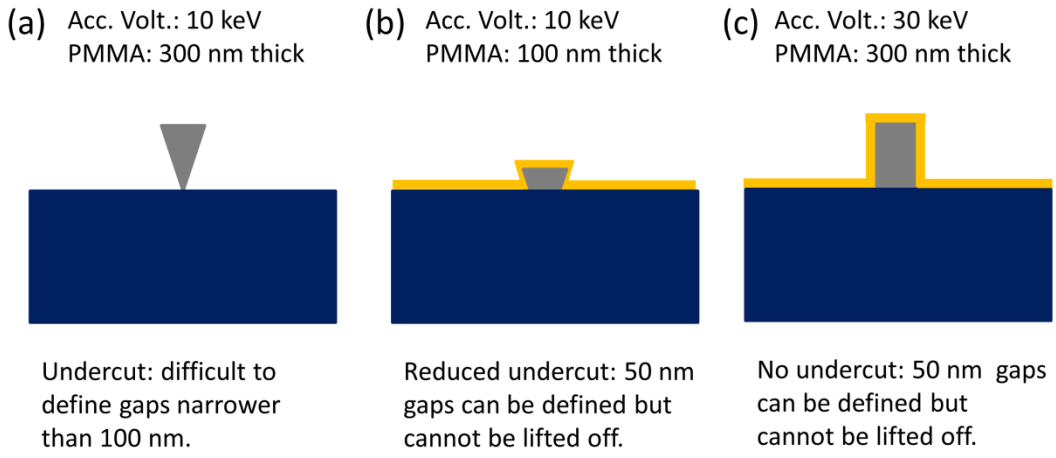

Figure 5.17 Schematic diagram of problems emerging in the lift-off process for different EBL parameters. (a) Narrow PMMA walls tend to collapse due to undercut. (b) Difficult to lift off due to thin PMMA layer. (c) Difficult to lift off since PMMA is fully covered by Nb layer. The PMMA is shown as grey. The metal is shown as yellow.

The experimental results above clearly show that we are facing contradicting requirements in fabricating electrodes with a narrow gap. On the one hand, defining a narrow PMMA wall requires us to get rid of the undercut effect, so thinner PMMA film and higher acceleration voltage are needed. On the other hand, the undercut is favourable for the lift-off, so thicker PMMA and lower acceleration voltage are

desirable. The difficulty in lift-off is further increased since high-quality Nb can only be deposited by sputtering, which is less directional than thermal evaporation, and more likely to deposit on the side walls of PMMA. However, it doesn't mean that EBL and lift-off are totally incompatible with sputtering. It just means that a careful optimisation of parameters is needed, which can be time-consuming and parameter-sensitive. Therefore, we turned to some other strategies to deposit the electrodes: either to define and to deposit two electrodes separately or to use double-layer PMMA as resist.

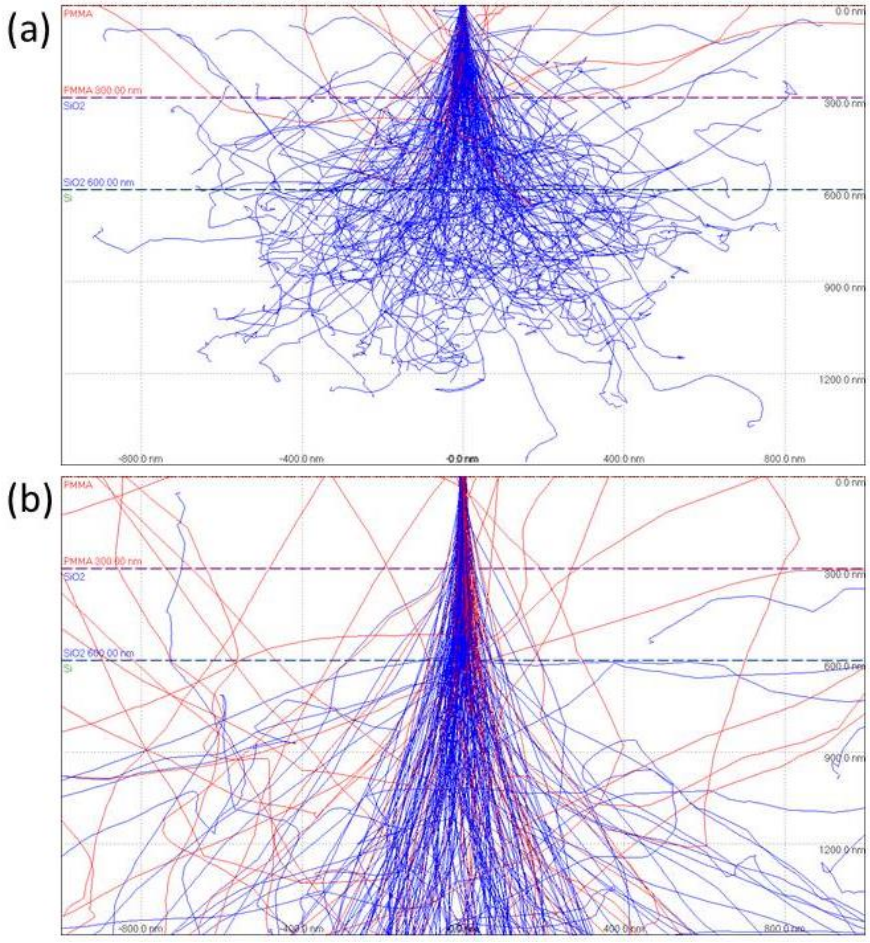

Figure 5.18 Distribution of electron beam propagating into a silicon substrate with an oxide layer and coated with PMMA, simulated by CASINO v2.4.8.1. The acceleration voltage is (a) 10 keV and (b) 30 keV, respectively.

5.3.2 Depositing the two Electrodes Separately

In this strategy, the two superconducting electrodes of the Josephson junction are defined and deposited in two EBL processes, one after another. Therefore, after each EBL process, the PMMA regions to be removed in lift-off are large in size, rather than narrow PMMA walls. The large-area PMMA regions can be easily lifted off with the help of undercut, without the trouble of structure collapse.

The challenge of such a double lift-off process is to precisely control the spacing and parallelism between the two electrodes. To find out whether the double lift-off could achieve the goal of depositing electrodes with a narrow gap, we performed another lift-off test on a substrate without graphene. Similarly, the test pattern is made up of parallel rectangular apertures designed with different spacings from 10 nm to 100 nm. However, any two adjacent apertures are set in two different layers so as to be patterned separately. In the first EBL process (10 keV acceleration voltage and 30 μm aperture), only half of the apertures are defined, together with all large and small cross markers designed for angle correction and writing field alignment in the second EBL process. Then the sample is sputtered with Nb and lifted off. In the second EBL process (the same parameters as the first), the cross markers are employed for angle correction and writing field alignment, in order to make the apertures defined in the second EBL coincide as much as possible with the electrodes defined in the first EBL. Then the sample is sputtered with Nb and lifted off again, and characterised by optical microscope and SEM.

In the optical microscope image (Figure 5.19(a)), we can see those electrode bars aligned in parallel, but it is hard to tell whether a gap exists between adjacent electrodes and how narrow the gap is. In SEM images, we can see the details of the gaps more clearly. Throughout the sample, gaps narrower than 200 nm can be easily

found, with the narrowest less than 50 nm wide (Figure 5.19(b)). However, since the electrode edges defined by EBL and lift-off are not straight enough, a narrow gap increases the probability of two electrodes connecting each other at some protruding point. Therefore, it is hard to find a gap narrower than 100 nm, at the same time, longer than 100 μm.

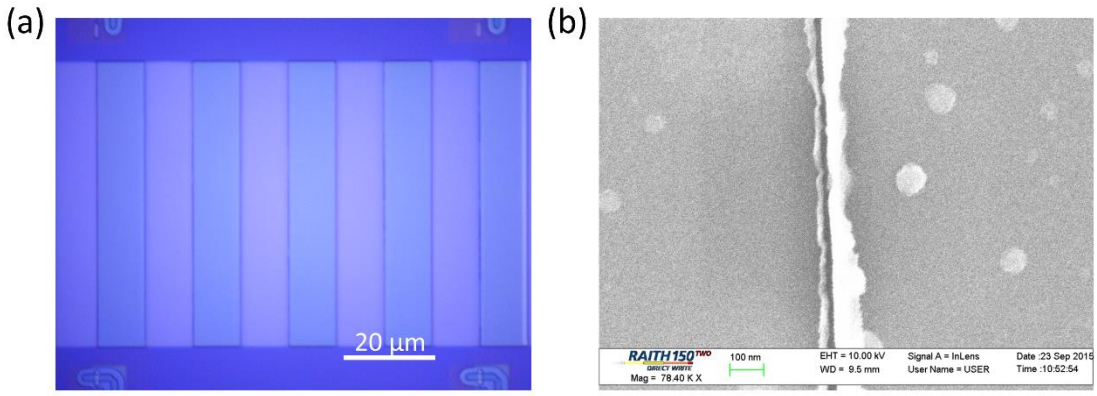

Figure 5.19 (a) Optical microscope and (b) SEM images of interspaced electrodes deposited separately. The SEM image in (b) shows a gap narrower than 50 nm between the two adjacent electrodes.

It is worthwhile to point out that the width of the gap is not the same as we designed in the blueprint, because of misalignment and the expansion of the pattern due to undercut. However, since we designed a series of gaps with different widths, it is easy to find a gap less than 200 nm in our as-fabricated devices.

In summary, the strategy of depositing the two electrodes one after another is successful in fabricating short and wide junctions. However, it also makes the fabrication more complicated. What's more, there will be some asymmetry between the two electrodes, as can be found in Figure 5.19. The first electrode is deposited when the graphene surface is the cleanest, while the second electrode is deposited when the graphene surface is already contaminated by some polymer resist. As we

will discuss in Section 5.6, this will induce much higher contact resistance between graphene and the second electrode. As a result, we finally abandoned this strategy and found another way to solve the problem of lifting off long and narrow PMMA walls.

5.3.3 Using Double-Layer Resist

Using two or more layers of resist with different sensitivity, different solubility or even different tones is a commonly-used strategy in EBL and optical lithography. Here we tried using a more sensitive and more soluble PMMA layer as the bottom layer and a less sensitive and less soluble PMMA layer as the top layer, in order to form a controllable undercut to facilitate lift-off, as shown in Figure 5.20. A PMMA 495 A2 solution was spin-coated at 2000 rpm to achieve a thickness of 70 nm, and

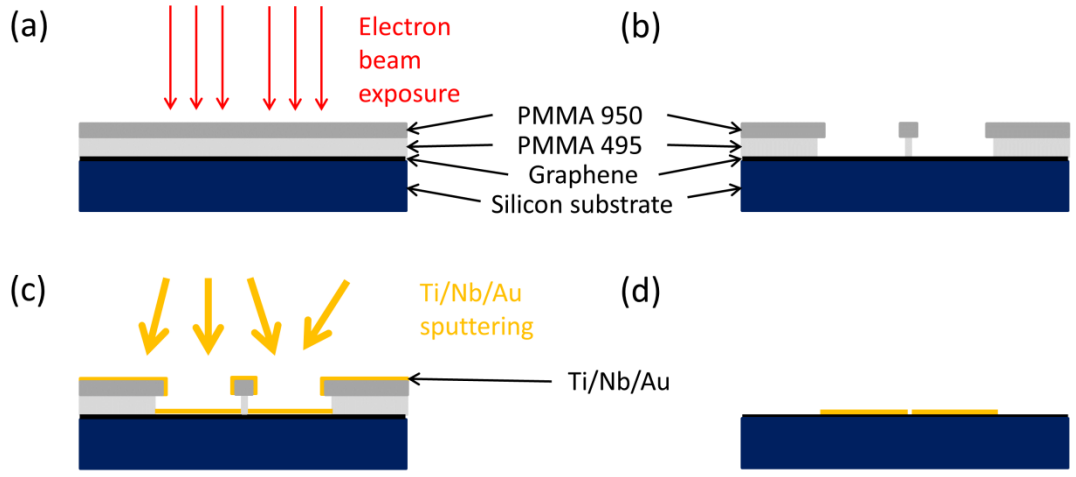

Figure 5.20 Schematic diagrams of defining and depositing superconducting electrodes using double-layer resist. (a) Double-layer PMMA resist is spin-coated on the substrate with graphene and exposed by electron beam. (b) After development, severe undercut appears since the bottom resist layer is more sensitive to the electron beam. (c) The Ti/Nb/Au tri-layer is sputtered. (d) After lift-off, the superconducting electrode is left with a sharp and straight edge.

baked at 180 °C for 5 min. Then a PMMA 950 A2 solution was spin-coated at 2000 rpm to achieve a thickness of 100 nm, and baked again at 180 °C for 5 min. As we have found, such double-layer resist proved to be a robust method to lift off the PMMA wall between the two electrodes, even though the dose factor varies in a large range from 1.2 to 2.0. By this method, junctions longer than 80 nm can be easily fabricated, with a high throughput of more than 95 %. It is also easy to find junctions as short as 50 nm without leakage, as shown in Figure 5.21. The length of the junction is still limited by the roughness of the electrode edge. Therefore, using double-layer resist is as effective as the strategy in the last section in terms of fabricating short and wide junctions. However, it gets rid of the asymmetry between the two electrodes and simplifies the fabrication procedure. Therefore, we adopted this method for all the devices we actually measured in the following chapters.

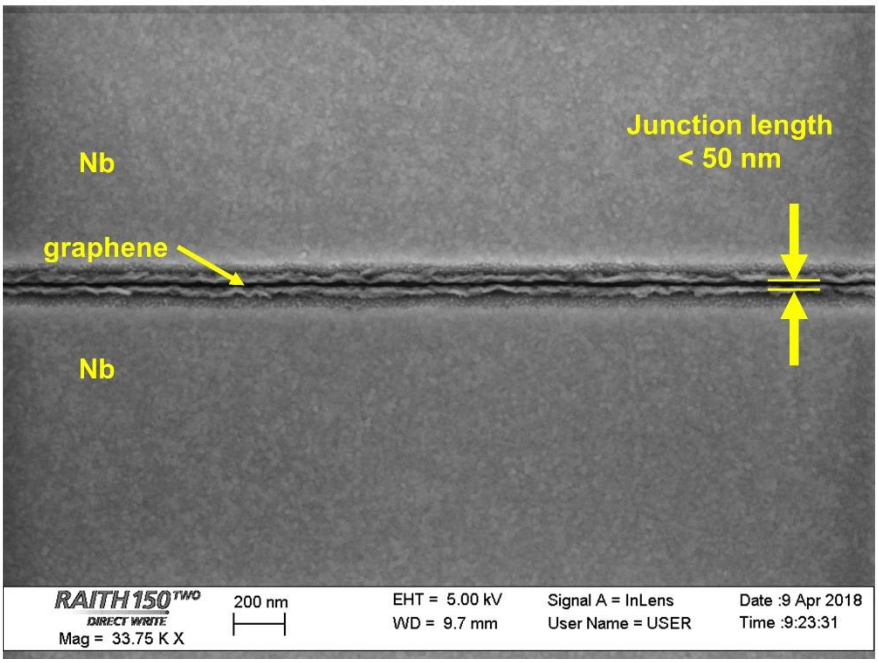

Figure 5.21 SEM image of electrodes deposited using double-layer resist. The gap between the two adjacent electrodes is narrower than 50 nm. Reproduced from [130] with permission from IEEE.

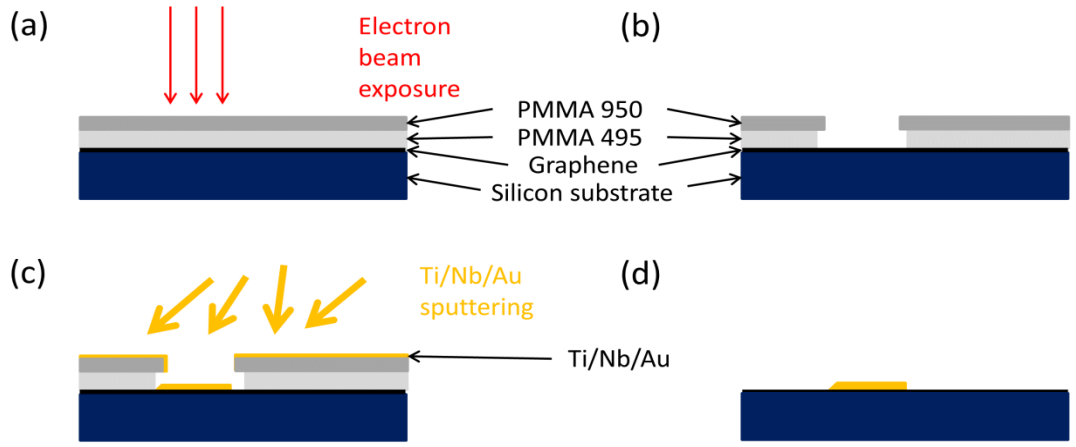

Figure 5.22 Schematic diagrams of defining and depositing superconducting electrodes using double-layer resist. (a) Double-layer PMMA resist is spin-coated on the substrate with graphene and exposed by electron beam. (b) After development, severe undercut appears since the bottom resist layer is more sensitive to the electron beam. (c) The Ti/Nb/Au tri-layer is sputtered at an angle. (d) After lift-off, the Nb electrode is left with a sharp and straight edge on the right and a sloped edge on the left.

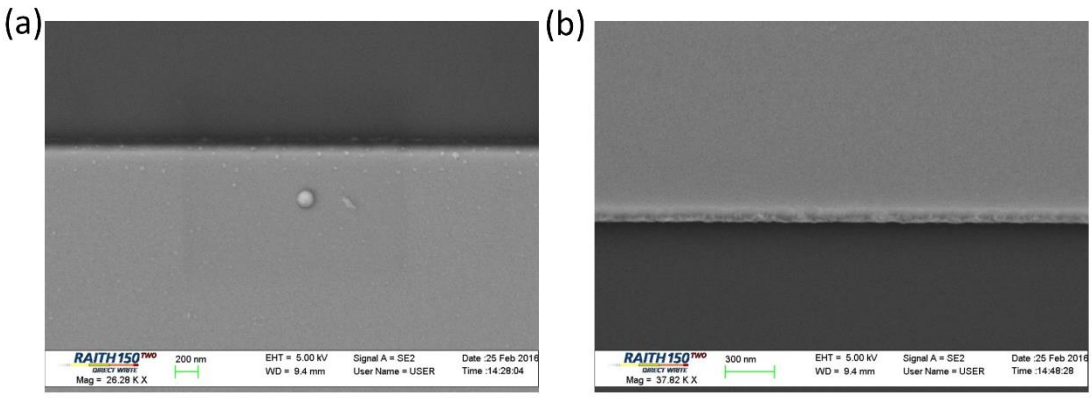

Figure 5.23 SEM images of electrode edges deposited using double-layer resist and tilted sputtering. (a) and (b) refer to the left and right edges in Figure 5.22(d) respectively.

We also tried combining the two strategies together: depositing the two electrodes together while using the double-layer resist for each EBL process. This allows us to control the tilted angle during sputtering, in order to reduce the sharpness of the electrode edges, as schematically shown in Figure 5.22. Normally, the sample stage is rotated during sputtering in order to form a uniform thickness. However, it also means the sputtered atoms are less directional so that the edge of the PMMA is easily covered by the them. If we sputter the metal film without rotating the sample stage, and carefully adjust the relative orientation of the sample and the target, the sputtered atoms can be more directional. Since a severe undercut can be formed by using double-layer PMMA resist, the sputtered metal layer can form a sharper and straighter edge on one side of the electrode while sacrificing the other side, as shown in the SEM images in Figure 5.23. Thus, this strategy of double-layer resist and tilted sputtering is useful for real devices only when the two electrodes are defined and deposited separately, so that the two electrodes can be sputtered in the opposite orientations. Again, such a strategy suffers from the drawback discussed in the last section, so it was finally abandoned and not systematically studied.

5.4 Stress Release and its Prevention: Type I

5.4.1 The Diagnosis

Ever since we started to use double-layer PMMA resist to facilitate lift-off and to acquire straight edges, we often suffered from defects after the lift-off. As you can see in either the optical microscope or SEM image (Figure 5.24 and 5.25), some roughly triangular structures appear on the edge of the superconducting electrodes. These structures tend to appear in the same position in each writing field, corresponding to the cross markers, as shown in Figure 5.24(a). Meanwhile, the electrodes are likely to suffer from some distortion. The optical microscope image in Figure 5.24(a) is taken

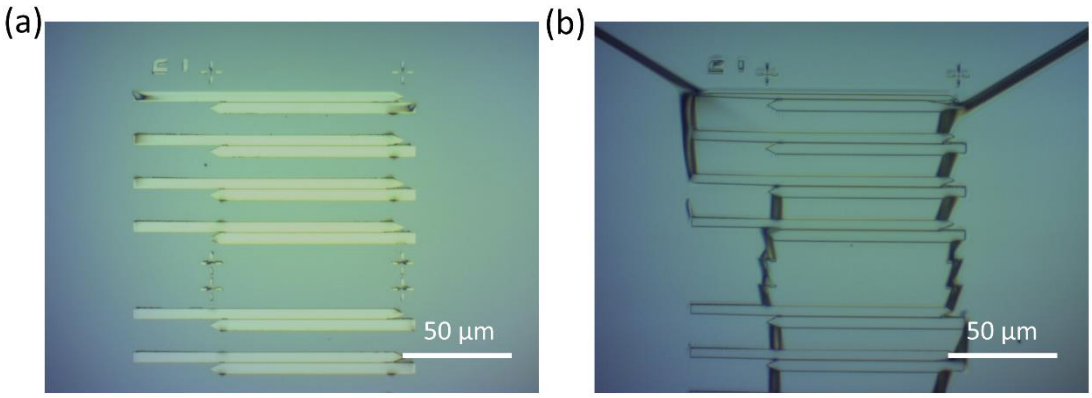

Figure 5.24 Optical microscope images of stress release and its effect. (a) A series of electrodes affected by the triangular structures (appearing black under optical microscope). (b) The same area after sputtering but before lift-off.

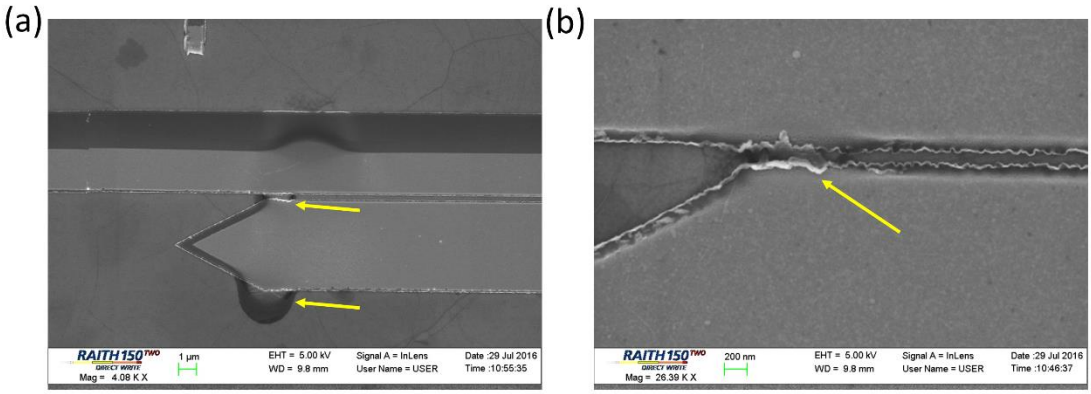

Figure 5.25 SEM images of stress release and its effect. (a) A pair of electrodes affected by the triangular structure, as indicated by the yellow arrows. (b) A higher magnification SEM image showing that the triangular structure is likely to cause leakage between two electrodes.

after the lift-off process. To understand what the triangles are made of and how they are formed, we need to observe them after sputtering but before lift-off, as shown in Figure 5.24(b). It indicates that the PMMA film together with the Ti/Nb/Au film on the top released the stress during the sputtering so that some arches were formed at

the weakest point (along the cross markers). Once those arches were formed, oblique incident metals could enter the arches, leaving those triangles after the lift-off. Therefore, those triangles are actually a layer of uneven metal film, which are likely to cause leakage between the two electrodes (Figure 5.25(b)).

Note that this phenomenon also happened to bare silicon substrates without graphene, so it is purely caused by the stress release of the double-layer PMMA and the tri-layer metal film. We have systematically studied the effects of post-baking after developing but before sputtering, the thickness of each layer of PMMA resist, and whether the spinning centre of the two layers of PMMA coincides. However, none of these parameters affects the stress release of the PMMA and tri-layer metal film.

5.4.2 Buffer Structure

A method to avoid the problem rather than to solve the problem is to define some buffer structure around the superconducting electrodes. As you can see in Figure 5.25, the topmost (and the bottommost) electrode is most severely distorted, while the electrodes in the middle are less affected. This is because that the top and bottom electrodes actually act as buffer area so that the stress from the top and the bottom cannot penetrate into the middle area. Similarly, we can define some other buffer structures on all the four sides of the electrodes just to protect the electrodes from being squeezed. But note that the buffer structure cannot be designed as a continuous loop. It must allow us to connect leads to the devices at a later stage. As shown in Figure 5.26, the buffer structure we designed was a series of discontinuous bars surrounding the electrodes, and it worked well on preventing the stress release affecting the electrodes.

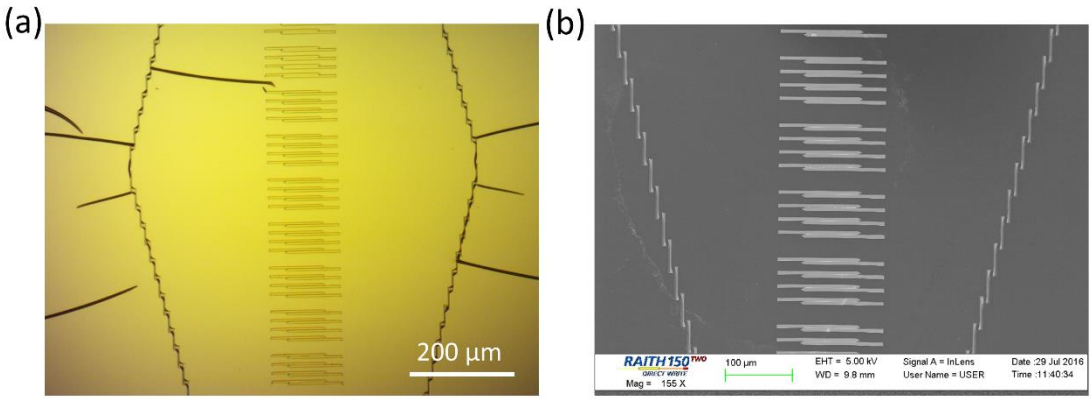

Figure 5.26 Images of buffer structures to prevent stress release. (a) Optical microscope image of a series of electrodes surrounded by the buffer structures. The image is taken after the sputtering but before lift-off. It shows the stress release mostly happens outside the buffer structures. (b) SEM image of the same electrodes after lift-off, showing no triangular structure and no distortion caused by the stress release.

5.4.3 The Prevention of Stress Release

The buffer structure discussed in the last section is only a temporary way to avoid the problem. The final solution of this problem was found by inspecting what triggered the stress release during sputtering. The sample is expected to be heated up by the incident atoms during sputtering. However, it is hard to estimate how high the temperature can be. We have done a simple test experiment on silicon substrates covered by double-layer PMMA and tri-layer metal layer, without any patterns. The samples were without any arches or wrinkles after sputtering. After baking them on a hot plate at 90 °C, arches started to appear and became very severe when the sample was heated to 100 °C. Thus, it is highly probable that the stress release is caused by the high local temperature during sputtering.

Now the problem becomes how to reduce the sample temperature during the sputtering. By lowering the sputtering power, the sputtering rate should decrease, which meant the average energy carried by each atom and the number of atom deposited per unit time both decreased. Thus the energy received per unit time would decrease, and so would the temperature. Previous Nb sputtering was done with a power of 150 W, and we did a test sputtering with a power of 100 W under the same pressure. After the sputtering none of the nine samples got wrinkles and arches, indicating the control of the temperature was successful. The sputtering rate was slightly lower than normal, according to the measurement by Dektak.

We later confirmed that the critical temperature of the Ti/Nb/Au tri-layer was not affected by altering sputtering parameters by a simple R-T measurement in the dipping probe. The result showed a T_c of 8.7 K of Ti (5 nm)/Nb (70 nm)/Au (8 nm) tri-layer.

We also found out another advantage of reducing the temperature during sputtering. The sample while the Nb was sputtered at a lower rate was extremely easy to lift off, taking only 1 to 2 min. While previous samples sputtered at a higher rate, it takes 5 to 10 min. This is because PMMA tends to crosslink at higher temperature, which makes it become difficult to dissolve in acetone. That refreshed our understanding of lift-off process. People have always been claiming that sputtering and lift-off are not compatible since sputtered material tends to form continuous film on the edge of the structure. However, there is another factor that is at least equivalently important, which is the temperature. The sputtered atoms tend to have higher energy than evaporated so that sample temperature is higher during sputtering. Once “burnt”, the PMMA layer becomes harder to dissolve in acetone. If the temperature during sputtering can be carefully controlled, sputtered samples can be very easy to lift off.

5.5 Stress Release and its Prevention: Type II

We have also encountered another type of stress release in the fabrication, which happens when sputtering the leads and pads, and has totally different mechanism. After the second EBL process and developing, the areas for the leads and pads are exposed. However, there still exists a layer of graphene, which means the Au leads and pads are to be deposited over the graphene layer. We once suspected whether the graphene layer could provide strong enough adhesion between the Au pads and the substrate, especially during wire-bonding. Thus we decided to do Ar milling to etch the graphene layer before sputtering the Au layer, so that the Au layer is directly adhered to the silicon substrate.

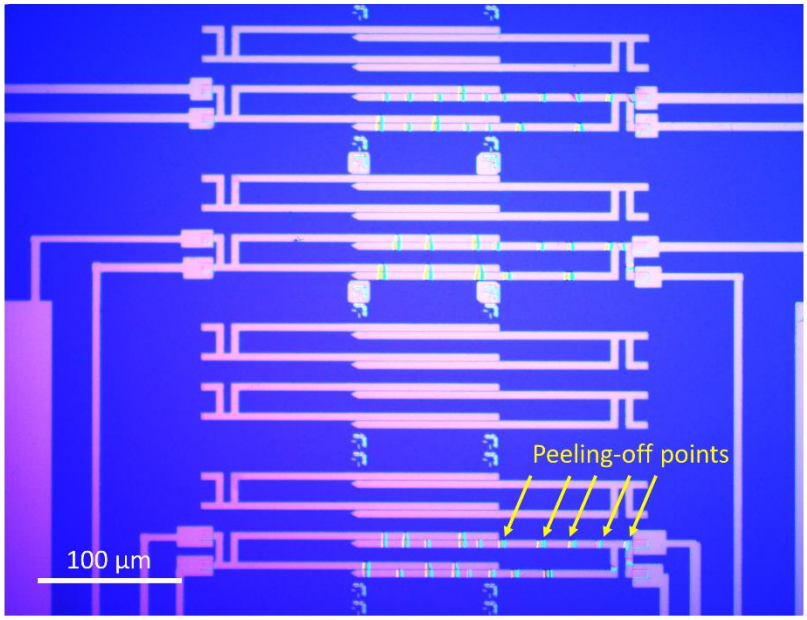

Figure 5.27 Optical microscope image of some devices suffering from peeling-off of electrodes. The image is taken after sputtering the Au pads and leads and lift-off.

However, such an additional milling process is likely to cause some defects after lift-off. As you can see in Figure 5.27, the superconducting electrodes deposited after

the first EBL process, tend to partly peel off from the substrate and form arches. Adjacent electrodes, although separated by a gap, tend to peel off at the same position, indicating that the stress is propagated by the graphene underneath and that graphene is peeled off from the silicon substrate as well. Considering the fact that such peeling-off only happens on devices that are linked to the electrode pads, we attribute the phenomenon to the stress introduced when sputtering the pads and leads.

A probable mechanism of the peeling-off is due to the different thermal expansion coefficients of Nb, silicon oxide and graphene. The thermal expansion coefficient of graphene varies in the reported literature [134–139]; however, there is no controversy that it is negative around room temperature. During the sputtering, the temperature increases and the substrate expands, but the graphene and pre-sputtered Ti/Nb/Au hardly expand or even shrink. The Au sputtered in this process well adheres to the substrate. As the temperature cools down, the Au tracks are pinned to the substrate and push the pre-sputtered Ti/Nb/Au inside, leading to stress in the pre-sputtered Ti/Nb/Au electrodes. Since the adhesive force between graphene and the substrate is not strong enough, such stress in Ti/Nb/Au film leads to peeling off Ti/Nb/Au together with graphene beneath. In short, the peeling-off happens because the Au layer is deposited over two substrates with different thermal expansion rate.

Therefore, an easy solution of this problem is to remove the etching process before sputtering Au, so that the Au leads and pads are also deposited on the graphene layer. We have tested that once we abandoned the Ar milling before sputtering Au, such peeling-off never happened. We have also verified that the adhesion between the pads and the substrate is strong enough for wire-bonding, as long as Al wires are used.

The problem and its solution above also explain the reason why we prefer to do the isolation of devices in the last EBL process. If we exchange the sequence of the second and the third EBL process, i.e. perform the isolation of the devices before

depositing the pads and leads, the pads and leads again will mainly be deposited on bare silicon substrate while overlapping the pre-deposited Ti/Nb/Au. In this case, the peeling-off of superconducting electrodes is likely to take place.

5.6 The Optimisation of the Graphene-Metal Contact

At the end of the last section, we have discussed why the second and the third EBL processes cannot be switched in their sequence. In this section, we will see why the deposition of superconducting electrodes must be done in the first EBL process.

As we have discussed in Section 5.3.1, it is crucial to reduce the normal state resistance of the Josephson junction in order to have a reasonably large critical current at a relatively high temperature. For our junctions, the normal state resistance is made up of two times the contact resistance between graphene and the superconducting electrode plus the resistance in graphene. In Section 5.1 and 5.3, we have discussed our effort to reduce the resistance in graphene by selecting graphene samples and reducing the junction length. Once the resistance in graphene is small enough, the normal state resistance is dominated by the contact resistance between graphene and the superconducting electrodes.

The contact between graphene and metal is of great importance not only to graphene-based Josephson junction, but to all sorts of electronics devices based on graphene, thus is extensively studied both theoretically and experimentally. Different kinds of metal and alloys had been tried. The contact resistance is normally measured by three different methods:

a) The transmission line method (TLM): measure the 2-probe resistance of a series of devices with different junction lengths, and plot the resistance as a function of junction length. The intercept of the linear fit is twice the contact resistance.

b) Comparison of 2-probe and 4-probe measurement on a Hall bar structure: the sheet resistance can be derived from the 4-probe measurement, so that the contribution of graphene can be deducted from the 2-probe resistance, leaving twice the contact resistance.

c) Fitting the 2-probe resistance versus gate voltage curve by a model [140]: the model assumes the contact resistance is independent of gate voltage while the resistance of graphene is inversely proportional to the carrier density, which is proportional to gate voltage except in the vicinity of the Dirac point.

The contact resistivity is defined in two different ways, either by the contact resistance times the contact area or by the contact resistance times the contact width. Considering the fact that the resistivity in a metal is much smaller than the resistivity in graphene, serious current crowding will take place on the edge of graphene-metal contact. Therefore, the contact resistivity defined by the contact area is meaningless and cannot act as a good comparison between different experiments. We adopt the definition of contact resistivity as the product of contact resistance and the contact width.

The contact resistance between graphene and the superconducting electrodes of our devices fabricated as above was measured using in both methods b) and c). The detailed measurement methods and results will be discussed in the next chapter. The average contact resistivity between graphene and the electrode was found to ~100 Ω·μm, which is amongst the lowest reported values in the literature for graphene/metal contact [141], thanks to the clean surface of graphene after transfer to the silicon substrate.

We have also found out that things can go wrong in some cases. For the sample GrapheneSQUID6, the first fabrication trial failed, and we tried to make use of the

spare space on the sample to restart from the beginning. It turned out that the normal state resistance of the new devices was thousands of ohms, two orders of magnitude higher than the normal values. Instead of decreasing as the temperature cools down, the normal state resistance gradually increased. That suggests, the surface of the graphene was already contaminated by a layer of polymer resist after the first round of fabrication process, so that a good contact could not form in the second fabrication trial. That reminded us that the deposition of the superconducting electrodes must be done in the first EBL process and it is better to deposit the pair of electrodes together.

5.7 Conclusion

In the chapter, we have demonstrated a reliable method to fabricate Nb/graphene/Nb Josephson junction and dc SQUIDs based on CVD graphene. We have characterised a few different kinds of CVD and epitaxial graphene samples before we selected the CVD graphene samples we would use in the fabrication. The whole optimised fabrication process consists of three EBL processes, each followed by deposition of metal layer or etching. The obstacles we have overcome include reducing the junction length, preventing the stress release and minimising the contact resistance between graphene and superconducting electrodes.

Chapter 6 Measurement of Josephson Junctions based on CVD graphene

In this chapter, we present the main results on the measurement of SGS junctions. After introducing the measurement system in Section 6.1, we will show how the *I-V* properties of the SGS junctions vary as a function of temperature, magnetic field, gate voltage and microwave radiation, respectively. Then we will show the evidence for ballistic transport in the shortest SGS junctions. We will also present the measurement results for graphene Hall bar structures fabricated in a similar way to the SGS junctions, deepening our understanding of important parameters such as the mean free path and contact resistivity. At last, we will introduce a variant of the SGS Josephson junction, which consists of four superconducting electrodes directly connected to graphene rather than two. We will show that the critical current can be tuned by the proportion of current flowing through the two electrodes on each side of the junction and we deduce that this is due to the heat locally generated by the normal current flowing through graphene.

6.1 Introduction to the Low-Temperature Measurement System

6.1.1 The Cryogenic System

The cryogenic system we used to measure the SGS Josephson junctions and SQUIDs is a “wet” system based on ^{3}He with a base temperature of 320 mK. Liquid helium (^{4}He) is a widely used cryogen with a boiling temperature of 4.2 K (at 1 atm), due to the low mass of helium atoms and the weak interaction between them. The only other

isotope of helium is ^{3}He, which has an even lower boiling temperature of 3.2 K (at 1 atm) since it is even lighter. To achieve even lower temperature, a commonly used strategy is to pump the cryogen liquid, so that the cryogen boils off under a lower pressure. In our cryogenic system, we first pump the liquid ^{4}He to cool the sample down to ~2 K and to condense the separated ^{3}He gas into liquid. Then the liquid ^{3}He is pumped by a sorption pump to reach the base temperature of 320 mK. As shown in Figure 6.1, the two kinds of cryogen in this system never mix with each other; there is only heat exchange between them. The ^{3}He is so rare and expensive that it is fully recycled in a closed chamber, while the ^{4}He is not recycled in our system.

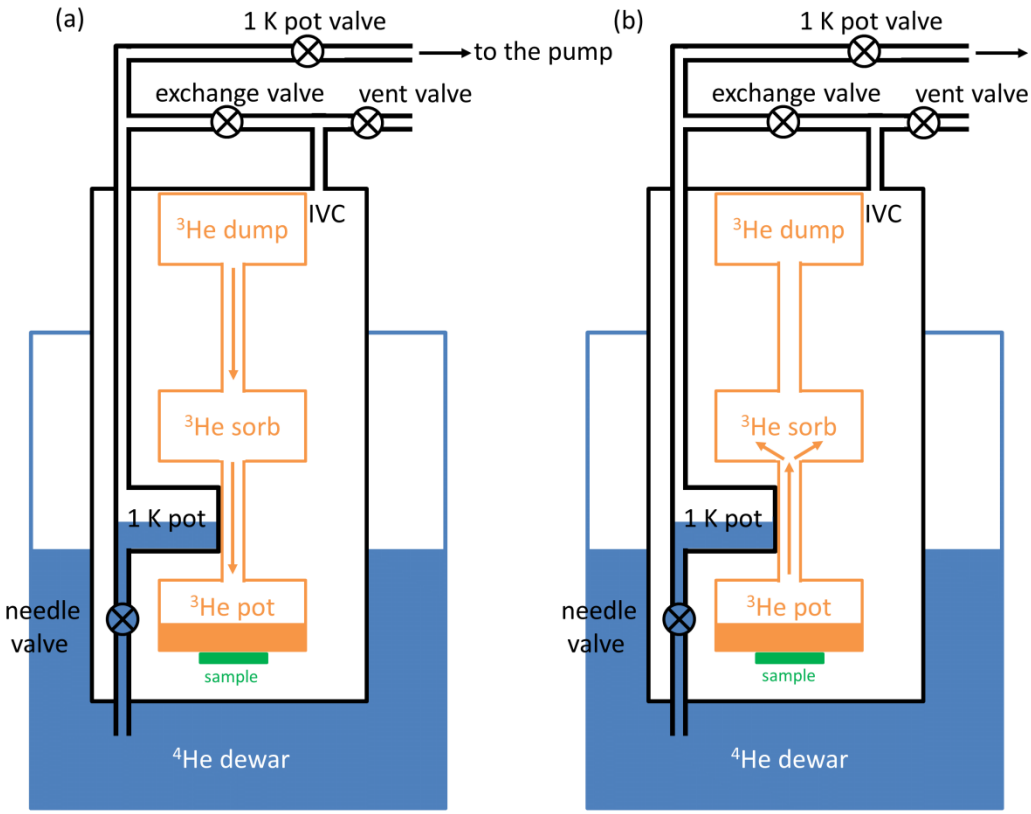

Figure 6.1 Schematic diagram of the working principle of the cryogenic system. (a) The ^{3}He is condensed into liquid by heat exchange with the 1 K pot. (b) The ^{3}He liquid is pumped by the sorption pump.

The cryogenic system works in a “single shot” way. There are three different cooling steps before the sample reaches the base temperature.

In the first step, the sample is cooled by dipping the probe into the liquid helium (^{4}He). The inner vacuum chamber (IVC), which stores the sample and all the measurement leads, is first pumped down to less than 2 mbar. It is then flushed with helium gas several times by alternately opening and closing the 1 K pot valve and the needle valve. The IVC is finally left with some exchange helium gas of ~ 5 mbar. The whole probe is then gradually lowered into the container of the liquid helium, which here is a storage dewar. The “hot” probe is in constant heat exchange with the cold helium gas and the liquid helium, and finally reaches the boiling temperature of ^{4}He, which is 4.2 K. This step normally takes about 2 hours.

In the second step, the sample is further cooled by pumping the liquid helium (^{4}He). As the temperature reaches 4.2 K, the needle valve, which controls the inlet of the 1 K pot, is opened again. The 1 K pot valve, which governs the outlet of the 1 K pot, is also open. Therefore, the liquid helium enters the 1 K pot through the needle valve and is pumped in the 1 K pot, so that the 1 K pot is cooled down. To reach the lowest temperature in this step, the needle valve needs to be carefully tuned. If the inlet is too large, the heat carried by those “hot” liquid helium will warm up the 1 K pot; while if the inlet is too little, the liquid in the 1 K pot will be fully pumped up and cannot provide enough cooling power. The lowest temperature that can be reached in this step is about 2 K. The 1 K pot is in good thermal contact with the sample stage and the ^{3}He pot. Note that before this step, the ^{3}He is stored in gaseous form, mainly in the ^{3}He dump. Once the ^{3}He pot becomes lower than the boiling temperature of ^{3}He, the ^{3}He gas starts to condensate into liquid, as shown in Figure 6.1(a).

In the third step, the sample is cooled down to the base temperature by pumping the liquid ^{3}He. The pumping is done in a closed system by the sorption pump, which is

made up of charcoal that can either absorb or desorb ^{3}He gas depending on the temperature. The sorption pump is located above the sample stage. As the probe cools down, the temperature at the sorption pump also decreases, but at a slower rate than the sample temperature. The temperature of the sorption pump should be still over 40 K at the end of the last step, which means it still desorbs ^{3}He. That helps more ^{3}He to condense into liquid. Once the temperature of the sorption pump falls below 40 K, the pumping of the ^{3}He is triggered, as shown in Figure 6.1(b). Since the ^{3}He pot is in good thermal contact with the sample temperature, the sample temperature will be cooled down to the base temperature within 1 hour.

For such a single shot cooling, the sample temperature can remain at the base temperature for approximately 25 hours. The time is limited by the amount of ^{3}He that can be condensed in the system, and may be affected by the strength of thermal leakage. Once the liquid ^{3}He is exhausted by the sorption pump, we need to lift the probe so that the temperature of the sorption pump will warm up over 40 K. This helps the charcoal to desorb ^{3}He so that all ^{3}He is in gas phase again. To continue measurement, we just restart from the first step to cool down the probe again.

The cryogenic system also allows for measurement above the base temperature. The pumping speed of the sorption pump depends on the local temperature. The lower the temperature, the higher is the pumping speed. To achieve a sample temperature between 300 mK and 2 K, we can heat up the sorption pump by an electric heater so that the pumping speed reduced. The sample temperature can stabilise at a desired temperature if proper PID control in introduced on the heater. Thus the sample temperature is controlled by adjusting the temperature of the sorption pump. The sample stage is not directly heated as it would evaporate too quickly. In the range between 2 K and 4.2 K, the sample temperature can be controlled by tuning the needle valve to adjust the pumping speed of liquid helium in the 1 K pot. In the range from

4.2 K to room temperature, the sample temperature is tuned by adjusting the level that the probe is immersed in the liquid helium.

6.1.2 The Electronic Measurement System

The sample stage used in the system is a piece of printed circuit board with a series of connectors on it, as shown in Figure 6.2. The sample, which is a 10 mm × 10 mm silicon chip, is glued onto the stage. Then the pads on sample are wire-bonded to the pads on the sample stage by Al wires. There are in total 12 dc leads, 4 filtered coaxial leads and 2 attenuated coaxial leads in the probe. We normally use the 12 dc leads for two devices: 6 leads for each device and 3 on each side of the device. One or two of the filtered coaxial leads are used for the gate electrodes. Once wire-bonded, the sample stage is mounted on the bottom of the probe. A solenoid magnet is then mounted and connected to provide a magnetic field perpendicular to the sample. The magnetic field can be as large as 70 mT.

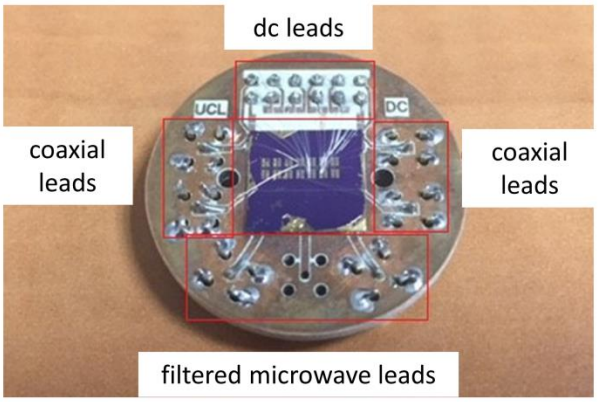

Figure 6.2 A picture of the sample stage of the 3He system. A sample is glued on the stage with Al wire bonded from the devices to the connectors. The connectors are categorised into the red boxes.

The measurement leads and the leads for the magnet are all connected to the

connectors on the top of the probe. The 12 dc leads are further connected to a break-out box where the 12 leads split into the inner conductors of 12 BNC connectors, where they can be further connected to different instruments.

The setup for 4-probe *I-V* measurement is schematically shown in Figure 6.3. The bias current is applied by Keithley 6220 DC Current Source, while the gate across the device is first amplified by a room-temperature SR560 Low Noise Preamplifier, then measured by Agilent 34401 Digital Multimeter. A Keithley 2400 Sourcemeter is used as a current source for the solenoid magnet. The gate voltage is applied between the gate electrode and one of the electrodes of the device by a Keysight E3631A Triple Output Power Supply. All the sources can be controlled by LabVIEW programs while the voltage readout is simultaneously collected.

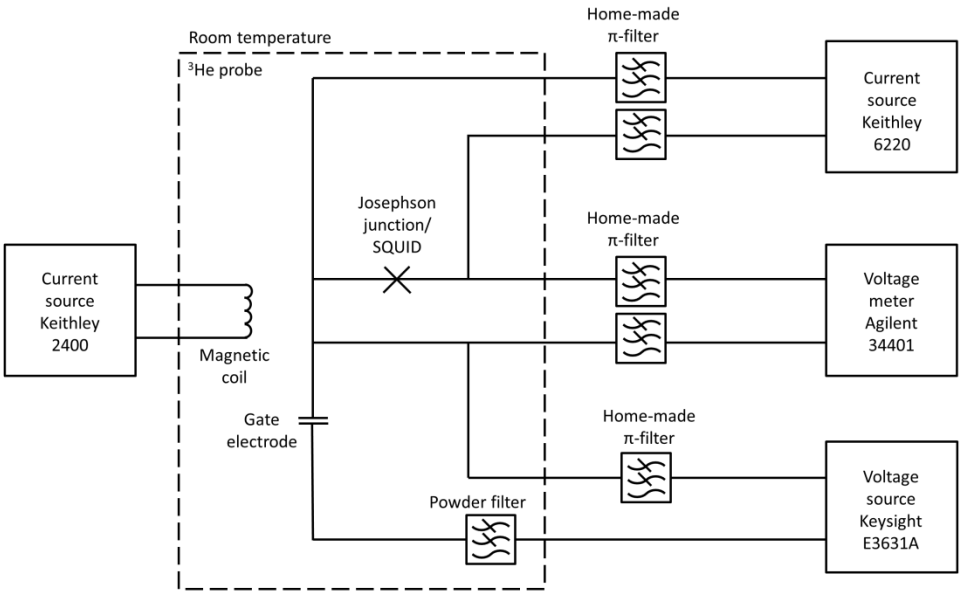

Figure 6.3 The setup for 4-probe *I-V* measurement of the SGS Josephson junctions and SQUIDs with variable magnetic field and gate voltage in the cryogenic system.

6.2 *I-V* Properties vs. Temperature

6.2.1 Resistance vs. Temperature

The *I-V* characteristics of Josephson junctions based on CVD graphene were continuously measured as a function of temperature when the probe was either dipped into or lifted out of the liquid helium. As the *I-V* curve is linear from room temperature down to the transition temperature of the junction (~2 K), we could simply derive the resistance in this regime by a linear fit to the data. Figure 6.4(a) shows the *R-T* curves of two Josephson junctions from the room temperature down to 2 K. Each *I-V* curve was taken up to ±10 μA. As we can see from the plot, a sharp transition happens to both junctions at 8.3 K, indicating the transition from the normal state to the superconducting state of the Ti/Nb/Au electrodes. For these junctions with different widths, we have found that the ranges of resistance jumps at 8.3 K are quite similar, around 20 Ω. This is reasonable since the resistive transition is only related to the resistance of the superconducting electrodes. The transition at the critical current is very sharp even in a high-resolution *R-T* curve of another SGS junction (Figure 6.4(b)), which is a proof of the high quality and uniformity of the superconducting electrodes.

Below the electrode transition, the resistance is roughly inversely proportional to the junction width. This is because the resistance is made up of contributions from the graphene and the contact resistance between graphene and the superconducting electrode, which are both inversely proportional to the junction width. As the temperature increases above the electrode transition, the resistance first stays constant, and then gradually starts to increase, until finally it increases almost linearly with the temperature, which is the typical behaviour of a metal. The slope in the linear region above 50 K should be the same for both devices if the linear increase only comes from

the superconducting electrode, as the effective length of the electrodes is the same for both devices. However, the slope of the 10-μm-wide junction is a bit higher than that of the 80-μm-wide junction, which means the resistance of graphene also contributes to the linear increase. This is reasonable since we expect the resistance of graphene increases linearly with temperature above 50 K due to electron-phonon interaction.

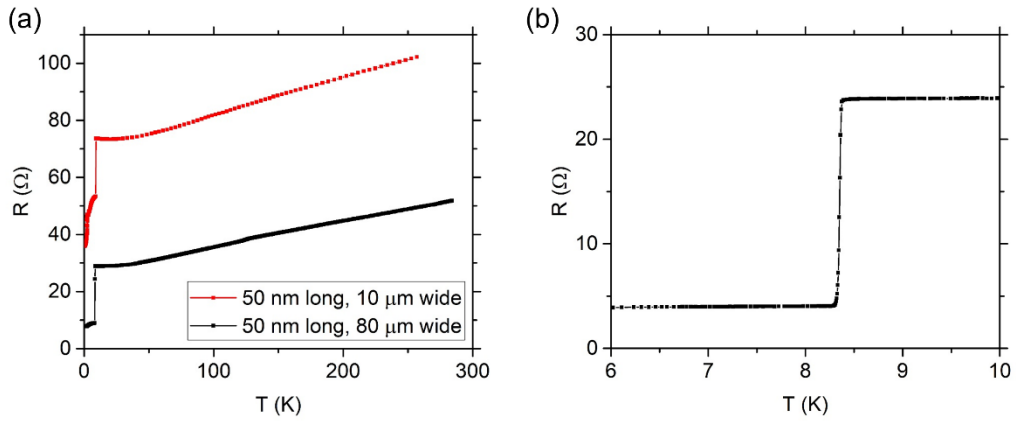

Figure 6.4 *R-T* characteristics of SGS junctions. (a) *R-T* characteristics of two SGS junctions with similar lengths but different widths. (b) *R-T* characteristics of another 50-nm-long, 80-μm-wide SGS junction with high temperature resolution, showing the transition at the critical temperature 8.3 K.

6.2.2 Critical Current vs. Temperature

Once the temperature is lower than approximately 2 K, Josephson effect starts to appear, and becomes more and more obvious as the temperature decreases to the base temperature. As shown in Figure 6.5(a) and (b), the junctions exhibit *I-V* characteristics at the base temperature without any hysteresis, as predicted by the resistively and capacitively shunted junction (RCSJ) model for over-damped junctions with Stewart-McCumber parameter, $\beta_c = 2\pi I_0 R_n^2 C/\Phi_0 < 1$. For the 250-nm-long, 80-μm-wide junction shown, the normal state resistance, $R_n \sim 5\ \Omega$, and we estimate

the capacitance of the junction (coupled via the back-gate) is $C \sim 2 \times 10^{-14}$ F so that $\beta_c = 0.02$, confirming that the junctions should be non-hysteretic, which is important for the standard operation and readout of many devices based on Josephson junctions such as the dc SQUID. As temperature gradually increases, the critical current I_0 becomes smaller, and the transition close to I_0 becomes slightly rounded, which is expected for a strongly overdamped junction with increasing thermal noise. For

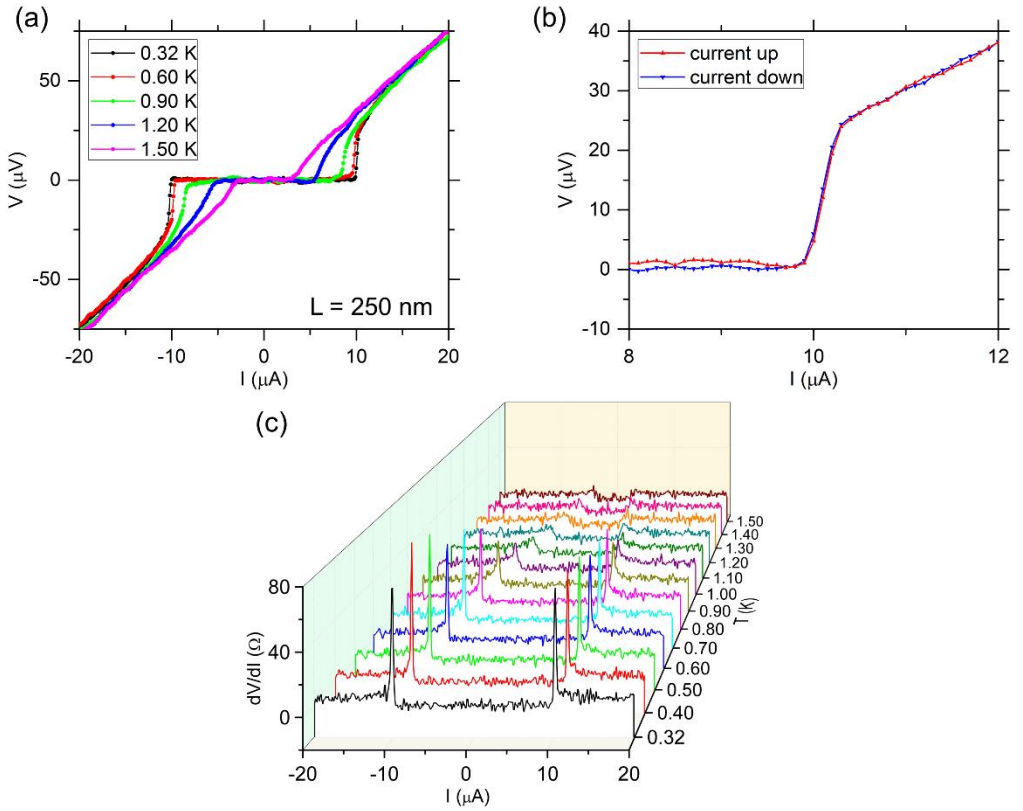

Figure 6.5 *I-V* characteristics of the SGS junctions versus temperature. (a) *I-V* characteristics of a 250-nm-long, 80-μm-wide SGS junction measured at different temperatures. (b) A zoomed-in view of the transition around the critical current at 0.32 K in (a) showing no hysteresis when current is swept upwards or downwards. (c) The differential resistance *dV/dI* versus bias current *I*, measured on this 250-nm-long SGS junction from 0.32 K to 1.50 K. Reproduced from [133].

junctions shorter than 250 nm, the Josephson effect is still obvious up to a critical temperature T_c around 1.5 K, indicating that such junctions can operate over a usefully wide temperature range. By plotting the differential resistance dV/dI as a function of bias current (Figure 6.5(c)), we can see the trend more clearly. The two peaks in the dV/dI curves, indicating the transition at $\pm I_0$, gradually become weaker in height and closer to each other as the temperature increases.

6.2.3 Reduction of Instrumentation Noise

As may be noticed in Figure 6.3, we have added a "home-made" π-filter on every lead directly connected to the device. As shown in the inset of Figure 6.6, the π-filter is simply made of an inductor (100 mH) with two capacitors (4.7 μF) connecting to ground on each side. Such a π-filter is a low-pass filter and has a cut-off frequency of 9.2 kHz.

Those π-filters were proved to be essential for the measurement of Josephson effect, as the devices we made were very sensitive to the rf noise in the measurement system. As we can see in Figure 6.6, the *I-V* characteristics of the same SGS junction were measured either with or without the π-filters. When measured with the π-filters, the *I-V* curves show reasonable Josephson effect with a sharp transition and zero resistance below the critical current. In comparison, the *I-V* curves measured without π-filters only show a limited slope change in the same current range.

We think the mechanism that the rf noise seriously suppresses the Josephson effect is similar to the dc *I-V* properties of a Josephson junction under an ac current, as discussed in Section 2.1.4. However, the rf noise may contain much wider frequency spectra rather than a single frequency signal, so that the *I-V* properties would be the superposition of the effect of a continuous spectrum of rf current. As each single frequency refers to a voltage step height proportional to the frequency value, the

superposition effect would contain a wide and continuous range of heights of voltage step, which appears as the suppression of the Josephson effect.

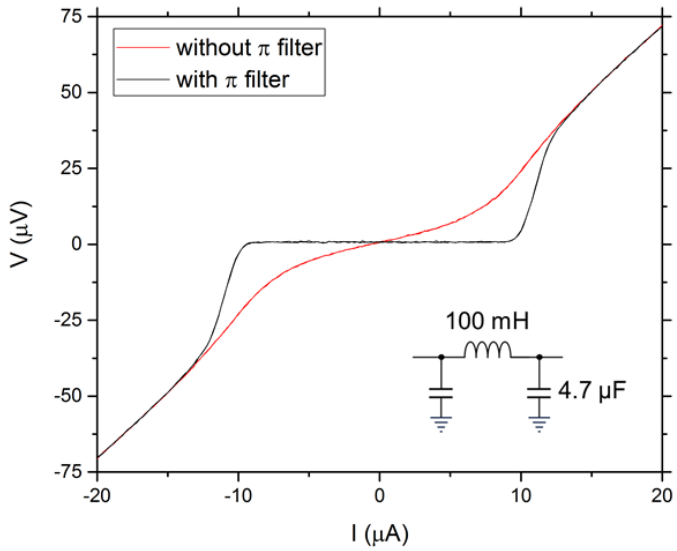

Figure 6.6 *I-V* characteristics of a 150-nm-long SGS junction measured at 320 mK with and without the π-filters. The inset shows the circuit diagram of the π-filter.

The effect of the rf noise can also be understood in a way similar as the thermal noise (as discussed in Section 2.1.3). When we study the effect of thermal noise by the Langevin equation, the noise term in Eq. (2.16) and (2.17) doesn't have to be thermal noise. In fact, it can represent any white noise, including the external rf noise from the measurement instrument, as long as it can be regarded as independent of frequency. If so, the rf noise from the instrument should have similar effects as the thermal noise on the *I-V* curves, as shown in Figure 2.4. That explains why the *I-V* curve is severely rounded without the π-filters in Figure 6.6.

6.3 *I-V* Properties vs. Magnetic Field

We have measured the electronic properties of the junctions in a perpendicular magnetic field. As Josephson junctions with finite area, they are expected to show the effect of quantum interference, since the perpendicular magnetic field can induce a phase difference between the supercurrent at different points across the junction width. In Figure 6.7, we plot dV/dI as a function of bias current I and magnetic field B in a 2D colour scale plot for a 250-nm-long, 80-μm-wide junction. An *I-V* curve is measured on every increment of magnetic field, and the differential resistance dV/dI

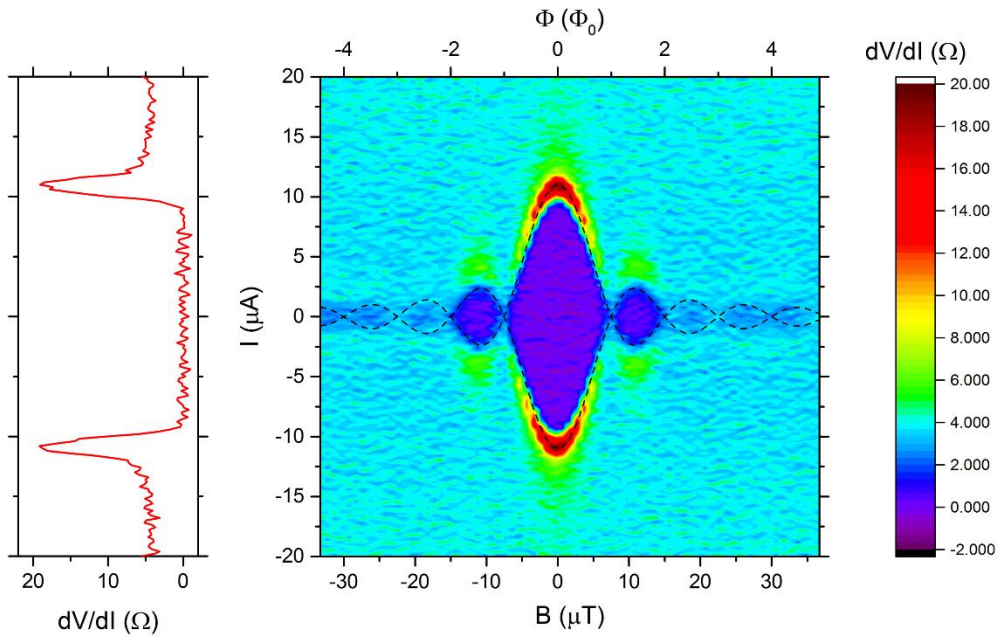

Figure 6.7 *I-V* characteristics of an SGS junction measured at 320 mK, under a perpendicular magnetic field. The junction is 250 nm long and 80 μm wide. The differential resistance *dV/dI* is plotted as a function of bias current *I* and magnetic field *B*, showing an ideal Fraunhofer-like interference pattern. The shape of the pattern can be well fitted by $I_0 \propto \sin(\pi B/\Delta B)/(B/\Delta B)$, as indicated by the black dashed lines, where Δ*B* is the field need to reach the first minimum. The left panel shows a cross-section of the plot along *B*=0. Reproduced from [133].

is calculated numerically from the *I-V* curve. The purple region is where the differential resistance is zero, and the outline of this region indicates the critical current. As can be seen in the plot, the outline of the purple region can be perfectly fitted by an ideal Fraunhofer-like pattern, $I_0 \propto \sin(\pi B/\Delta B)/(B/\Delta B)$, as indicated by the black dashed lines, where ΔB is the field needed to reach the first minimum. The higher-order peaks, though not as high in contrast as the central ones, are still clearly visible. In a wider field sweep on the same device, we managed to see peaks up to ±80 μT (Figure 6.8). Due to time limitation, as we increased the magnetic field range, we also doubled the scanning step of the magnetic field. As a result, the Fraunhofer-like pattern in Figure 6.8 has less resolution than that in Figure 6.7.

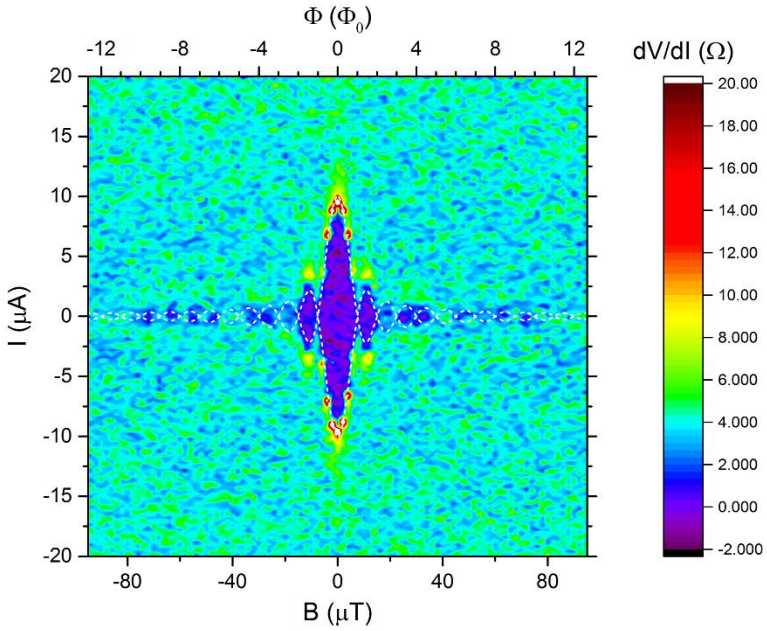

Figure 6.8 The differential resistance *dV/dI* as a function of bias current *I* and magnetic field *B*. The *I-V* characteristics were measured on the same junction as in Figure 6.6 at 320 mK. The critical current I_0 shows a Fraunhofer-like interference pattern up to ±80 μT. The shape of the pattern can be well fitted by $I_0 \propto \sin(\pi B/\Delta B)/(B/\Delta B)$, as indicated by the white dashed lines.

The observation of the Fraunhofer-like pattern indicates that the junction, although having an aspect ratio of $L/W = 1/320$ (the definitions of L and W are the same as in Figure 5.9), is still quite uniform in terms of the distribution of its supercurrent density. Since the first minimum corresponds to one flux quantum Φ_0 in the junction, we can calculate the measured effective area of the junction as $A_{\mathrm{eff}} = \Phi_0/\Delta B = 280\ \mu\mathrm{m}^2$. This is much larger than the simple theoretical estimate of $A_{\mathrm{theo}} = (L + 2\lambda_{\mathrm{L}})W = 26\ \mu\mathrm{m}^2$, corresponding to the area of the normal region plus the area of each electrode the field penetrates into over a distance of order of the London penetration depth, λ_{L} (which is approximately 37.5 nm for Nb). However, this estimate of A_{theo} ignores the strong flux focusing in the junction caused by the Meissner effect in the electrodes. Each electrode extends 5 μm away from the normal region and thus has a much larger area. The measured value A_{eff} corresponds to about 35% of the flux applied to each electrode being forced into the normal region, so this is a reasonable explanation for the discrepancy between A_{eff} and A_{theo}. Such strong flux focusing effect means that, as long as the junction is not too long, the effective area of the junction, thus the first minimum in the Fraunhofer-like pattern, almost solely depends on the junction width and the electrode length, and has little to do with the junction length. This is verified by the 10-μm-wide junction, for which the effective area calculated from the first minimum is 33 $\mu\mathrm{m}^2$, about 1/8 of that of the 80-μm-wide junction.

6.4 *I-V* Properties vs. Gate Voltage

6.4.1 Tuning the Critical Current

As we have described in Section 4.3, one of the key advantages of the SGS Josephson junction is that the critical current can be easily tuned by the gate voltage, V_{g}, thanks

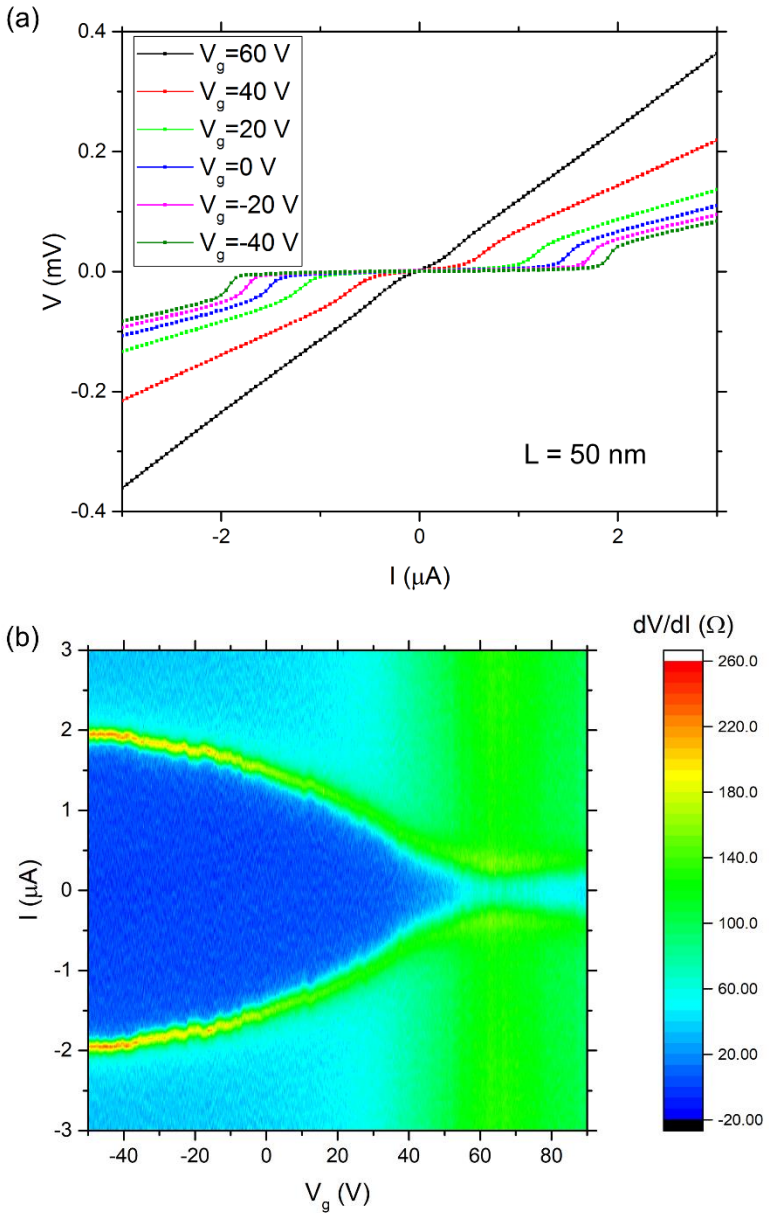

Figure 6.9 *I-V* characteristics of a SGS junction versus gate voltage. (a) *I-V* characteristics of a 50-nm-long, 10-μm-wide SGS junction at 320 mK, under different gate voltages. (b) Colour scale plot of the differential resistance *dV/dI* as a function of bias current *I* and gate voltage V_g. Reproduced from [133].

to the relatively low density of states in graphene. In Figure 6.9(a) we show *I-V* curves measured on a 50-nm-long, 10-μm-wide junction under different gate voltages. Unlike the dependence on temperature, the gate voltage not only affects the critical current I_0, but also the normal state resistance R_n. The effect is more clearly demonstrated if we plot dV/dI as a function of bias current and gate voltage in a 2D colour plot (Figure 6.9(b)). An *I-V* curve is measured on every step of gate voltage, and the differential resistance dV/dI is calculated numerically from the *I-V* curve. As the gate voltage increases from −50 V to +90 V, the critical current (the boundary of the dark blue region) gradually decreases from 1.8 μA, reaches the minimum of 0.14 μA at the Dirac point (where $V_\mathrm{g} = V_0 \equiv 63.85$ V), and then starts to increase. The critical current can be effectively tuned by an order of magnitude by the gate voltage, allowing more flexibility in the operation of Josephson junctions.

6.4.2 Fitting the R_n-V_g Relation

Although we can see indication that the normal state resistance R_n is tuned by the gate voltage V_g in Figure 6.9, the exact value of R_n cannot be derived from those *I-V* curves. This is because the differential resistance changes over a wide range of current above the critical current, as predicted by the RCSJ model discussed in Section 2.1. To acquire the exact value of normal state resistance, we need to do *I-V* measurements up to a much larger current range. Figure 6.10 shows an *I-V* curve of an SGS junction up to ~30 times the critical current, and the corresponding differential resistance curve derived numerically from the *I-V* curves. We can see that the differential resistance keeps increasing from the critical current to ~ ±150 μA, indicating that the *I-V* curve doesn't reach its asymptotic straight line until ~ ±150 μA, which is almost 15 times the critical current. Therefore, to precisely determine the normal state resistance R_n, we linearly fit the *I-V* curves from 200 μA to 300 μA, and

from -300 μA to -200 μA, and take an average of the two slopes. For narrower devices with a smaller critical current, we would adjust the current range above accordingly.

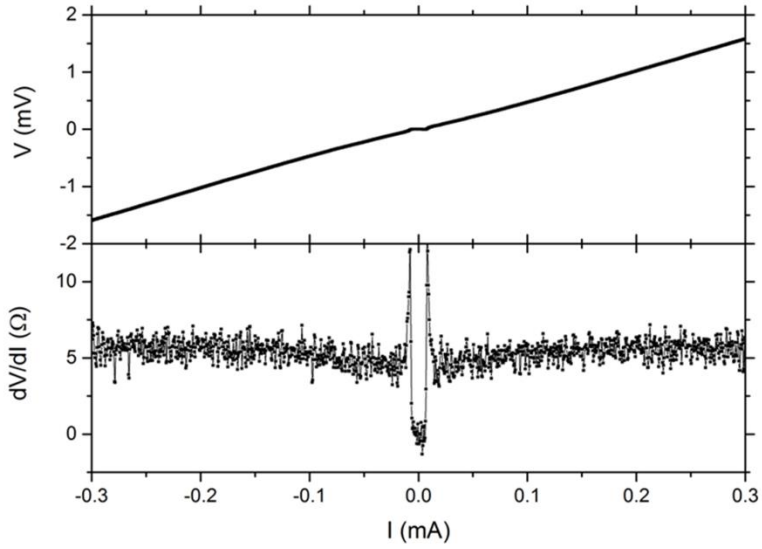

Figure 6.10 *I-V* characteristic of a SGS junction up to higher bias current range. Upper panel: *I-V* characteristic of a 150-nm-long, 80-μm-wide junction up to higher bias current range. Lower panel: The differential resistance *dV/dI* derived from the upper panel as a function of bias current.

The normal state resistance R_{n} is plotted as a function of gate voltage V_{g} in Figure 6.11. Each data point is derived as above from an *I-V* curve under the given gate voltage. The $R_{\mathrm{n}} - V_{\mathrm{g}}$ curve can be fitted to a simple model in which the normal state resistance is a sum of the contact resistance and the resistance of graphene between the electrodes [140]:

$$R_{\mathrm{n}} = 2R_{\mathrm{c}} + \frac{L/W}{e\mu\sqrt{n_{\mathrm{i}}^2 + \left[\frac{C_{\mathrm{ox}}}{e}\left(V_{\mathrm{g}} - V_0\right)\right]^2}} \tag{6.1}$$

where R_c is the contact resistance between the graphene and the electrode, μ is the mobility of graphene, n_i is the area carrier density of graphene caused by impurities, C_{ox} is the area capacitance between the gate electrode and graphene, and V_0 is gate voltage at the Dirac point. Such a fitting allows us to estimate the value of R_c, μ, the conductivity σ and the mean free path l of the device.

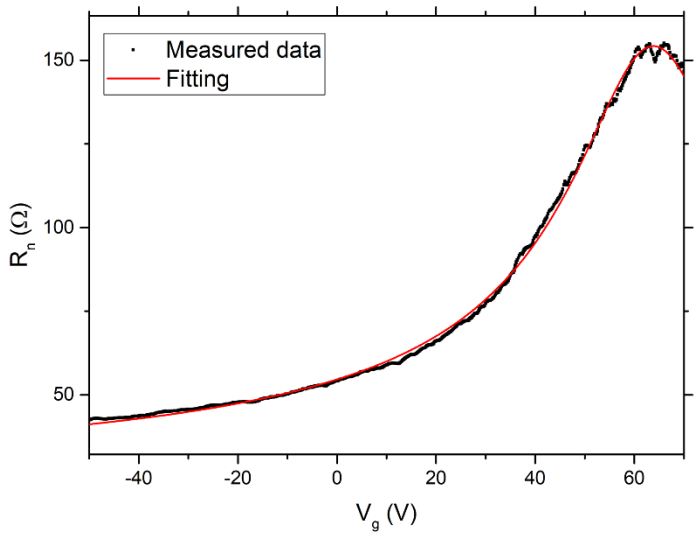

Figure 6.11 Normal state resistance R_n as a function of gate voltage V_g. The normal state resistance R_n was measured on the same device as in Figure 6.9 at 320 mK. The red curve shows a fitting by the model in Eq. (6.1).

Table 6.1 summaries the fitting results of the $R_n - V_g$ curves of five SGS junctions with different lengths and of a graphene-based Hall bar fabricated on the same batch of samples using similar techniques. In the fitting, R_c, μ, n_i, and V_0 are treated as independent fitting parameters, while C_{ox} is calculated using $C_{ox} = \varepsilon_0\varepsilon_r/d = 1.15 \times 10^{-4}$ F/m^2, using the manufacturer's data for the estimated oxide thickness of the SiO_2 layer. For the $R_n - V_g$ curve of the Hall bar, the contact resistance R_c is fixed to zero as the R_n is obtained from a 4-probe measurement.

Table 6.1 Fitting results of the R_n-V_g curves.

Device	Junction 5	Junction 6	Junction 7	Junction 2	Junction 8	Hall bar 1
Junction or Hall bar length *L* (nm)	50	50	50	150	850	5×10^4
Width *W* (μm)	10	80	80	80	80	10
V_g range fitted (V)	-50~70	-50~50	-25~25	-25~20	-50~0	-25~25
Contact resistance R_c (Ω)	11.65	0.9	1.0	1.28	2.28	0
Mobility μ (cm^2/Vs)	211	110	160	419	2850	1680
n_i (cm^{-2})	1.1×10^{12}	1.6×10^{8}	4.0×10^{12}	8.5×10^{7}	~0	2.9×10^{7}
V_0 (V)	63.85	155	85	125.7	68.2	113
Contact resistivity ρ_c (Ω•μm)	117	72	80	102.5	182.5	N/A
Conductivity σ (mS)	0.16	0.20	0.16	0.61	2.2	2.2
Area carrier density *n* (cm^{-2})	4.7×10^{12}	1.1×10^{13}	6.1×10^{12}	9.1×10^{12}	4.9×10^{12}	8.1×10^{12}
Mean free path *l* (nm)	5	4	5	15	72	56

The shape of Eq. (6.1) appears to fit well to all devices, but as we can see from the table, the fitted parameters of the three shorter junctions are not consistent with the

results of the longest junction and the Hall bar, with both the conductivity σ and mobility μ an order of magnitude smaller. As we will show in Section 6.7, the parameters obtained from the longest junction and the Hall bar are consistent with those from Hall measurement, if we compare Table 6.1 with Table 6.2. That means the model described in Eq. (6.1) is a good approximation for long junctions, however it deviates as the junction becomes shorter. Consequently, we used the longest junction for the fitting of the $R_{\mathrm{n}} - V_{\mathrm{g}}$ model in the main text. The reasons why the model fails for short junctions may include the following:

a) The contact resistance is also dependent on the gate voltage as has been reported by some authors [142]. For shorter junctions, the contact resistance accounts for a larger part in the normal state resistance, so that the deviation from the model is more obvious.

b) The junction length may be overestimated or underestimated due to the rough edge of the electrodes, and the relative error of junction length is higher for short junctions.

The fitting of the $R_{\mathrm{n}} - V_{\mathrm{g}}$ curve above also verifies that the contact resistance between the graphene and the superconducting electrodes accounts for a large proportion of the normal state resistance.

6.4.3 The I_0R_{n} Product

The product of critical current I_0 and normal state resistance R_{n} is the characteristic voltage V_{c} when the junction jumps from the superconducting state to the normal state around the critical current. For a short ideal SGS junction in either the dirty or the clean limit, the product I_0R_{n} is a figure of particular interest since it is solely determined by the operating temperature and the energy gap of the superconductor,

and should be independent of the gate voltage, as indicated by the form of Eq. (2.35) and (2.36). In Figure 6.12 we plot both the normal state resistance R_{n} and the product I_0R_{n} as a function of the gate voltage, for a 50-nm-long junction. As the gate voltage draws closer to the Dirac point, the critical current decreases while the normal state resistance increases. Their product I_0R_{n} remains constant when the gate voltage is far away from the Dirac point; however, it drops as the gate voltage approaches the Dirac point. Even in the constant regime, the measured value of I_0R_{n} is only ~1/6 of the theoretical one determined by Eq. (2.35) or (2.36).

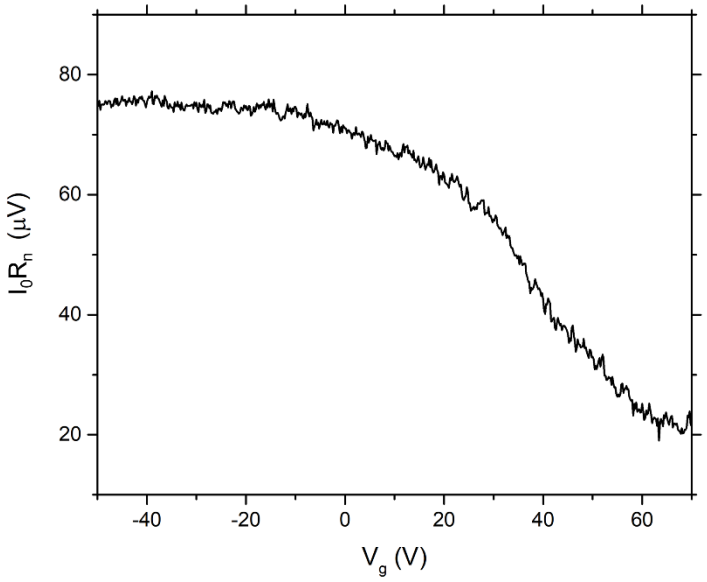

Figure 6.12 The product I_0R_n versus gate voltage V_g. The critical current I_0 and normal state resistance R_n were derived from the dataset of Figure 6.9 and 6.11, respectively.

Such suppression of I_0R_{n} around the Dirac point is similar to many other reports on graphene-based Josephson junctions as discussed in Section 4.5, and there remain some controversies on the exact reason. Here we propose a new explanation based on the thermal noise. As we discussed in Section 2.1.3, the thermal noise level is

characterised by the noise parameter $\Gamma \equiv 2\pi k_B T / I_0 \Phi_0$. When the critical current of the junction is tuned by the gate voltage, the noise parameter can be different even though at the same temperature. Around the Dirac point, the critical current is particularly low, so that the noise parameter Γ is high. As a result, the *I-V* curve becomes more rounded and the critical current measured is lower than the intrinsic value. Therefore, the produce $I_0 R_n$ is suppressed around the Dirac point.

6.5 *I-V* Properties vs. Microwave Radiation

We also investigated the *I-V* properties of SGS junctions under microwave radiation. The microwave radiation is applied by a monopole antenna close to the device, the length of which was designed for 6 GHz frequency. When sweeping the microwave

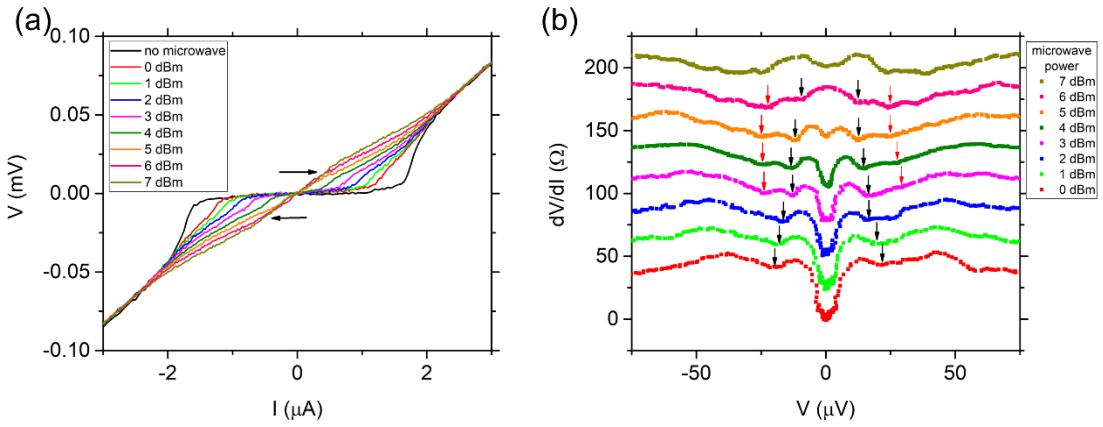

Figure 6.13 *I-V* characteristics of a SGS junction under microwave radiation. (a) *I-V* characteristics of a 50-nm-long, 10-μm-wide SGS junction, measured at 320 mK under 6 GHz microwave radiation, under a gate voltage of -40 V. The black arrows indicate the position of the first step. (b) Differential resistance vs voltage, derived from numerical differential of the curves in (a). The black arrows indicate the first local minima beside the central well, which correspond to the first step on the *I-V* curve. The red arrows refer to the second local minima, which are not that obvious.

power, we clearly observed some change in the *I-V* properties (Figure 6.13(a)). The effect of microwaves is most obvious when the power is between 0 dBm and 7 dBm. At 3 dBm and 4 dBm, we can see at least one Shapiro step on either side of the curve. If we plot the differential resistance against voltage (Figure 6.13(b)), we can find at least one local minimum on each side of the central well, which corresponds to the first Shapiro step on the *I-V* curve. The step size is about 10~15 μV, which matches well with the theoretical value of 12.4 μV, given by Eq. (2.19). The disappearance of higher order Shapiro steps is probably because the coupling between the antenna and the SGS junction is not perfect.

6.6 Evidence for Ballistic Transport

6.6.1 Evidence from the I_0-T Relation

In Section 6.4.2 we have shown that the mean free path in graphene is in the range of tens of nanometres, which is in the same range as the length of the shortest junctions. That indicates that the shortest junctions should be in the ballistic regime. In fact, we have found some evidence that in junctions as short as 50 nm, the transport in truly in the ballistic regime.

The first piece of evidence comes from the $I_0 - T$ relation. We plot the critical current as a function of temperature for junctions with lengths from 50 nm to 450 nm, in Figure 6.14(a)-(d) respectively. For each device, the critical current I_0 increases as the temperature T decreases. Here we redefine T_c of the junction as the temperature where the critical current I_0 vanishes. If you take a closer look, you can find that the $I_0 - T$ curves are not identical in shape. For the 150-nm- and 250-nm-long junctions, the critical current I_0 tends to saturate when $T \lesssim T_c/3$; whereas for the 50-nm-long junction, the critical current I_0 is still increasing at the lowest temperatures. For the

450-nm-long junction, the critical current I_0 also tends to saturate, however, as its T_c is smaller than that of the other junctions, the saturation is not quite fully realised at the lowest temperature we can reach.

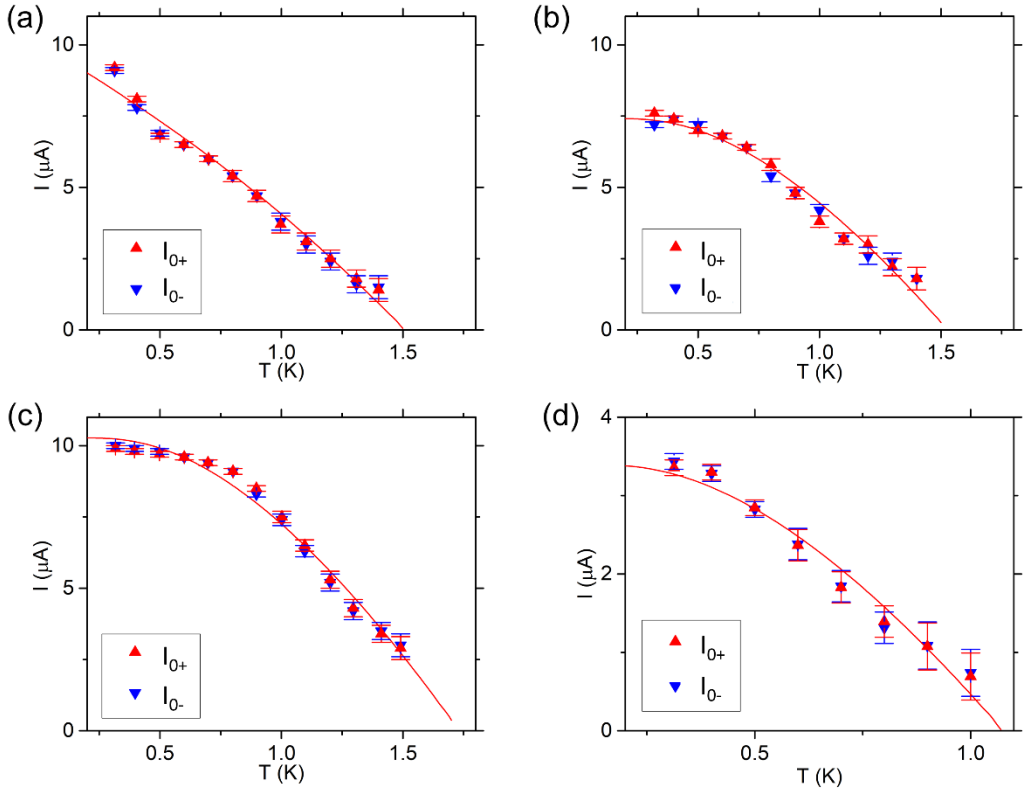

Figure 6.14 The critical current I_0 versus temperature T, measured on SGS junctions with different lengths. (a) 50 nm in length. (b) 150 nm in length. (c) 250 nm in length. (d) 450 nm in length. The red curve in (a) is the fitting of I_{0+} (from the positive I-V branch) by KO-2 theory, while the red curves in (b), (c) and (d) are the fitting of I_{0+} by KO-1 theory, as described in the main text. The error bars indicate the uncertainty of determining the critical current from a given I-V curve, and does not include other errors such as those due to thermal noise or switching current. All the junctions are 80 μm wide. Reproduced from [133].

Such a difference in the $I_0 - T$ curves can be well explained by the theory of a weak-link in either the "dirty" or "clean" limit developed by Kulik and Omelyanchuk (the KO-1 and KO-2 theories), as described in Section 2.2.2. As shown by the red curves in Figure 6.13, the measured $I_0 - T$ curves of the junctions longer than 150 nm can be well fitted by the KO-1 theory, while the $I_0 - T$ curve of the 50-nm-long junction is better fitted by the KO-2 theory. The KO-1 and KO-2 theories do not provide a simple expression for the $I_0 - T$ relation, as Eq. (2.35) and (2.36) have to be maximised over φ to determine $I_0(T)$. As a result, commercial software cannot straightforwardly perform the fitting of $I_0 - T$ curves in Figure 6.14. We have instead written a custom program in MATLAB to numerically calculate the I_0 values determined by Eq. (2.35) and (2.36), and to fit the parameters by the least squares method. The temperature dependent BCS energy gap of the superconductor $\Delta(T)$ does not have a precise analytic expression over all temperatures. However, the normalised energy gap $\Delta(T)/\Delta(0)$ has been tabularised as a function of the normalised temperature T/T_c in the literature [11]. In our fitting, we first fit the discrete $\Delta(T)/\Delta(0)$ versus T/T_c data in Ref. [11] by a spline, so that the normalised energy gap at any normalised temperature can be interpolated. In the fitting to Eq. (2.35) and (2.36), T_c is treated as an independent fitting parameter, while the energy gap at zero temperature is taken from the BCS expression, $\Delta(0) = 1.764 k_\mathrm{B} T_\mathrm{c}$. We also introduce an additional coefficient α that is multiplied on the right-hand side of Eq. (2.35) and (2.36), and which we treat as another independent fitting parameter. The coefficient α represents a reduction in the measured value of $I_0 R_\mathrm{n}$ compared to the ideal value which other authors have also observed in SGS junctions, which has been discussed in Section 6.4.3. The fitting results of the $I_0 - T$ curves in Figure 6.14 are summarised in Table 6.2, in which we tried to fit each curve with the two equations and compared the result. The quality of the fittings can be indicated by comparing the standard deviation of residuals. For the 50-nm-long junction, the fitting

to Eq. (2.36) is better than the fitting to Eq. (2.35). For the 150-nm-long junction, the fittings to the two equations show comparable standard deviation of residuals. For the 250-nm-long junction, the fitting the fitting to Eq. (2.35) is better than the fitting to Eq. (2.36). For the 450-nm-long junction, since the saturation is not quite fully realised at the lowest temperature we can reach, it is not reasonable to judge the quality of the fitting by the standard deviation of residuals.

Table 6.2 Fitting results of the I_0-T curves.

Device	**Junction 1**			**Junction 2**		**Junction 3**		**Junction 4**	
Junction length L (nm)	50			150		250		450	
Fitting expression	(2.35)	(2.36)	(6.3)	(2.35)	(2.36)	(2.35)	(2.36)	(2.35)	(2.36)
α	0.0957	0.0757	0.0756	0.0661	0.0510	0.0814	0.0593	0.0583	0.0476
T_c (K)	1.452	1.510	1.510	1.527	1.615	1.732	1.887	1.075	1.114
Transmission probability τ	N/A	N/A	0.99	N/A	N/A	N/A	N/A	N/A	N/A
Standard deviation of residuals (μV)	0.676	0.382	0.403	0.364	0.307	0.335	0.690	0.181	0.121

Both the KO-1 and KO-2 theories have been shown by Beenakker [143] to agree with a more general multi-channel analysis of short weak links in the disordered regime (for $T\rightarrow 0$) and ballistic regime (for all T in the classical limit):

$$I_{\mathrm{s}}(T,\varphi)=\frac{e\Delta}{2\hbar}\sum_{p=1}^{N}\frac{T_{\mathrm{p}}\sin\varphi}{\left[1-T_{\mathrm{p}}\sin^{2}(\varphi/2)\right]^{1/2}}\tanh\left(\frac{\Delta}{2k_{\mathrm{B}}T}\left[1-T_{\mathrm{p}}\sin^{2}(\varphi/2)\right]^{1/2}\right)$$

(6.2)

where T_{p} is the eigenvalue of the transmission matrix through the normal region. In the clean limit, where the junction length is smaller than the mean free path, the Josephson current travels across the junction via a pair of Andreev bound states (ABS) per conducting channel with energies $\pm\ \varepsilon$. This leads to a simplified relation that has been used in the literature for analyzing ballistic transport in SGS junctions[107,114]:

$$I_{s}(T,\varphi)=\frac{\pi\Delta}{2eR_{\mathrm{n}}}\frac{\sin\varphi}{[1-\tau\sin^{2}(\varphi/2)]^{1/2}}\tanh\left(\frac{\Delta}{2k_{B}T}[1-\tau\sin^{2}(\varphi/2)]^{1/2}\right)$$

(6.3)

where τ is the transmission probability at the S-N interface (averaged over all conducting channels). Eq. (6.3) degenerates to Eq. (2.36) in the KO-2 theory if the transmission probability is 1.

We therefore have tried to fit the I_0-T curve of the 50-nm-long device to Eq. (6.3) with the transmission probability τ as an additional fitting parameter. As shown in Table 6.2, the transmission probability τ obtained is very close to 1, which means the interface between the graphene under the electrode and the exposed graphene is quite transparent. Therefore, it is valid to use the KO-2 theory for the 50-nm-long junction.

The fitting suggests that junctions longer than 150 nm are in the dirty regime where

the transport of charge carriers in the graphene is diffusive, while the 50-nm-long junction is in the clean regime where ballistic transport takes place in the graphene. According to the fits, the junction transition temperature T_c is 1.08~1.73 K, which is smaller than that of the superconducting electrodes (T_c~9 K). This is probably because the interface between the graphene and the superconducting electrode is not highly transparent, so that the superconducting pairing induced in the graphene by the proximity effect is weakened.

The absolute value of the critical current also shows reasonable dependence on junction length. As we can see in Figure 6.14(d), the critical current I_0 of the 450-nm-long junction is much smaller than others. We also fabricated and measured an 850-nm-long junction which shows no Josephson effect at all. This allows us to estimate the normal state coherence length in graphene, ξ_n, to be of order several hundred nanometres, consistent with the results in Table 5.3. For the three shorter junctions, the critical current I_0 at the base temperature does not show a strong dependence on the junction length. This is because the contact resistance between the graphene and the superconducting electrode, which shows some device-to-device variation, makes a large contribution to the measured normal state resistance R_n, as verified by the $R_n - V_g$ fitting in Section 6.4.2. This leads to some device-to-device variation in I_0 since it is inversely proportional to R_n in both the KO-1 and KO-2 theories and masks any dependency on the junction length for the shorter devices.

6.6.2 Evidence from the R_n-V_g Relation

The second piece of evidence for ballistic transport comes from the $R_n - V_g$ relation. As you can find in Figure 6.11, small oscillations can be seen over a wide range of gate voltages in the $R_n - V_g$ curve, the physical origin of which is worth

investigating. These may be caused by universal conductance fluctuations in the graphene; or they may instead be due to the phase-coherent interference of charge carriers in the Fabry-Pérot cavity defined by the n-p-n junction that arises from the different doping levels in the exposed graphene (in the normal region of the junction) and the non-exposed graphene (under the electrodes). If the oscillation is dominated by universal conductance fluctuations, the oscillation will be reproducible but random without any periodicity. However, for the Fabry-Pérot mechanism we would expect to see a local minimum whenever an integer multiple of the Fermi wavelength $\lambda_{\mathrm{F}}(V_{\mathrm{g}})$ of the charge carriers is equal to the effective length of the n-p-n junction.

To investigate the mechanism of the oscillation, we plot the normal state resistance R_{n} versus the Fermi wavenumber $k_{\mathrm{F}} = \sqrt{2\pi C_{\mathrm{ox}}|V_{\mathrm{g}} - V_0|/e}$, where C_{ox} is the area capacitance between the gate electrode and graphene, and then fit the $R_{\mathrm{n}} - k_{\mathrm{F}}(V_{\mathrm{g}})$ curve by a smooth polynomial. We can see the oscillation more clearly in the fitting residuals, as shown in Figure 6.15. The upper and lower panels display the fitting residuals when k_{F} is swept upwards and downwards respectively, which shows that the oscillation is highly reproducible. For both curves, beyond the small amplitude fluctuations, there exist periodic minima with an even spacing of $\Delta k_{\mathrm{F}} \sim 75\ \mu\mathrm{m}^{-1}$. If such periodic minima result from the phase-coherent interference of charge carriers in the Fabry-Pérot cavity defined by the n-p-n junction, this implies the effective length of the n-p-n junction is $2\pi/\Delta k_{\mathrm{F}} \sim 83$ nm, which is quite reasonable considering the geometric length. Such periodic oscillation thus provides more compelling evidence that the junction is in the ballistic regime. Similar oscillations were observed in a series of 50-nm-long junctions with different widths (the narrower the junction, the higher the oscillation amplitude), but not in any junctions longer than 150 nm. This suggests that the shortest junctions are ballistic while the longer ones are diffusive, allowing us to estimate the mean free path in the graphene to be between 50 nm and

150 nm. This value is in excellent agreement with the mean free path value derived from the $R_n - V_g$ fitting in Section 6.4.2 and from the Hall measurement in Section 6.7.

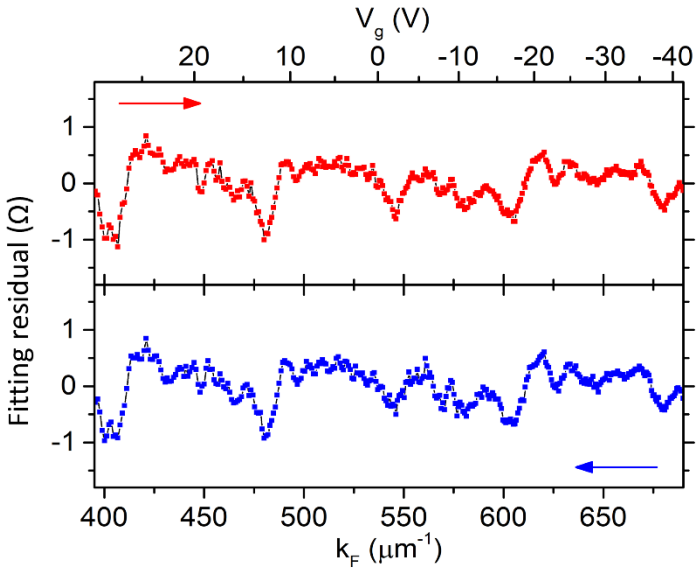

Figure 6.15 The fitting residual versus either V_g or the equivalent Fermi wavenumber k_F. k_F is proportional to $\sqrt{|V_g - V_0|}$. The R_n-k_F(V_g) curve is fitted by a smooth polynomial. The red points are for k_F swept upwards (V_g swept downwards); the blue points are for k_F swept downward (V_g swept upwards). The two sweep directions show similar periodic oscillations. All data was measured at 320 mK. Reproduced from [133].

6.7 Measurement of Graphene Hall Bars

As we have mentioned in Section 6.4.2, we have fabricated some Hall bar structures on the same CVD graphene sample, using the same fabrication technique as for the junctions. We have shown in Section 6.4.2 that a Hall bar structure allows us to measure the sheet resistance as a function of gate voltage, in a 4-probe measurement

configuration shown in Figure 6.16(a). By fitting the $R_s - V_g$ relation we can obtain the transport parameters such as mobility μ and mean free path l. Here in this section we show that these parameters can also be derived by a Hall measurement on the same device, as shown in Figure 6.16(b), and the two measurements share similar results. In Table 6.3 we summaries the 4-probe and Hall effect measurement results on two Hall bars based on graphene.

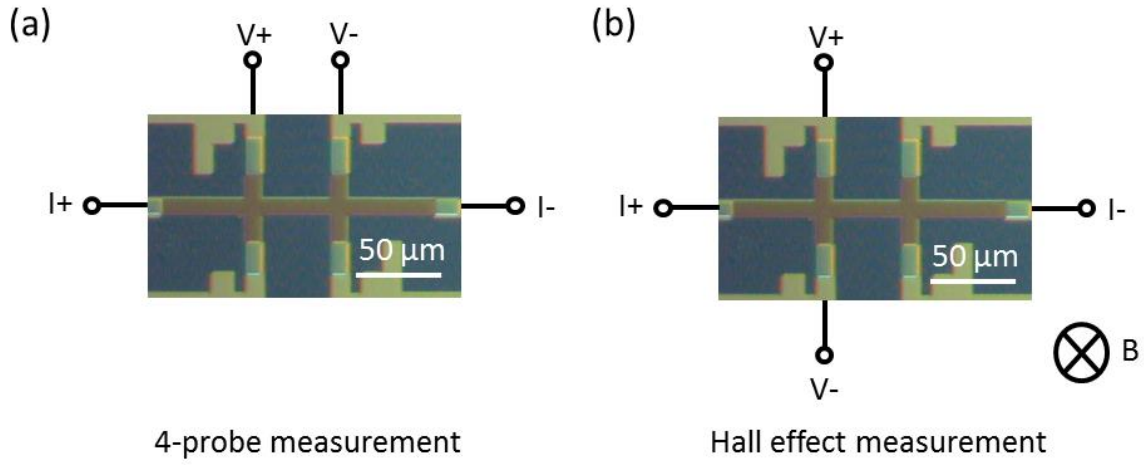

Figure 6.16 Optical microscope images of a Hall bar structure based on CVD graphene. The schematic circuit diagrams show (a) the 4-probe measurement, and (b) the Hall effect measurement.

The sheet resistance and mobility in Table 6.3 are in good agreement with the data provided by the supplier Graphenea™ ($R_s = 450 \pm 40\ \Omega/\square$, $\mu = 2000{\sim}3500\ \mathrm{cm^2/Vs}$). Note that the data in Table 6.3 is all measured at room temperature. For Hall bar 1, we also repeated the 4-probe measurement at a lower temperature. From room temperature to 19 K, the sheet resistance under zero gate voltage changes from 490 Ω/□ to 456 Ω/□, which is a 7% decrease. Since the area carrier density does not change too much from room temperature to low temperature, we expect the mean free path l at low temperature should only increase by a small

fraction from its room temperature value.

Table 6.3 4-probe and Hall effect measurement results on Hall bars based on CVD graphene at room temperature.

Device	Hall bar 1	Hall bar 2
Length between V+ and V- (μm)	50	50
Width (μm)	10	10
Sheet resistance R_s (Ω/□)	521.8	550.0
Conductivity σ (mS)	1.916	1.818
Mobility μ (cm^2/Vs)	2140	2150
Area carrier density n (cm^{-2})	5.59×10^{12}	5.28×10^{12}
Mean free path l (nm)	59	58

6.8 4-Probe SGS Josephson Junctions

6.8.1 Geometry and Measurement Setup

The special geometry of SGS Josephson junctions we discussed in the last few chapters allows us to connect more than two superconducting electrodes directly to the non-superconducting material, which is hard to realise in normal sandwich junctions or nano-bridge junctions. That inspired us to design and to fabricate a variant of the normal Josephson junction, for which we connect four Nb electrodes directly to graphene. We name such devices as “4-probe SGS Josephson junctions”. Note that this should be distinguished from a 4-probe measurement of a normal SGS Josephson junction that we discussed in Section 6.1.2. For a conventional SGS Josephson junction, the graphene as well as the superconducting electrodes are both

considered as parts of the device to be measured, so that a 4-probe measurement means that the non-superconducting current leads and the non-superconducting voltage leads directly connect to the superconducting electrodes separately. For a 4-probe SGS Josephson junction, the graphene alone is considered as the "device" to be measured, so that the four superconducting electrodes directly connect to the graphene separately.

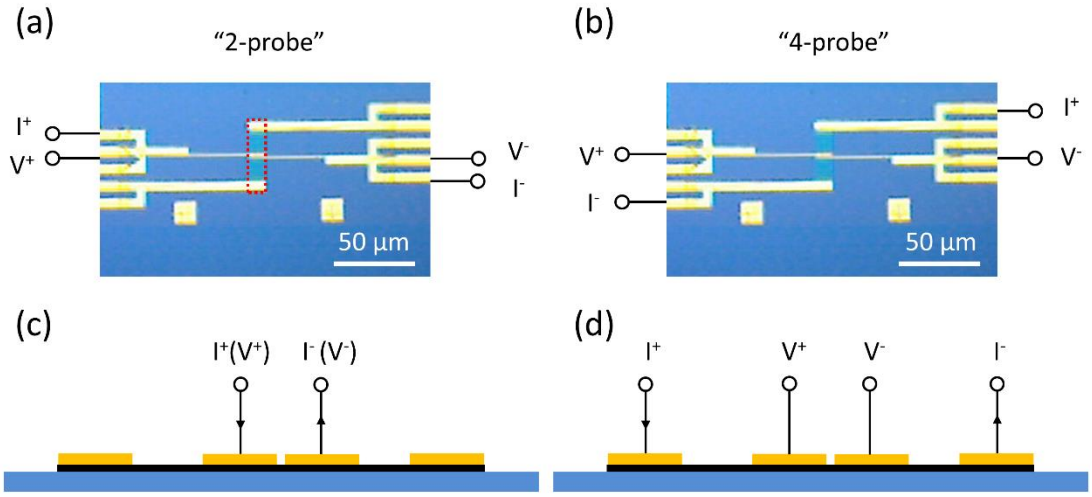

Figure 6.17 4-probe SGS Josephson junctions. (a) and (b) are optical microscope images of a 4-probe SGS Josephson junction. The circuit diagrams show the connection for (a) 2-probe and (b) 4-probe measurements respectively. The red dashed box in (a) indicates where the graphene layer is preserved in the etching process. (c) and (d) schematically show the vertical cross-section of the junction region, corresponding to (a) and (b) respectively. The silicon substrate is shown as blue. The graphene is shown as black. The superconducting electrodes are shown as yellow.

In Figure 6.17 we show the optical microscope image of a 4-probe SGS Josephson junction. The 4-probe junction was fabricated in a similar way to the normal SGS

junctions we discussed in the last few chapters. Note that for this device, the distance between the inner electrode and the outer electrode is as large as 10 μm, which is much larger than the normal state coherence length in graphene, so that the graphene between the inner and the outer electrode is in the normal state. As shown by the circuit diagram, a 4-probe SGS junction allows for both 2-probe measurement and 4-probe measurement. In a 2-probe measurement, both the current leads and the voltage leads are connected to the two inner electrodes; whereas in a 4-probe measurement, the current leads are connected to the two outer electrodes, and the voltage leads are connected to the two inner electrodes.

6.8.2 2-Probe and 4-Probe *I-V* Characteristics

We conducted 2-probe and 4-probe measurements on the same device at 320 mK. As shown in Figure 6.18, the 2-probe *I-V* characteristics of the 4-probe junction are quite similar to the *I-V* characteristics of a normal junction, as discussed in Section 6.2.2. This is reasonable since the 2-probe measurement of the 4-probe junction is equivalent to the measurement of a normal junction, if we neglect the outer electrodes and graphene between the inner and the outer electrodes. In contrast, the 4-probe *I-V* characteristics shown in Figure 6.18 have a more rounded transition with much lower critical current. In other words, when the current is applied through the outer electrodes, the 4-probe junction shows a much weaker Josephson effect compared to when the current is applied through the inner electrodes.

Such a phenomenon has been repeatedly observed in several 4-probe SGS junctions. We found that the difference between 2-probe and 4-probe measurements is more obvious if the width of the inner electrode is smaller. In Figure 6.17, the length of the inner electrode is around 1 μm. The phenomenon for this device is stronger than for devices with 5-μm-long inner electrodes.

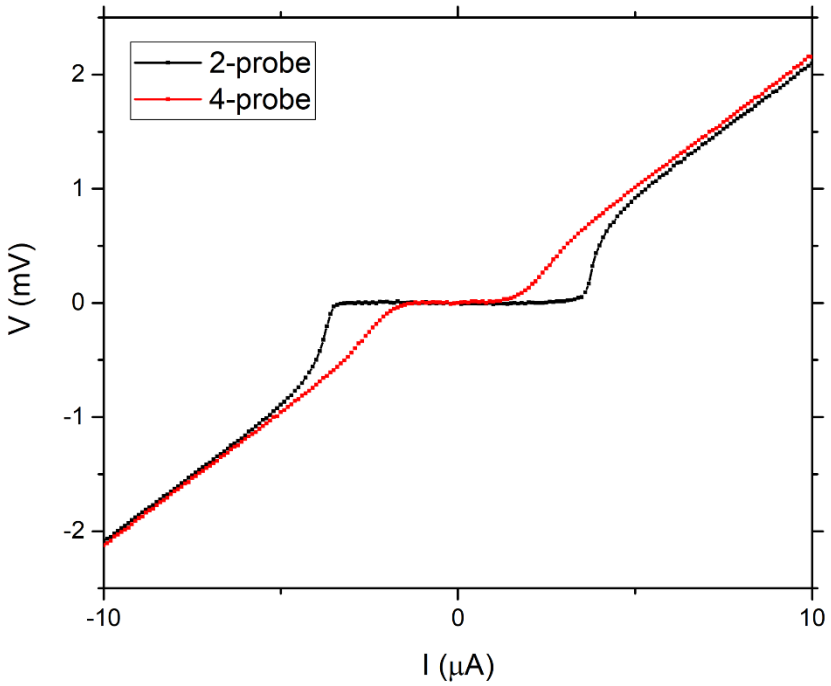

Figure 6.18 *I-V* characteristics of a 4-probe SGS junction by 2-probe and 4-probe measurements respectively. Both measurements were conducted at 320 mK.

The cause of such an apparent difference between 2-probe and 4-probe measurements is worth considering. We have proposed two possible explanations for the possible cause of this phenomenon.

The first explanation is that it is caused by the heat generated by the normal current flowing through the graphene between the inner and the outer electrode. We have measured that the 2-probe resistance between the two outer electrodes at 320 mK is 2.3 kΩ, which is consistent with the sheet resistance of graphene and the contact resistivity between graphene and the superconducting electrode that were measured in Section 6.7. When a normal current of 4 μA passes through such a resistance, it will locally generate heat with a power of 37 nW. Since the thermal conductance of CVD graphene is as high as $10^2 \sim 10^3$ $\mathrm{Wm^{-1}K^{-1}}$, the heat will mostly be removed by thermal conduction through the graphene layer. If we considering a simplified thermal

model that the heat is evenly conducted in every direction in the plane and reaches the heat sink (gold bonding pads) within several millimetres [144], such a power will increase the local temperature by roughly a few hundred millikelvin. Therefore the 4-probe *I-V* curve is actually measured at a much higher local temperature than the 2-probe *I-V* curve. That explains why the 4-probe *I-V* curve is much rounded with much lower critical current.

The other explanation is based on non-equilibrium superconductivity. In the 2-probe measurement, the current flowing through the junction comes from the long superconducting electrode, in which the supercurrent is carried by the Cooper pairs. As a result, the excitation from Cooper pairs to quasi-particles within the junction is limited and keeps at thermal equilibrium. However, in the 4-probe measurement, the current comes from the non-superconducting graphene between the inner and the outer electrodes, and it can inject more “hot” quasi-particles into the junction than at thermal equilibrium. As a result, the population of quasi-particles and Cooper pairs is in a non-equilibrium state. That can also explain why the Josephson effect is weaker in the 4-probe measurement.

Although the two explanations above both involve the change of the population of the quasi-particles in the junction, they are fundamentally different in physics, as in the first explanation, the population of quasi-particles is in thermal equilibrium; whereas in the second explanation, the population of quasi-particles is out of thermal equilibrium. In the next section we will introduce an experiment that helps us rule out of one of the explanations above.

6.8.3 Critical Current Tuned by the Distribution of Current

To find out the exact reason for the difference in the *I-V* curves of 2-probe and 4-probe measurements, we performed some more measurements on the 4-probe SGS Josephson junctions. As shown in Figure 6.19, we apply the current through both the inner and outer electrodes (named as I_{in} and I_{out}), while measuring the voltage through the two inner electrodes. As a result, the total current that flows through the junction equals the sum of I_{in} and I_{out}, while the current that flows through the graphene between the inner and the outer electrodes equals I_{out}. By this means, we can separately tune I_{in} and I_{out} (or effectively tune the distribution of the current), and study their effect on the *I-V* characteristics respectively.

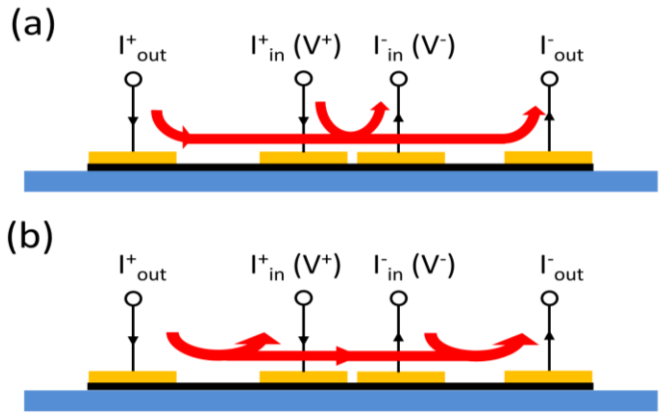

Figure 6.19 Schematic diagram of a 4-probe SGS Josephson junction. The circuit diagram shows that the current is applied through both the inner and the outer electrodes while the voltage is measured through the two inner electrodes. (a) shows actual current flow when I_{in} is positive. (b) shows the actual current flow when I_{in} is negative.

Figure 6.20 shows the effect of the distribution of the current on the *I-V* characteristics. We fix the value of I_{out} and sweep I_{in} while measuring the voltage.

In each the *I-V* curve, the voltage is plotted against the total current $I_{\mathrm{total}} = I_{\mathrm{in}} + I_{\mathrm{out}}$. The red arrows show the direction that the value of I_{out} gradually increases. In Figure 6.20(a), I_{out} gradually increases from 0 μA to 3 μA, with a step of 0.25 μA; while in Figure 6.20(b), I_{out} gradually increases from 0 μA to 10 μA, with a step of 1 μA. Both Figure 6.20(a) and (b) show that the *I-V* curve becomes more and more rounded as the proportion of I_{out} increases, and that such a trend gradually slows down as I_{out} increases but doesn't stop even when I_{out} is as large as 10 μA. Note that the critical currents I_0 in those *I-V* curves are less than 4 μA. That means when I_{out} is larger than 4 μA, the regime of I_{total} between $\pm I_0$ refers to I_{in} being negative, in which case the actual current flow is shown in Figure 6.19(b). In other words, when I_{out} is larger than 4 μA and I_{total} is less than 4 μA, the proportion of I_{out} is always 100%, and the exceeding I_{out} just flows through the inner electrodes, contributing to the negative I_{in}.

Such a regime is of particular interest in understanding the mechanism that cause the difference between 2-probe and 4-probe measurements. Since the proportion of I_{out} among the current through the junction in this regime is always 100%, further increasing the value of I_{out} cannot increase the proportion of I_{out} any more. However, we can observe in Figure 6.20(b) that the *I-V* curves keep becoming rounded when I_{out} increases from 4 μA to 10 μA. If the difference between 2-probe and 4-probe measurements is caused by non-equilibrium superconductivity, we would expect the shape of the *I-V* curve stops changing with I_{out} in this regime when the proportion of I_{out} among the current through the junction is always 100%. On the other hand, if the difference between 2-probe and 4-probe measurements is caused by the heat generated by the normal current flowing through the graphene between the inner and the outer electrodes, the local temperature will keep increasing when I_{out} increases from 4 μA to 10 μA, even when the proportion of I_{out} among the current through the junction already saturates. Therefore, the experiments

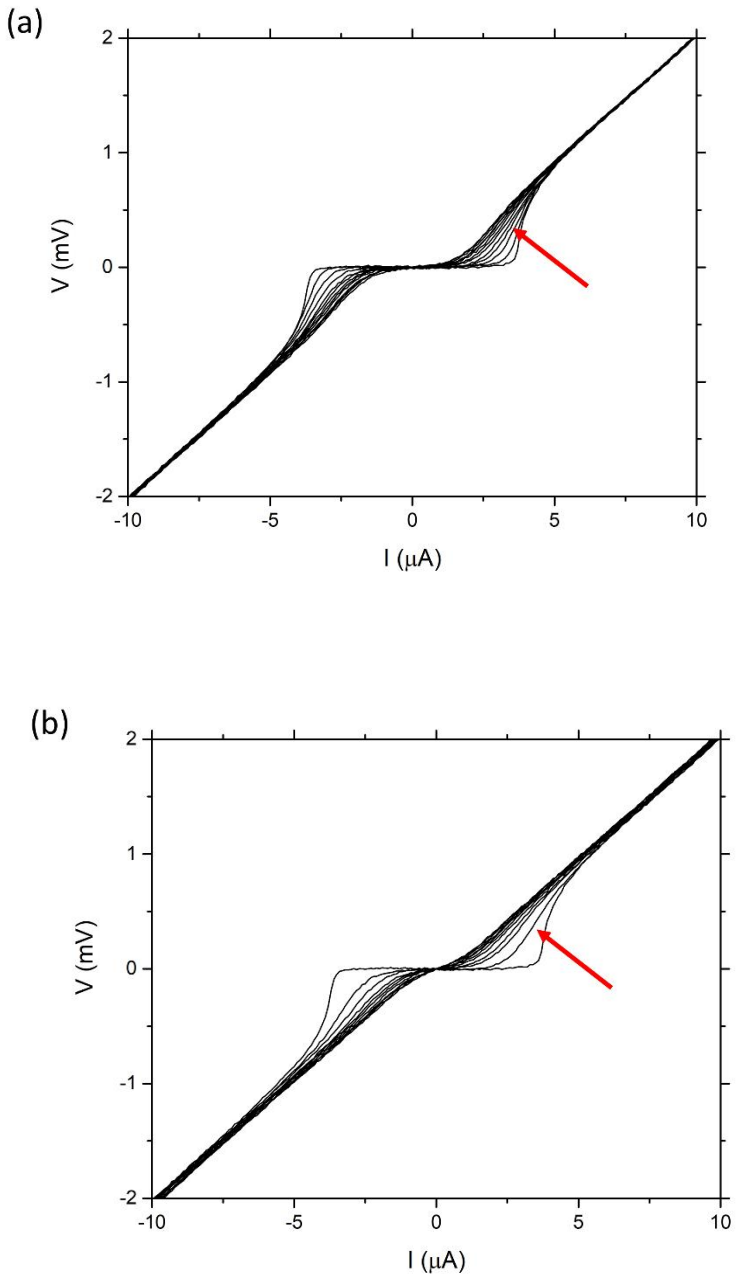

Figure 6.20 *I-V* characteristics of the 4-probe SGS Josephson junction measured in the configuration shown in Figure 6.19 at 320 mK. For each *I-V* curve, I_{out} is fixed while I_{in} is swept, and the *x*-axis is the total current. The red arrows show the direction that the value of I_{out} gradually increases (a) from 0 μA to 3 μA with a step of 0.25 μA, and (b) from 0 μA to 10 μA with a step of 1 μA.

we performed in this section confirms that the difference between 2-probe and 4-probe *I-V* curves of the 4-probe SGS junction is most probably a thermal effect caused by the heat generated by the normal current flowing through the graphene between the inner and the outer electrodes.

Beyond the physical mechanism behind the phenomenon, the dependence of *I-V* characteristics (especially the critical current I_0) on the distribution of current between the inner and the outer electrodes is probably promising for potential applications. The unique structure of the 4-probe SGS junctions provides a way to control the critical current of the Josephson junction by the path of the current through its thermal effect.

6.9 Conclusion

In this chapter, we have shown a series of experiment demonstrating the ideal electrical properties of Josephson junctions based on CVD graphene. The junctions can work over a wide temperature range from 320 mK to 1.5 K without any hysteresis, and exhibit an ideal Fraunhofer-like interference pattern in a perpendicular magnetic field, showing the uniform distribution of the supercurrent in the junction. The critical current can be effectively tuned by the gate voltage up to an order of magnitude. For junctions as short as 50 nm, we have found evidence for ballistic transport from both the $I_0 - T$ and the $R_\mathrm{n} - V_\mathrm{g}$ relations. As far as we know, this was the first time that ballistic transport was observed in a Josephson junction based on CVD graphene.

We have also studied the 4-probe Josephson junction, a variant of Josephson junction allowed by the unique geometry of SGS junctions. When performing *I-V* measurement, the voltage is measured between the two inner electrodes, while the current can be applied through either the two inner or the two outer electrodes, or

through a mixture of both. We have found that the Josephson effect becomes weaker when the current is applied through the two outer electrodes, compared with when the current is applied through the two inner electrodes. By varying the distribution of current between the inner and the outer electrodes, we validated that such an effect is caused by the heat generated locally by the normal current flowing through the graphene between the inner and the outer electrodes. Such a tuneability may find its applications in superconducting electronics, especially when the conventional ways to control the critical current (such as by magnetic field or gate voltage) are not applicable.

Chapter 7 Measurement of dc SQUIDs based on CVD graphene

In this chapter we present the measurement results of dc SQUIDs based on CVD graphene. In Sections 7.1 and 7.2, we will show how their *I-V* properties vary with the magnetic field and the gate voltage. The measurement results allow us to estimate the asymmetry and the noise level in Sections 7.3 and 7.4. In the Section 7.5, we will demonstrate the measurement on the gate respond speed of the SQUIDs.

7.1 *I-V* Properties vs. Magnetic Field

As we have shown in Section 5.2, we can fabricate dc SQUIDs made up of two SGS junctions in parallel in similar ways as fabricating single junctions. Here we show the measurement result of dc SQUIDs shown in Figure 5.13(b) with an inner loop size of 500 μm^2, which is made up with two Josephson junctions (~50 nm length and 20 μm width) in parallel. The SQUID loop was chosen to be large compared with the effective area of the junctions so that the interference of the two junctions can be easily distinguished from the self-interference of a single junctions. Meanwhile, the SQUID loop should not be too large since if the screening factor β_L is too large, the modulation depth of critical current and voltage will be much reduced, as discussed in Section 2.3. The *I-V* characteristics of such a dc SQUID under a perpendicular magnetic field are shown in Figure 7.1(a). The critical current of the SQUID shows high frequency oscillation enveloped by a Fraunhofer-like pattern. The high frequency oscillation is due to the interference between the two branches of the SQUID loop, while the Fraunhofer-like pattern comes from the self-interference within the single finite-size junctions. Due to flux focusing, the effective area of a

single junction is non-negligible compared with the loop area. Thus, we can clearly see the change in amplitude within several oscillation periods of the high frequency response.

In Figure 7.1(b), we focus on the small range around the centre of the main peak. The period of the oscillation is 2.2 μT, corresponding to an effective area of 910 μm^2. This is reasonable since the inner loop of the SQUID is 500 μm^2, while the outer loop is 1500 μm^2. If we assume that the effective area of the SQUID is defined by the midpoint of each track around the SQUID loop, the effective loop area is 975 μm^2, which matches well with the measured value from our experiment. An alternative method to estimate the effective area of the SQUID is to use the geometric mean of the inner and the outer loop. In this case, the effective loop area is 866 μm^2, which is also in good agreement with the measured value.

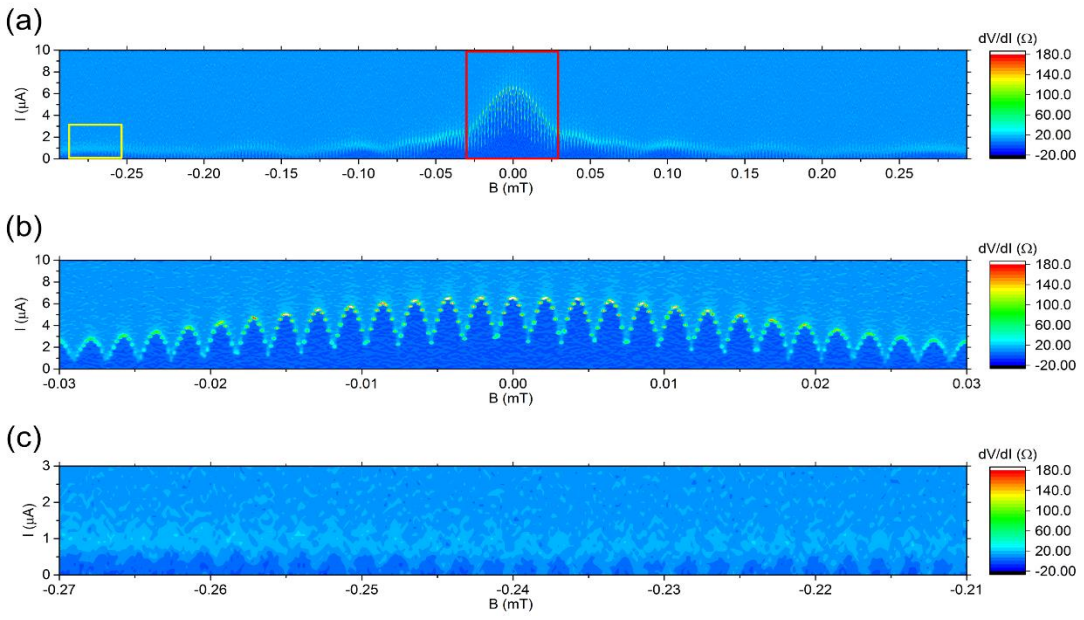

Figure 7.1 Differential resistance as a function a bias current and magnetic field. The *I-V* characteristics were measured on a dc SQUID of inner loop size of 500 μm^2 at 320 mK. (b) and (c) are zoomed-in views of the red and yellow boxes in (a), respectively.

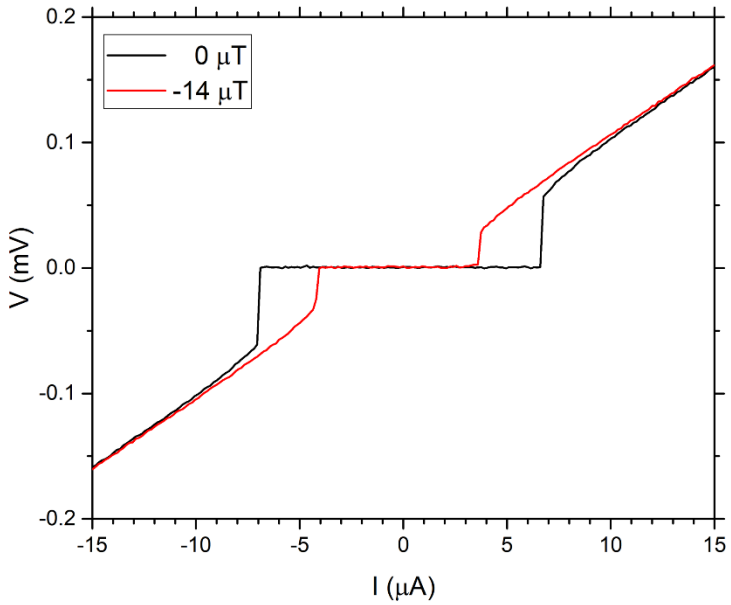

Figure 7.2 *I-V* characteristics of the same dc SQUID as in Figure 7.1. The black curve was measured without external magnetic field, which corresponds to the largest critical current. The red curve was measured under a magnetic field of -14 μT, which corresponds to the first minimum of critical current beside the maximum.

In Figure 7.2 we plot two I-V curves corresponding to the peak and the valley of the high frequency oscillation in Figure 7.1. The black curve was measured when the external magnetic field is zero, so that the critical current is at its maximum, whereas the red curve was measured when the external magnetic field is -14 μT, which corresponds to the first minimum of critical current beside the maximum. The maximum critical current is 6.6 μA, which is similar to a single junction with a width of 40 μm. The normal state resistances in the two curves are almost the same, about 11.3 Ω, which is also close to the value for a 40-μm-wide single junction.

From the dataset of Figure 7.1, we can directly extract the *V-B* properties of the SQUID. During a measurement like in Figure 7.1, we fix the magnetic field and scan

the bias current; while in a normal *V-B* measurement, we fix the bias current and scan the magnetic field. Whichever way we conduct the measurement; we finally have a matrix of voltages, with each element corresponding to a specific combination of bias current and magnetic field. As a comparison, in Figure 7.3(a), we plot the *V-B* curves extracted from the dataset of Figure 7.1; while in Figure 7.3(b), we plot the *V-B* curves obtained by fixing the bias current and scanning the magnetic field. As you can see, there is no obvious difference except that the magnetic field step was half in Figure 7.1(a). The voltage values in Figure 7.1(b) are slightly higher than those in Figure 7.1(a), which is most probably due to a slight drift of normal state resistance in different cooling cycles.

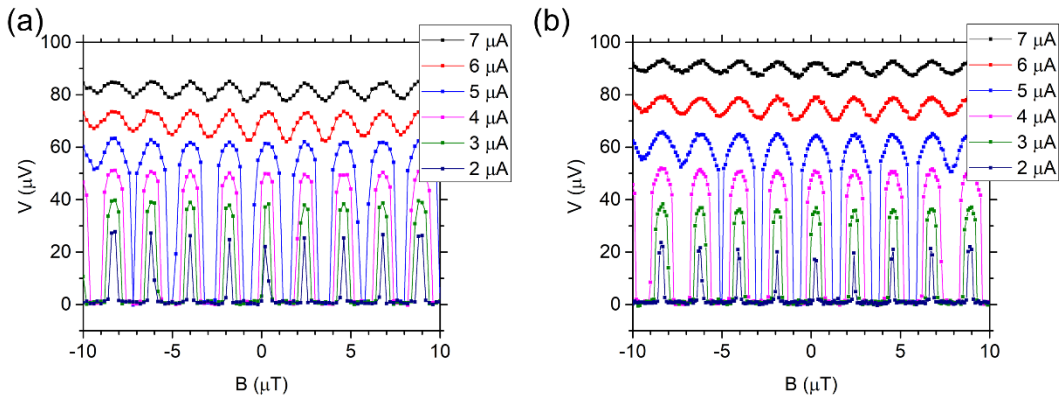

Figure 7.3 *V-B* characteristics of the same dc SQUID as in Figure 7.1. (a) Curves exacted from the dataset of Figure 7.1 (fixing magnetic field and scanning current). (b) Curves obtained by fixing current and scanning magnetic field, measured at 320 mK.

As we can see in Figure 7.3(b), the modulation of bias voltage reaches its maximum when the bias current is 5 μA, and the maximum modulation $\Delta V = 65$ μV. To compare it with the theoretical expectation $\Delta V \approx I_0 R/(1+\beta_L)$ in Eq. (2.42), we first need to evaluate the value the inductance of the SQUID loop. This can be done by simulation using the finite-element software package 3D-MLSI, which is a

finite-element package specially designed for superconductors [145]. To build a model using 3D-MLSI, we need to define the geometric shape of the superconductor thin film, and to set up the mesh size. The mesh size needs to be smaller than the finest structure of the superconductor film and smaller than the London penetration depth, so that the current distribution on edges can be simulated. A trick in building the model is how to simulate the current distribution in the junction, if we simply build a model with the exactly the same geometry as our SQUID (Figure 7.4(a)), we are actually assuming the current mainly flows on one edge of each junction, since the current tends to flow around the inner perimeter of the superconducting loop. However, in reality, the current should be more or less evenly distributed along the junction width. Therefore, to mimic this, we developed a model that replaced the junctions with nano-constrictions (Figure 7.4(b)). By assuming the current flows in the centre of the junction, we can get a better simulation of the real case. In fact, the self-inductance of the loop in Figure 7.4(b) is 72 pH, a bit higher than the loop in Figure 7.4(a) (67 pH).

With $L = 72$ pH and $2I_0 = 6.5$ μA, the screening parameter (introduced in Section 2.3.1) can be calculated as $\beta_{\mathrm{L}} = 2LI_0/\Phi_0 = 0.23$. The normal state resistance of the dc SQUID can be derived from the *I-V* characteristics, $R_{\mathrm{n}} = R/2 = 11.5$ Ω. The maximum modulation depth predicted by Eq. (2.42) is $\Delta V \approx I_0 R/(1+\beta_L) = 60.8$ μV, which is in good agreement with the measurement results.

The maximum $|\partial V/\partial \Phi_{\mathrm{a}}|$ is also reached when the bias current is 5 μA. From Figure 7.3(b) we can easily calculate that $\max(|\partial V/\partial \Phi_{\mathrm{a}}|) = 5.77 \times 10^{11}$ s^{-1}. This is slightly higher than the theoretical estimation in Section 2.3.2 that $\max(|\partial V/\partial \Phi_{\mathrm{a}}|) \approx R/L = 3.19 \times 10^{11}$ s^{-1}, which is reasonable as the conditions for the estimation are not totally satisfied. The screening parameter for our SQUID is smaller than 1, and the noise parameter $\Gamma = 2\pi k_{\mathrm{B}} T/\mathrm{I}_0 \Phi_0 = 0.003$ is also smaller than the

case considered in the estimation.

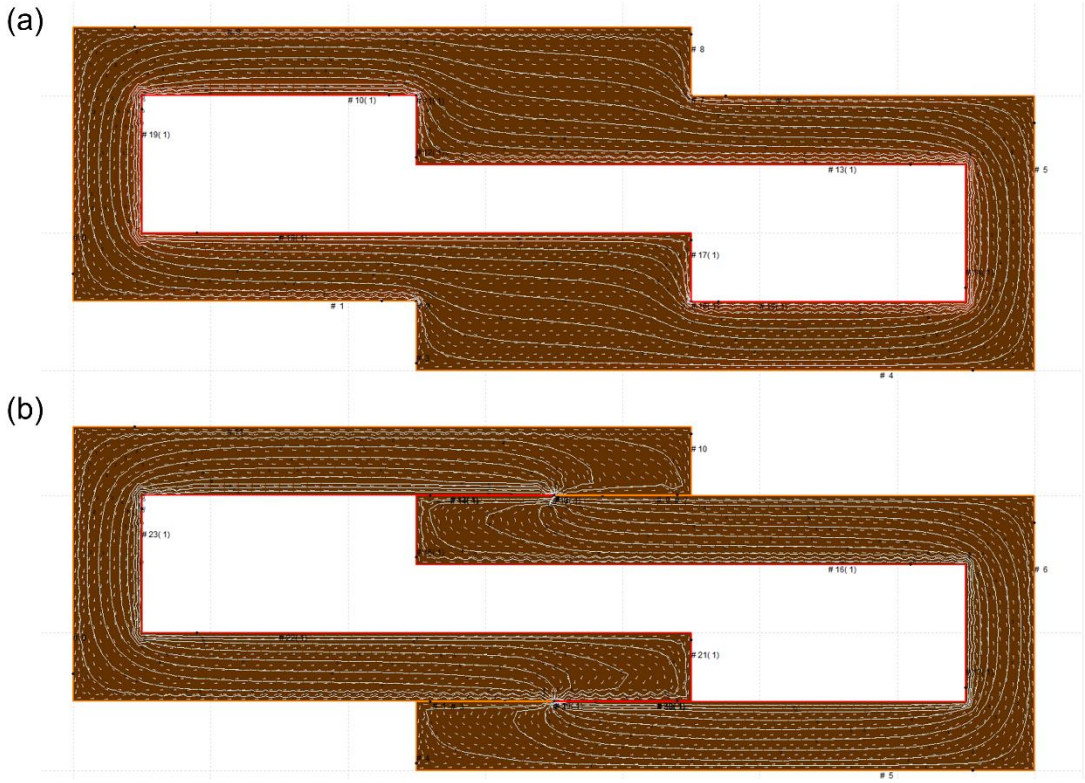

Figure 7.4 3D-MLSI models of an SGS SQUID. (a) The geometry is exactly the same as the fabricated SQUID, which assumes the circulating supercurrent mostly flowing on the one edge of the junction area; (b) The junctions are replaced by nano-bridges, which assumes the circulating supercurrent flowing in the centre of the junction area.

7.2 *I-V* Properties vs. Gate Voltage

One of the advantages of dc SQUIDs based on SGS junction is that the critical current can be tuned by both the magnetic field and the gate voltage. In Figure 7.5, we show the critical current as a function of both magnetic field and gate voltage, in a 2D contour plot and a 3D surface plot respectively. Both plots show that the critical current has a periodic dependence on the magnetic field and a monotonic dependence

on the gate voltage (as the gate voltages are only on one side of the Dirac point).

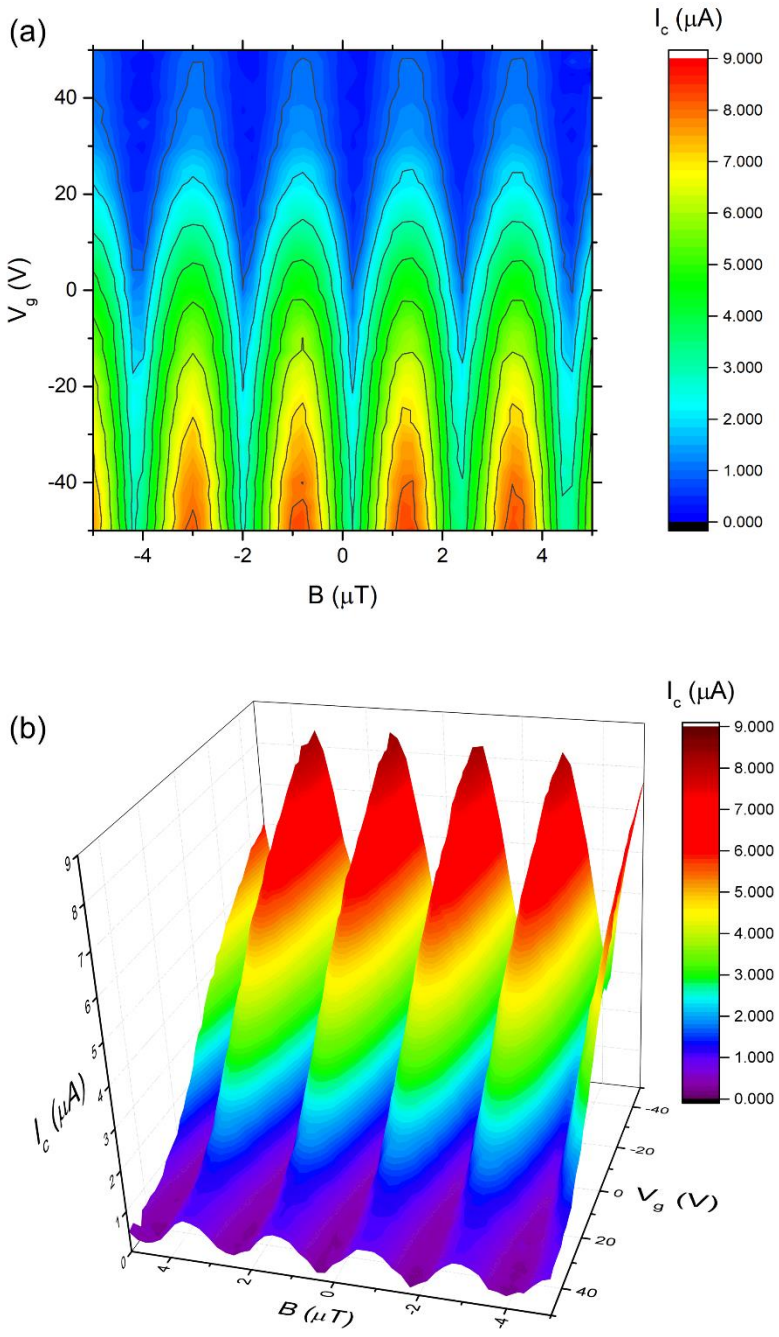

Figure 7.5 Critical current as a function of magnetic field and gate voltage. The *I-V* characteristics were measured on the same device as in Figure 7.1. (a) 2D contour plot. (b) 3D surface plot.

7.3 Asymmetry of the SQUIDs

As discussed in Section 2.3.3, the *I-V* characteristics under the magnetic field allow us to estimate the asymmetry of the two SGS junctions of the dc SQUID. For an asymmetric SQUID, the positive and negative branches of bias current are no longer symmetric, the maxima (or the minima) $|I_c|$ in the two branches are shifted by $\Delta\Phi/\Phi_0 = \beta_L(\alpha_I + \alpha_L)$, where the screening parameter $\beta_L = 2LI_0/\Phi_0$, α_I and α_L are the asymmetry parameters of current and inductance, as defined by Eq. (2.45).

To precisely determine the sum of α_I and α_L of the SQUID, we need to accurately measure the shift of the $I_c - B$ curve in the positive and negative branches. The measurement before and in Figure 7.1 only has a resolution of 0.1 μT in magnetic field, which hinders us from determine the shift precisely. Therefore, we performed a sweep of magnetic field from -2.5 μT to 2.5 μT, with 5 times higher resolution, as shown in Figure 7.6. This allows us to determine the relative shift between the positive and negative branches to be -0.18 μT, while a quantum flux corresponds to 2.16 μT. For a critical current of $2I_0 = 7.5$ μA, the screening parameter $\beta_L = 0.27$. Since $\Delta\Phi/\Phi_0 = \beta_L(\alpha_I + \alpha_L)$, we can determine that $\alpha_I + \alpha_L = -0.309$.

Ref. [6] also shows that "for variable bias current, the minima in the $V(\Phi_a)$ characteristics are shifted along the flux axis proportional to $\alpha_L LI/2$, independent of the value of α_I". We tried to analyse the data in Figure 7.6 to see how the minima of $V(\Phi_a)$ is shifted proportional to *I*, however, the shift is even more tiny than the uncertainty of the minima of $V(\Phi_a)$, so that no convincible α_L can be calculated. In fact, if we want to determine α_L to an accuracy of 0.1, according to the claim above, we need to measure shift of the minimum of *V*(*B*) by 3.6×10^{-3} Φ_0 ≈ 7 nT, which is much smaller than the magnetic field resolution in Figure 7.6. Therefore, the method to separate α_I from α_L seems not very practical given the current

measurement accuracy. However, since inductance of each branch of the SQUID scales with branch length and since the fabrication errors are very small compared to the branch length, we estimate that α_L is quite small and that α_I is the dominant factor of asymmetry. If we assume that $\alpha_I = 0.3$, the critical currents of the two branches will be different by a factor of two.

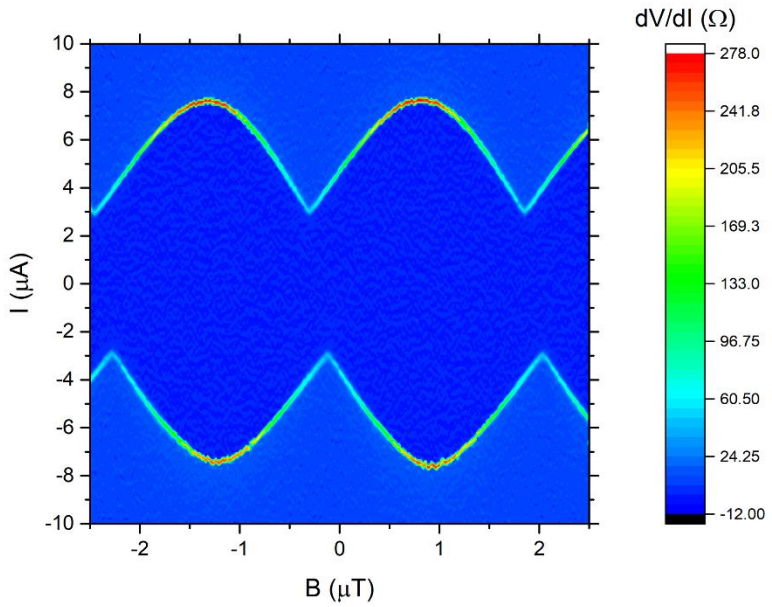

Figure 7.6 Differential resistance vs bias current and magnetic field. The *I-V* characteristics were measured on the same device as in Figure 7.1, with much higher resolution in magnetic field.

7.4 Estimation of Noise Level and Possible Optimisation of the SQUID Loop

Due to the lack of a preamplifier working at low temperature in our measurement system, we didn't measure the intrinsic noise level of the dc SQUID based on SGS junctions. Here we present a rough estimation of the ideal white noise level based on the conclusion in Section 2.3.2.

Given that $\Gamma = 2\pi k_B T/I_0\Phi_0 = 0.003 \ll 1$ and $\beta_L = 0.23$, we can estimate the voltage white noise minimum at 320 mK as

$$S_V^{1/2}(f) \approx 4\sqrt{k_B TR} = 27.6 \text{ pV/Hz}^{1/2} \tag{7.1}$$

Thus, the flux white noise minimum at 320 mK is

$$S_\Phi^{1/2}(f) = \frac{S_V^{1/2}(f)}{\max(|\partial V/\partial \Phi_a|)} = 24 \text{ n}\Phi_0/\text{Hz}^{1/2} \tag{7.2}$$

The energy sensitivity at 320 mK is

$$\epsilon(f) = \frac{S_\Phi(f)}{2L} = 1.7 \times 10^{-35} \text{ J/Hz} = 0.16\hbar \text{ Hz} \tag{7.3}$$

which is below the quantum limit for the smallest energy that can be detected in a given time, set by Heisenberg's uncertainty principle. This is probably because the derivation of Eq. (7.1) in Ref. [22] assumes perfect RSJ-like IV curves while the transfer function $\max(|\partial V/\partial \Phi_a|)$ we measured is higher than they assume.

Similarly, we can estimate the voltage white noise minimum at 1 K as

$$S_V^{1/2}(f) \approx 4\sqrt{k_B TR} = 48.8 \text{ pV/Hz}^{1/2} \tag{7.4}$$

We didn't measure the maximum of $|\partial V/\partial \Phi_a|$ at 1 K. However, according to the $I_0 - T$ curve in Figure 6.14(a), we estimate the critical current at 1 K is about half of its value at 320 mK, while the normal state resistance is almost independent of temperature. Thus, the maximum of $|\partial V/\partial \Phi_a|$ should be half of the value at

320 mK. Therefore, the flux white noise minimum at 1 K is

$$S_{\Phi}^{1/2}(f) = \frac{S_{\mathrm{V}}^{1/2}(f)}{\max(|\partial V/\partial \Phi_{\mathrm{a}}|)} \approx 85 \ \mathrm{n}\Phi_0/\mathrm{Hz}^{1/2} \tag{7.5}$$

Note that at temperatures well below 1 K the measured flux noise level of typical dc SQUIDs can often be higher than such simple predictions because they ignore hot electron effects and other noise sources [146]. The energy sensitivity at 1 K is

$$\epsilon(f) = \frac{S_{\Phi}(f)}{2L} = 2.1 \times 10^{-34} \ \mathrm{J/Hz} = 2.0\hbar \ \mathrm{Hz} \tag{7.6}$$

which is close to the quantum limit set by the uncertainty principle.

Note that for the SQUIDs measured above, the SQUID loop was chosen to enable easy observation of SQUID response with the magnetic field available in the measurement system and to easily distinguish the effect of the interference between the two branches and the self-interference of a single Josephson junction, rather than to optimise the SQUID sensitivity. Here we try to optimise the design of the SQUID based on the performance of the SGS junctions and SQUIDs that we have measured, to minimise the noise level and to maximise the sensitivity.

If we consider using the SQUID as a flux sensor, we need to minimise the flux noise $S_{\Phi}^{1/2}(f)$. As we have discussed in Section 2.3.2, for $\beta_{\mathrm{c}} \leq 1$, $\beta_{\mathrm{L}} \approx 1$, and $\Gamma = 0.05$,

$$S_{\Phi}^{1/2}(f) \approx 4\sqrt{k_{\mathrm{B}}TL^2/R} \tag{7.7}$$

We can assume that the inductance L roughly scale with the inner perimeter of the SQUID loop. To minimise the flux noise, the size of SQUID loop should to be as small as possible. As schematically shown in Figure 7.7, if we decrease the size of SQUID loop to a minimum, it will finally be limited by the size of the single Josephson junction, as shown in Figure 7.7(b), which is equivalent to a single junction, as shown in Figure 7.7(c). Therefore, the design of the most sensitive flux sensor should be a single SGS junction as narrow as possible. Considering the practical fabrication possibilities, an SGS junction as narrow as 1 μm can be easily achievable. Such a junction should have a critical current $I_c = 2I_0 \approx 0.13$ μA and a normal state resistance $R_n \approx 4.4$ kΩ. If we still consider the junction as a SQUID and simulate it using a model as shown in Figure 7.7(d), the inductance of the SQUID loop would be $L = 1.2$ pH, so that $\beta_L = 2LI_0/\Phi_0 = 8 \times 10^{-5} \ll 1$. In such a case, the assumption for Eq. (7.7) is no longer satisfied, so that we cannot estimate the exact value of the transfer function $\max(|\partial V/\partial \Phi_a|)$ and the flux noise $S_\Phi^{1/2}(f)$.

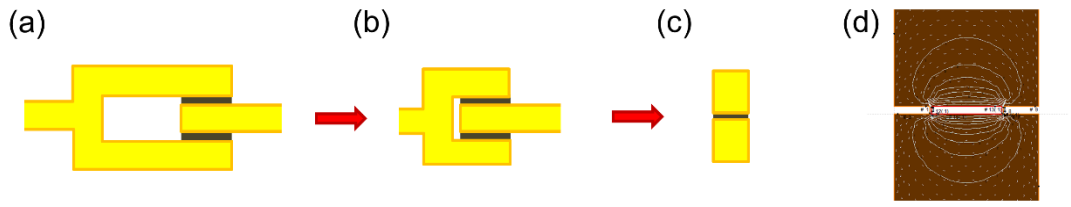

Figure 7.7 Schematic diagrams of SGS SQUID with different loop size. (a)–(c) By reducing the loop size to its minimum, a dc SQUID will turn to a single Josephson junction. Superconducting electrodes are in yellow. The graphene is in black. (d) The 3D-MLSI model of a 1-μm-wide SGS junction, while is still considered a dc SQUID made up of two nano-bridge junctions.

If we consider using the SQUID as a field sensor, we need to minimise the magnetic field sensitivity $S_B^{1/2}(f) = S_\Phi^{1/2}(f)/A_{\text{eff}}$, where A_{eff} is the effective area

of the SQUID loop. If we assume that the conditions for Eq. (7.7) are still satisfied, the magnetic field sensitivity

$$S_B^{1/2}(f) \approx 4\sqrt{k_\mathrm{B}TL^2/RA_\mathrm{eff}^2} \tag{7.8}$$

Since $\beta_\mathrm{L} = 2LI_0/\Phi_0$ should be close to 1, and the product of I_0R_n is a constant at a given temperature, $R \propto 1/I_0 \propto L$. Since L roughly scale with the inner perimeter of the SQUID loop, $A_\mathrm{eff} \propto L^2$. As a result, $S_B^{1/2}(f) \propto L^{-3/2}$. Therefore, to minimise $S_B^{1/2}(f)$, the SQUID loop should be as large as possible, while the critical current needs to be small to keep $\beta_\mathrm{L} \approx 1$. So the maximum SQUID loop is again limited by how narrow a single SGS junction can be. If we still assume the minimum width of a practical SGS junction to be 1 μm, the inductance L can be as large as 7.7 nH. For large SQUID loops, we should also consider the requirement that the magnetic flux generated by circulating current due to thermal fluctuation needs to be much smaller than flux quantum, so that the SQUID action is not washed out by thermal fluctuation. That requires the inductance $L \ll L_\mathrm{F} \equiv (\Phi_0/2\pi)^2/k_\mathrm{B}T = 24.5$ nH [6], and the inductance value above is close to the limit. Therefore we think that an inductance $L = 0.1L_\mathrm{F} \approx 2.5$ nH is a sensible choice. By rough simulation using 3D-MLSI we found out that such an inductance refers to a SQUID loop as large as $A_\mathrm{eff} \approx 0.1$ mm^2. In such a case, the magnetic field sensitivity at 320 mK would be as small as

$$S_B^{1/2}(f) \approx 4\sqrt{\frac{k_\mathrm{B}TL^2}{RA_\mathrm{eff}^2}} = 3 \times 10^{-16}\ \mathrm{T/Hz^{1/2}} \tag{7.9}$$

7.5 Measurement of Gate Response Speed

7.5.1 Measurement Principle and Setup

With a lock-in amplifier, we can measure the respond speed of the SQUID to the gate voltage. As shown in Figure 7.8, we connect the gate electrode to the reference source "sine out" of the lock-in amplifier and connect the voltage across the device to the "signal in" of the lock-in amplifier. As we scan the bias current at a much lower rate, the *I-V* characteristics of the SQUID will oscillate between the two *I-V* curves shown in Figure 7.9(a), so that the voltage across the SQUID will have a component with the same frequency as the gate. The amplitude of the component should be as shown in Figure 7.9(b): theoretically, the amplitude should be zero when the bias current is smaller than the critical current; it should have a peak close to the critical current and increase linearly when bias current is larger than the critical current.

To obtain what we expect experimentally, there are actually a few considerations in the experimental setup. Normally, when we do a dc measurement of our device, the device is floating from the ground, and we connect the negative end of the gate voltage V_g- to one of the leads of the device (through a π-filter). However, this time, we want to apply an ac signal on the gate electrode. Since the Josephson effect of our device will vanish under rf noise (as shown in Section 6.2.3), we choose to connect the negative end of the gate voltage to ground. At the same time, we ground our device on one of the current leads. Since the π-filter on the current lead is applied between the lead and the ground, it guarantees that the ground to which the device is connected has less rf noise. We ran a few tests to verify that a dc gate voltage applied in this way has the same effect of modulating the critical current.

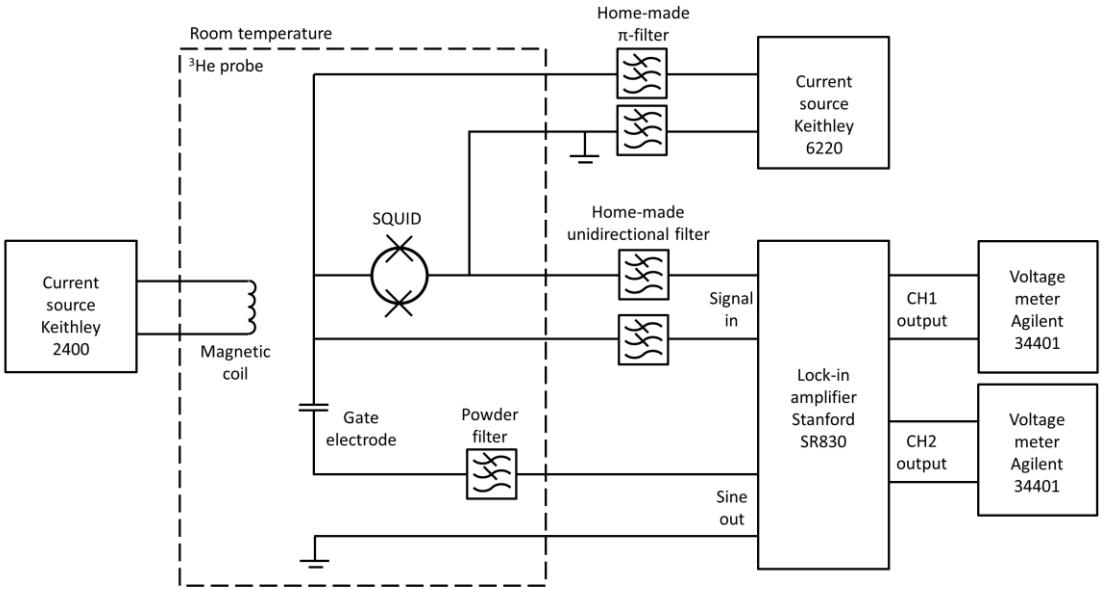

Figure 7.8 Experimental setup for measuring the gate speed of the SQUID.

Another concern is on the signal-in of the lock-in amplifier. In principle, as we are connecting an ac voltage signal from the device, we shouldn't apply any filter between the device and the signal-in of the lock-in amplifier. However, a measurement performed in this way was found to only have a linear response for either $I_{\mathrm{bias}} > 0$ or $I_{\mathrm{bias}} < 0$, forming a "V" shape without any features close to and lower than the critical current. We suspected that it was because there exists some backward rf noise that suppresses the Josephson effect. What we observed (linear part in Figure 7.9(b)) is just the modulation of the normal state resistance by the gate voltage (without the feature of the Josephson effect). Thus, we tried to apply a unidirectional filter on each of the signal-inputs of the lock-in amplifier. The unidirectional filter is just the modified from the π-filter in Figure 6.6 by removing one of the capacitors. In principle, such a unidirectional filter allows the ac signal from the device to pass through to the signal-in of the lock-in amplifier, but prevents backward rf noise from the lock-in amplifier.

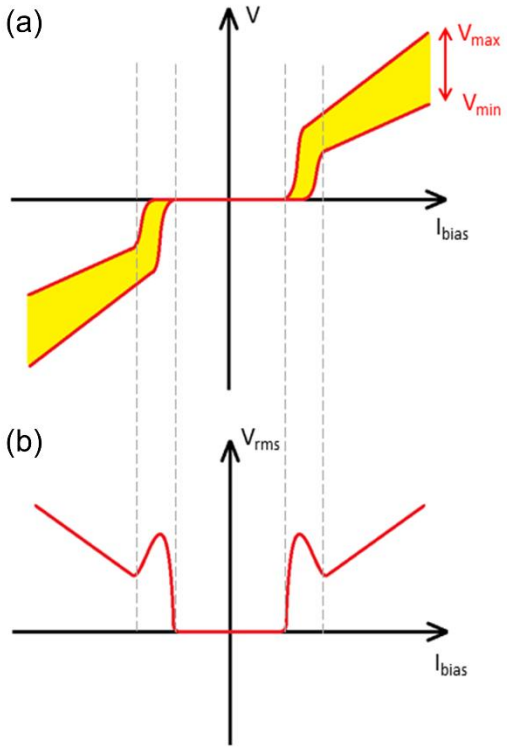

Figure 7.9 Schematic explaning of the principle of measuring the gate speed of the SQUID. (a) The *I-V* curve will oscillate between the two red curves when the gate is connected to an ac signal. Thus when fixing the bias current, the output voltage will oscillates between V_{max} and V_{min}. (b) By connecting the output voltage of the SQUID to a lock-in amplifier, the lock-in output, which is proportional to the height of the yellow area in (a), will have a peak close to the critical current.

7.5.2 Measurement Results

In Figure 7.10, we show the amplitude of the component of the SQUID bias voltage with the same frequency as the ac gate voltage and its phase angle compared with the ac gate voltage. As we can see in Figure 7.10(a), the black curve which corresponds to the amplitude of the component under an ac gate voltage of 7 Hz, clearly shows the three parts as expected: a flat part when $|I| < I_c$, a peak when $|I| \cong I_c$, and a linear

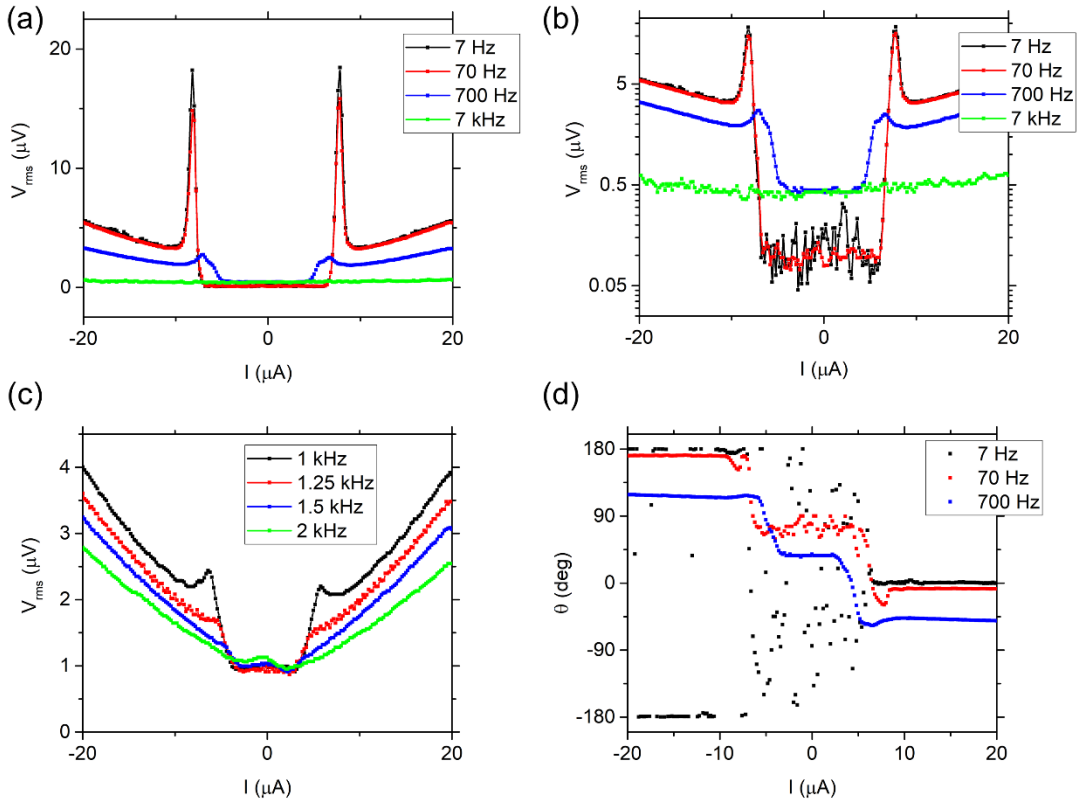

Figure 7.10 The amplitude and the phase angle of the component of the SQUID bias voltage with the same frequency as the ac gate voltage. (a) The amplitude of the oscillating component of the voltage across the SQUID, when an ac signal is applied at the gate electrode, measured on the same SQUID as in Figure 7.1, at 320 mK. The frequency of the gate voltage varies from 7 Hz to 7 kHz. (b) The same data as in (a) plotted in log scale. (c) The amplitude of the oscillating component of the voltage across the SQUID, when an ac signal is applied at the gate electrode, measured on the same SQUID as in (a), at 320 mK. The frequency of the gate voltage varies from 1 kHz to 2 kHz. (d) The phase angle of the oscillating component of the voltage across the SQUID, compared with the ac gate voltage.

part when $|I| > I_c$. As the frequency gradually increases from 7 Hz to 7 kHz, we can see two major changes: one is that the slope of the linear part decreases significantly

(so that the curve at 7 kHz is almost flat in Figure 7.10(a), even in the log scale plot in Figure 7.10(b)), the other is that the peak gradually becomes lower, and can hardly be seen in the curve at 7 kHz (as shown in Figure 7.10(b)). The possible reason for the first change is that the impedance of the capacitance between the gate and the device becomes smaller at higher frequencies so that the effective gate voltage becomes smaller. As a result, the modulation amplitude of the normal state resistance becomes smaller. This can also explain the second change observed above. Therefore, although the features around and below the critical current are not visible at 7 kHz, it does not mean that the SQUID can only respond to gate voltage as fast as 7 kHz. It only tells the lower limit of gate respond speed. In Figure 7.10(c), we focused on the frequencies between 700 Hz and 7 kHz and found out that highest frequency that the features around and below the critical current are still visible is 1.5 kHz. Thus, our conclusion is that the respond speed to the gate voltage is at least 1.5 kHz. The response at higher frequencies is limited by the fact that the gate voltage cannot be effectively applied between the SQUID and the gate electrode at high frequencies.

The corresponding phase angle is plotted in Figure 7.10(d). For the 7 Hz signal, the phase angle is around 0° when $I > I_c$, around 180° when $I < -I_c$ and is totally random when $|I| < I_c$. This is exactly what we expected considering the dependence of the SQUID bias voltage on gate voltage as shown in Figure 7.9(a). When $I > I_c$, the SQUID bias voltage is higher for higher gate voltage; when $I < -I_c$, the SQUID bias voltage is lower for higher gate voltage; and when $|I| < I_c$, the SQUID bias voltage does not depend on the gate voltage.

For higher frequency signal, the phase angle when $I > I_c$ and when $I < -I_c$ shift from 0° and 180° by the same amount, and the phase angle when $|I| < I_c$ is always half-way between the positive and negative ends. The reason for the overall shift of the phase angle is not clearly known. However, the fact that the phase angle when

$|I| < I_c$ is 90° behind the phase angle when $I > I_c$ clearly indicates the existence of leakage current between the SQUID and the gate electrode. The leakage current from the gate electrode to the SQUID becomes larger as the impedance of the capacitance between the device and the gate becomes smaller at higher frequency. The leakage current is 90° behind the gate voltage due to the capacitive coupling between the gate and the device. The leakage current will generate an ac bias voltage across the SQUID which will also be 90° behind the gate voltage, which is also detectable by the lock-in amplifier. When $I > I_c$ and when $I < -I_c$, the SQUID bias voltage is dominated by the contribution from the bias current while the contribution from the leakage current can be neglected; when $|I| < I_c$, the only contribution comes from the leakage current so that the phase angle of the bias voltage is 90° behind the phase angle when $I > I_c$.

7.6 Conclusion

In this chapter, we have shown the ideal electrical properties of dc SQUIDs based on CVD graphene. In a perpendicular magnetic field, the critical current shows periodic oscillation enveloped by Fraunhofer-like interference pattern, which is the reasonable behaviour of dc SQUIDs made up of finite-size junctions. What made the SQUIDs based on CVD graphene unique is that the critical current can also be tuned by the gate voltage. We have estimated that the sensitivity of the SQUIDs can be as low as $24\ \mathrm{n}\Phi_0/\mathrm{Hz}^{1/2}$ at 320 mK if only the white noise is considered, and we have measured that the properties of the SQUIDs can respond to the gate voltage at least as fast as 1.5 kHz.

Chapter 8 Josephson Penetration Depth and Edge Effect

The motivation for this chapter is to understand why the supercurrent can still be uniformly distributed even for the widest junctions. We will first show that the normal derivation of the Josephson penetration depth is no longer valid for coplanar junctions and a new expression will be introduced. The Josephson penetration depth given by the new expression is much larger than reasonable junction widths, which means we can only numerically study how the interference pattern gradually varies from the usual Fraunhofer-like pattern as the junction width is increased to become larger than the Josephson penetration depth, as described in Sections 8.3 and 8.4. Finally, we will show how the interference is affected by a manually induced edge effect using a localised top gate to supress the supercurrent in part of the junction.

8.1 Redefinition of Josephson Penetration Depth for Coplanar Junctions

8.1.1 Josephson Penetration Depth for Pure 2D Junctions

In Section 2.1.6, we have shown the derivation of the Josephson penetration depth for normal 3D tunnel junctions. For typical parameters of the SGS junctions, the Josephson penetration depth is only a few micrometres. However, the ideal Fraunhofer-like interference pattern indicates that the supercurrent is uniformly distributed even in junctions as wide as 80 μm. If we take a closer look at the

derivation of Josephson penetration depth, we can easily find that some assumptions are no longer valid for 2D coplanar Josephson junctions. Therefore, we need to find out a new expression for Josephson penetration depth for 2D coplanar junctions.

In this section we will use a similar method as in Section 2.1.6 to study pure 2D junctions. As shown in Figure 8.1, we define such a pure 2D junction to be one in which the supercurrent only exists in the plane of $y = 0$. The supercurrent is evenly distributed between $x = -W/2$ and $x = W/2$, with a surface current density of j_{2D} (with a unit of ampere per metre). To simplify the model, we also assume that the supercurrent extends to infinity along the z direction. The differential equation that governs the local gauge invariant phase difference φ is the same as Eq. (2.27):

$$\frac{\partial^2 \varphi}{\partial x^2} = -\frac{2\pi(t + 2\lambda_L)}{\Phi_0}\frac{\partial B_y}{\partial x} \tag{8.1}$$

where *t* is now the length of the junction, λ_L is the London penetration depth and B_y is the *y*-component of the magnetic field generated by the supercurrent. Note that here λ_L refers to the characteristic length that the magnetic field enters the superconducting electrode. For superconducting films thinner than λ_L, this characteristic length should be replaced by the Pearl length $\Lambda = \lambda_L^2/d$, where d is the thickness of the superconducting film. Since the superconducting electrode in our junctions are thicker than λ_L, it is still valid to use λ_L in Eq. (8.1) and in the following discussion. Thus, the only difference between the pure 2D model and the 3D model relates to the magnetic field B_y. In the 3D model, we can assume the junction is infinitely long in the y direction, so that $\partial B_y/\partial x$ can be simply derived from the 4th Maxwell equation. However, in the pure 2D model, the assumption above is no longer valid. The magnetic field B_y at a given position on the $y = 0$ plane is only related to the *x* coordinate, and can be calculated by integrating the contributions

of a series of line currents

$$B_y(x) = -\int_{-W/2}^{W/2} \frac{\mu_0 j_{2D}}{2\pi(x-x')} dx' = \frac{\mu_0 j_{2D}}{2\pi} \ln\left|\frac{x-W/2}{x+W/2}\right| \tag{8.2}$$

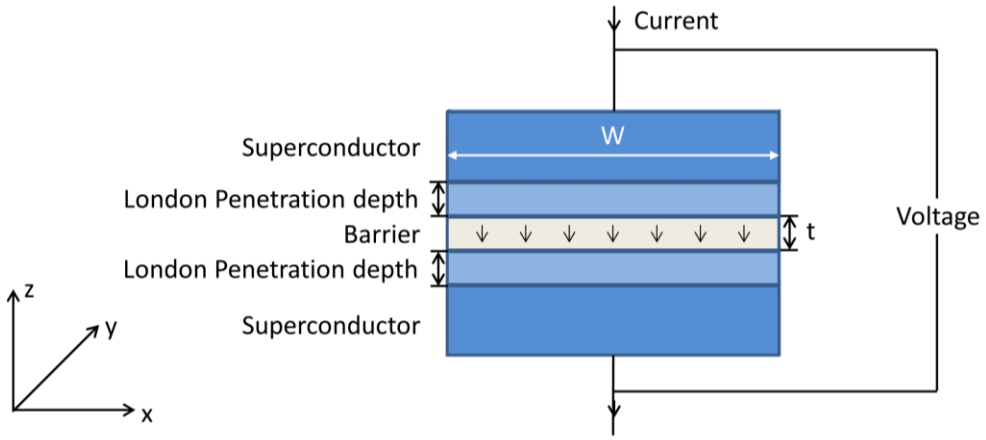

Figure 8.1 Schematic diagram of a pure 2D Josephson junction. The thickness of the junction in the *y* direction is infinitely small. For quasi-2D Josephson junctions considered in Section 8.1.2, the thickness is instead comparable to a single atomic layer.

We then differentiate B_y with respect to x,

$$\frac{\partial B_y}{\partial x} = -\frac{\mu_0 j_{2D}}{2\pi}\left(\frac{1}{x+W/2} - \frac{1}{x-W/2}\right) = \frac{\mu_0 j_{2D} W}{2\pi(x+W/2)(x-W/2)} \tag{8.3}$$

Substituting Eq. (8.3) into Eq. (8.1), we have

$$\frac{\partial^2 \varphi}{\partial x^2} = \frac{(t+2\lambda_L)W}{\Phi_0(W/2+x)(W/2-x)} \mu_0 j_{0,2D} \sin\varphi \tag{8.4}$$

where $j_{0,2D}$ is the surface critical current density. The parameter in front of $\sin\varphi$ on the right side is a washbowl-shaped function of x, which can be regarded as the sum of two inversely proportional functions. The bottom of the washbowl shape is rather flat, with its minimum value $2\mu_0 j_{2D}/\pi W$, reached in the middle of the junction $x = 0$.

In such a pure 2D model, the parameter in front of $\sin\varphi$ is no longer a constant, so even though we can similarly introduce a Josephson penetration depth λ_J to characterise the variation of φ over x, λ_J will be a function of x itself:

$$\lambda_J = \sqrt{\frac{\Phi_0(W/2+x)(W/2-x)}{\mu_0 j_{0,2D}(t+2\lambda_L)W}} \tag{8.5}$$

What's more, λ_J will be zero at the edges of the surface current, $x = -W/2$ and $x = W/2$, which means the supercurrent will only flow at the very edges. That's a reasonable inference based on the pure 2D model, because at the two boundaries, the magnetic field generated by the line current very close to it will have no counterpart to cancel out, resulting in an infinite magnetic field and an infinite derivative of the magnetic field. Therefore, the second order derivative of φ is infinitely large. However, to describe real quasi-2D coplanar junctions such as the SGS junctions in our experiment, we need to build a more meticulous model that includes the thickness of the graphene which we term a quasi-2D model.

8.1.2 Josephson Penetration Depth for Quasi-2D Junctions

For the SGS junctions we fabricated on mono-layer graphene, we expect the supercurrent flows in a layer with a finite thickness d comparable to the single

atomic layer, which is a few angstroms. So in the quasi-2D model, we assume that the supercurrent is evenly distributed in a rectangular cross-section with width W and thickness d, with a current density of $j_{2\mathrm{D}} = j_{3\mathrm{D}}d$. To simplify the model, we also assume that the supercurrent extends to infinity along the z direction.

In this model, we can similarly calculate the magnetic field B_y in a given position on the $y = 0$ plane. This time the integration is done in both x and y directions within the rectangular domain:

$$B_y(x) = -\int_{-W/2}^{W/2}\int_{-d/2}^{d/2} \frac{\mu_0 j_{2\mathrm{D}}}{2\pi d\sqrt{(x-x')^2+y'^2}} \frac{(x-x')}{\sqrt{(x-x')^2+y'^2}}\, dy'\, dx'$$

$$= -\frac{\mu_0 j_{2\mathrm{D}}}{2\pi d}\int_{-W/2}^{W/2}\int_{-d/2}^{d/2} \frac{x-x'}{(x-x')^2+y'^2}\, dy'\, dx'$$

$$= -\frac{\mu_0 j_{2\mathrm{D}}}{\pi d}\int_{-W/2}^{W/2} \arctan\left[\frac{d}{2(x-x')}\right] dx'$$

$$= -\frac{\mu_0 j_{2\mathrm{D}}}{\pi d}\left\{\frac{d}{4}\ln\frac{d^2+4\left(x+\frac{W}{2}\right)^2}{d^2+4\left(x-\frac{W}{2}\right)^2} - \left(x-\frac{W}{2}\right)\arctan\left[\frac{d}{2\left(x-\frac{W}{2}\right)}\right] + \left(x+\frac{W}{2}\right)\arctan\left[\frac{d}{2\left(x+\frac{W}{2}\right)}\right]\right\} \tag{8.6}$$

Differentiating with respect to *x* yields

$$\frac{\partial B_y}{\partial x} = -\frac{\mu_0 j_{2D}}{\pi d}\left\{\arctan\left[\frac{d}{2(x+W/2)}\right] + \arctan\left[\frac{d}{2(x-W/2)}\right]\right\} \tag{8.7}$$

It is lucky to have a simple analytical expression for $\partial B_y/\partial x$ as above even for such a more complicated model.

If $x = -W/2$ or $x = W/2$,

$$\frac{\partial B_y}{\partial x} \approx -\frac{\mu_0 j_{2D}}{\pi d}\left(\frac{\pi}{2} + \frac{d}{2W}\right) \approx -\frac{\mu_0 j_{2D}}{2d} \tag{8.8}$$

which is half of the constant value in the 3D model.

If $x = 0$,

$$\frac{\partial B_y}{\partial x} = -\frac{2\mu_0 j_{2D}}{\pi d}\arctan\left(\frac{d}{W}\right) \approx -\frac{2\mu_0 j_{2D}}{\pi W} \tag{8.9}$$

which is exactly the same as in the pure 2D model.

That provides us the key to understand the Josephson penetration depth in the quasi-2D junction. It will be similar to the pure 2D model when far away from the boundaries, and will converge to half of the finite constant of the 3D model when approaching the boundary, as shown in Figure 8.2.

In Figure 8.2, for clearness, we overestimate the value of d, so that the constant $2\pi/d$ is not too high compared with the washbowl. If we consider the actual ratio of W and d, the red curve will be much higher than the bottom of the blue curve, so that the blue curve will almost coincide with the axes. The point where the 3D model and the pure 2D model cross is significant, as it shows in how large a range $1/\lambda_J^2$

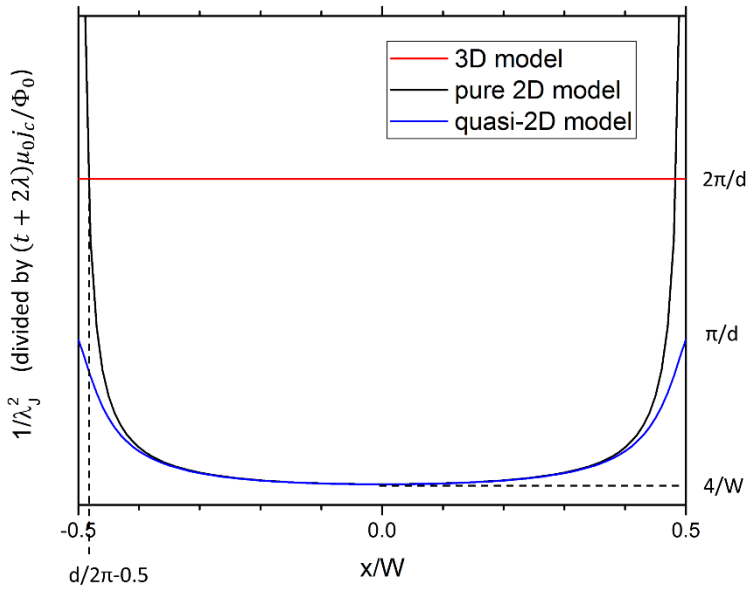

Figure 8.2 A comparison of $1/\lambda_J^2$ in the three different models, with a given W/d ratio of 10. The ratio of W/d is underestimated to show the three models more clearly.

will stay at a relatively high value in the quasi-2D model. The crossing point is approximately $d/2\pi$ away from the edge, which is in the same order of magnitude as the thickness d. In other words, for the quasi-2D model, the local gauge invariant phase difference across the junction φ will decay at half rate as in the 3D model with respect to x, only within a tiny range comparable to the thickness of the supercurrent close to the boundary. In the much wider range in the middle of the junction, the decay rate is not a constant, but keeps at a much lower value compared with the boundary. In fact, since the decay rate doesn't change very quickly with x, we can roughly define the Josephson penetration depth using the minimum decay rate in the middle of the junction:

$$\lambda_{\mathrm{J}} = \sqrt{\frac{\Phi_0 W}{4\mu_0 j_{0,2\mathrm{D}}(t + 2\lambda_{\mathrm{L}})}} \tag{8.10}$$

As a comparison, we rewrite the Josephson penetration depth of the 3D model using the same definition of surface critical current density as in the 2D models:

$$\lambda_{\mathrm{J}} = \sqrt{\frac{\Phi_0 d}{2\pi\mu_0 j_{0,2\mathrm{D}}(t + 2\lambda_{\mathrm{L}})}} \tag{8.11}$$

For typical SGS junctions we fabricated, the length $t = 50$ nm, the width $W = 80$ μm, the critical current density $j_{0,2\mathrm{D}} = 0.1$ A/m, the London penetration depth $\lambda_{\mathrm{L}} = 37.5$ nm. The thickness of the supercurrent can be assumed to be $d = 0.3$ nm, which is the interlayer distance of graphite crystal. Substituting these values to the expressions above, the 3D Josephson penetration depth is 2.5 μm, while the quasi-2D Josephson penetration depth is 1.6 mm, a thousand times as in the 3D model. That means although φ has a relatively short characteristic length at the boundary, such a high decay rate only exists in range of ~0.1 nm, so the total change of φ accumulated in this range is still very small. In the much wider range in the middle of the junction, φ is decaying with a characteristic length of 1.6 mm. So the effect of magnetic field generated by the supercurrent on φ is negligible. That explains why we can still see a conventional Fraunhofer-like pattern due to self-interference, even for junctions as wide as 80 μm.

Note that for the quasi-2D model, the Josephson penetration length is a function of junction width *W*. By setting the Josephson penetration depth equal to the width

$$\lambda_J = \sqrt{\frac{\Phi_0 W}{4\mu_0 j_{0,2D}(t + 2\lambda_L)}} = W \tag{8.12}$$

we find $W \approx 30$ mm, which means the junction must be as wide as 3 cm to show the effect of the magnetic field generated by the supercurrent. Such a size is impractically large for the SGS junctions we developed.

8.1.3 Josephson Penetration Depth for Finite-size 3D Junctions

It is worth noticing that the quasi-2D model above doesn't require $d \ll W$. If we no longer assume $d \ll W$, the quasi-2D model becomes a finite-size 3D model. We can tune the ratio of W/d in the model in order to see how the Josephson penetration depth gradually changes from the quasi-2D model to the 3D model, as shown in Figure 8.3. In the most extreme case where the d is infinitely large (shown as the pink line in Figure 8.3),

$$\frac{\partial B_y}{\partial x} = -\frac{\mu_0 j_{2D}}{\pi d}\left\{\arctan\left[\frac{d}{2(W-x)}\right] + \arctan\left(\frac{d}{2x}\right)\right\} \approx -\mu_0 j_{3D} \tag{8.13}$$

which reduces to the 3D model we discussed in Section 2.1.6. Here $j_{3D} = j_{2D}/d$ is the usual current density (same as j used in Chapter 2), with a unit of ampere per square metre. It is worth noticing that for 3D junctions with a square-shaped cross-section ($W/d = 1$, shown as the black line in Figure 8.3), $1/\lambda_J^2$ is only about 60% of the value predicted by the 3D model. That means for 3D junctions with a square-shaped cross-section, 3D model overestimates the variation of φ so that the Josephson penetration depth calculated by Eq. (2.30) is underestimated. Therefore, for

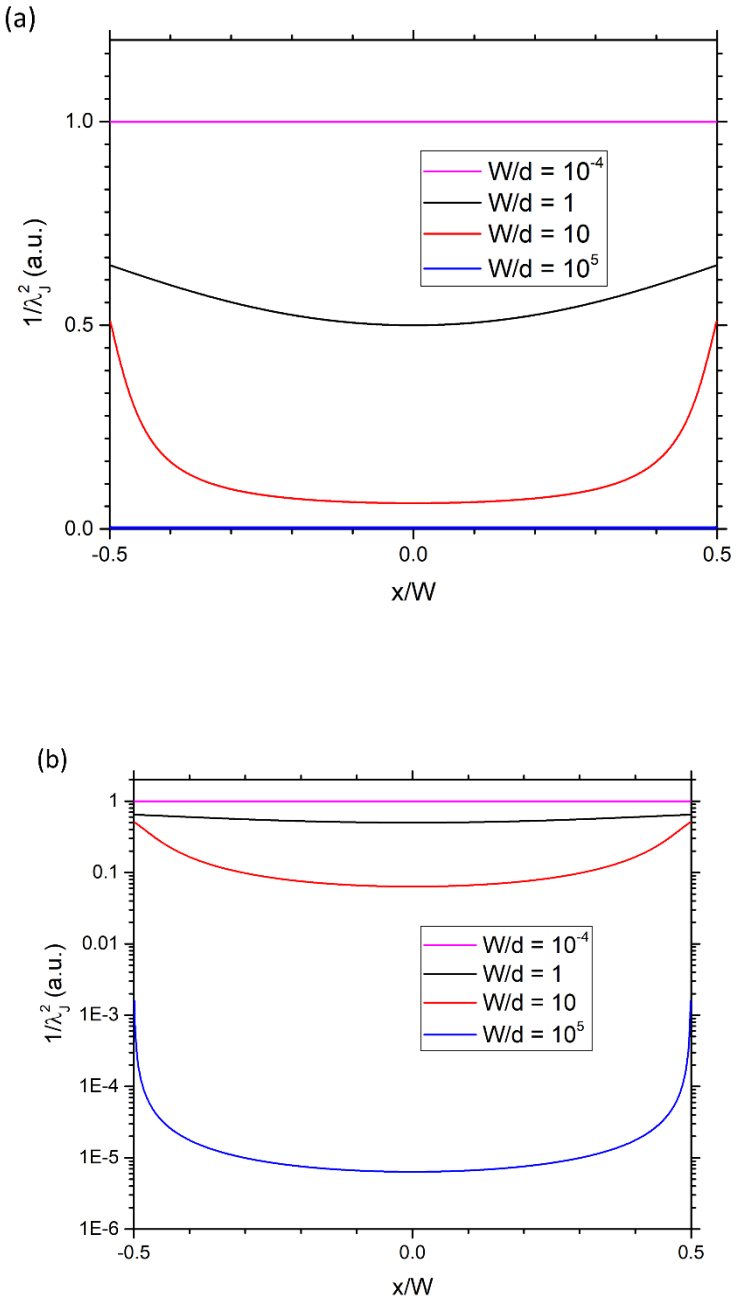

Figure 8.3 A comparison of $1/\lambda_J^2$ in the quasi-2D model, with different W/d ratios, in (a) linear scale and (b) log scale respectively. The blue curve (W/d=10^5) is the closest to the SGS junction, which can hardly be seen in the linear scale plot. Note that this comparison assumes the same critical current density per unit area for each case.

finite-size 3D junctions (which include most of the practical sandwich junctions), we recommend using the Josephson penetration depth defined as

$$\lambda_{\mathrm{J}} = \sqrt{\frac{\Phi_0 W}{4\mu_0 j_{0,3\mathrm{D}} d(t + 2\lambda_{\mathrm{L}})}} \tag{8.14}$$

which takes the ratio of W/d into consideration. It is worth mentioning that a similar redefinition of the Josephson penetration depth has been provided for planar thin-film high-T_c Josephson junctions [147]. However, in the case of thin-film high-T_c Josephson junctions, the thickness of the superconducting film is usually comparable with or smaller than the London penetration depth, so that the magnetic field generated by the supercurrent is dominated by the kinetic inductance. For Josephson junctions based on 2D materials such as graphene, the thickness of the superconducting electrodes is normally higher than the London penetration depth, so that the magnetic field generated by the supercurrent is still dominated by the geometric inductance as we considered above. That's why the expression for Josephson penetration depth proposed in Ref. [147] is not appropriate for junctions based on 2D materials.

8.2 Numerical Calculation of the Gauge Invariant Phase Difference φ

8.2.1 The Differential Equations and the Boundary Conditions

In the previous section, we have worked out a new expression for the Josephson penetration depth that works for 2D coplanar junctions as well as 3D junctions with

finite thickness. In this section, I will visualise the distribution of gauge invariant phase difference φ along the coordinate x, by numerically solving the differential equations in MATLAB. Here we rewrite the difference equation satisfied by φ in both the 3D model and the quasi-2D model.

For the 3D model, the differential equation of the phase difference φ is

$$\frac{\partial^2 \varphi}{\partial x^2} = \frac{2\pi(t + 2\lambda_{\mathrm{L}})}{\Phi_0} \mu_0 j_{0,3\mathrm{D}} \sin\varphi \tag{8.15}$$

where $j_{0,3\mathrm{D}}$ is the usual critical current density (same as j_0 used in Chapter 2).

For the quasi-2D model, the differential equation of the phase difference φ is

$$\frac{\partial^2 \varphi}{\partial x^2} = \frac{2(t + 2\lambda_{\mathrm{L}})\mu_0 j_{0,2\mathrm{D}}}{\Phi_0 d} \left\{ \arctan\left[\frac{d}{2(W/2 - x)}\right] + \arctan\left[\frac{d}{2(W/2 + x)}\right] \right\} \sin\varphi \tag{8.16}$$

For either model, to solve φ as a function of x, we also need a pair of boundary conditions for φ and $\partial\varphi/\partial x$ at either boundary. This is not a trivial question as each pair of boundary conditions selected will correspond to a distribution of φ over x. The supercurrent, which is the integration of the supercurrent density (which is related to the phase difference by the first Josephson relation) over the junction width, is then a function of the boundary conditions we selected. As we are more interested in the critical current, we need to maximise the supercurrent over all allowed boundary conditions. Therefore, there is no straightforward method to determine the boundary conditions that corresponds to the critical current.

We first consider the cases ignoring the magnetic field generated by the

supercurrent. When there is no external magnetic field, the phase difference is a constant over the junction width, so the critical current corresponds to a constant $\varphi = \pi/2$ all over the junction.

Once there exists a perpendicular external magnetic field $B = B_y$, the $\varphi(x)$ curve would be linear

$$\frac{\partial \varphi}{\partial x} = -\frac{2\pi B(t + 2\lambda_{\mathrm{L}})}{\Phi_0} \tag{8.17}$$

In this case, the boundary condition corresponding the critical current would be $\varphi = \pm\pi/2$ at the middle point of the junction.

These two cases above have guided us that, for a $\varphi(x)$ distribution that only changes slightly with x, the $\varphi(x = 0)$ should be close to $\pi/2$ to reach the critical current. To see how φ changes with x as an effect of the magnetic field generated by the supercurrent, a good pair of boundary condition to start with is

$$\begin{aligned} \varphi|_{x=0} &= \pi/2 \\ \left.\frac{\partial \varphi}{\partial x}\right|_{x=0} &= 0 \end{aligned} \tag{8.18}$$

In the second boundary condition, $\partial\varphi/\partial x$ is set to be zero as the external magnetic field is zero. Both boundary conditions are set at $x = 0$, the middle point of the junction, so they are not really "boundary conditions". We would solve the differential equation in $0 \le x \le W/2$, and $-W/2 \le x \le 0$, respectively. Note again that solution of $\varphi(x)$ under this set of boundary conditions is not the one that can reach the critical current, but will be very close to it if the junction width is smaller than the Josephson penetration depth. Thus it is a good starting point to study the dependence

of φ on x.

8.2.2 The 3D Model

To numerically solve Eq. (8.15) under the boundary conditions Eq. (8.18), I wrote a simple MATLAB script to calculate $\varphi(x)$ in the range of $0 \le x \le W/2$ and $-W/2 \le x \le 0$, using the built-in function "ode45", as shown in Appendix B.

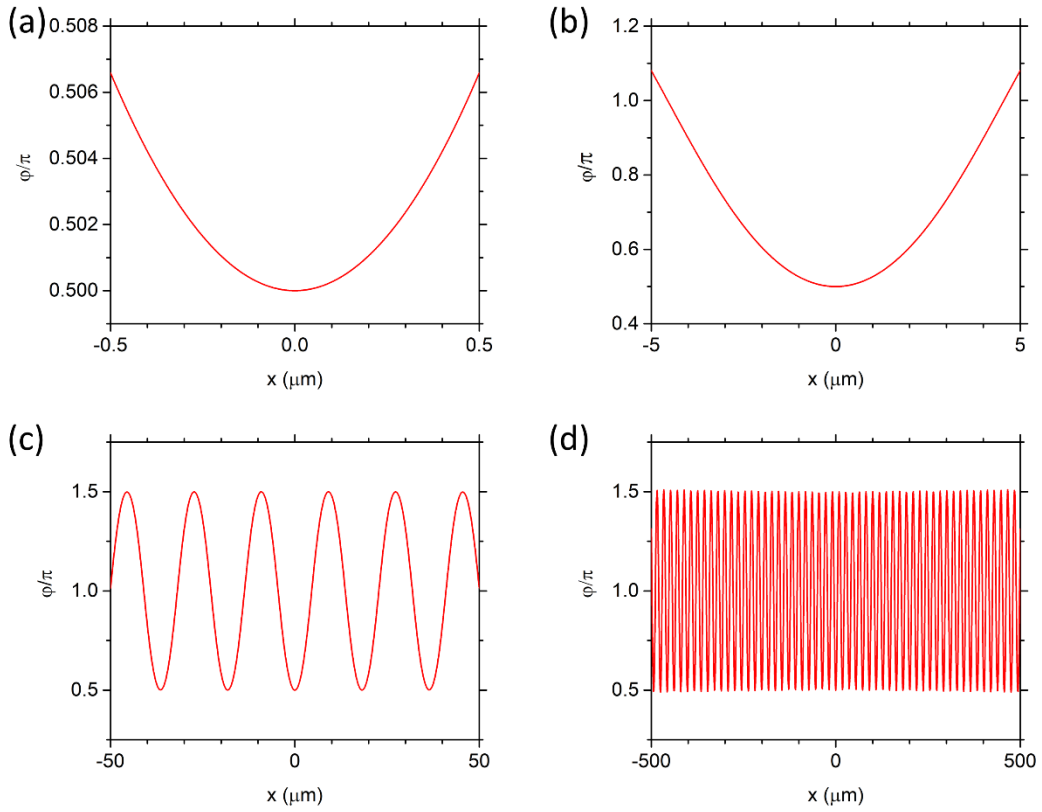

Figure 8.4 The phase difference φ along the junction width, numerically calculated based on the 3D model. The four plots corresponding to junctions with different widths. Note the difference in the scale of φ. (a)-(d) are for junctions with widths increasing from 1 μm to 1 mm by factors of ten respectively.

The parameters in the script are chosen as typical values of the SGS junctions. By

varying the width of the junction, we can see how the phase difference φ changes within different junction width scales, as shown in Figure 8.4. For a junction as wide as 1 μm, the variation of φ caused by the magnetic field of the supercurrent is negligible, while for junctions as wide as 10 μm, the variation of φ is large enough to be considered. That indicates the Josephson penetration depth should be several μm, which is consistent with the value we calculated from Eq. (8.11), which is 2.5 μm. For junctions with widths much larger than the Josephson penetration depth, φ will oscillate around π with a period several times larger than the Josephson penetration depth.

8.2.3 The Quasi-2D Model

Similar to the 3D model, I wrote another MATLAB script to calculate $\varphi(x)$ for the quasi-2D model, to numerically solve Eq. (8.16) under the boundary condition Eq. (8.18), as shown in Appendix B.

By varying the width of the junction, we can see how the phase difference φ changes within different junction width scales, as shown in Figure 8.5. Note that for the quasi-2D model, the differential equation contains the width of the junction W. Thus, for every different junction width, we are solving differential equations with different parameters. For junctions less than 10 mm, the variation of φ along the junction width is tiny. The variation of φ becomes non-negligible for 100-mm-wide junctions. This is consistent with the value we derived for λ_J from Eq. (8.12), which is 30 mm. For even wider junctions, φ would oscillate around π. The amplitude and the period of the oscillation get smaller when approaching the boundaries.

In summary, by numerically solving the differential equations for the two models, we have visualised the distribution of phase difference φ for junctions with different widths. Under the same junction parameters, the numerical results for 3D model and

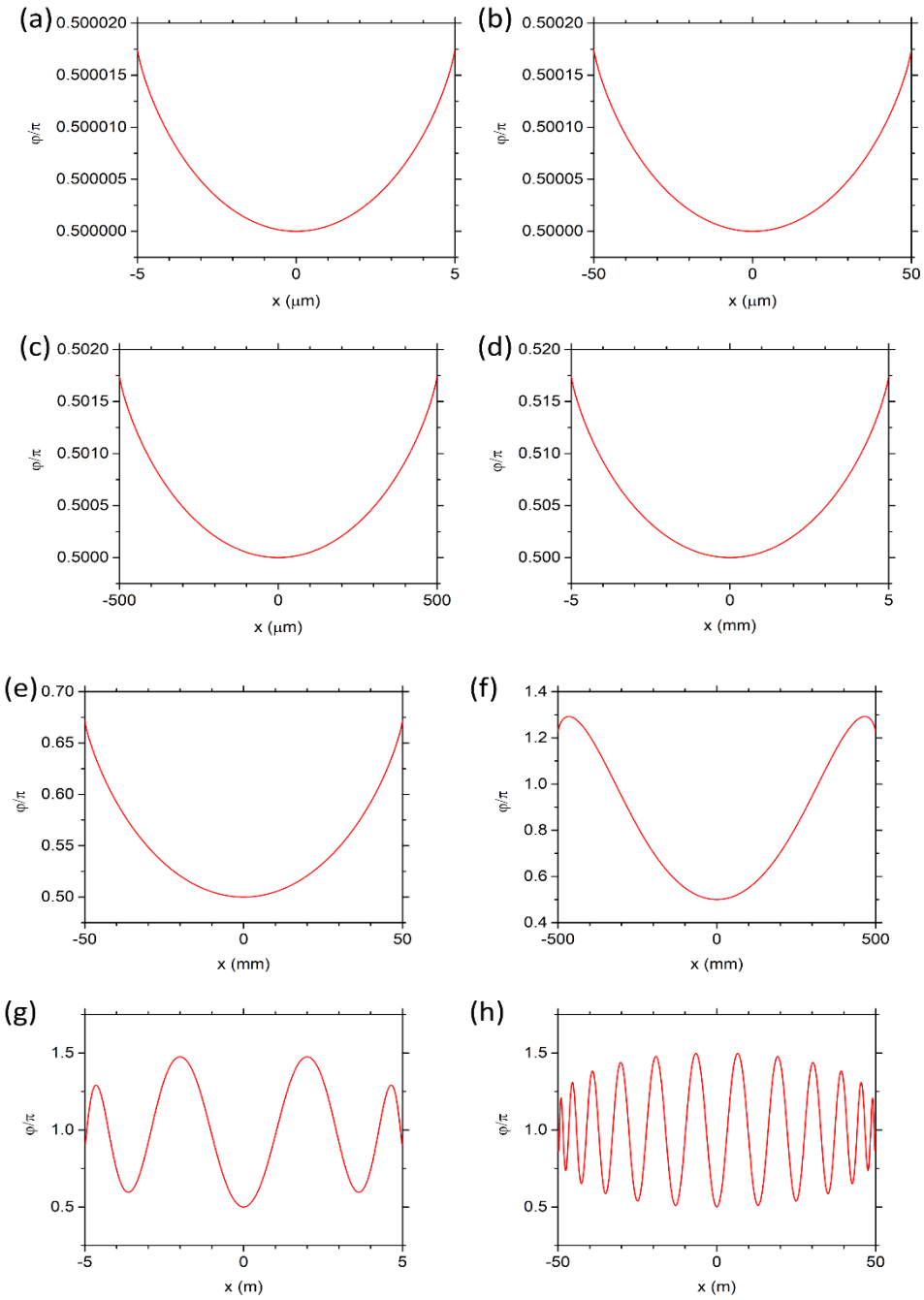

Figure 8.5 The phase difference φ along the junction width, numerically calculated based on the quasi-2D model. The eight plots correspond to junctions with different widths. Note the difference in the scale of φ. (a)-(h) are for junctions with widths increasing from 10 μm to 100 m by factors of ten respectively.

quasi-2D model each agree with corresponding Josephson penetration depth given by the analytical results in the last section.

8.3 The Effect on the Interference Pattern

8.3.1 The Interference Pattern Considering only the External Magnetic Field

The analytical study in Section 8.1 and the numerical study in Section 8.2 both show that the Josephson penetration depth is larger than any reasonable junction width. On the one hand, it means we don't need to worry about the effect of Josephson penetration depth on the distribution of the supercurrent; on the other hand, it means that it is difficult to really fabricate a junction with its width longer than the Josephson penetration depth and experimentally study the effect on the interference pattern. Numerical simulation becomes the only way to study how the interference pattern varies when the junction width is larger than the penetration depth. In this section, we will numerically simulate the interference patterns for junctions with different widths, varying from ones much smaller than the Josephson penetration depth to ones much larger than the Josephson penetration depth.

To draw the $I_0(\Phi)$ curve, we need to find out the maximum allowed supercurrent under a given external magnetic field. To numerically find out the maximum supercurrent, we need to sweep the boundary condition $\varphi(x=0)$ from 0 to 2π, and calculate the supercurrent under each boundary condition. In the programming language, we need to add two nested loops outside the solution of the differential equations under a given boundary condition. The inner loop is to sweep the boundary condition $\varphi(x=0)$ from 0 to 2π, while the outer loop is to sweep the external magnetic field within a range of interest.

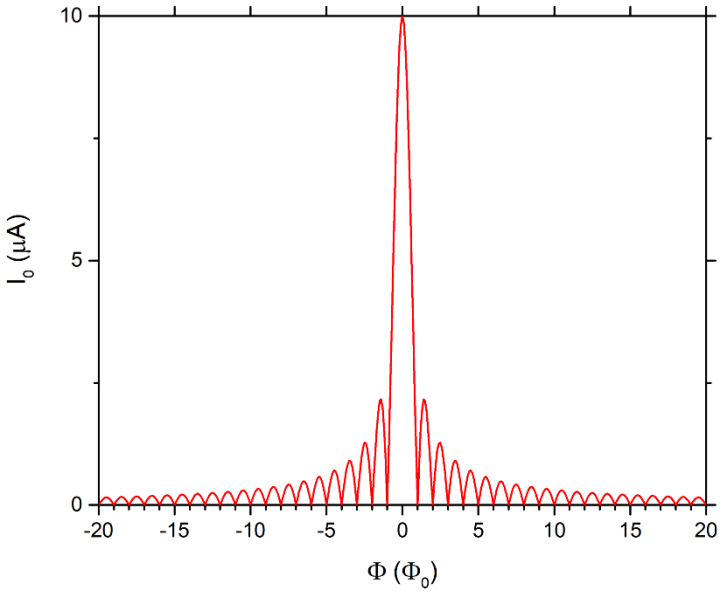

Figure 8.6 The interference pattern numerically calculated by considering the external magnetic field only.

To test that such an algorithm is reliable, we first consider the case ignoring the magnetic field generated by the supercurrent. In Section 8.2.1, we have shown that in this case, the critical current is reached when $\varphi|_{x=0} = \pm\pi/2$. However, to test the algorithm, we still sweep the boundary condition $\varphi(x = 0)$ from 0 to 2π in the MATLAB script (shown in Appendix C).

The interference pattern we obtained by this program is shown in Figure 8.6. It is an ideal Fraunhofer-like pattern, which means the algorithm works well. So we are confident to use the same algorithm to calculate the interference pattern when considering the magnetic field generated by the supercurrent.

8.3.2 The 3D Model

For each model, when we consider both the external magnetic field and the magnetic

field generated by the supercurrent, the differential equation to be solved is still the same as Eq. (8.15). That's because for a uniform external magnetic field, the contribution from the external magnetic field to $\partial B_y/\partial x$ is zero. The first boundary condition $\varphi(x=0)$ is to be swept from 0 to 2π, while the second boundary condition is chosen to be

$$\left.\frac{\partial \varphi}{\partial x}\right|_{x=0} = -\frac{2\pi B(t+2\lambda)}{\Phi_0} \tag{8.19}$$

This boundary condition is valid since in the first-order approximation, we only consider the magnetic field generated by evenly distributed supercurrent. In other words, we haven't taken into consideration the redistributed supercurrent and magnetic field generated by it. We will discuss the closed-loop simulation that takes this into consideration in Section 8.4.

The MATLAB script written in this case (shown in Appendix C) is similar to that in the last subsection, except the method to calculate the distribution of $\varphi(x)$. The script calls the function "ode45" thousands of times.

The interference pattern we obtained by this program is shown in Figure 8.7. We have set the junction width as a series of values close to the Josephson penetration depth, in order to see how the Josephson penetration depth affects the interference pattern. As the junction width becomes comparable with or larger than the Josephson penetration depth, the first few minima of the interference pattern does not reach zero. Another feature for wide junctions is that the central peak fails to increase linearly with the junction width.

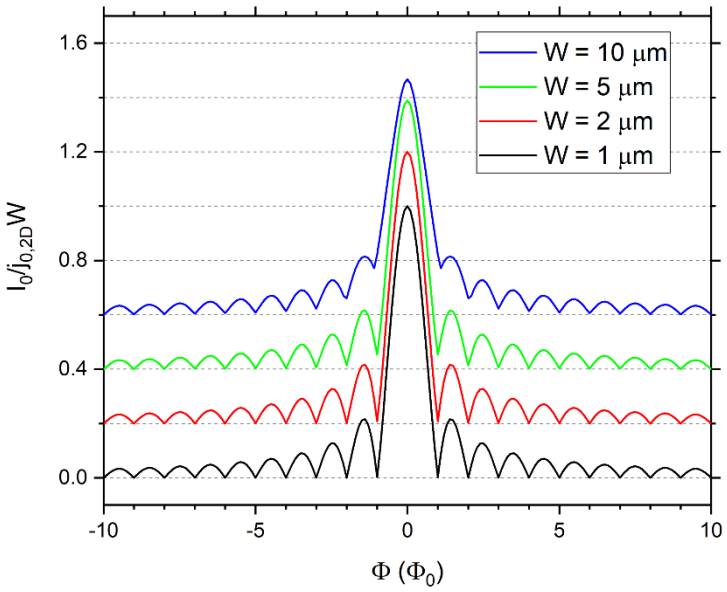

Figure 8.7 The interference pattern numerically calculated by the 3D model. The curves correspond to junctions with different widths. The critical current is normalised by the critical current density times the junction width. For clarity, each curve is offset by 0.2 along the y-axis. The Josephson penetration depth for the same parameters (critical current density, junction length and London penetration depth) calculated by Eq. (8.11) is 2.5 μm.

8.3.3 The Quasi-2D Model

We can do similarly using the quasi-2D model, expect that the interesting junction width is much larger. The MATLAB script is also shown in Appendix C.

The interference pattern calculated by the script above is plotted in Figure 8.8. Again, for the junction with a width comparable to the Josephson penetration depth, the interference pattern is still quite close to the ideal Fraunhofer-like pattern. When the junction width far exceeds the Josephson penetration depth, the first few minima

of the interference pattern does not reach zero.

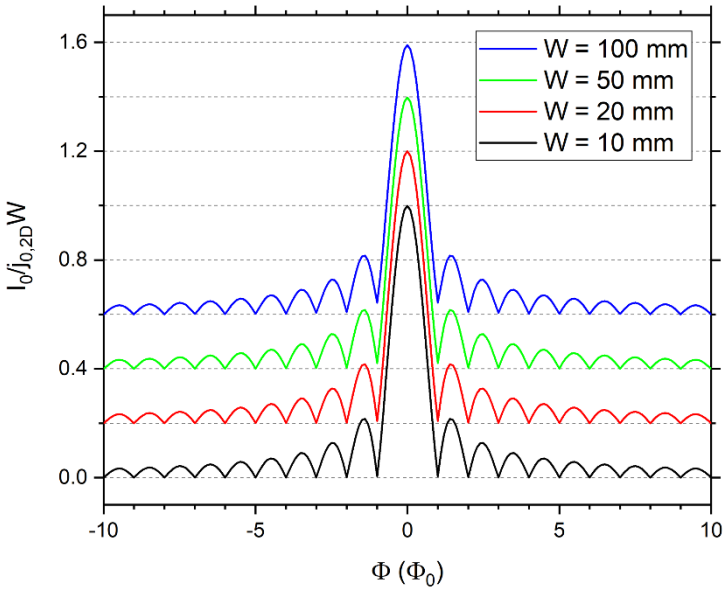

Figure 8.8 The interference pattern numerically calculated by the quasi-2D model. The curves correspond to junctions with different widths. The critical current is normalised by the critical current density times the junction width. For clarity, each curve is offset by 0.2 along the y-axis. For the same parameters (critical current density, junction length and London penetration depth), the junction width needs to be larger than 30 mm to be larger than Josephson penetration depth, as calculated by Eq. (8.12).

In summary, by numerical calculation, we have shown how the Josephson penetration depth would affect the interference pattern for the two models. For the 3D model, the Fraunhofer-like pattern is obviously disrupted when the junction is as wide as several micrometres; while for the quasi-2D model, this number is tens of millimetres. The order of magnitude of the widths again coincide with the analytical study in Section 8.1. The simulation has shown us that for junctions fabricated with

current techniques, the interference pattern should always be an ideal Fraunhofer-like pattern with almost no visible deviation. However, it is still of fundamental interest to find out how the interference pattern will deviate from the Fraunhofer-like pattern once the junction width is comparable with or larger than the Josephson penetration depth.

8.4 Closed-Loop Simulation of the Effect of Josephson Penetration Depth

8.4.1 The Concept of Closed-Loop Simulation

In the simulation in the last section, we only considered the magnetic field generated by evenly distributed supercurrent. However, once we obtained the distribution of the phase difference $\varphi(x)$, we could then acquire the new distribution of supercurrent $j_s(x)$ by the first Josephson relation (Eq. (2.7)), and the new distribution is unlikely to be uniform. In real physics, the effect on $\varphi(x)$ by $j_s(x)$ and the effect on $j_s(x)$ by $\varphi(x)$ take place simultaneously and soon reach an equilibrium. In the simulation, once we obtain the new distribution of $j_s(x)$, we can iterative it back to the differential equation of $\varphi(x)$. Such a process can be repeated several times until the solution converges. By this we mean a "closed-loop simulation". In contrast, all the simulations we performed earlier didn't take the redistribution of $j_s(x)$ into consideration, which are "open-loop simulations". That's normally enough when the junction width is smaller or comparable than the Josephson penetration depth, so that the redistribution of $j_s(x)$ is not obvious. Thus, the numerical determination of Josephson penetration depth we performed in Section 8.2 is still valid, so are the interference patterns in Section 8.3 when the junction width is not too large. However, for junctions with widths much exceeding the Josephson penetration depth, such

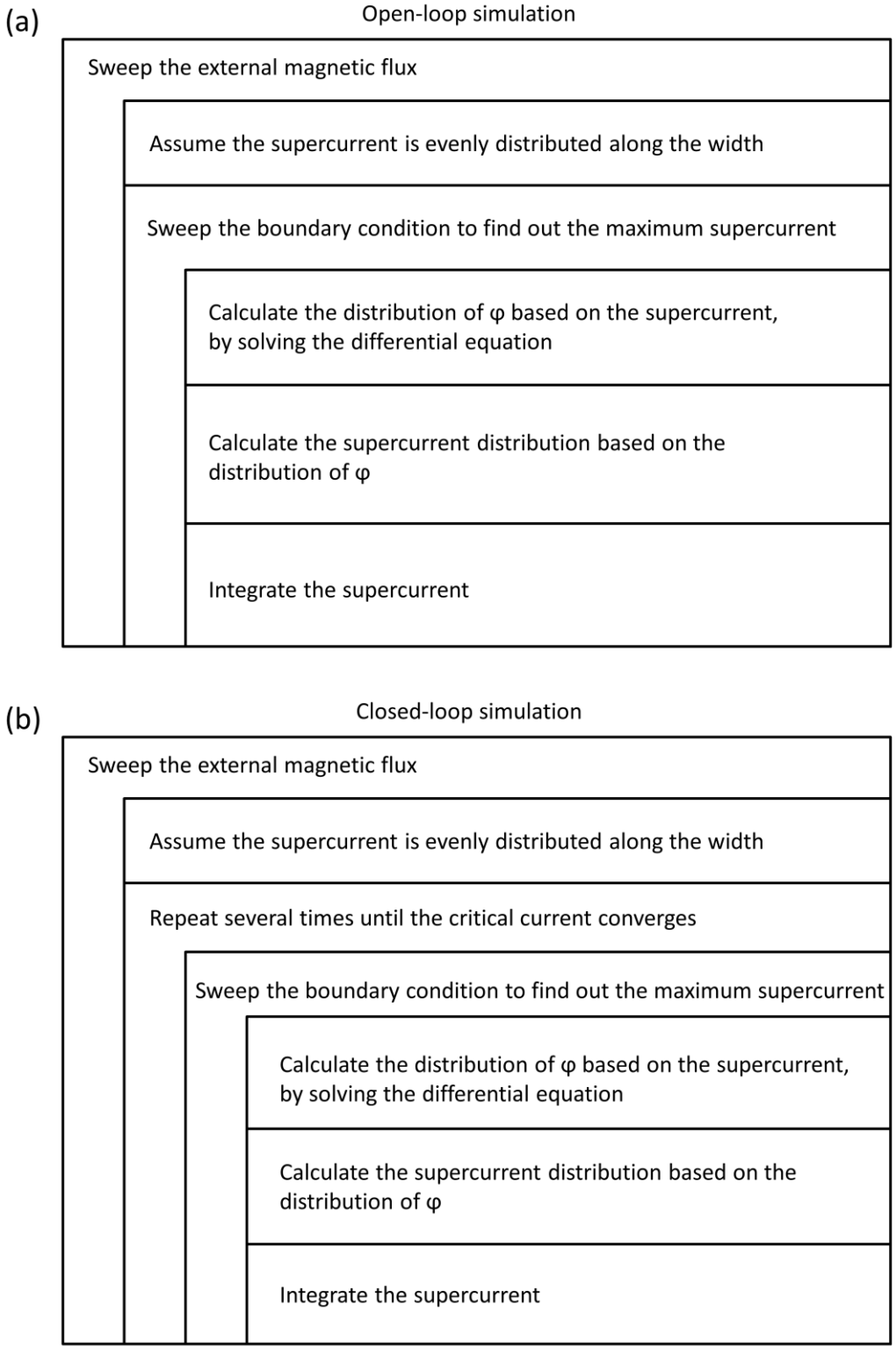

Figure 8.9 Schematic charts of (a) open-loop and (b) closed-loop simulation.

"closed-loop" simulations are necessary. The concepts of open-loop and closed-loop simulation are more clearly explained in the schematic charts in Figure 8.9.

8.4.2 The Closed-Loop Quasi-2D Model

As we have shown in the last section, in the closed-loop simulation, once the supercurrent is redistributed according to the $\varphi(x)$ obtained in the first cycle of iteration, from the second cycle of iteration, the parameters of the differential equation become functions of x. In other words, the differential equation becomes non-linear. That means we cannot use the built-in function "ode45" in MATLAB to solve the differential equation. Therefore, we have to write our own algorithm to solve the differential equation from the second cycle of iteration.

Actually, since $\partial B_y/\partial x$ cannot be expressed as a simple function of φ, we no longer need to solve the second-order differential equation. The problem can be simplified to solving the first-order differential equation

$$\frac{\partial \varphi}{\partial x} = -\frac{2\pi(B + B')(t + 2\lambda_{\mathrm{L}})}{\Phi_0} \tag{8.20}$$

where B is the external magnetic field and B' is magnetic field generated by the supercurrent obtained in the last cycle

$$B'(x) = -\frac{\mu_0 j_{0,2\mathrm{D}}}{\pi d}\int_{-W/2}^{W/2} \sin\varphi(x')\arctan\left[\frac{d}{2(x-x')}\right]dx' \tag{8.21}$$

In the MATLAB script (shown in Appendix D), the integration above is estimated by a sum of different elements while the differential equation is solved as a difference equation. Note that in the first cycle, the differential equation is still solved by the

built-in function “ode45” for better accuracy.

The maximum number of iterations is set to be 200. However, if the difference of critical current from one cycle to the previous one is smaller than $j_{0,2\mathrm{D}}W/500$, we regard that the solution has already converged and will stop the iteration earlier. As we will see, if the junction width doesn't exceed the Josephson penetration depth too much, the convergence would normally be reached within several cycles. Before we plot the converged interference pattern, let’s take an example to see how the redistribution of $\varphi(x)$ causes the redistribution of $j_{\mathrm{s}}(x)$, which once again will redistribute $\varphi(x)$, and how the solution finally converges.

Consider the case of a junction with width $W = 100$ mm under an external magnetic flux of $0.7\Phi_0$, which takes 13 cycles to converge. The distribution of $\varphi(x)$, $j_{\mathrm{s}}(x)$, and local magnetic field generated by the supercurrent $B_{\mathrm{sc}}(x)$ in each cycle are displayed in Figure 8.10.

For a given set of junction parameters, the iteration process above is repeated for every value of the external magnetic field, to acquire an $I_0(\Phi)$ interference pattern. Generally speaking, the lower the external magnetic field, the more steps it would take to converge. The larger the junction width, the longer it would take to converge. The $I_0(\Phi)$ interference patterns of a series of junction widths are shown in Figures 8.11. As shown in Figure 8.11, when the junction width is 10 mm, the $I_0(\Phi)$ interference pattern is still quite close to an ideal Fraunhofer-like pattern. As the junction width increases, the $I_0(\Phi)$ interference pattern becomes distorted from an ideal Fraunhofer-like pattern. Compared with Figure 8.8, the $I_0(\Phi)$ interference pattern obtained by closed-loop simulation is more distorted than the open-loop simulation for the same junction width. Apart from the phenomena we already observed in Figure 8.8, we can see that for a 50-mm-wide junction, a tiny peak appears around the first few minima of the interference pattern; for a 100-mm-wide

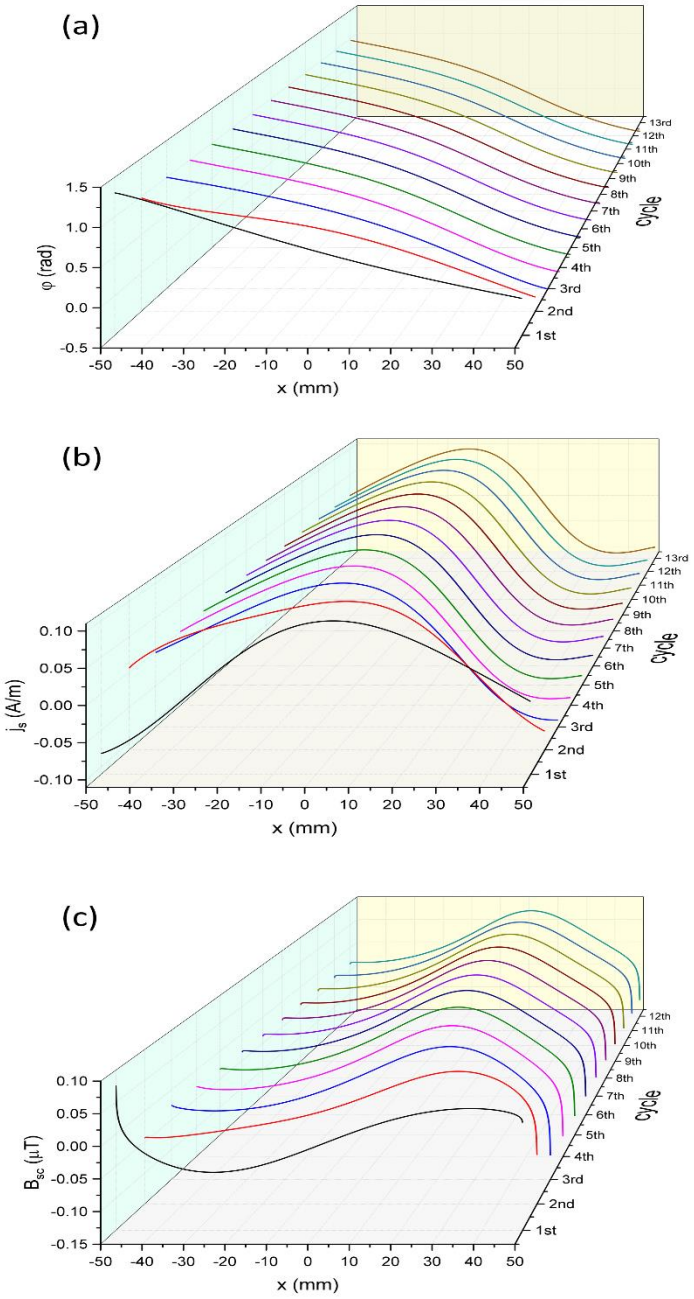

Figure 8.10 The distribution of (a) $\varphi(x)$, (b) $j_s(x)$, and (c) local magnetic field generated by the supercurrent in each cycle. The curves were simulated for a junction with width $W = 100$ mm under an external magnetic flux of $0.7\Phi_0$, using the closed-loop quasi-2D model. The first-cycle results are the same as the results in the open-loop simulation.

junction, there are almost no periodic peaks visible in the interference pattern. The trend that the interference pattern is distorted from an ideal Fraunhofer-like pattern is consistent with the Josephson penetration depth predicted in Section 8.1 (30 mm). Such a conclusion is the same as we made in the last section, however, the interference pattern predicted by the closed-loop simulation is more accurate than the open-loop simulation in the last section.

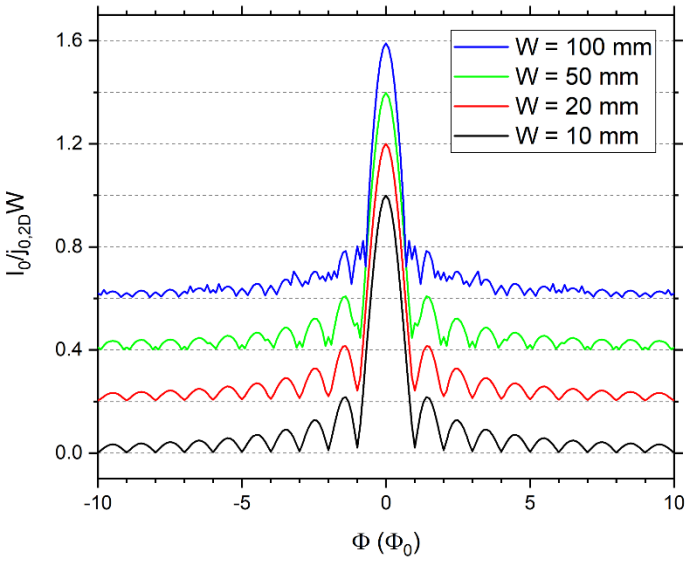

Figure 8.11 The interference pattern numerically calculated by the closed-loop qausi-2D model. The curves correspond to junctions with different widths. The critical current is normalised by the critical current density times the junction width. For clarity, each curve is offset by 0.2 along the y-axis. For the same parameters (critical current density, junction length and London penetration depth), the junction width needs to be larger than 30 mm to be larger than Josephson penetration depth, as calculated by Eq. (8.12).

8.4.3 The Closed-Loop 3D Model

Similarly, we wrote a MATLAB script for the closed-loop 3D model, as shown in Appendix D. The $I_0(\varphi)$ interference patterns are plotted in Figures 8.12 below. Again, comparing with Figure 8.7, we find that the $I_0(\Phi)$ interference pattern obtained by closed-loop simulation is more distorted than the open-loop simulation for the same junction width. The trend that the interference pattern is distorted from an ideal Fraunhofer-like pattern indicates that the Josephson penetration depth is in the range of several micrometres, which is consistent with the value predicted in Section 8.1 (2.5 μm).

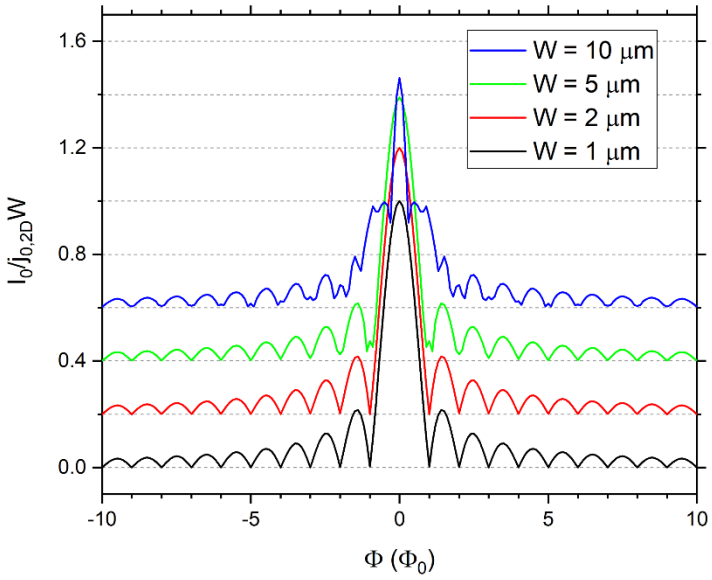

Figure 8.12 The interference pattern numerically calculated by the closed-loop 3D model. The curves correspond to junctions with different widths. The critical current is normalised by the critical current density times the junction width. For clarity, each curve is offset by 0.2 along the y-axis. The Josephson penetration depth for the same parameters (critical current density, junction length and London penetration depth) calculated by Eq. (8.11) is 2.5 μm.

8.5 Manually Induced Edge Effect on the Interference Pattern

8.5.1 Fabrication of Local Top-Gates

As we have discussed in the last few sections, both analytical and numerical studies show that the Josephson penetration depth for the 2D coplanar SGS junctions is much larger than the junction width, so that its effect can be hardly seen in any experiments. On the other hand, the large Josephson penetration depth of 2D planar junctions allows us to fabricate Josephson junctions with tiny aspect ratio ($L/W \ll 1$) that still have uniform critical current distribution. Such extremely wide junctions allow us more freedom to control the local supercurrent density by local gate electrodes. The position and width of the local gate electrodes and their individual gate voltages can be engineered, so that the critical current can show a desired and much more complicated dependence on the external magnetic field.

One of the most basic examples of such “critical current engineering” that we considered is to apply two local top-gates at the two edges of the junction, while the whole junction can be controlled by a universal back-gate. The idea is that when we tune the back-gate to reach the Dirac point of graphene, the critical current can be almost “turned off”. At that moment, if we apply a voltage on the two top-gates at the ends, only the supercurrent at the two edges can flow, and the two flows of supercurrent would have a phase difference depending on the magnetic flux inside the junction area. Essentially, by a combination of the universal gate and local gates, we can turn a wide single Josephson junction into a dc SQUID.

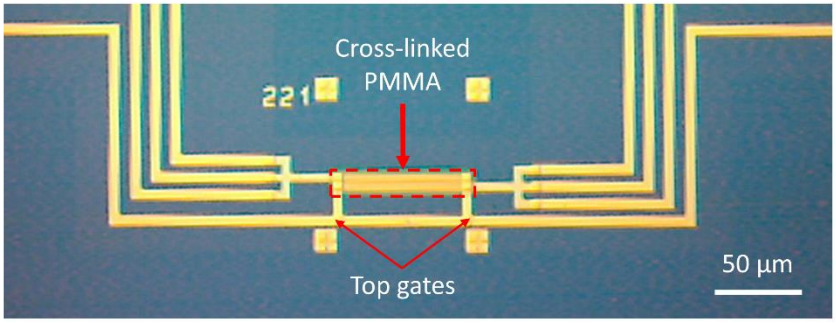

Figure 8.13 Optical microscope image of a wide SGS junction with local top-gates at the two ends. The junction width is 80 µm, while the width of the top-gates is 5 µm.

We tried to fabricate three wide SGS junctions with top-gates at the two ends (see Figure 8.13 for the optical microscope image). The insulating layer between the top-gates and the junction is made up of cross-linked PMMA. PMMA is normally used as a positive e-beam resist. However, when the dose of the e-beam is extremely high, it becomes a negative resist, i.e. the overexposed PMMA becomes cross-linked so that it cannot be removed by acetone. In our fabrication, we spin-coated 80-nm-thick PMMA 950A2, and exposed it to the e-beam with a dose as high as 15000 µC/cm^2. Such an insulating layer has been proved to withstand a voltage difference of up to ±8 V, according to literature [104]. The top-gates are made of non-superconducting Ti/Au so that they won't affect the distribution of magnetic flux. Of the three devices fabricated, only one worked well, and we obtained some interesting preliminary results.

8.5.2 Interference Patterns of SGS Junctions with Top Gates

In this section we show three interference patterns of the same device under difference gate voltage. They were all measured on the same device as shown in Figure 8.13 in a similar experimental setup as in Chapter 6. Figure 8.14 shows the interference pattern

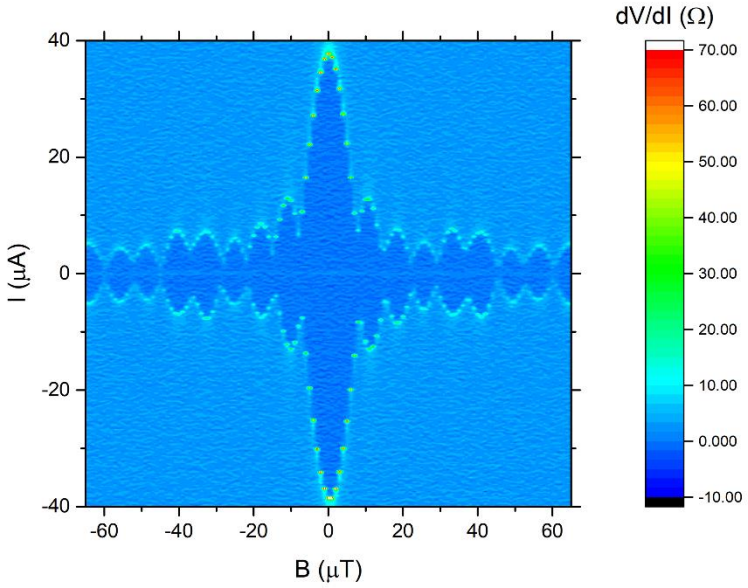

Figure 8.14 Differential resistance of a device with top gates as a function of critical current and external magnetic field, measured without gate voltage.

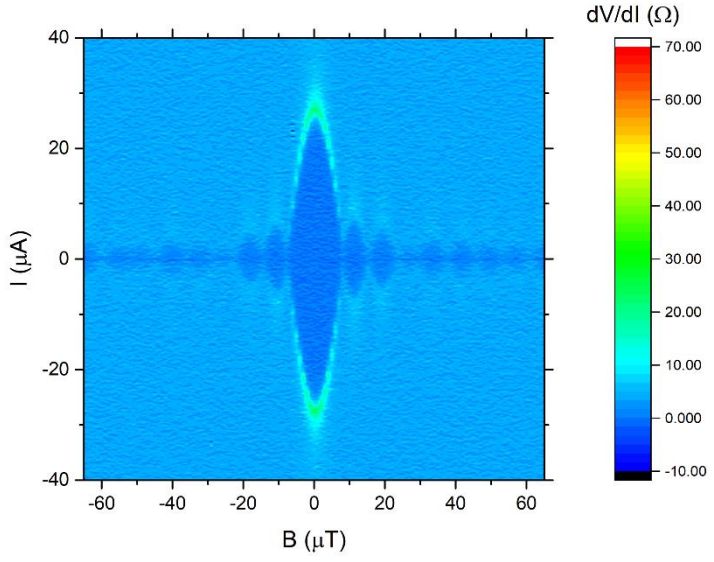

Figure 8.15 Differential resistance of a device with top gates as a function of critical current and external magnetic field, measured when the back-gate voltage is 50 V.

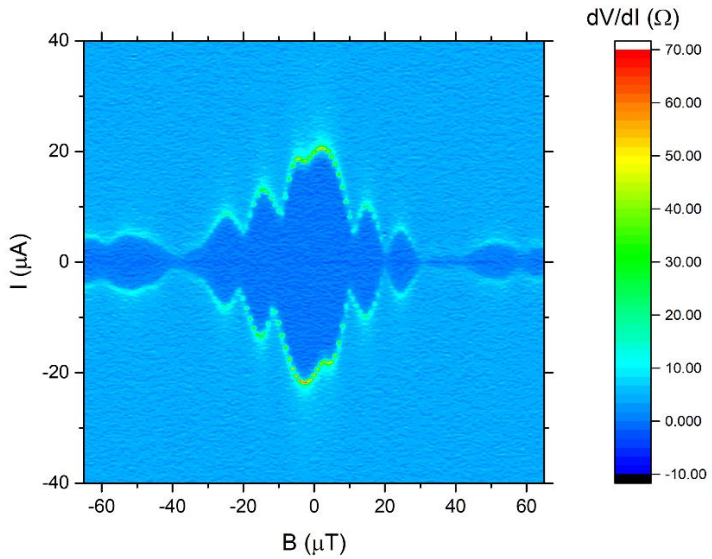

Figure 8.16 Differential resistance of a device with top gates as a function of critical current and external magnetic field, measured when the back-gate voltage is 50 V and the top-gate voltages are -8 V.

measured without either top- or back-gate. The pattern is similar to the ideal Fraunhofer-like pattern in Figure 6.7, but with some slight differences: the height of the peaks does not always decay as the absolute value of the magnetic field increases. This probably means the existence of the top-gates already destroys the uniformity of the junction somehow (for example by changing the local capacitance), even though no voltage is applied. Figure 8.15 shows the interference pattern measured when the back-gate voltage is 50 V. Normally such a voltage is not high enough to reach the Dirac point, but it risks breaking the insulating oxide layer to apply even higher voltage. We can see that the critical current is almost halved, and the interference pattern is still quite like an ideal Fraunhofer-like pattern, indicating the distribution of supercurrent is still quite uniform. Figure 8.16 shows the interference pattern measured when the back-gate voltage is 50 V and the top-gate voltages are -8 V. The insulating layer for the top-gate is only 80 nm, and the typical value of the relative

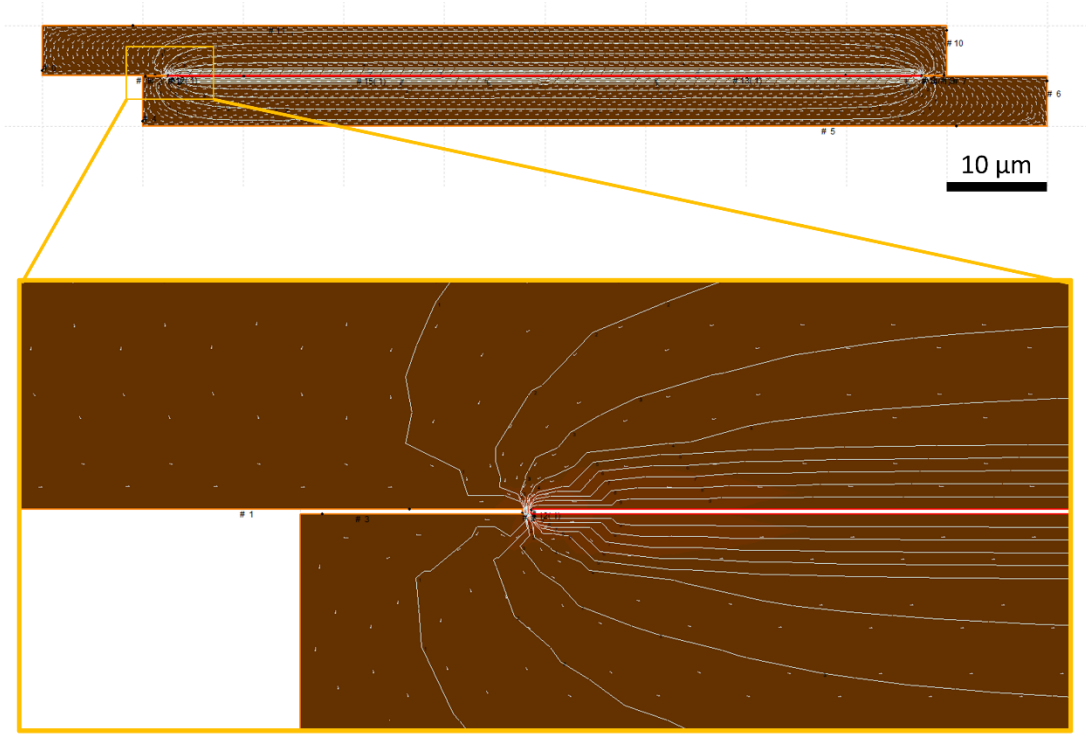

Figure 8.17 3D-MLSI model of the SQUID formed by the two Josephson junctions under the top gates. Similarly to the model shown in Figure 7.4, the two Josephson junctions are here replaced by nano-bridges, as shown in the zoom-in box.

permittivity of the PMMA layer is 3~4 [148], similar to the permittivity of silicon oxide. So the capacitance per unit area between the top gate and the graphene is about 4 times larger than the capacitance per unit area between the bottom gate and the graphene. Therefore, although the top-gate voltage is only -8 V, its ability to tune the Fermi level should be comparable with the bottom-gates. The interference pattern in Figure 8.16 consists of many asymmetrically located peaks, and the valleys between the peaks do not reaches zero. If we consider the two branches of current under the top gates forming a dc SQUID, we can estimate the self-inductance of the "SQUID" loop by running finite-element simulation in 3D-MLSI similar as in Section 7.1. As shown in Figure 8.17, by assuming the current only flows through the centres of the two regions covered by top gates, the self-inductance of the SQUID loop is 33 pH. If

we assume that $2I_0 = 6.5$ μA, the screening parameter (introduced in Section 2.3.1) can be calculated as $\beta_L = 2LI_0/\Phi_0 = 0.33$. Referring to Figure 2.13, such a screening factor means the modulation of critical current by magnetic field cannot reach zero, which matches the case in Figure 8.16.

We try to understand the positions and relative heights of the peaks in Figure 8.16 by running closed-loop simulations similar as in Section 8.4. The effect of top gates is simulated by setting different critical current densities for the regions covered by top gates (edges) and for regions not affected by the top gates (centre). In Figure 8.18 we show two simulated interference patterns that assumes different ratios of the critical current density on the edges to the critical current density in the centre. In Figure 8.18(a), the critical current density in the centre is 1/20 of the critical current density on the edges, which is close to the ideal case that the critical current density in the centre is totally "turned off". In Figure 8.18(b), the critical current density in the centre is 1/2 of the critical current density on the edges, which is close to case in our measurement. As we can see in both Figure 8.18(a) and (b), the interference patterns of these devices are a high-frequency Fraunhofer-like pattern enveloped by another low-frequency Fraunhofer-like pattern. The high-frequency Fraunhofer-like pattern comes from the self-interference of the whole width of the junction, while the low-frequency Fraunhofer-like pattern comes from the self-interference of the "junctions" on the edge, under the effect of the top gates. Thus, from the positions of the 1st minima of the envelope, which are not affected by the ratio of the critical current density on the edges to the critical current density in the centre, we can derive the size of the area affected by the top gates. The relative peak amplitudes show strong dependence on the ratio of the critical current density on the edges to the critical current density in the centre. In Figure 8.18(a), the supercurrent on the edge dominates, so the interference pattern looks more similar to that of a SQUID made up

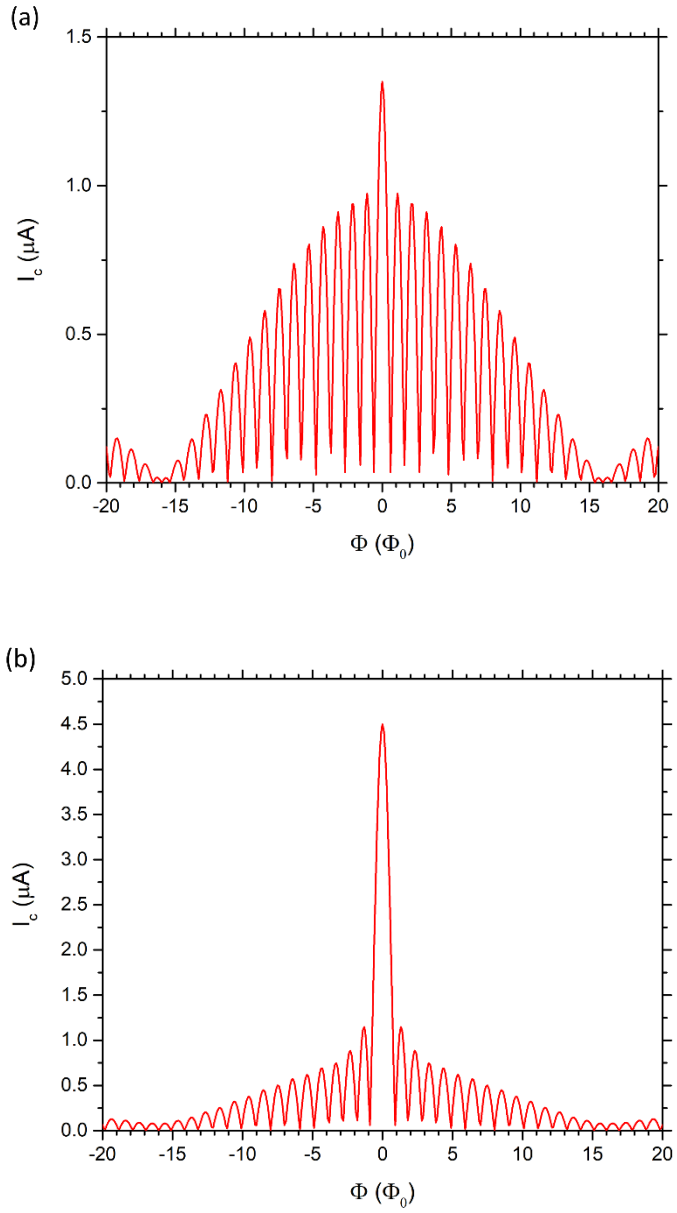

Figure 8.18 The interference pattern numerically calculated for an 80-μm-wide junction with a 5-μm-wide edge region on each side of the junction, by the closed-loop simulation. (a) The critical current density in the centre is 1/20 of the critical current density on the edge. (b) The critical current density in the centre is 1/2 of the critical current density on the edge. The magnetic flux is calculated based on the area of the whole junction.

of two finite-size junctions, such as the pattern in Figure 7.1; while in Figure 8.18(b), the supercurrent in the whole device contributes, so the interference pattern looks more similar to that of a wide single junction, such as the pattern in Figure 6.7.

If we compare the patterns in Figure 8.18 with that in Figure 8.16, we find it difficult to understand the experimental result in Figure 8.16 with the existing model. However, we clearly see that there exist 1st minima of critical current envelope at about ± 40 μT. Considering the similar flux focusing effect as in Section 6.3, the Fraunhofer-like pattern here corresponds to the self-interference of a Josephson junction with a width of 14 μm, which is almost three times as the physical width of the top gates. That raises the question whether the charge induced by the top gates is distributed locally under the top gates or spread to a wider range. To answer this question, we wrote another MATLAB script (shown in Appendix E) to simulate the charge distribution as an effect of the top gates. In Figure 8.19, we plot the charge distribution in both the graphene and in the top gates. We can see that although there exist some spikes on the edges of the top gates, the distribution of the charge induced by the top gates is rather uniform under the top gates and is quite local. It rules out the possible effect of the stray field from the top gates, and cannot quantitatively explain minima of critical current at about ± 40 μT.

In summary, we find it difficult to understand the shape and the period in the interference pattern in Figure 8.16. We therefore think the interference pattern in Figure 8.16 is not convincing enough as evidence for a manually induced edge effect. In future, we need to further improve the techniques to fabricate top gates that can withstand higher electric fields and to fabricate the two top gates as symmetric as possible. We also need to fully consider the effect of the top gates on the local junction parameters such as capacitance. However, due to time limitation and refurbishment of the LCN cleanroom, this wasn't possible during the present project.

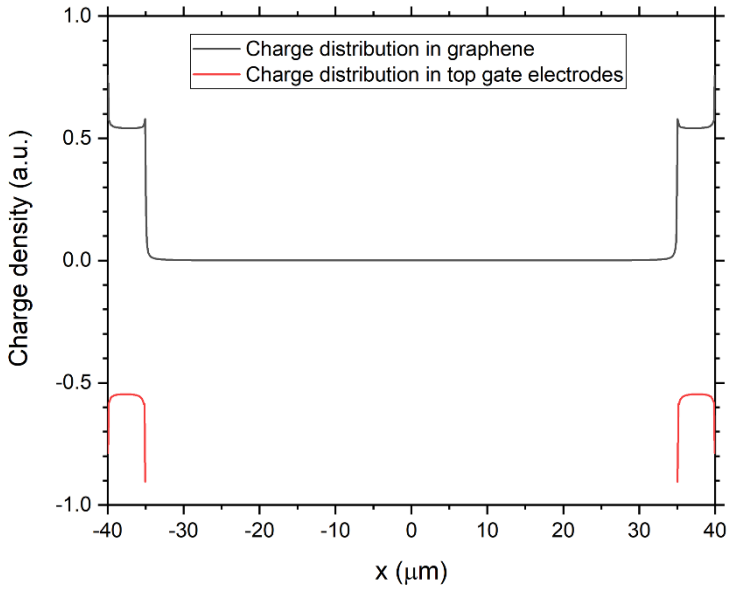

Figure 8.19 Charge distribution in graphene and in top gate electrodes when a voltage is applied between the top gates and graphene, simulated by MATLAB. Although there are peaks of charge density on the edges of electrode, the overall density is rather uniform and the effect of top gates is quite local.

8.6 Conclusion

In this chapter we have focused on how the width of the SGS junction affects its *I-V* properties in a magnetic field. We have found that the normal derivation for Josephson penetration depth is no longer valid for 2D coplanar junctions, and a bit too coarse even for junctions with a square cross-section. As a result, we proposed a new derivation of Josephson penetration depth for 2D coplanar junctions, which also works well for finite-sized 3D junctions. We then numerically studied the distribution of supercurrent and verified the validity of the new derivation. Based on the new derivation, the Josephson penetration depth is much larger than any reasonable junction width, so that it will not affect the distribution of supercurrent in both normal

3D junctions and 2D coplanar junctions. Thus, the effect on interference pattern when the junction width is larger than the Josephson penetration depth can only be studied by numerical simulation.

Chapter 9 Conclusions and Suggestions for Future Work

In conclusion, we have developed a method to fabricate scalable and tuneable Josephson junctions and dc SQUIDs based on CVD graphene. The two major research themes of the project are i) the tuneability of the electronic properties (by magnetic field, gate voltage and distribution of current) of SGS junctions and SQUIDs, and ii) the unique geometry of SGS junctions allowed by its properties, such as ultra-wide junctions and 4-probe junctions.

The excellent quality of the junctions and SQUIDs has been demonstrated by a series of measurements. The junctions can work over a wide temperature range from 320 mK to 1.5 K without hysteresis, and exhibit an ideal Fraunhofer-like interference pattern in a perpendicular magnetic field, showing the uniform distribution of the supercurrent in the junction. The critical current can be effectively modulated by the gate voltage, allowing more flexibility for device operation. Such tuneable and scalable SGS junctions are especially useful for applications involving arrays of Josephson junctions, such as superconducting qubits and single flux quantum (SFQ) devices, where the properties of the junctions could be tuned to be identical by local electric gates. By carefully optimising the fabrication process, we have managed to reduce the junction length to 50 nm, shorter than the mean free path of charge carriers in graphene, so that evidence for ballistic transport can be observed. As far as we know, this was the first time that ballistic transport had been observed in a Josephson junction based on CVD graphene.

We also studied a variant of the SGS junction, which is named as “4-probe

Josephson junctions". We have found that the critical current of the 4-probe Josephson junction can be tuned by the distribution of current between the inner and the outer electrodes. We have verified experimentally that this is due to the heat generated locally when the normal current flows through graphene between the inner and the outer electrodes. Such path-dependent critical current may find its way to applications in superconducting electronics or superconducting sensors.

For the dc SQUIDs based on CVD graphene, we have shown that their *I-V* characteristics have periodic dependence on the perpendicular magnetic field, similar as normal dc SQUIDs. The $I_c(B)$ interference pattern of the SQUIDs is enveloped by Fraunhofer-like pattern because of the finite size of the SGS junctions. The critical current of the dc SQUIDs can be modulated not only by the magnetic field but also by the gate voltage. We have estimated that the intrinsic flux sensitivity of the SQUIDs could be as low as $24\ \mathrm{n}\Phi_0/\mathrm{Hz}^{1/2}$ at 320 mK if only the white noise is considered, and we have shown experimentally that the properties of the SQUIDs can respond to changes in the gate voltage at least as fast as 1.5 kHz.

We further studied the reason why the supercurrent can be uniform in junctions as wide as 80 μm. By theoretical analysis and numerical simulation, we have found that the usual derivation for Josephson penetration depth is no longer valid for 2D coplanar junctions such as SGS junctions. We have proposed a new expression for the Josephson penetration depth for 2D coplanar junctions and numerically simulated the effect in a perpendicular magnetic field when the junction width is longer than this Josephson penetration depth.

For future work, we suggest investigating the proximity effect that happens at the superconductor/graphene interface. This can help to solve some of the mysteries of SGS junction, such as the suppression of I_0R_n product compared with the theoretical prediction. We need to figure out how the Cooper pair wave function changes from

the superconducting electrode to the graphene under the electrode, and then to the exposed graphene. We recommend using the current crowding effect on the edge of the electrode as a probe to study the ratio of the contact resistivity and the sheet resistance of graphene under the electrode. The 4-probe junction structure we discussed in Section 6.8 can be useful for this reseach.

For applications, we suggest integrating CVD graphene-based Josephson junctions and dc SQUIDs into superconducting resonators or qubits, so that the gate-tuneability of the SGS junctions and SQUIDs can really show the advantage over conventional tunnel junctions. Such gate-tuneability is especially desirable for qubits or resonators working under relatively large magnetic field, such as qubits based on topological insulators. We noticed that there have been papers published recently [149–151]. However, the Q factor of the resonators and the relaxation time of the qubits are still far from expected. Many physical and technical problems remain to be solved to make them competitive with those based on tunnel junctions, such as integrating the fabrication of SGS junctions with the fabrication of superconducting circuits without introducing too much loss, reducing loss channels such as the capacitance between the gate electrode and the device, and so on.

We also suggest future work on exploring the possibility of SGS junctions allowed by the ultra-long Josephson penetration depth, both theoretical and experimental. In the model we used in Chapter 8 to derive the Josephson penetration depth, we assume the supercurrent is evenly distributed in the superconducting electrodes. In a more accurate model, the supercurrent distribution in the superconducting electrodes can be taken into consideration. The ultra-long Josephson penetration depth also allows to design and fabricate Josephson junctions with arbitrary interference pattern under an external magnetic field using a combination of top and bottom gates.

Appendix A

Proof that the sheet resistance of epitaxial graphene samples measured by non-contact microwave method equals the sheet resistance of graphene on each surface in parallel:

According to the perturbation theory, the frequency shift Δf_s and peak width change Δw_s from empty housing to bare substrate have the same expression as in Ref. [83],

$$\Delta f_s = f_0 \frac{\epsilon_0(\epsilon_s' - 1) \iiint E^2 dV}{W} \tag{A.1}$$

$$\Delta w_s = 2 f_0 \frac{\epsilon_0 \epsilon_s'' \iiint E^2 dV}{W} \tag{A.2}$$

where f_0 is the centre frequency of the TE_{001} mode of bare housing, ϵ_s' and ϵ_s'' are the real and imaginary parts of the permittivity of the substrate, E is the electric field, W is the total energy stored in the microwave mode. The integration of the electric field energy is done over the volume of the substrate.

The peak width change due to the introduction of substrate with graphene Δw_g becomes

$$\Delta w_g = 2 f_0 \epsilon_0 \frac{\epsilon_s'' \iiint E^2 dV + \epsilon_{g1}'' \iiint E^2 dv_1 + \epsilon_{g2}'' \iiint E^2 dv_2}{W} \tag{A.3}$$

where ϵ_{g1}'' and ϵ_{g2}'' are the imaginary parts of the permittivity of the graphene on the bop and the bottom of the substrate, respectively. Correspondingly, the second and the third integrations are done over the volume of the top and the bottom graphene layer,

respectively.

Thus

$$\Delta w_{\mathrm{g}} - \Delta w_{\mathrm{s}} = 2f_0\epsilon_0 \frac{\epsilon''_{\mathrm{g}1} \iiint E^2 dv_1 + \epsilon''_{\mathrm{g}2} \iiint E^2 dv_2}{W}$$
$$= \frac{2\Delta f_{\mathrm{s}}\left(\epsilon''_{\mathrm{g}1} t_{\mathrm{g}1} + \epsilon''_{\mathrm{g}2} t_{\mathrm{g}2}\right)}{(\epsilon'_{\mathrm{s}} - 1)t_{\mathrm{s}}} \tag{A.4}$$

where t_{s} is the thickness of the substrate and $t_{\mathrm{g}1}$ and $t_{\mathrm{g}2}$ are the thickness of the graphene layer on the top and bottom of the substrate respectively.

Since for either surface ($i = 1$ or 2), the conductivity of graphene

$$\sigma_i = 2\pi f_0 \epsilon_0 \epsilon''_{\mathrm{g}i} \tag{A.5}$$

The sheet resistance of either surface is

$$R_{\mathrm{s}i} = \frac{1}{\sigma_i t_{\mathrm{g}i}} = \frac{1}{2\pi f_0 \epsilon_0 \epsilon''_{\mathrm{g}i} t_{\mathrm{g}i}} \tag{A.6}$$

The sheet resistance calculated using the normal formula (Eq. (3.14)) is

$$R_{\mathrm{s}} = \frac{\Delta f_{\mathrm{s}}}{\pi f_0 \epsilon_0 \left(\Delta w_{\mathrm{g}} - \Delta w_{\mathrm{s}}\right)(\epsilon'_{\mathrm{s}} - 1)t_{\mathrm{s}}}$$

$$= \frac{1}{\pi f_0 \epsilon_0 \left(\epsilon''_{\mathrm{g}1} t_{\mathrm{g}1} + \epsilon''_{\mathrm{g}2} t_{\mathrm{g}2}\right)} = \frac{1}{\frac{1}{R_{\mathrm{s}1}} + \frac{1}{R_{\mathrm{s}2}}} \tag{A.7}$$

which equals the sheet resistance of two surfaces in parallel.

Appendix B

The MATLAB script that calculates the distribution of the gauge invariant phase difference $\varphi(x)$ in the 3D model:

```
%This script calculates the distribution of phi and the integration
of the supercurrent based on the 3D model, for given boundary
conditions at x = 0;
format long;
%Parameters to be set:
t = 5e-8;
lambda = 4e-8;
jc = 0.1;
d = 3e-10;
W = 1e-4;
step = 500; %the number of mesh from x = 0 to x = W/2.
%Boundary conditions:
phi0 = pi/2;
B = 0;

u0 = 4e-7*pi;
Phi0 = 2.067e-15;
syms y(x);
[ODE] = odeToVectorField(diff(y, 2) ==
2*pi*(t+2*lambda)*u0*jc*sin(y)/Phi0/d);
Equation = matlabFunction(ODE,'vars', {'x','Y'});
Sol_3D_r = ode45(Equation,[0 W/2],[phi0
-2*pi*B*(t+2*lambda)/Phi0]);
Sol_3D_l = ode45(Equation,[0 -W/2],[phi0
-2*pi*B*(t+2*lambda)/Phi0]);
%The integration of the supercurrent density is done by summing
the supercurrent in each mesh
X_r = linspace(0,W/2,step+1);
phi_r = deval(X_r, Sol_3D_r, 1);
X_l = linspace(-W/2,0,step+1);
phi_l = deval(X_l, Sol_3D_l, 1);
X = [X_l(:,1:step), X_r];
```

```
phi = [phi_l(:,1:step), phi_r];
X_output = X.';
phi_output = phi.';
%The current in the mesh at the boundary is halved due to its halved
width.
j = jc*W/2/step*sin(phi);
j(1,1) = j(1,1)/2;
j(1,2*step+1) = j(1,2*step+1)/2;
is = sum(j);
```

The MATLAB script that calculates the distribution of the gauge invariant phase difference $\varphi(x)$ in the quasi-2D model:

```
%This script calculates the distribution of phi and the integration
of the supercurrent based on the quasi-2D model, for given boundary
conditions at x = 0.
format long;
%Parameters to be set:
t = 5e-8;
lambda = 4e-8;
jc = 0.1;
d = 3e-10;
W = 1e-4;
step = 500; %the number of mesh from x = 0 to x = W/2.
%Boundary conditions:
phi0 = pi/2;
B = 0;

u0 = 4e-7*pi;
Phi0 = 2.067e-15;
syms y(x);
[ODE] = odeToVectorField(diff(y, 2) ==
2*(t+2*lambda)*u0*jc*(atan(d/2/(W/2-x))+atan(d/2/(x+W/2)))*sin
(y)/Phi0/d);
Equation = matlabFunction(ODE,'vars', {'x','Y'});
Sol_quasi2D_r = ode45(Equation,[0 W/2],[phi0
-2*pi*B*(t+2*lambda)/Phi0]);
Sol_quasi2D_l = ode45(Equation,[0 -W/2],[phi0
-2*pi*B*(t+2*lambda)/Phi0]);
```

```
%The integration of the supercurrent density is done by summing
the supercurrent in each mesh.
X_r = linspace(0,W/2,step+1);
phi_r = deval(X_r, Sol_quasi2D_r, 1);
X_l = linspace(-W/2,0,step+1);
phi_l = deval(X_l, Sol_quasi2D_l, 1);
X = [X_l(:,1:step), X_r];
phi = [phi_l(:,1:step), phi_r];
X_output = X.';
phi_output = phi.';
%The current in the mesh at the boundary is halved due to its halved
width.
j = jc*W/2/step*sin(phi);
j(1,1) = j(1,1)/2;
j(1,2*step+1) = j(1,2*step+1)/2;
is = sum(j);
```

Appendix C

The MATLAB script that calculates the interference pattern $I_0(\Phi)$ considering only the external magnetic field:

```
format long
%Parameters to be set:
Phi_step = 400; %The number of steps in external field
phi0_step = 360; %The number of steps in boundary condition
x_step = 100;
Phi = linspace(-20, 20, Phi_step+1);
t = 5e-8;
lambda = 3.75e-8;
jc = 0.1;
W = 1e-4;

Phi0 = 2.067e-15;
B = Phi*Phi0/(t+2*lambda)/W;
X = linspace(-W/2,W/2,2*x_step+1);
for n = 1:Phi_step+1 %To sweep the external magnetic flux
    Ic(1,n) = 0;
    for m = 1:phi0_step %To sweep the boundary condition at x=0
        phi0 = m*2*pi/phi0_step;
        phi = phi0-2*pi*B(1,n)*(t+2*lambda)*X/Phi0;
        j = jc*W/2/x_step*sin(phi);
        j(1,1)=j(1,1)/2;
        j(1,2*x_step+1)=j(1,2*x_step+1)/2;
        ic(1,n) = sum(j);
        if ic(1,n) > Ic(1,n) %To find out the maximum over the
boundary condition
            Ic(1,n)= ic(1,n);
            m_max(1,n) = m*360/phi0_step;
        end
    end
end
Phi_output = Phi.';
Ic_output = Ic.';
```

```
plot(Phi, Ic);
```

The MATLAB script for open-loop simulation of the interference pattern $I_0(\Phi)$ in the 3D model:

```
format long
%Parameters to be set:
Phi_step = 400;
phi0_step = 360;
x_step = 100;
Phi = linspace(-20, 20, Phi_step+1);
t = 5e-8;
lambda = 3.75e-8;
jc = 0.1;
d = 3e-10;
W = 1e-4;

u0 = 4e-7*pi;
Phi0 = 2.067e-15;
B = Phi*Phi0/(t+2*lambda)/W;
X_r = linspace(0,W/2,x_step+1);
X_l = linspace(-W/2,0,x_step+1);
syms y(x);
[ODE] = odeToVectorField(diff(y, 2) ==
2*pi*(t+2*lambda)*u0*jc*sin(y)/Phi0/d);
Equation = matlabFunction(ODE,'vars', {'x','Y'});
for n = 1:Phi_step+1 %To sweep the external magnetic flux
    Ic(1,n) = 0;
    for m = 1:phi0_step %To sweep the boundary condition at x=0
        phi0 = m*2*pi/phi0_step;
        Sol_3D_r = ode45(Equation,[0 W/2],[phi0
-2*pi*B(1,n)*(t+2*lambda)/Phi0]);
        Sol_3D_l = ode45(Equation,[0 -W/2],[phi0
-2*pi*B(1,n)*(t+2*lambda)/Phi0]);
        phi_r = deval(X_r, Sol_3D_r, 1);
        phi_l = deval(X_l, Sol_3D_l, 1);
        phi = [phi_l(:,1:x_step), phi_r];
        j = jc*W/2/x_step*sin(phi);
        j(1,1)=j(1,1)/2;
        j(1,2*x_step+1)=j(1,2*x_step+1)/2;
```

```
        ic(1,n) = sum(j);

        if ic(1,n) > Ic(1,n)
        %To find out the maximum over the boundary condition
            Ic(1,n)= ic(1,n);
            m_max(1,n) = m*360/phi0_step;
        end
    end
end
Phi_output = Phi.';
Ic_output = Ic.';
plot(Phi, Ic);
```

The MATLAB script for open-loop simulation of the interference pattern $I_0(\Phi)$ in the quasi-2D model:

```
format long
%Parameters to be set:
Phi_step = 400;
phi0_step = 360;
x_step = 100;
Phi = linspace(-20, 20, Phi_step+1);
t = 5e-8;
lambda = 3.75e-8;
jc = 0.1;
d = 3e-10;
W = 1e-4;

u0 = 4e-7*pi;
Phi0 = 2.067e-15;
B = Phi*Phi0/(t+2*lambda)/W;
X_r = linspace(0,W/2,x_step+1);
X_l = linspace(-W/2,0,x_step+1);
syms y(x);
[ODE] = odeToVectorField(diff(y, 2) ==
2*(t+2*lambda)*u0*jc*(atan(d/2/(W/2-x))+atan(d/2/(x+W/2)))*sin
(y)/Phi0/d);
Equation = matlabFunction(ODE,'vars', {'x','Y'});
for n = 1:Phi_step+1 %To sweep the external magnetic flux
    Ic(1,n) = 0;
```

```
    for m = 1:phi0_step %To sweep the boundary condition at x=0
        phi0 = m*2*pi/phi0_step;
        Sol_3D_r = ode23(Equation,[0 W/2],[phi0
-2*pi*B(1,n)*(t+2*lambda)/Phi0]);
        Sol_3D_l = ode23(Equation,[0 -W/2],[phi0
-2*pi*B(1,n)*(t+2*lambda)/Phi0]);
        phi_r = deval(X_r, Sol_3D_r, 1);
        phi_l = deval(X_l, Sol_3D_l, 1);
        phi = [phi_l(:,1:x_step), phi_r];
        j = jc*W/2/x_step*sin(phi);
        j(1,1)=j(1,1)/2;
        j(1,2*x_step+1)=j(1,2*x_step+1)/2;
        ic(1,n) = sum(j);

        if ic(1,n) > Ic(1,n)
        %To find out the maximum over the boundary condition
            Ic(1,n)= ic(1,n);
            m_max(1,n) = m*360/phi0_step;
        end
    end
end
Phi_output = Phi.';
Ic_output = Ic.';
plot(Phi, Ic);
```

Appendix D

The MATLAB script for closed-loop simulation of the interference pattern $I_0(\Phi)$ in the quasi-2D model:

```
format long
%Parameters to be set:
Phi_step = 200;
phi0_step = 360;
x_step = 500;
Phi = linspace(-10, 10, Phi_step+1);
t = 5e-8;
lambda = 3.75e-8;
jc = 0.1;
d = 3e-10;
W = 0.01;
Iteration_step = 100;

u0 = 4e-7*pi;
Phi0 = 2.067e-15;
B = Phi*Phi0/(t+2*lambda)/W;
X_r = linspace(0,W/2,x_step+1);
X_l = linspace(-W/2,0,x_step+1);
syms y(x);
[ODE] = odeToVectorField(diff(y, 2) ==
2*(t+2*lambda)*u0*jc*(atan(d/2/(W/2-x))+atan(d/2/(x+W/2)))*sin
(y)/Phi0/d);
Equation = matlabFunction(ODE,'vars', {'x','Y'});
for n = 1:Phi_step+1 %To sweep the external magnetic flux
    Ic(1,n) = 0;
    for m = 1:phi0_step %To sweep the boundary condition at x=0
        phi0 = m*2*pi/phi0_step;
        %The first cycle is still solved by the built-in function
        "ode45"
        Sol_quasi2D_r = ode45(Equation,[0 W/2],[phi0
-2*pi*B(1,n)*(t+2*lambda)/Phi0]);
```

```
        Sol_quasi2D_l = ode45(Equation,[0 -W/2],[phi0
-2*pi*B(1,n)*(t+2*lambda)/Phi0]);
        phi_r = deval(X_r, Sol_quasi2D_r, 1);
        phi_l = deval(X_l, Sol_quasi2D_l, 1);
        phi = [phi_l(:,1:x_step), phi_r];
        j = jc*W/2/x_step*sin(phi);
        %Calculate the supercurrent based on the redistributed phi
        j(1,1)=j(1,1)/2;
        j(1,2*x_step+1)=j(1,2*x_step+1)/2;
        ic(1,n) = sum(j);

        if ic(1,n) > Ic(1,n)
        %To find out the maximum over the boundary condition
            Ic(1,n)= ic(1,n);
            phi_max(1,:) = phi(1,:);
            m_max(1,n) = m*360/phi0_step;
        end
    end
    for p = 1:2*iternation_step
    %Since the second cycle, the differential equation is solved
    as difference equation
        Ic(p+1,n) = 0;
        for q = 1:2*x_step+1
        %Calculate the magnetic field based on the redistributed
        supercurrent
            B_sc(p,q) = 0;
            for r = 1:2*x_step+1
                if r ~= q
                    B_sc(p,q) =
B_sc(p,q)+u0*j_max(p,r)/pi/d*atan(d/2/(q-r)/W*2*x_step);
                end
            end
        end
        for v = 1:2*x_step+1
            dphi(p+1,v) =
-2*pi*(B(1,n)+B_sc(p,v))*(t+2*lambda)/Phi0;
        end
        for m = 1:phi0_step %To sweep the boundary condition at x=0
            phi(p+1,x_step+1) = m*2*pi/phi0_step;
            for u = 1:x_step
```

```
                phi(p+1,u+x_step+1) =
phi(p+1,x_step+u)+(dphi(p+1,u+x_step)+dphi(p+1,u+x_step+1))/2*
W/2/x_step;
                phi(p+1,x_step+1-u) =
phi(p+1,x_step+2-u)-(dphi(p+1,x_step+1-u)+dphi(p+1,x_step+2-u)
)/2*W/2/x_step
            end
            j(p+1,:) = jc*W/2/x_step*sin(phi(p+1,:));
            %Calculate the supercurrent based on the redistributed
            phi
            j(p+1,1) = j(p+1,1)/2;
            j(p+1,2*x_step+1) = j(p+1,2*x_step+1)/2;
            ic(p+1,n) = sum(j(p+1,:));

            if ic(p+1,n) > Ic(p+1,n)
            %To find out the maximum over the boundary condition
                Ic(p+1,n)= ic(p+1,n);
                phi_max(p+1,:) = phi(p+1,:);
                m_max(p+1,n) = m*360/phi0_step;
                j_max(p+1,:) = j(p+1,:);
            end
        end
        if abs(Ic(p+1,n)-Ic(p,n)) < jc*W/500
        %Stop iteraction if converges
            Ic_final(n,1) = Ic(p+1,n);
            break;
        end
        if p == interation_step
        %Manually reset if does not converges
            j_max(iteration_step+1,:) =
mean(j_max(iteration_step-19: iteration_step,:),1);
        end
    end
end

Phi_output = Phi.';
Ic_output = Ic.';
plot(Phi, Ic_output);
```

The MATLAB script for open-loop simulation of the interference pattern $I_0(\Phi)$ in

the 3D model:

```
format long
%Parameters to be set:
Phi_step = 200;
phi0_step = 360;
x_step = 500;
Phi = linspace(-10, 10, Phi_step+1);
t = 5e-8;
lambda = 3.75e-8;
jc = 0.1;
d = 3e-10;
W = 1e-4;
Iteration_step = 100;

u0 = 4e-7*pi;
Phi0 = 2.067e-15;
B = Phi*Phi0/(t+2*lambda)/W;
X_r = linspace(0,W/2,x_step+1);
X_l = linspace(-W/2,0,x_step+1);
syms y(x);
[ODE] = odeToVectorField(diff(y, 2) ==
2*pi*(t+2*lambda)*u0*jc*sin(y)/Phi0/d);
Equation = matlabFunction(ODE,'vars', {'x','Y'});
for n = 1:Phi_step+1 %To sweep the external magnetic flux
    Ic(1,n) = 0;
    for m = 1:phi0_step %To sweep the boundary condition at x=0
        phi0 = m*2*pi/phi0_step;
        %The first cycle is still solved by the built-in function
        "ode45"
        Sol_3D_r = ode45(Equation,[0 W/2],[phi0
-2*pi*B(1,n)*(t+2*lambda)/Phi0]);
        Sol_3D_l = ode45(Equation,[0 -W/2],[phi0
-2*pi*B(1,n)*(t+2*lambda)/Phi0]);
        phi_r = deval(X_r, Sol_3D_r, 1);
        phi_l = deval(X_l, Sol_3D_l, 1);
        phi = [phi_l(:,1:x_step), phi_r];
        j = jc*W/2/x_step*sin(phi);
        %Calculate the supercurrent based on the redistributed phi
        j(1,1)=j(1,1)/2;
```

```
        j(1,2*x_step+1)=j(1,2*x_step+1)/2;
        ic(1,n) = sum(j);

        if ic(1,n) > Ic(1,n)
        %To find out the maximum over the boundary condition
            Ic(1,n)= ic(1,n);
            phi_max(1,:) = phi(1,:);
            m_max(1,n) = m*360/phi0_step;
        end
    end
    for p = 1:200
    %Since the second cycle, the differential equation is solved
    as difference equation
        Ic(p+1,n) = 0;
        for q = 1:2*x_step+1
        %Calculate the magnetic field based on the redistributed
        supercurrent
            B_sc(p,q) = 0;
            for r = 1:2*x_step+1
            %To sweep the boundary condition at x=0
                if r ~= q
                    B_sc(p,q) =
B_sc(p,q)+u0*j_max(p,r)/2*(q-r)/abs(q-r)/d;
                end
            end
        end
        for v = 1:2*x_step+1
            dphi(p+1,v) =
-2*pi*(B(1,n)+B_sc(p,v))*(t+2*lambda)/Phi0;
        end
        for m = 1:phi0_step
            phi(p+1,x_step+1) = m*2*pi/phi0_step;
            for u = 1:x_step
                phi(p+1,u+x_step+1) =
phi(p+1,x_step+u)+(dphi(p+1,u+x_step)+dphi(p+1,u+x_step+1))/2*
W/2/x_step;
                phi(p+1,x_step+1-u) =
phi(p+1,x_step+2-u)-(dphi(p+1,x_step+1-u)+dphi(p+1,x_step+2-u)
)/2*W/2/x_step
            end
            j(p+1,:) = jc*W/2/x_step*sin(phi(p+1,:));
```

```
            %Calculate the supercurrent based on the redistributed
            phi
             j(p+1,1) = j(p+1,1)/2;
             j(p+1,2*x_step+1) = j(p+1,2*x_step+1)/2;
             ic(p+1,n) = sum(j(p+1,:));

             if ic(p+1,n) > Ic(p+1,n)
            %To find out the maximum over the boundary condition
                 Ic(p+1,n)= ic(p+1,n);
                 phi_max(p+1,:) = phi(p+1,:);
                 m_max(p+1,n) = m*360/phi0_step;
                 j_max(p+1,:) = j(p+1,:);
             end
        end
        if abs(Ic(p+1,n)-Ic(p,n)) < jc*W/500
        %Stop iteraction if converges
             Ic_final(n,1) = Ic(p+1,n);
             break;
        end
        if p == interation_step
        %Manually reset if does not converges
             j_max(iteration_step+1,:) =
mean(j_max(iteration_step-19: iteration_step,:),1);
        end

    end
end

Phi_output = Phi.';
Ic_output = Ic.';
plot(Phi, Ic_output);
```

Appendix E

The MATLAB script for the simulation of the charge distribution under local top gates:

```
clear;
W = 8e-5;
W_edge = 5e-6;
No_step = 800;
No_step_edge = 50;
Thickness = 8e-8; %Thickness of the dielectric layer

step_size = W/No_step;
step_size_edge = W_edge./No_step_edge;
x = step_size/2:step_size:W-step_size/2;

P = zeros(No_step+No_step_edge*2,No_step+No_step_edge*2);
%P is the matrix of electric potential of any pixel generated on
any other pixel. To simply the model, we assume the model is
infinitely long in the direction of the supercurrent and the charge
is evenly distributed in that direction.
for m = 1: No_step
    for n = 1: No_step
        if m == n
            P(m,n) = -log(step_size/2)+1/2;
        else
            P(m,n) = -log(abs(m-n)*step_size);
        end
    end
end

for m = No_step+1: No_step+No_step_edge
    for n = No_step+1: No_step+No_step_edge
        if m == n
            P(m,n) = -log(step_size_edge/2)+1/2;
        else
            P(m,n) = -log(abs(m-n)*step_size_edge);
```

```
        end
    end
end

for m = No_step+No_step_edge+1: No_step+No_step_edge*2
    for n = No_step+No_step_edge+1: No_step+No_step_edge*2
        if m == n
            P(m,n) = -log(step_size_edge/2)+1/2;
        else
            P(m,n) = -log(abs(m-n)*step_size_edge);
        end
    end
end

for m = 1: No_step
    for n = No_step+1: No_step+No_step_edge
        P(m,n) =
-log(((m*step_size-(n-No_step)*step_size_edge)^2+Thickness^2)^
(1/2));
        P(n,m) = P(m,n);
    end
end

for m = 1: No_step
    for n = No_step+No_step_edge+1: No_step+No_step_edge*2
        P(m,n) =
-log((((W-m*step_size)-(W_edge-(n-No_step-No_step_edge)*step_s
ize_edge))^2+Thickness^2)^(1/2));
        P(n,m) = P(m,n);
    end
end

for m = No_step+1: No_step+No_step_edge
    for n = No_step+No_step_edge+1: No_step+No_step_edge*2
        P(m,n) =
-log(abs((W-(m-No_step)*step_size_edge)-(W_edge-(n-No_step-No_
step_edge)*step_size_edge)));
        P(n,m) = P(m,n);
    end
end
```

```
V = zeros(No_step+No_step_edge*2,1);

V(1:No_step,1) = 1;
V(No_step+1:No_step+No_step_edge*2,1) = -1;

Q = mldivide(P,V); %solve the linear matrix equation
Q_top = zeros(No_step,1);
Q_top(1:No_step_edge,1) = Q(No_step+1:No_step+No_step_edge,1);
Q_top(No_step-No_step_edge+1:No_step,1) =
Q(No_step+No_step_edge+1:No_step+No_step_edge*2,1);
plot(x, Q(1:No_step,1), x, Q_top);
legend({'graphene', 'top gate'}, 'Location', 'north');
```

Reference

[1] Bardeen J, Cooper L N and Schrieffer J R 1957 Theory of superconductivity *Phys. Rev.* **108** 1175–204

[2] Josephson B D 1962 Possible new effects in superconductive tunnelling *Phys. Lett.* **1** 251–3

[3] Josephson B D 1965 Supercurrents through barriers *Adv. Phys.* **14** 419–51

[4] Stewart W C 1968 Current-voltage characteristics of Josephson junctions *Appl. Phys. Lett.* **12** 277–80

[5] McCumber D E 1968 Effect of ac impedance on dc voltage-current characteristics of superconductor weak-link junctions *J. Appl. Phys.* **39** 3113–8

[6] Clarke J and Braginski A I 2006 *The SQUID handbook* (Weinheim: Wiley-VCH)

[7] Hamilton C A, Introduction I and Josephson B 2000 Josephson voltage standards **71** 3611–23

[8] Behr R, Kieler O, Kohlmann J, Müller F and Palafox L 2012 Development and metrological applications of Josephson arrays at PTB *Meas. Sci. Technol.* **23** 124002

[9] Ferrell R A and Prange R E 1963 Self-field limiting of Josephson tunneling of superconducting electron pairs *Phys. Rev. Lett.* **10** 479–81

[10] Ambegaokar V and Baratoff A 1963 Tunneling Between Superconductors

Phys. Rev. Lett. **11** 486–9

[11] Mühlschlegel B 1959 Die thermodynamischen funktionen des supraleiters *Zeitschrift für Phys.* **155** 313–27

[12] Lam S K H 2006 Noise properties of SQUIDs made from nanobridges *Supercond. Sci. Technol.* **19** 963–7

[13] Troeman A G P, Derking H, Borger B, Pleikies J, Veldhuis D and Hilgenkamp H 2007 NanoSQUIDs based on niobium constrictions *Nano Lett.* **7** 2152–6

[14] Hao L, Macfarlane J C, Gallop J C, Cox D, Beyer J, Drung D and Schurig T 2008 Measurement and noise performance of nano-superconducting-quantum-interference devices fabricated by focused ion beam *Appl. Phys. Lett.* **92** 192507

[15] Kulik I O and Omelyanchuk A N 1975 Contribution to the microscopic theory of the Josephson effect in superconducting bridges *JETP Lett.* **21** 96–7

[16] Kulik I O and Omelyanchuk A N 1977 Properties of superconducting microbridges in the pure limit *Fiz. Nizk. Temp.* **3** 945–8

[17] Likharev K K 1979 Superconducting weak links *Rev. Mod. Phys.* **51** 101–59

[18] Buckel W, Kleiner R and Huebener R P 2004 *Superconductivity : fundamentals and applications* (Weinheim: Wiley-VCH)

[19] Clarke J 1980 Advances in SQUID magnetometers *IEEE Trans. Electron Devices* **27** 1896–908

[20] Clarke J 1989 Principles and applications of SQUIDS *Proc. IEEE* **77** 1208–23

[21] Ryhänen T, Seppä H, Ilmoniemi R K J 1989 SQUID magnetometers for low-frequency applications. *J. Low Temp. Phys.* **76** 287–386

[22] Tesche C D and Clarke J 1977 DC SQUID: noise and optimization *J. Low Temp. Phys.* **29** 301–31

[23] Novoselov K S, Geim A K, Morozov S V, Jiang D, Zhang Y, Dubonos S V, Grigorieva I V and Firsov A A 2004 Electric field effect in atomically thin carbon films *Science* **306** 666–9

[24] Geim A K and Novoselov K S 2007 The rise of graphene. *Nat. Mater.* 183–91

[25] Wallace P R 1947 The band theory of graphite *Phys. Rev.* **71** 622–34

[26] Saito R, Dresselhaus G and Dresselhaus M S 1998 *Physical properties of carbon nanotubes* (London: Imperial College Press)

[27] Castro Neto A H, Guinea F, Peres N M R, Novoselov K S and Geim A K 2009 The electronic properties of graphene *Rev. Mod. Phys.* **81** 109–62

[28] Abergel D S L, Apalkov V, Berashevich J, Ziegler K and Chakraborty T 2010 Properties of graphene: a theoretical perspective *Adv. Phys.* **59** 261–482

[29] Novoselov K S, Geim A K, Morozov S V, Jiang D, Katsnelson M I, Grigorieva I V, Dubonos S V and Firsov A A 2005 Two-dimensional gas of massless Dirac fermions in graphene *Nature* **438** 197–200

[30] Zhang Y B, Tan Y W, Stormer H L and Kim P 2005 Experimental observation of the quantum Hall effect and Berry's phase in graphene *Nature* **438** 201–4

[31] Katsnelson M I, Novoselov K S and Geim A K 2006 Chiral tunnelling and the Klein paradox in graphene *Nat. Phys.* **2** 620–5

[32] Novoselov K S and Castro Neto A H 2012 Two-dimensional crystals-based heterostructures: materials with tailored properties *Phys. Scr.* **2012** 014006

[33] Novoselov K S, Jiang D, Schedin F, Booth T J, Khotkevich V V, Morozov S V and Geim A K 2005 Two-dimensional atomic crystals *Proc. Natl. Acad. Sci.* **102** 10451–3

[34] Blake P, Hill E W, Castro Neto A H, Novoselov K S, Jiang D, Yang R, Booth T J and Geim A K 2007 Making graphene visible *Appl. Phys. Lett.* **91** 063124

[35] Soldano C, Mahmood A and Dujardin E 2010 Production, properties and potential of graphene *Carbon* **48** 2127–50

[36] Muñoz R and Gómez-Aleixandre C 2013 Review of CVD synthesis of graphene *Chem. Vap. Depos.* **19** 297–322

[37] Kim K S, Zhao Y, Jang H, Lee S Y, Kim J M, Ahn J H, Kim P, Choi J Y and Hong B H 2009 Large-scale pattern growth of graphene films for stretchable transparent electrodes *Nature* **457** 706–10

[38] Kwon S Y, Ciobanu C V, Petrova V, Shenoy V B, Bareno J, Gambin V, Petrov I and Kodambaka S 2009 Growth of semiconducting graphene on palladium *Nano Lett.* **9** 3985–90

[39] Sutter P W, Flege J I and Sutter E A 2008 Epitaxial graphene on ruthenium *Nat. Mater.* **7** 406–11

[40] Coraux J, N'Diaye A T, Busse C and Michely T 2008 Structural coherency of graphene on Ir(111) *Nano Lett.* **8** 565–70

[41] Li X S, Cai W W, An J H, Kim S, Nah J, Yang D X, Piner R, Velamakanni A, Jung I, Tutuc E, Banerjee S K, Colombo L and Ruoff R S 2009 Large area

synthesis of high quality and uniform graphene films on copper foils *Science* **324** 1312–4

[42] Bae S, Kim H, Lee Y, Xu X F, Park J S, Zheng Y, Balakrishnan J, Lei T, Kim H R, Song Y I, Kim Y J, Kim K S, Ozyilmaz B, Ahn J H, Hong B H and Iijima S 2010 Roll-to-roll production of 30-inch graphene films for transparent electrodes *Nat. Nanotechnol.* **5** 574–8

[43] Mattevi C, Kim H and Chhowalla M 2011 A review of chemical vapour deposition of graphene on copper *J. Mater. Chem.* **21** 3324–34

[44] Kumar A and Lee C H 2013 Synthesis and biomedical applications of graphene: present and future trends *Advances in Graphene Science* (InTech) pp 55–75

[45] Berger C, Song Z M, Li T B, Li X B, Ogbazghi A Y, Feng R, Dai Z T, Marchenkov A N, Conrad E H, First P N and de Heer W A 2004 Ultrathin epitaxial graphite: 2D electron gas properties and a route toward graphene-based nanoelectronics *J. Phys. Chem. B* **108** 19912–6

[46] Berger C, Song Z M, Li X B, Wu X S, Brown N, Naud C, Mayou D, Li T B, Hass J, Marchenkov A N, Conrad E H, First P N and de Heer W A 2006 Electronic confinement and coherence in patterned epitaxial graphene *Science* **312** 1191–6

[47] De Heer W A, Berger C, Wu X, First P N, Conrad E H, Li X, Li T, Sprinkle M, Hass J, Sadowski M L, Potemski M and Martinez G 2007 Epitaxial graphene *Solid State Commun.* **143** 92–100

[48] Hass J, De Heer W A and Conrad E H 2008 The growth and morphology of epitaxial multilayer graphene *J. Physics-Condensed Matter* **20** 323202

[49] Emtsev K V, Bostwick A, Horn K, Jobst J, Kellogg G L, Ley L, McChesney J L, Ohta T, Reshanov S A, Rohrl J, Rotenberg E, Schmid A K, Waldmann D, Weber H B and Seyller T 2009 Towards wafer-size graphene layers by atmospheric pressure graphitization of silicon carbide *Nat. Mater.* **8** 203–7

[50] Zhou S Y, Gweon G H, Fedorov A V, First P N, De Heer W A, Lee D H, Guinea F, Castro Neto A H and Lanzara A 2007 Substrate-induced bandgap opening in epitaxial graphene *Nat. Mater.* **6** 770–5

[51] Jobst J, Waldmann D, Speck F, Hirner R, Maude D K, Seyller T and Weber H B 2010 Quantum oscillations and quantum Hall effect in epitaxial graphene *Phys. Rev. B* **81** 195434

[52] Shen T, Gu J J, Xu M, Wu Y Q, Bolen M L, Capano M A, Engel L W and Ye P D 2009 Observation of quantum-Hall effect in gated epitaxial graphene grown on SiC (0001) *Appl. Phys. Lett.* **95** 2007–10

[53] Hass J, Varchon F, Millan-Otoya J E, Sprinkle M, Sharma N, De Heer W A, Berger C, First P N, Magaud L and Conrad E H 2008 Why multilayer graphene on 4H- SiC(000$\bar{1}$) behaves like a single sheet of graphene *Phys. Rev. Lett.* **100** 125504

[54] Wu X, Hu Y, Ruan M, Madiomanana N K, Hankinson J, Sprinkle M, Berger C and De Heer W A 2009 Half integer quantum Hall effect in high mobility single layer epitaxial graphene *Appl. Phys. Lett.* **95** 223108

[55] Stankovich S, Dikin D A, Dommett G H B, Kohlhaas K M, Zimney E J, Stach E A, Piner R D, Nguyen S T and Ruoff R S 2006 Graphene-based composite materials *Nature* **442** 282–6

[56] Stankovich S, Dikin D A, Piner R D, Kohlhaas K A, Kleinhammes A, Jia Y,

Wu Y, Nguyen S T and Ruoff R S 2007 Synthesis of graphene-based nanosheets via chemical reduction of exfoliated graphite oxide *Carbon* **45** 1558–65

[57] Hummers W S and Offeman R E 1958 Preparation of graphitic oxide *J. Am. Chem. Soc.* **80** 1339

[58] Allen M J, Tung V C and Kaner R B 2010 Honeycomb carbon: a review of graphene *Chem. Rev.* **110** 132–45

[59] Meyer J C, Geim A K, Katsnelson M I, Novoselov K S, Booth T J and Roth S 2007 The structure of suspended graphene sheets. *Nature* **446** 60–3

[60] Hwang E H, Adam S and Sarma S Das 2007 Carrier transport in two-dimensional graphene layers *Phys. Rev. Lett.* **98** 186806

[61] Chen J H, Jang C, Adam S, Fuhrer M S, Williams E D and Ishigami M 2008 Charged-impurity scattering in graphene *Nat. Phys.* **4** 377–81

[62] Bolotin K I, Sikes K J, Jiang Z, Klima M, Fudenberg G, Hone J, Kim P and Stormer H L 2008 Ultrahigh electron mobility in suspended graphene *Solid State Commun.* **146** 351–5

[63] Du X, Skachko I, Barker A and Andrei E Y 2008 Approaching ballistic transport in suspended graphene *Nat. Nanotechnol.* **3** 491–5

[64] Castellanos-Gomez A, Buscema M, Molenaar R, Singh V, Janssen L, van der Zant H S J and Steele G a 2014 Deterministic transfer of two-dimensional materials by all-dry viscoelastic stamping *2D Mater.* **1** 011002

[65] Geim A K and Grigorieva I V 2014 Van der Waals heterostructures *Nature* **499** 419–25

[66] Liu Y, Weiss N O, Duan X, Cheng H, Huang Y and Duan X 2016 Van der Waals heterostructures and devices *Nat. Rev. Mater.* **1** 16042

[67] Wang L, Meric I, Huang P Y, Gao Q, Gao Y, Tran H, Taniguchi T, Watanabe K, Campos L M, Muller D A, Guo J, Kim P, Hone J, Shepard K L and Dean C R 2013 One-dimensional electrical contact to a two-dimensional material. *Science* **342** 614–7

[68] Banszerus L, Schmitz M, Engels S, Dauber J, Oellers M, Haupt F, Watanabe K, Taniguchi T, Beschoten B and Stampfer C 2015 Ultrahigh-mobility graphene devices from chemical vapor deposition on reusable copper *Sci. Adv.* **1** e15000222

[69] Banszerus L, Schmitz M, Engels S, Goldsche M, Watanabe K, Taniguchi T, Beschoten B and Stampfer C 2016 Ballistic transport exceeding 28 μm in CVD grown graphene *Nano Lett.* **16** 1387–91

[70] Novoselov K S, Fal'ko V I, Colombo L, Gellert P R, Schwab M G and Kim K 2012 A roadmap for graphene *Nature* **490** 192–200

[71] Datta S S, Strachan D R, Mele E J and Johnson A T C 2009 Surface potentials and layer charge distributions in few-layer graphene films *Nano Lett.* **9** 7–11

[72] Filleter T, Emtsev K V., Seyller T and Bennewitz R 2008 Local work function measurements of epitaxial graphene *Appl. Phys. Lett.* **93** 133117

[73] Ziegler D, Gava P, Guttinger J, Molitor F, Wirtz L, Lazzeri M, Saitta A M, Stemmer A, Mauri F and Stampfer C 2011 Variations in the work function of doped single- and few-layer graphene assessed by Kelvin probe force microscopy and density functional theory *Phys. Rev. B* **83** 235434

[74] Ferrari A C and Basko D M 2013 Raman spectroscopy as a versatile tool for studying the properties of graphene. *Nat. Nanotechnol.* **8** 235–46

[75] Ferrari A C, Meyer J C, Scardaci V, Casiraghi C, Lazzeri M, Mauri F, Piscanec S, Jiang D, Novoselov K S, Roth S and Geim A K 2006 Raman spectrum of graphene and graphene layers *Phys. Rev. Lett.* **97** 187401

[76] Thomsen C and Reich S 2000 Doable resonant Raman scattering in graphite *Phys. Rev. Lett.* **85** 5214–7

[77] Ferrari A C and Robertson J 2001 Resonant Raman spectroscopy of disordered, amorphous, and diamondlike carbon *Phys. Rev. B* **64** 075414

[78] Faugeras C, Nerriere A, Potemski M, Mahmood A, Dujardin E, Berger C and de Heer W A 2008 Few-layer graphene on SiC, pyrolitic graphite, and graphene: A Raman scattering study *Appl. Phys. Lett.* **92** 011914

[79] Zhou Z, Dou X, Ci L, Song L, Liu D, Gao Y, Wang J, Liu L, Zhou W, Xie S and Wan D 2006 Temperature dependence of the Raman spectra of individual carbon nanotubes. *J. Phys. Chem. B* **110** 1206–9

[80] Van der Pauw L J 1958 A method of measuring the resistivity and Hall coefficient on lamellae of arbitrary shape *Philips Tech. Rev.* **20** 220–4

[81] Van der Pauw L J 1958 A method of measuring specific resistivity and Hall effect of discs of aribtrary shape *Philips Res. Reports* **13** 1–11

[82] Bierwagen O, Pomraenke R, Eilers S and Masselink W T 2004 Mobility and carrier density in materials with anisotropic conductivity revealed by van der Pauw measurements *Phys. Rev. B* **70** 165307

[83] Hao L, Gallop J, Goniszewski S, Shaforost O, Klein N and Yakimova R 2013

Non-contact method for measurement of the microwave conductivity of graphene *Appl. Phys. Lett.* **103** 123103

[84] Shaforost O, Wang K, Goniszewski S, Adabi M, Guo Z, Hanham S, Gallop J, Hao L and Klein N 2015 Contact-free sheet resistance determination of large area graphene layers by an open dielectric loaded microwave cavity *J. Appl. Phys.* **117** 024501

[85] Titov M and Beenakker C W J 2006 Josephson effect in ballistic graphene *Phys. Rev. B* **74** 041401

[86] Heersche H B, Jarillo-Herrero P, Oostinga J B, Vandersypen L M K and Morpurgo A F 2007 Bipolar supercurrent in graphene *Nature* **446** 56–9

[87] Sato T, Moriki T, Tanaka S, Kanda A, Goto H, Miyazaki H, Odaka S, Ootuka Y, Tsukagoshi K and Aoyagi Y 2008 Gate-controlled superconducting proximity effect in ultrathin graphite films *Phys. E Low-Dimensional Syst. Nanostructures* **40** 1495–7

[88] Sato T, Kanda A, Moriki T, Goto H, Tanaka S, Ootuka Y, Miyazaki H, Odaka S, Tsukagoshi K and Aoyagi Y 2008 A different type of reentrant behavior in superconductor/thin graphite film/superconductor Josephson junctions *Phys. C Supercond. its Appl.* **468** 797–800

[89] Du X, Skachko I and Andrei E Y 2008 Josephson current and multiple Andreev reflections in graphene SNS junctions *Phys. Rev. B* **77** 184507

[90] Girit C, Bouchiat V, Naamanth O, Zhang Y, Crommie M F, Zetti A, Siddiqi I, Naaman O, Zhang Y, Crommie M F, Zettl A and Siddiqi I 2009 Tunable graphene dc superconducting quantum interference device *Nano Lett.* **9** 198–9

[91] Miao F, Bao W Z, Zhang H and Lau C N 2009 Premature switching in graphene Josephson transistors *Solid State Commun.* **149** 1046–9

[92] Chialvo C and Moraru I 2010 Current-phase relation of graphene Josephson junctions *arXiv Prepr.* arXiv:1005.2630

[93] Ojeda-Aristizabal C, Ferrier M, Gueron S, Bouchiat H, Guéron S and Bouchiat H 2009 Tuning the proximity effect in a superconductor-graphene-superconductor junction *Phys. Rev. B* **79** 165436

[94] Kanda A, Sato T, Goto H, Tomori H, Takana S, Ootuka Y and Tsukagoshi K 2010 Dependence of proximity-induced supercurrent on junction length in multilayer-graphene Josephson junctions *Phys. C Supercond. its Appl.* **470** 1477–80

[95] Choi J H, Lee H J and Doh Y J 2010 Above-gap conductance anomaly studied in superconductor-graphene-superconductor Josephson junctions *J. Korean Phys. Soc.* **57** 149–55

[96] Jeong D, Choi J H, Lee G H, Jo S, Doh Y J and Lee H J 2011 Observation of supercurrent in PbIn-graphene-PbIn Josephson junction *Phys. Rev. B* **83** 094503

[97] Lee G H, Jeong D, Choi J H, Doh Y J and Lee H J 2011 Electrically tunable macroscopic quantum tunneling in a graphene-based Josephson junction *Phys. Rev. Lett.* **107** 146605

[98] Borzenets I V, Coskun U C, Jones S J and Finkelstein G 2011 Phase diffusion in graphene-based Josephson junctions *Phys. Rev. Lett.* **107** 137005

[99] Coskun U C, Brenner M, Hymel T, Vakaryuk V, Levchenko A and Bezryadin

A 2012 Distribution of supercurrent switching in graphene under the proximity effect *Phys. Rev. Lett.* **108** 097003

[100] Popinciuc M, Calado V E, Liu X L, Akhmerov A R, Klapwijk T M and Vandersypen L M K 2012 Zero-bias conductance peak and Josephson effect in graphene-NbTiN junctions *Phys. Rev. B* **85** 205404

[101] Komatsu K, Li C, Autier-Laurent S, Bouchiat H and Gueron S 2012 Superconducting proximity effect in long superconductor/graphene/superconductor junctions: From specular Andreev reflection at zero field to the quantum Hall regime *Phys. Rev. B* **86** 115412

[102] Borzenets I V, Coskun U C, Mebrahtu H and Finkelstein G 2012 Pb-Graphene-Pb josephson junctions: Characterization in magnetic field *IEEE Trans. Appl. Supercond.* **22** 1800104

[103] Tsumura K, Ohsugi M, Hayashi T, Watanabe E, Tsuya D, Nomura S and Takayanagi H 2012 Development of superconducting interference device based on graphene *J. Phys. Conf. Ser.* **400** 042064

[104] Choi J-H H, Lee G-H H, Park S H, Jeong D C, Lee J-O O, Sim H-S S, Doh Y-J J and Lee H-J J 2013 Complete gate control of supercurrent in graphene p-n junctions *Nat. Commun.* **4** 2525

[105] Mizuno N, Nielsen B and Du X 2013 Ballistic-like supercurrent in suspended graphene Josephson weak links. *Nat. Commun.* **4** 2716

[106] Borzenets I V, Coskun U C, Mebrahtu H T, Bomze Y V, Smirnov A I and Finkelstein G 2013 Phonon bottleneck in graphene-based Josephson junctions at millikelvin temperatures *Phys. Rev. Lett.* **111** 027001

[107] Lee G, Kim S, Jhi S and Lee H 2015 Ultimately short ballistic vertical graphene Josephson junctions *Nat. Commun.* **6** 6181

[108] Calado V E, Goswami S, Nanda G, Diez M, Akhmerov A R, Watanabe K, Taniguchi T, Klapwijk T M and Vandersypen L M K 2015 Ballistic Josephson junctions in edge-contacted graphene *Nat. Nanotechnol.* **10** 761–4

[109] Jouault B, Charpentier S, Massarotti D, Michon A, Paillet M, Huntzinger J R, Tiberj A, Zahab A A, Bauch T, Lucignano P, Tagliacozzo A, Lombardi F and Tafuri F 2016 Josephson coupling in junctions made of monolayer graphene grown on SiC *J. Supercond. Nov. Magn.* **29** 1145–50

[110] Allen M T, Shtanko O, Fulga I C, Wang J I-J, Nurgaliev D, Watanabe K, Taniguchi T, Akhmerov A R, Jarillo-Herrero P, Levitov L S and Yacoby A 2016 Visualization of phase-coherent electron interference in a ballistic graphene Josephson junction *Nat. Phys.* **12** 128–33

[111] Ke C T, Borzenets I V, Draelos A W, Amet F, Bomze Y, Jones G, Craciun M, Russo S, Yamamoto M, Tarucha S and Finkelstein G 2016 Critical current scaling in long diffusive graphene-based Josephson junctions *Nano Lett.* **16** 4788–91

[112] English C D, Hamilton D R, Chialvo C, Moraru I C, Mason N and Van Harlingen D J 2016 Observation of nonsinusoidal current-phase relation in graphene Josephson junctions *Phys. Rev. B* **94** 115435

[113] Tsumura K, Furukawa N, Ito H, Watanabe E, Tsuya D and Takayanagi H 2016 Non-equilibrium photoexcited carrier effects in a graphene-based Josephson junction *Appl. Phys. Lett.* **108** 033109

[114] Borzenets I V., Amet F, Ke C T, Draelos A W, Wei M T, Seredinski A,

Watanabe K, Taniguchi T, Bomze Y, Yamamoto M, Tarucha S and Finkelstein G 2016 Ballistic graphene Josephson junctions from the short to the long junction regimes *Phys. Rev. Lett.* **117** 237002

[115] Kumaravadivel P and Du X 2016 Signatures of evanescent transport in ballistic suspended graphene-superconductor junctions. *Sci. Rep.* **6** 24274

[116] Li C, Guéron S, Chepelianskii A and Bouchiat H 2016 Full range of proximity effect probed with superconductor/graphene/superconductor junctions *Phys. Rev. B* **94** 115405

[117] Shalom M Ben, Zhu M J, Fal V I, Mishchenko A, Kretinin A V, Novoselov K S, Woods C R, Watanabe K, Taniguchi T, Geim A K and Prance J R 2016 Quantum oscillations of the critical current and high-field superconducting proximity in ballistic graphene *Nat. Phys.* **12** 318–22

[118] Allen M T, Shtanko O, Fulga I C, Akhmerov A, Watanabi K, Taniguchi T, Jarillo-Herrero P, Levitov L S and Yacoby A 2016 Spatially resolved edge currents and guided-wave electronic states in graphene *Nat. Phys.* **12** 128–33

[119] Amet F, Ke C T, Borzenets I V, Wang Y-M, Watanabe K, Taniguchi T, Deacon R S, Yamamoto M, Bomze Y, Tarucha S and Finkelstein G 2016 Supercurrent in the quantum Hall regime *Science* **352** 966–9

[120] Thompson M D, Ben Shalom M, Geim A K, Matthews A J, White J, Melhem Z, Pashkin Y A, Haley R P and Prance J R 2017 Graphene-based tunable SQUIDs *Appl. Phys. Lett.* **110** 162602

[121] Nanda G, Aguilera-Servin J L, Rakyta P, Kormányos A, Kleiner R, Koelle D, Watanabe K, Taniguchi T, Vandersypen L M K and Goswami S 2017 Current-phase relation of ballistic graphene Josephson junctions *Nano Lett.* **17**

3396–401

[122] Draelos A W, Tso M, Andrew W, Ting C, Yash K, Russell M, Kenji C, Taniguchi T, Yamamoto M, Tarucha S, Borzenets I V, Amet F and Finkelstein G 2018 Investigation of supercurrent in the quantum Hall regime in graphene Josephson junctions *J. Low Temp. Phys.* **191** 288–300

[123] Song S M, Park J K, Sul O J and Cho B J 2012 Determination of work function of graphene under a metal electrode and its role in contact resistance *Nano Lett.* **12** 3887–92

[124] Borisenko V E and Ossicini S 2013 *What is what in the Nanoworld: A Handbook on Nanoscience and Nanotechnology* (John Wiley & Sons)

[125] Shailos A, Nativel W, Kasumov A, Collet C, Ferrier M, Guéron S, Deblock R, Bouchiat H, Gueron S, Deblock R and Bouchiat H 2007 Proximity effect and multiple Andreev reflections in few-layer graphene *Europhys. Lett.* **79** 57008

[126] Beenakker C W J 2008 Colloquium: Andreev reflection and Klein tunneling in graphene *Rev. Mod. Phys.* **80** 1337–54

[127] Beenakker C W J 2006 Specular andreev reflection in graphene *Phys. Rev. Lett.* **97** 1–4

[128] Belzig W 2006 Device physics: Super-semiconducting nanowires *Nat. Nanotechnol.* **1** 167–8

[129] Kaemmar S B 2011 Introduction to Bruker's ScanAsyst and PeakForce Tapping Atomic Force Microscopy Technology *Bruker Nano Surfaces Div.* **133** 1–12

[130] Li T, Gallop J, Hao L and Romans E 2019 Scalable, tunable Josephson

junctions and dc SQUIDs based on CVD graphene *IEEE Trans. Appl. Supercond.* **29** 1101004

[131] De Gennes P G 1964 Boundary effects in superconductors *Rev. Mod. Phys.* **36** 225–37

[132] Das Sarma S, Adam S, Hwang E H and Rossi E 2011 Electronic transport in two-dimensional graphene *Rev. Mod. Phys.* **83** 407–70

[133] Li T, Gallop J, Hao L and Romans E 2018 Ballistic Josephson junctions based on CVD graphene *Supercond. Sci. Technol.* **31** 045004

[134] Yoon D, Son Y W and Cheong H 2011 Negative thermal expansion coefficient of graphene measured by raman spectroscopy *Nano Lett.* **11** 3227–31

[135] Li C, Liu Q, Peng X and Fan S 2016 Measurement of thermal expansion coefficient of graphene diaphragm using optical fiber Fabry-Perot interference *Meas. Sci. Technol.* **27** 075102

[136] Singh V, Sengupta S, Solanki H S, Dhall R, Allain A, Dhara S, Pant P and Deshmukh M M 2010 Probing thermal expansion of graphene and modal dispersion at low-temperature using graphene nanoelectromechanical systems resonators *Nanotechnology* **21** 165204

[137] Bao W, Miao F, Chen Z, Zhang H, Jang W, Dames C and Lau C N 2009 Controlled ripple texturing of suspended graphene and ultrathin graphite membranes *Nat. Nanotechnol.* **4** 562–6

[138] Mann S, Kumar R and Jindal V K 2017 Negative thermal expansion of pure and doped graphene *RSC Adv.* **7** 22378–87

[139] Ogurtani O T, Senyildiz D and Cambaz Buke G 2018 Wrinkling of graphene

because of the thermal expansion mismatch between graphene and copper *Surf. Interface Anal.* **50** 547–51

[140] Kim S, Nah J, Jo I, Shahrjerdi D, Colombo L, Yao Z, Tutuc E and Banerjee S K 2009 Realization of a high mobility dual-gated graphene field-effect transistor with Al_2O_3 dielectric *Appl. Phys. Lett.* **94** 062107

[141] Xia F, Perebeinos V, Lin Y, Wu Y and Avouris P 2011 The origins and limits of metal-graphene junction resistance *Nat. Nanotechnol.* **6** 179–84

[142] Russo S, Craciun M F, Yamamoto M, Morpurgo A F and Tarucha S 2010 Contact resistance in graphene-based devices *Phys. E Low-Dimensional Syst. Nanostructures* **42** 677–9

[143] Beenakker C W J 1992 Three “universal” mesoscopic Josephson effects *Transport Phenomena in Mesoscopic Systems* (Berlin, Heidelberg: Springer) pp 235–53

[144] Smirnov S, Fulvio P F, Lavrik N V, Ivanov I, Chi M, Meyer H, Vlassiouk I, Datskos P, Dai S and Hensley D 2011 Electrical and thermal conductivity of low temperature CVD graphene: the effect of disorder *Nanotechnology* **22** 275716

[145] Khapaev M M 2001 Inductance extraction of multilayer finite-thickness superconductor circuits *IEEE Trans. Microw. Theory Tech.* **49** 217–20

[146] Wellstood F C, Urbina C and Clarke J 1989 Hot-electron limitation to the sensitivity of the dc superconducting quantum interference device *Appl. Phys. Lett.* **54** 2599–601

[147] Tolpygo S K, Gurvitch M, Tolpygo S K and Gurvitch M 1996 Critical

currents and Josephson penetration depth in planar thin-film high-Tc Josephson junctions *Appl. Phys. Lett.* **69** 3914–6

[148] Zhang H Q, Jin Y and Qiu Y 2015 The optical and electrical characteristics of PMMA film prepared by spin coating method *IOP Conf. Ser. Mater. Sci. Eng.* **87** 012032

[149] Kroll J G, Uilhoorn W, van der Enden K L, de Jong D, Watanabe K, Taniguchi T, Goswami S, Cassidy M C and Kouwenhoven L P 2018 Magnetic field compatible circuit quantum electrodynamics with graphene Josephson junctions *Nat. Commun.* **9** 4615

[150] Schmidt F E, Jenkins M D, Watanabe K, Taniguchi T and Steele G A 2018 A ballistic graphene superconducting microwave circuit *Nat. Commun.* **9** 4069

[151] Wang J I J, Rodan-Legrain D, Bretheau L, Campbell D L, Kannan B, Kim D, Kjaergaard M, Krantz P, Samach G O, Yan F, Yoder J L, Watanabe K, Taniguchi T, Orlando T P, Gustavsson S, Jarillo-Herrero P and Oliver W D 2018 Coherent control of a hybrid superconducting circuit made with graphene-based van der Waals heterostructures *Nat. Nanotechnol.* **14** 120–6

Acknowledgement

I would like to express my special acknowledge to my supervisor, Dr Edward Romans, who gave me the opportunity to carry out this wonderful project and offered me brilliant suggestions whenever I met difficulties. He was always ready to discuss with me about the latest results and to answer my questions, no matter how busy he was. I would also thank my industrial supervisor, Prof Ling Hao, who kindly offered me the chance to access the expertise and the facilities in National Physical Laboratory and gave me generous help in life.

During the four years of my PhD project, I received enormous help from my colleagues in both London Centre for Nanotechnology and National Physical Laboratory. Prof John Gallop instructed me the microwave measurement techniques and provided many remarkable insights and constructive suggestions throughout the project. Prof Paul Warburton, Dr Jonathan Fenton and Dr Jonathan Burnett kindly assisted me with the cryogenic and measurement systems. Dr Arnaud Blois, and Dr David Cox gave me many helpful suggestions on EBL and other fabrication processes. Dr Ruth Hill-Pearce patiently taught me how to use AFM and KPFM. I would like to give my sincere thanks to all my colleagues for their generous help.

I would like to thank all the supporting staff in the LCN cleanroom, especially Dr Suguo Huo, Vijay Krishnan, Rohit Khanna, and Steve Etienne, who have done a wonderful job in the management and maintenance of the cleanroom. Without their expert guidance on the equipment and processes, I could hardly have developed the fabrication process within a relatively short time.

I would also thank other PhD students who provided me many inspirational ideas in everyday discussion, including Dr Trupti Patel, Dr Nuno Braz, Dr Oscar Kennedy,

Jamie Potter, Dr Timothy Wootton, Dr Nicolas Constantino, Dr Muhammad Shahbaz Anwar, Dr Yuvaraj Dhayalan, Thomas Godfrey, Dr Bo Li, Rui Wang, Dr Limin Ma, Dr Chenguang Liu, Dr Zaihua Yang, and Dr Xueshen Wang.

I would greatly thank the UCL Outstanding Research Scholarship, LCN Doctoral Training Grant PhD Studentship, UK Engineering and Physical Sciences Research Council (EPSRC), the UK National Measurement System (NMS), and the European Metrology Programme for Innovation and Research (EMPIR) for generously supporting my PhD research. I also thank Institute of Physics (IOP) for kindly offering me the travel grant to attend the ASC 2018 conference.

At last, I would like to thank my wife, Dr Shiqi Wang, for her genuine love and wholehearted support in my life.